SAR POLARIMETRY FOR CHARACTERIZATION AND RETRIEVAL OF EARTH AND LUNAR SURFACE

Ph.D. THESIS

by

POOJA MISHRA

DEPARTMENT OF ELECTRONICS AND COMMUNICATION ENGINEERING
INDIAN INSTITUTE OF TECHNOLOGY ROORKEE
ROORKEE - 247667 (INDIA)
JULY, 2014

SAR POLARIMETRY FOR CHARACTERIZATION AND RETRIEVAL OF EARTH AND LUNAR SURFACE

A THESIS

Submitted in partial fulfilment of the
requirements for the award of the degree
of
DOCTOR OF PHILOSOPHY
in
ELECTRONICS AND COMMUNICATION ENGINEERING

by

POOJA MISHRA

DEPARTMENT OF ELECTRONICS AND COMMUNICATION ENGINEERING
INDIAN INSTITUTE OF TECHNOLOGY ROORKEE
ROORKEE - 247667 (INDIA)
JULY, 2014

INDIAN INSTITUTE OF TECHNOLOGY ROORKEE
ROORKEE

CANDIDATE'S DECLARATION

I hereby certify that the work which is being presented in the thesis entitled **"SAR POLARIMETRY FOR CHARACTERIZATION AND RETRIEVAL OF EARTH AND LUNAR SURFACE"** in partial fulfilment of the requirements for the award of the Degree of Doctor of Philosophy and submitted in the Department of Electronics and Communication Engineering of the Indian Institute of Technology Roorkee, Roorkee is an authentic record of my own work carried out during a period from July, 2010 to July, 2014 under the supervision of Dr. Dharmendra Singh, Professor, Department of Electronics and Communication Engineering, Indian Institute of Technology Roorkee, Roorkee.

The matter presented in this thesis has not been submitted by me for the award of any other degree of this or any other Institute.

(POOJA MISHRA)

This is to certify that the above statement made by the candidate is correct to the best of my knowledge.

(Dharmendra Singh)
Date: Supervisor

The Ph.D. Viva-Voce Examination of **Ms. Pooja Mishra,** Research Scholar, has been held on.....

Signature of Supervisor Chairman, SRC Signature of External Examiner

Head of the Department/Chairman, ODC

Preface

This thesis "SAR Polarimetry for Characterization and Retrieval of Earth and Lunar Surface" explores the utilization of polarimetric Synthetic Aperture Radar (SAR) data for extracting constructive information in the form of polarimetric parameters to be used in various applications, like land cover identification, classification, and surface parameter retrieval for Earth and lunar surface. The main objective of the thesis is to pursue these tasks by using concepts of SAR polarimetry and electromagnetic wave modelling with emphasis on developing algorithms, which may require minimum or no '*a priori*' information.

Four tasks have been carried out in this thesis; (i) Study of model based decomposition methods and its analysis to visualize the effect of decomposition and deorientation for enhancement of land cover identification using polarimetric SAR data, (ii) Development of adaptive land cover classification algorithm using spatial statistics of polarimetric indices, (iii) Application of transmission line theory for development of algorithm for retrieval of soil moisture in bare soil and vegetation covered soil using minimum or no '*a priori'* information, and (iv) Study and analysis of hybrid polarimetric MiniSAR data, and the development of algorithm for possible existence of water-ice deposits on lunar surface.

Fully polarimetric ALOS PALSAR and/or Radarsat-2 data of Roorkee city in the state of Uttarakhand, India, have been used for characterization and soil moisture retrieval of Earth surface. The characterization of lunar surface in terms of identification of possible water-ice deposits has been performed by using hybrid polarimetric MiniSAR data of Peary and Rozhdestvenskiy craters.

The thesis includes seven chapters. *Chapter one* presents the introduction, which consists of motivation, scope, and objectives of the thesis.

In *Chapter two,* the state-of-the-art in the fields of advances made in SAR polarimetry, land cover classification methods, and soil moisture retrieval approaches has been briefly described. This chapter also elucidates the theoretical background for the presence of water-ice deposits on lunar surface. Critical reviews of presently available approaches for identifying regions having possible water-ice deposits on lunar surface have been presented, along with the

discussion of limitations and challenges associated with them.

In *Chapter three*, the study of incoherent model based decomposition methods with and without applying deorientation has been performed. The advantage of model based decomposition methods is their ability to extract polarimetric information from SAR data by expressing average scattering mechanism as the summation of individual scattering components, such as volume (P_v), surface (P_s), double-bounce (P_d), and/or helix component (P_c). In literature, there are several three- and four component model based decomposition methods. However, it is observed that due to similar polarimetric response, several land covers such as vegetation and oriented building blocks, decomposed into same volume scattering component by model based decomposition methods. In order to overcome this problem, it is suggested to apply deorientation i.e., rotation of target matrix (coherency or covariance) by radar line-of-sight, prior to decomposition. The deorientation effect results in getting same scattering response from differently oriented similar targets, and different scattering response from distinct targets, which might be producing same response before deorientation. Thus, this chapter analyses seven different three- and four-component model based decomposition methods, in which two methods are without deorientation, and other five are with deorientation. The methods without deorientation are, three component model based decomposition (TCM) proposed by Freeman and Durden in 1998 and four component model based decomposition (FCM) proposed by Yajima et al. in 2008. Model based decomposition methods with deorientation are, three component model based decomposition method with deorientation (TCMD) proposed by An et al. in 2010; three component model based decomposition method with double deorientation and adaptive volume scattering model (TCMDDA) proposed by Cui et al. in 2012; four component model based decomposition method with deorientation (FCMD) proposed by Yamaguchi et al. in 2011; four component model based decomposition with deorientation and additional volume scattering model (FCMDA) proposed by Sato et al. in 2012; and four component model based decomposition method with double deorientation (unitary transformation along with rotation) (FCMDD) proposed by Singh et al. in 2013. The results of these decomposition methods have been evaluated by performing visual and quantitative analyses for ALOS PALSAR data sets of Roorkee, Meerut, and Delhi cities of India. Two types of quantitative analysis have been performed; first, by analysing the variation in number of pixels for each scattering contribution; and second, by observing the scattering behaviour in terms of percentage of scattering power for different land covers. First quantitative

analysis shows that in TCMD and TCMDDA, the pixel percentages of P_s and P_d increase as compared with TCM. In FCMD, FCMDA, and FCMDD, P_d increases drastically in terms of pixel percentage as compared with FCM. The pixel percentage of P_s is incremented by approximately 2% in FCMDA, and is invariant in FCMDD, as compared with FCMD. Pixel percentage having helix contribution (i.e., P_c) is increased by 2% in FCMD as compared with FCM, and is invariant in both FCMDA and FCMDDA. By second quantitative analysis, it has been observed that uncertainty always lies in the description of scattering mechanism of urban, tall vegetation, and short vegetation regions, because there is no distinct scattering mechanism which is dominant for these land covers in all decomposition methods. Only bare soil provides distinct pattern by having very strong contribution of surface scattering. After deorientation, double-bounce power is definitely enhanced, however, it is not the dominant scattering mechanism in urban area. This may occur due to the presence of large amount of vegetation within urban area (Roorkee city).

In *Chapter four,* the problems associated with fixed-threshold based land cover classification algorithms and the need for the development of adaptive classification algorithm have been discussed. This chapter presents the development procedure for image statistics (median and standard deviation) based adaptive land cover classification algorithm by using best-selected polarimetric indices on the basis of separability index criterion. The algorithm provides optimum value of polarimetric indices on the basis of user-specific requirements (i.e., overall accuracy). The algorithm has been developed and validated on two different ALOS PALSAR data of same site i.e., Roorkee. For first ALOS PALSAR data, the overall accuracy is obtained as 87.59%, whereas producer accuracy is obtained as 98%, 71%, 86%, 92% and 95% for bare soil, water, tall vegetation, short vegetation, and urban, respectively, For second ALOS PALSAR data, the overall accuracy is obtained as 78.43%, whereas producer accuracy is obtained as 98%, 57%, 66%, 84%, and 97% for bare soil, water, tall vegetation, short vegetation, and urban, respectively.

In *Chapter five,* the key issues related to the problems involved with the retrieval of soil moisture under vegetation cover by SAR data have been discussed. Considering the limitations of currently available soil moisture retrieval algorithms, this chapter presents multilayer model for retrieval of soil moisture in both bare soil and vegetation covered soil using the classical concept of transmission line theory. In this chapter, two different models have been developed for characterization of scattering from vegetation and bare soil regions. In case of vegetation,

three layer model having one layer of vegetation canopy and two layers of soil have been considered, whereas in case of bare soil, due to exclusion of vegetation layer the model consists of only two layers of soil. For both the models, calculated backscattering coefficients have been obtained as a function of complex dielectric constant and thickness of each layer involved in respective models. The observation depth for retrieval of soil moisture varies from one tenth of wavelength to one quarter wavelength. Therefore, the first layer of soil is considered to have thickness of 5 cm and second layer of soil is taken as infinite. In case of three layer model, the thickness of vegetation-air mixed layer is considered to have thickness in the range 5 cm to 400 cm, assuming all agricultural vegetation fall within this range. Now, the complex dielectric constant of each layer involved in respective models are retrieved though Genetic Algorithm (GA) approach by minimizing cost function. The cost function is formed by taking backscattering coefficient calculated by each model and HH polarized backscattering coefficient measured by SAR data. The developed algorithm has been applied on two data sets of ALOS PALSAR and one data set of Radarsat-2 of Roorkee city, and quite satisfactory results have been obtained by comparing the retrieved soil moisture values with observed soil moisture values. The advantages of the proposed approach are its capability to estimate soil moisture with good accuracy and requirement of minimum '*a priori'* information.

In *Chapter six*, a decision tree algorithm has been developed for finding the possibilities of water-ice deposits on lunar surface using MiniSAR data. In radar based missions, high value of received radar circular polarization ratio (μ_c >1) has been traditionally used as a key criterion for determining the evidences of possible water-ice deposits in cold dark permanently shadowed regions. However, rough and dry surfaces containing rocks, lava flows, ejecta etc., also represent μ_c >1 due to double-bounce effect. Differentiation on the basis of criterion μ_c > 1 is very challenging because of two different phenomenon associated with lunar surface, namely volume scattering caused due to presence of planetary water-ice, and surface roughness caused by ejecta, rocks, or lava flows. Therefore, in this chapter, the information of two different approaches has been fused which are polarimetric approach (*m*-δ and *m*-χ decomposition) and fractal approach (fractal dimension '*D*'). The polarimetric approach helps in obtaining scattering information of lunar surface, whereas fractal dimension '*D*' helps in retrieving roughness information. After exhaustive study, various criteria have been obtained and incorporated in a decision tree. In this decision tree, the criteria for icy craters proposed by Thompson et al., have also included in order to provide confidence about regions having

possibility of water-ice deposits. It has been observed that there are certain common regions inside anomalous craters on the floor of Peary and Rozhdestvenskiy craters which satisfy all the conditions of proposed approach. In this chapter, the study of electrical and physical properties like, dielectric constant of lunar surface ($\varepsilon = \varepsilon' - j\,\varepsilon''$), loss tangent ($\tan\delta$), and regolith bulk density (ρ_0), has also been performed.

Finally, the work carried out in this thesis has been concluded in *Chapter seven*. This chapter presents the contributions of the thesis and the prospects of extending the tasks of thesis in future.

Acknowledgements

Reaching at the final stage of my Ph.D., I feel grateful to several people who helped me one way or other, for making this thesis possible. I am thankful to them for what I am achieving, and for what I have become now. At this moment, I am realizing that I cannot thank enough the people, whom I owe the most.

First and foremost, I would like to express my profound sense of reverence to my guide Professor Dharmendra Singh, for introducing me to the field of SAR Polarimetry. I am grateful to him for his expert guidance, motivation, rapt and laconic approach followed by persistent support throughout my doctoral study. Despite his "*very busy*" schedule, he always spared his valuable time to discuss several welters during my research period. I admit feeling sorry to bother him on several occasions, but he never revealed any unwillingness to assist me. Rather he always asked me "Yes! What's the Problem?", whenever I entered his office, and he listened to me patiently. By using his foreboding capabilities, he always gave a tenacious remedy for the hurdle. During most demanding stage of thesis writing, he gave me strength, moral support, and zeal that I required to move on. It would be hard to encompass that how much I benefited from his deep insight, ratiocination, and invaluably accurate intuitions, which remarkably help me grow as a student and a researcher. I hope this is not the end, and there are far more things to learn from him in future.

My sincere thanks to the member of my research committee Prof. M. K. Arora, Dr. R. Balasubramanian, Dr. A. Patnaik, and Prof. M. V. Kartikeyan, for their critic review and valuable suggestions for improving the quality of my research work. I am thankful to the Head of Department, Prof. M. V. Kartikeyan for providing computing and other facilities required for my research work. My sincere thanks to Prof. S. N. Sinha, Prof. Bharoti Sinha, Dr. N. P. Pathak, and Dr. Debashish Ghosh, for their encouragement and concern about my progress.

A special mention goes to all my lab colleagues in Microwave Imaging and Space Technology Applications (MISTA) lab, with whom I shared several joyous moments in last four years. First, I would like to express my regards to former research students Dr. Rishi Prakash, Dr. A. N. Gaikwad, and Dr. Triloki Pant, for their encouragement and assistance during initial phase of my Ph.D. It was wonderful to share workspace with Tasneem and Dr.

Abhishek, who were always considerate, respectful, and helpful at times in need and a favour. I am thankful to Mr. Dharmveer for never saying *'no'* to anything I asked for, be it fixing computer related problems, or typing Hindi text. I will always cherish the moments shared with Smitha mam, Ravi, Shruti, Nazim, Ankita mam, and Akanksha, who were always kind and supportive, and with whom I had the opportunity to enjoy little things, like small conversation, tea break etc., in my everyday life. I am thankful to former and present M. Tech. and IDD students: Shashikant, Prashant, Ajaey, Vishal, Shailesh, Ghanshyam, Sandeep, Yogendra, Ankit, Rajashekar, Ganpati, Yogesh, Maj. Prashant, Amit sir, Ashish, Sandeep Shukla, Isha, Kirti, and Namrata, for providing cheerful company in lab. Thanks are due to former and present JRFs Vivek, Shivangi, Shweta, Nupur, Varsha, and Priyanka, who were always supportive and reverential. I would like to acknowledge the support extended by Shravan by making tea, coffee, and bringing snacks at countless occasions for small treats and parties, we had in our lab. With all my heart, I am thankful to all my lab mates, and I wish them very bright future ahead.

I am thankful to, Shrabony, Rakhi, Sudesh, Kanika, and Meera, for extending their cordial friendship to me. Without them, the hostel life would have been very tiring and irksome. Their affection, care, and support always kept me elated. Meeting them in hostel, after spending several hours in lab, with exhaustive state of mind, was very refreshing.

Last, but not the least, I would like to thank my family for their unconditional love, support, and encouragement. I would like to pay my deep regards to my parents (Mr. Atul Mishra and Mrs. Neelam Mishra) for their sincere encouragement and inspiration during all these years of study, which made me to surpass this spasmodic phase of life. I find it hard to thank them enough for understanding me, and letting me do whatever I want. My regards are due to my elder sister (Mrs. Priya Shukla) and brother-in-law (Mr. Upendra Shukla) for their affection, concern, and for making me feel protected. I thank them and my little sister (Sakshi) for keeping me away from all the disquietudes, and letting me do my work peacefully. I would like to acknowledge my two little packets of pleasure, my little sister (Mani) and niece (Ishi) for their cheerful and endless telephonic conversations, full of flair and usually overjoying. Most importantly, I would like to acknowledge my solid support system, Vibhore, my best friend and fiancée, for his warmth, attention, affection, and patronage, throughout my research work. I am thankful to him for being there for me any time I need. I thank him for making me feel-at-home by bringing delicious home-made food caringly sent by his mother (Mrs. Mithlesh

Devi). I affectionately show appreciation to him for his offer to proofread my thesis for grammatical mistakes, which I often make.

You all have contributed irrevocably in shaping my life. It is difficult for me to thank you enough.

-Pooja Mishra

Table of Contents

List of Figures

List of Tables

List of Symbols

Chapter 3

P_c	Power contribution for helix scattering
P_d	Power contribution for double-bounce (dihedral) scattering
P_s	Power contribution for single-bounce (surface) scattering
P_v	Power contribution for volume scattering
$p(\theta)$	Probability density function
[S]	Scattering matrix
$[T_c]$	Coherency matrix with helix scattering contribution
$[T_d]$	Coherency matrix with dihedral scattering contribution
$[T_s]$	Coherency matrix with surface scattering contribution
$[T_v]$	Coherency matrix with volume scattering contribution
$R_2(\theta)$	2×2 rotation matrix
$R(\theta)$	3×3 orthogonal rotation matrix
$R(\varphi)$	3×3 unitary transformation matrix

Chapter 4

μ	Mean
σ^0	Backscattering coefficient
M	Median
S	Standard deviation
SI	Separability Index

Chapter 5

ε	Complex dielectric constant
ε'	Real part of dielectric constant
ε''	Imaginary part of dielectric constant
ε_{rS}	Complex dielectric constant of soil layer
ε_{rV}	Complex dielectric constant of vegetation-air mixed layer
μ	Complex permeability
f	Frequency
λ	Wavelength

Γ	Reflection coefficient
γ	Propagation constant
θ_i	Incidence angle
ω	Angular frequency
E	Electric field intensity
H	Magnetic field intensity
k	Wave number
m_v	Volumetric soil moisture
t_S	Thickness of soil layer
t_V	Thickness of vegetation-air mixed layer
Z_0	Intrinsic wave impedance
Z_C	Effective series impedance
Z_L	Parallel impedance
Z_S	Impedance of soil layer
Z_T	Total input impedance looking towards media
Z_V	Impedance of vegetation-air mixed layer

Chapter 6

χ	Polarimetric ellipticity angle
ψ	Polarimetric orientation angle
μ_c	Circular polarization ratio
μ_L	Linear polarization ratio
α	Enhancement in same sense circularly polarized echoes
γ	Enhancement in opposite sense circularly polarized echoes
δ	Relative phase shift between LH-LV component
ρ_0	Regolith bulk density
g	Stokes vector
D	Fractal dimension
m	Degree of polarization
m_c	Degree of circular polarization
m_L	Degree of linear polarization
Me	Mean
$tan\ \delta$	Loss tangent

List of Acronyms

2DVM	Two Dimensional Variation Method
AIEM	Advanced Integral Equation Model
ALOS	Advanced Land Observing Satellite
ASAR	Advanced Synthetic Aperture Radar
CBOE	Coherent Backscatter Opposition Effect
CPR	Cross Polarization Ratio
EM	Electromagnetic Wave
ENVISAT	ENVIronmental SATellite
ERS	European Remote Sensing Satellite
FCM	Four Component Model based decomposition
FCMD	Four Component Model based decomposition with Deorientation
FCMDA	Four Component Model based decomposition with Deorientation and Additional volume scattering model
FCMDD	Four Component Model based decomposition with Double Deorientation
GA	Genetic Algorithm
GO	Geometrical Optics
HH	Horizontal transmit Horizontal receive
HV	Horizontal transmit Vertical receive
IEM	Integral Equation Model
ISRO	Indian Space Research Organisation
JERS	Japanese Earth Resource Satellite
KA	Kirchhoff's Approximation
LAI	Leaf Area Index
lb	Lower bound
LCROSS	Lunar Crater Observation and Sensing Satellite
LH	Left circular transmit Horizontal receive
LL	Left circular transmit Left circular receive

LPND	Lunar Explorer Neutron Detector
LPNS	Lunar Prospector Neutron Spectrometer
LR	Left circular transmit Right circular receive
LRO	Lunar Reconnaissance Orbiter
LV	Left circular transmit Vertical receive
MAP	Maximum a Posteriori
M^3	Moon Mineralogy Mapper
MIMICS	MIchigan MIcrowave Canopy Scattering
Mini-RF	Miniature Radio Frequency
MiniSAR	Miniature Synthetic Aperture Radar
NASA	National Aeronautics and Space Administration
NDPI	Normalized Difference Polarization Index
OA	Overall Accuracy
OC	Opposite sense Circular
PALSAR	Phased Array L-band Synthetic Aperture Radar
PDF	Probability Density Function
PO	Physical Optics
PolSAR	Polarimetric Synthetic Aperture Radar
PWC	Plant Water Content
RADAR	Radio Detection and Ranging
RAR	Real Aperture Radar
RGB	Red Green Blue
RISAT	Radar Imaging Satellite
RMS	Root Mean Square
ROI	Region of Interest
RR	Right circular transmit Right circular receive
RT	Radiative Transfer
RVI	Ratio Vegetation Index
SAR	Synthetic Aperture Radar
SC	Same sense Circular
SLC	Single Look Complex
SPM	Small Perturbation Model

SSA	Small Slope Approximation
SVM	Support Vector Machine
TCM	Three Component Model based decomposition
TCMD	Three Component Model based decomposition with Deorientation
TCMDDA	Three Component Model based decomposition with Double Deorientation and Adaptive volume scattering
TM	Transverse Magnetic
TPSAM	Triangular Prism Surface Area Method
ub	Upper bound
VV	Vertical transmit Vertical receive
WCM	Water Cloud Model
WPS	Weighted Polarization Sum

Chapter 1

Introduction

Synthetic Aperture Radar (SAR) polarimetry is an important tool for land cover characterization and surface parameter (soil moisture, surface roughness, electrical, and physical, etc.,) retrieval of Earth and other planetary surfaces such as Moon. SAR polarimetry is related to transmission of known polarization and reception of modified polarization in the form of backscattered wave received from different scatterers. The interaction of propagating electromagnetic (EM) waves with these scatterers produces unique signature by representing distinct scattering mechanisms. Polarized backscattered wave contains crucial information related to scattering behaviour as well as geometrical, physical, and electrical properties of scatterers. Thus, SAR polarimetry provides a way to explore and characterize different land covers because of its capability of providing large spatial coverage and high resolution images.

Polarimetric SAR sensors exploit abundant information about scatterers than conventional radars by measuring phase along with amplitude for multi-polarization acquisitions. This multidimensional information (phase and amplitude of different polarizations) obtained from polarimetric SAR images helps in resolving the uncertainties about the source of scattering [437]. These characteristics have made SAR polarimetry a crucial science for land cover identification, characterization, and retrieval of surface parameters. There are several reasons for which land cover characterization and parameter retrieval is required, which are as follows:

- Land cover identification and classification is required for proper planning and management of resources available on Earth's surface. Changes appearing over Earth's surface owing to increase in population, change in environmental conditions, occurrence of disasters (e.g., flood, earthquake, drought, etc.,) require continuous monitoring.
- One of the most important surface parameters of Earth is soil moisture, which plays an important role for improving hydrologic, weather, and climate modelling. The soil moisture represents only 0.00012% of volume of water as compared to total water present on the Earth's surface [402]. Still, it plays an important role in determining the

prospective of infiltration, surface run-off, flood, overland flow, erosion, etc., [94]. In agronomy, soil moisture is beneficial in prediction of plant water requirement, vegetation growth, productivity, irrigation requirement, and cultivation time [402].

- Lunar surface characterization is required for exploring the possibility of resources such as minerals, water-ice deposits, etc., available over the surface of Moon. It is required to determine radio-physical and electrical properties of lunar surface for understanding the nature of lunar surface and its scattering behaviour. Due to its proximity to Earth, the study carried out over Moon may act as an archetype for exploring other planetary surfaces.

The property of SAR sensors to provide day-night acquisition independent of weather conditions, and their capability to collect scattering response from surfaces and sub-surfaces due to penetration capability of EM waves [437] help in above mentioned surface monitoring applications.

1.1. Motivation

The polarimetric SAR carries out measurement in multiple polarizations, multiple frequencies, and multiple incidence angles. Therefore, it has become possible to retrieve detailed information about scattering mechanisms for identification of different scatterers. By controlling the polarization of the incident wave, and measuring the full polarization properties of backscattered wave, the fully polarimetric SAR system can be used to obtain more information about the targets than by using a single and dual polarized SAR systems.

SAR polarimetry is renowned for the extraction of constructive information in the form of polarimetric parameters, to be utilized in various applications, such as land cover identification, classification, and retrieval of surface parameters. Researchers have developed various methods for land cover identification, classification, and surface parameter retrieval, by using polarimetric SAR data. However, challenges still persist in performing aforesaid tasks with requirement of minimum or no '*a priori'* information.

The fully polarimetric SAR systems measure four complex polarization combinations, which are HH (horizontal transmit-horizontal receive), HV (horizontal transmit-vertical receive), VV (vertical transmit-vertical receive), and VH (vertical transmit-horizontal receive).

The full vector nature of polarimetric SAR data allows it to be synthesized into any non-linear polarizations (Appendix-A).These non-linear polarizations are, *circular* (LL: left transmit-left received, LR: left transmit-right received, RL: right transmit-left received, and RR: right transmit-right received), *linear 45°* **(**45C: co-polarized elliptical, and 45X: cross-polarized elliptical), and *hybrid* (LH: left transmit-horizontal received, LV: left transmit-vertical received, RH: right transmit-horizontal received, and RV: right transmit-vertical received) polarizations. Thus, by fully polarimetric SAR data, advantages of any polarization can be obtained. This is beneficial in describing scattering mechanisms (e.g., volume, surface, and double-bounce scattering) of various targets due to sensitivity of scattering response of targets to polarization. Still challenges occur in discriminating targets on the basis of scattering mechanisms due to complex nature of targets, which produce combination of various scattering mechanisms [27].

Model based decomposition methods have been developed with the aim to separate scattering mechanisms obtained from different targets [138, 425, 426, 428]. However, it is observed that some similarly oriented different targets produce same scattering response. For example, oriented building blocks in urban area decompose into volume scattering component, as in vegetation, instead of exhibiting double-bounce scattering. In order to resolve this ambiguity, the concept of rotation of coherency matrix around radar line-of-sight, also known as deorientation process [210], has been suggested to be applied prior to decomposition for enhancing the performance of decomposition methods in terms of scattering response [10, 42, 90, 325, 344, 427]. However, still major concern is segregation of various land covers by scattering mechanisms. Thus, contemplative study is required to visualize the effect of decomposition and deorientation in enhancing the identification of various land covers from point of view of scattering mechanisms.

The fully polarimetric information can be exploited usefully in terms of polarimetric indices (parameters), which describe scattering, physical, and electrical behaviour of different targets. There exist several classification approaches that use fixed value of polarimetric indices as in [27, 129, 130, 250, 293, 306, 351]. The problem in these classification approaches is that the value of polarimetric indices usually vary in accordance with change in environmental conditions, observational sites, and satellite images. Another problem in these classification approaches is the selection of appropriate polarimetric index that provide separation of two different classes accurately. In order to overcome these problems, there is a need to develop

such a classification algorithm that is able to select polarimetric indices capable of segregating various land covers, and then, may use adaptive threshold of these polarimetric indices. In a nutshell, there is a requirement of developing an adaptive classification method that provides automated segregation of different land covers.

Soil moisture is one of the most important surface parameters of Earth, for which significant amount of research has been carried out by researchers all over the world using polarimetric SAR data. The sensitivity of backscattered wave to dielectric constant allows the retrieval of soil moisture by polarimetric SAR data [388]. Several soil moisture retrieval algorithms have been developed using theoretical/physical [46, 228, 353, 354, 401, 407, 436], empirical [17, 255, 409, 410, 445], and semi-empirical approaches [115, 231, 273, 274, 333, 353]. Most of these algorithms perform well only for retrieval of soil moisture in bare soil region, and under-estimate soil moisture in vegetated region. This happens due to complex scattering phenomenon associated with vegetation structure, in which the scattering from bare soil surface is very much influenced by the vegetation canopy layer that attenuates the scattering from soil, while adding its own contribution [175]. The requirement of large amount of '*a priori*' information by most of these algorithms, for their implementation, is also one of the major limitations. The retrieval of soil moisture under vegetation cover requires isolation or minimization of backscattering response obtained from soil underneath vegetation. This task requires a lot of efforts. Therefore, attention is needed to develop an algorithm for retrieval of soil moisture in vegetated region that may require minimum or no '*a priori'* information.

Radar polarimetry has got new dimensions with the inception of hybrid polarimetry, in which transmission is done at circular polarization (right/left handed), while reception is done at two linear polarizations (horizontal and vertical) in coherent manner [308]. This unique architecture provides information comparable to fully polarimetric SAR, but with wider swath coverage, reduced system complexity (mass and power consumption), and absence of range ambiguity and Faraday rotation. Thus, hybrid polarimetry is not only an optimum design for exploring planetary surfaces, but also is a worthy choice for future Earth monitoring SAR missions [308]. MiniSAR on-board Chandrayaan-1 mission, India's first lunar exploration mission launched by Indian Space Research Organisation (ISRO), was one such attempt. It was the first polarimetric SAR flown outside the Earth's orbit. The objective of this mission was to characterize lunar surface, and to find the possible evidences of water-ice deposits on lunar surface [252, 359]. This is very challenging yet fascinating task, which requires a lot of

attention.

The summary of above discussion has been presented below, keeping in mind the tasks where more attention is required:

- Critical analysis of model based decomposition methods and deorientation process for characterization of land covers.
- Investigating the effect of deorientation on scattering mechanisms associated with distinct land covers.
- Identifying the role of various polarimetric indices for classification of various land covers.
- Development of adaptive land cover classification approach providing optimum classification accuracy.
- Development of algorithm for retrieval of soil moisture under vegetation cover with minimum usage of prior information about test site.
- Critical analysis of hybrid polarimetric SAR data for characterization of lunar surface.
- Study of hybrid polarimetry for identification and characterization of various land covers.
- Development of algorithm to find the possible evidences of water-ice deposits on lunar surface by using hybrid polarimetric SAR data.
- Estimation of electrical and physical properties of lunar surface.

1.2. Problem Statement

The objective of this thesis is to extract polarimetric parameters from polarimetric SAR data for identification, classification, characterization, and parameter retrieval of Earth and Moon surfaces. In the present research work, emphasis has been given to develop algorithms for land cover characterization and surface parameter retrieval with the use of minimum or no *'a priori'* information. The discussion in section 1.1, followed by careful engrossment, actuated the present work, which consists of following tasks that have been carried out in this thesis;

1) To investigate the role of model based decomposition methods, and to critically analyse the effect of decomposition and deorientation in enhancement of land cover identification.

2) To develop adaptive land cover classification algorithm using spatial statistics of polarimetric indices.

3) To explore the use classical transmission line theory for retrieval of soil moisture in bare soil and vegetation covered soil by using minimum '*a priori'* information.

4) To develop an algorithm for possible presence of water-ice deposits on lunar surface using polarimetric and fractal based approach, and to estimate electrical and physical properties of lunar surface by using hybrid polarimetric MiniSAR data of Chandrayaan-1.

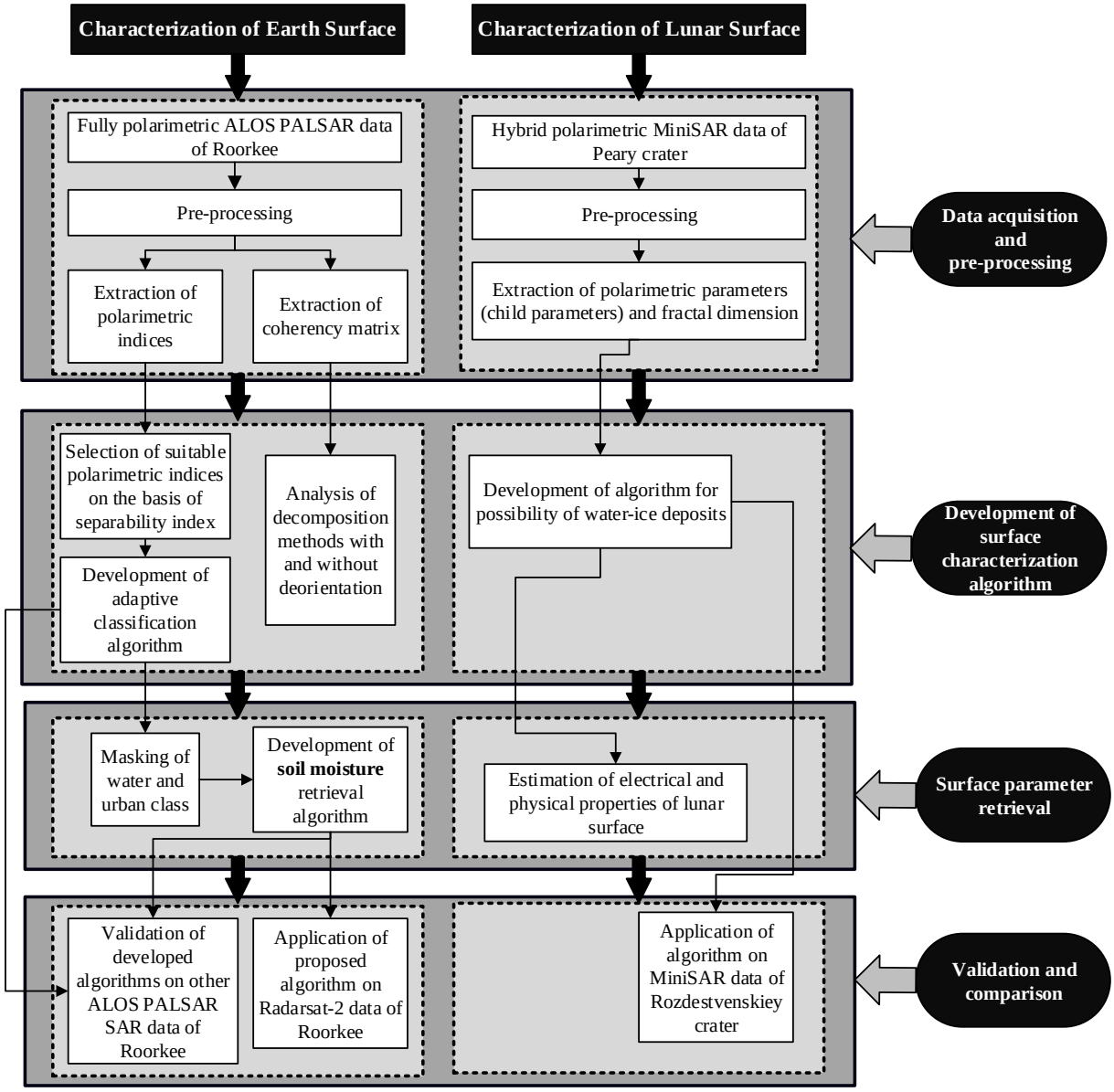

Figure 1.1: Flowchart for research framework.

1.3. Framework of Research

The framework of research is presented in Figure 1.1. The research work is divided into two parts- (i) polarimetric approach for characterization and soil moisture retrieval of Earth's surface, and (ii) polarimetric approach for possible water-ice detection and surface parameters (electrical and physical) retrieval of lunar surface.

The research work for both the parts i.e., Earth and Moon, was carried out in four stages-

1. Data acquisition and pre-processing.
2. Development of surface characterization algorithm.
3. Retrieval of surface parameters.
4. Validation and comparison of proposed algorithms.

Following subtasks have been carried out for completing the considered four tasks, as discussed in section 1.2:

- Review of literature corresponding to each task and suggesting proposal of appropriate methodologies stating the limitations of existing approaches.
- Pre-processing of ALOS PALSAR data and extraction of coherency matrix.
- Analysis of scattering components, obtained by model based decomposition methods with and without deorientation, for their usefulness in characterization of different land covers.
- Extraction of various polarimetric indices from pre-processed data.
- Selection of polarimetric indices, providing best separation between two class pair, based on separability index criterion.
- Development of adaptive land cover classification algorithm.
- Validation of proposed classification algorithm by another ALOS PALSAR data.
- Masking of water and urban area in classified image, so as to obtain only bare soil and vegetation region.
- Development of soil moisture retrieval algorithm.
- Application of proposed soil moisture algorithm on another ALOS PALSAR data and C-band Radarsat-2 data.
- Selection of hybrid polarimetric MiniSAR data of Peary crater for characterization of lunar surface.
- Pre-processing of MiniSAR data, and extraction of polarimetric parameters of hybrid

SAR, known as child parameters.

- Critical analysis of all the child parameters for obtaining the criteria satisfying possibility of water-ice deposits on lunar surface.
- Critical analysis of fractal dimension for obtaining roughness information.
- Development of algorithm incorporating all the conditions for possible presence of water-ice.
- Estimation of electrical and physical properties of lunar surface.
- Application of proposed algorithm developed, on another MiniSAR data of Rozhdestvenskiy crater.

1.4. Organisation of Thesis

The thesis includes seven chapters.

Chapter two provides the brief literature review of the tasks undertaken in the thesis. The review related to advancements made in the field of SAR polarimetry, target decomposition methods, classification methods, and soil moisture estimation methods has been provided. The limitations of existing approaches, and need of developing new algorithms, has also been discussed. The theory of water-ice deposits on lunar surface, and state-of-the-art methods for possible existence of water-ice deposits on lunar surface, have been discussed.

Chapter three deals with the task of studying seven different three and four component model based target decomposition methods, with and without applying deorientation approach. This chapter analyses the role of deorientation in improving the scattering response of various land covers. The analysis has been performed by both visual and quantitative methods.

Chapter four presents an adaptive land cover classification algorithm. The algorithm has been developed by using spatial statistics (i.e., median and standard deviation) of best-selected polarimetric indices on the basis of separability index criterion. The algorithm uses optimized values of polarimetric indices based on overall classification accuracy as required by the end user.

Chapter five includes the development of multilayer model based on transmission line theory for retrieving soil moisture in bare soil and vegetation underlying soil, by using fully polarimetric SAR data with minimum requirement of '*a priori*' information. This model is based on conventional transmission line theory which facilitates the estimation of impedance,

and hence, backscattering coefficient as a function of dielectric constant and thickness of each layer in the model. The dielectric constant in turn has been used for retrieval of soil moisture for 5 cm depth of soil.

Chapter six explores the use of hybrid polarimetric MiniSAR data of Chandrayaan-1 for lunar surface characterization, and finding the possibility of water-ice deposits on lunar surface. In this chapter, an algorithm has been proposed for identifying the regions having possible presence of water-ice deposits on lunar surface by fusing polarimetric and fractal-based approach. After obtaining possible locations of water-ice deposits on lunar surface, the electrical and physical properties, such as dielectric constant of lunar surface, loss tangent, and regolith bulk density have been computed.

Finally, *Chapter seven* provides the summary of obtained results and enlists the major contributions made in the thesis. The perspectives of future investigation, utilizing the current results, is also discussed.

Chapter 2

Background and State-of-the-Art

This chapter starts with the brief literature review related to the advancements made in the field of SAR polarimetry and its applications. Now SAR polarimetry is a well-known concept to all. Therefore, the description related to basics of SAR polarimetry is avoided in this chapter. However, the basic concepts of SAR polarimetry, polarization, and mathematical formulations for describing scattering behaviour are discussed in Appendix-A. This chapter only meditates upon the literature review, which is relevant to the tasks commenced in the thesis.

Firstly, the literature review of target decomposition theorems along with the need of analysing existing decomposition theorems with and without applying the concept of deorientation using polarimetric SAR data, has been discussed. Secondly, literatures related to land cover classification approaches based on polarimetric SAR data have been reviewed. In this section, the limitations of existing fixed decision threshold based classification algorithms, and the need of further development of adaptive classification algorithm have been discussed. Thirdly, the application of SAR polarimetry for retrieval of soil moisture along with the brief review of existing theoretical, empirical, and semi-empirical soil moisture retrieval approaches, has been discussed. Based on this review, requirement for development of soil moisture retrieval algorithm for bare soil and vegetation underlying soil by using minimum '*a priori*' knowledge has been debated in this section. Finally, the review of theoretical concept of possible water-ice deposits on the surface of Moon has been presented. This section comprises the review of work exhibiting possibility of water-ice deposits on lunar surface using radar-based and other methods, like spectroscopic methods. Thereafter, based on the review of aforesaid SAR polarimetric applications, this chapter has been concluded for further scope of research.

2.1. Review Related to Background and Advances in SAR Polarimetry

The ability of microwaves to provide radio-physical information of ground and beneath the

ground make them suitable choice for extracting information from various land covers. This information extraction is performed by both active and passive way. A*ctive illumination system* is equipped with a transmitting system, and a receiving system to accept the signal backscattered from the illuminated surface, unlike *passive illumination system*, which makes use of radiation naturally emitted (*i.e.* sunlight) or reflected by Earth [345]. Passive microwave sensors, like radiometers are used in several applications, such as meteorology [198, 235, 397-399], oceanography [21, 288, 300], and hydrology [22, 366]. Although passive sensors (infrared and visible radiometers) provide fine surface spatial resolution and excellent spectral details, their use is limited due to lack of independent source of radiation, and their inability to penetrate cloud and fog covering the area of interest. Active microwave sensors belong to imaging and non-imaging category. Non-imaging microwave sensors are scatterometer and altimeter, which are used in several applications, such as soil moisture estimation, rainfall estimation, weather forecasting, hydrological modelling, etc., [31, 104, 154, 222, 287, 302, 303, 312, 342, 343, 346]. However, their only drawback is that they provide information for particular area and specific land cover type. Active imaging sensors, mostly realized by radar systems, overcome these limitations. In conventional radar systems, usually referred to as *Real Aperture Radars (*RARs), the information about the target was taken in the form of magnitude only, and any information on phase was ignored due to static radar system. The main limitation of these sensors is the poor azimuth resolution. The only solution to this problem was to use short radar pulses of very high energy achievable only with very large aperture antenna, which was practically not feasible. The development of *Synthetic Aperture Radar* (SAR) sensors was a revolution in this field. In SAR system, forward motion of actual antenna is used to synthesize a very long antenna, and thus, high resolution is achieved even with antenna structure of reasonable size. SAR systems, being coherent, are capable of recording both magnitude and phase values. This quality of SAR sensors leads to the concept of SAR polarimetry [277].

SAR polarimetry is the science of acquiring, processing, analysing, and characterizing the polarization state of electromagnetic (EM) wave. The time-varying behaviour of transverse EM wave leads to the formation of an ellipse in the plane perpendicular to propagation, which is one of the most significant phenomenon affecting the interaction of EM wave with any object and medium of propagation. The propagation of EM wave through a medium having varying refractive index, changes the polarization state of EM wave upon reflection. This polarization

transformation behaviour is designated as *Ellipsometry* in optical imaging, and *Polarimetry* in radar imaging [165, 219, 377].

SAR polarimetry exploits the concept of polarization to describe the change of polarization state by measuring backscattered wave through vector measurement in order to utilize full polarization information. This allows measurement of both amplitude and phase of backscattered wave for any assumed combination of transmitted and received polarization. In linear basis, four complex polarization combinations are calculated- HH, HV, VV, and VH for each resolution cell of image [122]. Due to this full vector nature of linearly polarized components, it is possible to retrieve components in any other polarization basis i.e., circular and elliptical, by using simple mathematical formulations as discussed in Appendix-A. Thus, advantages of any polarization can be exploited by fully polarimetric SAR data for discrimination of different targets because of dependence of backscattering coefficient on polarization. Although a distributed target represents several scattering mechanisms, one of the scattering mechanisms—surface, double-bounce, or diffuse/volume scattering, always dominates [245], which can be described by different polarizations. For VV backscatter greater than or equal to HH backscatter, and RL backscatter (circular cross-polarized) significantly greater than RR (circular co-polarized) backscatter, represent dominant surface scattering (e.g., in bare soil) [27]. Linear cross polarized returns (i.e., HV) represent multiple scattering from rough surfaces, or volume scattering due to depolarization of targets [165]. Linear cross-polarized backscatter (HV) and depolarization ratios (HV/VV, HV/HH) maximize the difference between surface and volume scattering, and therefore, have the capability to discriminate bare soil and vegetation. The low values of HV/VV and HV/HH represent scattering from smooth surfaces, like bare soil [306]. For double-bounce scattering, HH backscatter is larger than VV and HV backscatter, and there is a very small difference between RR and RL backscatter [27, 162]. Thus, concept of SAR polarimetry helps in identification, detection, and classification of various targets.

The era of radar polarimetry was started in late 19^{th} century and early 20^{th} century. In 1920s, Wiener described the polarization properties of EM waves, which inspired Jones to introduce 2×2 Jones forward scattering matrix [182], and Mueller to introduce 4×4 averaged power density Mueller matrix for forward scattering case. At the inception of dual polarized antenna technology in 1940s [185], Sinclair claimed that transmitted and received polarization state are different, and therefore, he developed 2×2 Sinclair matrix for representing radar cross-

section of coherent targets by assuming four different combinations of transmitted and received polarization states [339]. Advancing the work of Deschamps [102], who emphasized on using Poincare sphere as a tool for representing polarization states of EM wave (Figure A.3 in Appendix-A), Kennaugh formulated the radar backscattering concept by defining "characteristic polarization states" for the components of Sinclair matrix, and developed 4×4 averaged power density Kennaugh matrix [185] for backscattering scenario. In this regards, subtle but remarkable contributions were made by Deschamps [102], Rumsey [320], Graves [156], Kales [183], Copeland [83] etc., until 1960 when Huynen introduced the concept of "*Phenomenological Approach to Radar Polarimetry*" [170, 171] in backscattering case. He modelled nine physical parameters, which became significant tool in identification and determination of geometrical, electrical, and physical characteristics of targets. For defining the characteristic polarization states of various targets, he developed the theory of "*Polarization Fork*" or "*Huynen Fork*" [171] elucidating that a fork is formed on Poincare sphere by joining co-polarized and cross-polarized nulls to the center of sphere. After this scientific contribution, the field of radar polarimetry was reinvented with keen interest of researchers all over the world.

In 1980s, Ionnidis revealed that polarization helps in segregating radar response from targets and background clutter [173]. Another concept of polarization wave synthesis and polarization signature was given by van Zyl for implementation of polarimetric imaging radars [396]. Polarization signatures were used to graphically represent the radar cross-section in terms of ellipticity and orientation angles of transmit antenna, and to describe complete polarimetric behaviour of scattering properties [116, 437, 438]. In 1980s and 90s, remarkable contributions were made by Boerner and his co-researcher by augmenting the work of Kennaugh and Huynen in target decomposition [3, 40, 95, 134], proposing several polarimetric observables, such as polarization ratios [38], inverse problems for defining polarimetric properties of scattering [37, 39, 134], and target identification approaches [3, 37, 39, 192-194].

The field of polarimetry remained undervalued until the end of 1980's, due to technological constraints, restricting practical application and implementation of polarimetric radars. SAR polarimetry reached at pinnacle in 1985 with the development of first polarimetric airborne SAR launched by National Aeronautics and Space Administration (NASA) and Jet Propulsion Laboratory (JPL). It was a L-band (1.225 GHz) quad polarimetric SAR providing the measurement of all the components of scattering matrix [84]. Since then various airborne

SAR sensors have been developed, such as Environmental Research Institute of Michigan (ERIM) at P-, L-, C-, and X-bands; Consolidated vultee aircraft (Convair-580) at X-, C-, and P-bands; Experimental Synthetic Aperture Radar (ESAR) at P-, L-, and S-bands; Phased Array Universal SAR (PHARUS) at C-band; Electromagnetics Institute's SAR (EMISAR) at L- and C-bands; Polarimetric and interferometric Synthetic Aperture Radar (PiSAR) at L-band; and ONERA's RAMSES (Radar Aéroporté Multi-spectral d'Etude des Signatures) at P-, L-, S-, C-, X-, and Ku-bands [219].

The era of space-borne polarimetric SAR was marked in 1994, with the launch of Shuttle Imaging Radar-C/X band SAR (SIR-C/X) on-board the Space Shuttles having capability to measure single polarization at X-band and quad polarization at L- and C- bands. Earlier to this endeavour, several SAR sensors were launched, such as single polarimetric (HH) SEASAT at L-band in 1978; single polarimetric (HH) SIR-A and SIR-B at L-band in 1981 and 1984, respectively; single polarimetric (VV) European Remote Sensing (ERS) satellites: ERS-1/2 at C-band in 1991/1995; single polarimetric (HH) Japanese Earth Resources Satellite-1 (JERS-1) at L-band in 1992; single polarimetric (HH) RADARSAT at C-band in 1995; and single/dual polarimetric Environmental Satellite/Advanced Synthetic Aperture Radar (ENVISAT/ASAR) at C-band in 2002. In 2006, new beginning of fully polarimetric space-borne SAR systems was started with the launch of single/dual/fully polarimetric ALOS (Advanced Land Observing Satellite) PALSAR (Phased Array L-band Synthetic Aperture Radar) at L-band. Since then several fully polarimetric SAR satellites have been launched which are X-band SAR-Lupe in 2006; C-band RADARSAT-2 in 2007; X-band Constellation of small Satellites for the Mediterranean basin Observation (Cosmo) SkyMed in 2007; X-band TerraSAR-X in 2007; X-band TanDEM-X in 2009 [219, 280]. In 2012, a new satellite named Radar Imaging Satellite-1 (RISAT-1) has been launched, which has the capability of imaging in linear and circular (or hybrid) polarizations at C-band [251].

From architectural viewpoint, fully polarimetric SAR systems appear more complex as compared with single and dual polarimetric SAR. Despite several advantages, certain limitations exist in fully polarimetric systems, such as increased pulse repetition frequency (prf), reduced coverage (swath), increased complexity, increased cost, requirement of twice the average power, and limited choice of incidence angles [63]. Thus, the concept of partial polarimetry (compact/hybrid polarimetry) was introduced, which was based on the transmission of non-linear polarization (linear 45° or circular) and reception of linear

polarization coherently [308, 309, 355, 356]. This unique architecture is considered to provide several advantages, like wider swath coverage, reduced system complexity (mass and power consumption), absence of range ambiguity and Faraday rotation, which not only is an optimum design for exploring planetary surfaces but also is a worthy choice for future Earth monitoring SAR missions. It is difficult to replace quad polarimetry by hybrid polarimetry because of complete polarimetric information provided by fully polarimetric SAR systems [63]. However, it has been reported by Panigrahi et al. [289], that information obtained from both quad and hybrid polarimetric systems is comparable, and hybrid polarimetric SAR systems are required in situations where wider swath coverage is required, like in astronomy and planetary exploration [360]. A complete comparison of these systems is provided by Touzi [375]. Based on the concept of hybrid polarimetry, polarimetric imaging radars outside the Earth orbit are Miniature Synthetic Aperture Radar (MiniSAR) on-board Chandrayaan-1 [357] and Miniature Radio Frequency (Mini-RF) on-board Lunar Reconnaissance Orbiter (LRO) [311] for characterization of lunar surface. Earth observing hybrid polarimetric satellite is RISAT-1 [251].

One inherent problem occurring in SAR images is presence of speckle. For point scatterers, scattering matrix completely describes the scattering response associated with target. However, for distributed scatterers, scattering matrix becomes random due to coherent nature of SAR imaging systems. This non-deterministic behaviour of SAR data is known as speckle [208]. Speckle noise causes granular appearance of SAR images, and thus, making it difficult to interpret, analyse, and classify SAR data for discrimination of various targets. Assuming the multiplicative nature of noise, several speckle filters have been developed, namely Lee's filter based on local statistics [206, 208] and refined local statistics [207], Frost's filter [141, 142], Kuan's filter [197], Sigma filter [209], Gamma filter, and Maximum a Posteriori (MAP) filter [196]. The applicability of these filters is limited to single polarized SAR data. Therefore, polarimetric filters, which are able to preserve fully polarimetric information and statistical relationships between individual polarizations, have been developed. Some of the notable filters are, Boxcar or Multilook filter, Lee filter [216], Refined Lee filter, Scattering Model Based filter [217], Wishart Gamma MAP filter [232], Distribution Entropy MAP (DE MAP) filter [263], Trace Based filter [136], etc. Speckles in SAR images can also be reduced by ensemble averaging or multilook process [296]. There exist several polarimetric filters. However, MAP filters (Wishart Gamma MAP and DE-MAP filter) work well by preserving

polarimetric information and very acute details of SAR image [117].

A lot of research has been done in the field of SAR polarimetry in last seven decades and still advancements are in progress on in this field. A brief review, and other theoretical and practical aspects of SAR polarimetry [35, 36, 41, 377] are described in Appendix-A.

2.2. Review Related to Target Decomposition Methods

With the advancements in SAR polarimetry, the requirement of evaluating and understanding the scattering phenomenon of ground targets and determining their dominant characteristics, was increased. Due to amalgamation of various scattering mechanisms in backscatter response from distributed targets, it was required to separate these scattering mechanisms in order to infer geophysical properties of those targets. Therefore, the concept of target decomposition has been devised, which plays an important role in land cover monitoring. The parameters extracted from decomposition theorem have extensively been used by many researchers for analysing the characteristics of various land covers. Decomposition methods represent average scattering mechanism as the weighted sum of distinct independent scattering mechanisms which are modelled by physical interpretation [377]. The idea of target decomposition was proposed by Huynen [171], which had its origins in the work of Chandrashekhar, who exhibited that scattering by a cloud of small anisotropic elements can be decomposed into the summation of a Rayleigh scattering and randomly polarized noise [62]. Since then, great interest has been shown in this field, and these decomposition methods are classified as follows:

1. Coherent decomposition methods.
2. Target dichotomy based decomposition methods.
3. Incoherent decomposition methods.

1. Coherent decomposition methods

Coherent target decomposition performs the decomposition of the first-order matrix i.e., scattering matrix for characterization of the scattering from coherent or point targets only. This can be possible only in the case, when both incident and scattered EM waves are completely polarized. Some common coherent target decomposition techniques are *Pauli, Krogager, and Cameron decompositions*. The well-known *Pauli decomposition* forms the basis of coherency matrix by expressing scattering matrix in the form of Pauli vector by using Pauli basis [78, 152,

322, 323]. This decomposition method works well for detection of natural targets, whereas it is difficult to detect man-made objects by this method [439]. The *Krogager decomposition* performs the decomposition of symmetric first-order scattering matrix into three coherent components exhibiting the scattering from spherical, dihedral, and helix scatterers [195]. Hence, it is also called SDH (Sphere-Diplane-Helix) decomposition. This decomposition method satisfactorily distinguishes man-made targets from natural targets, but exhibits inability to differentiate two different types of man-made targets [439]. *Cameron decomposition* decomposes the scattering matrix into six canonical scattering mechanisms including dipole, di-plane, trihedral, quarter-wave device, cylinder, and narrow di-plane [51]. This method works well for symmetric or point targets due to maximization of symmetric scattering component. However, the performance of this decomposition method degrades in the presence of asymmetric targets [439]. The detailed description of these decomposition methods has been given in [219, 439]. The additive nature and non-requirement of estimating second-order matrix i.e., target coherency or covariance matrix, make aforesaid decomposition methods prone to speckle noise, which is multiplicative in nature. Therefore, a multiplicative decomposition termed as *Polar decomposition* was proposed for reducing the effect of speckle noise [55]. The major problem with aforesaid decomposition methods is their inability to provide unique and basis-invariant decomposition without having prior knowledge [80, 219]. Therefore, an improvement in Cameron decomposition was proposed by Touzi [374], to develop unique and basis-invariant coherent decomposition method for detecting scattering from coherent (or pure) targets.

2. Target dichotomy based decomposition methods

Huynen decomposition falls in this category of decomposition. Huynen postulated the concept of phenomenological theory of radar targets for extracting physical and geometrical properties of coherent radar targets by nine '*Huynen parameters*'[171]. He proposed the concept of target dichotomy by expressing Mueller matrix (or Kennaugh matrix) as the summation of single target (coherent or point target) and N-target (distributed target). The retrieval of coherent target was easy. However, in case of distributed targets (section A2.4 in Appendix-A), the retrieval was difficult due to their non-symmetrical and time-invariant nature caused by noise or clutter in the environment. Thus, it was required to perform statistical averaging in order to obtain expected value of Mueller matrix. *Branes-Holm decomposition* was based on this concept [219]. This decomposition was easy and had physical basis.

However, limitations of this decomposition method were its non-unique, unstable nature, and rotation-invariance of Mueller matrix corresponding to N-target. Some modifications have been introduced in order to improve the Huynen decomposition. For example, Yang modified Huynen decomposition by simple transform of Kennaugh matrix [430], Li proposed generalized concept of Huynen target dichotomy [224], and You proposed the method of decomposing Kennaugh matrix in order to extract coherent targets from non-coherent targets [431].

3. Incoherent decomposition methods

Incoherent target decomposition deals with the decomposition of coherency or covariance matrix (second-order matrices derived from scattering matrix). The decomposition of polarimetric SAR covariance/coherency matrices has received significant attention in extraction of geophysical parameters due to its ability to emphasize radar backscatter from particular scattering mechanism. These matrices characterize the scattering process from distributed targets. Consequently, incoherent target decomposition deals with partially polarized case. Incoherent target decomposition methods can be categorized in two ways: *eigenvalue decomposition methods* [80, 81, 374] and *model based decomposition methods* [8-10, 12-14, 69-71, 88-90, 138, 213, 330, 344, 394, 395, 425-428, 440, 442].

Cloude and Pottier [77, 80] proposed *eigenvalue decomposition* for determining the dominant scattering by extracting largest eigenvalue. He introduced four parameters, namely, anisotropy '*A*', entropy '*H*', alpha 'α' (scattering type parameter), and beta 'β' (orientation angle) for expressing dominant scattering mechanism among volume, double-bounce, and surface scattering components. Therefore, these parameters emerged out as standard tool for target identification and characterization due to their ability of describing physical characteristic of targets [81, 132, 215]. Holm proposed a hybrid decomposition method based on eigenvector analysis [77] and Huynen decomposition [171], by expressing average scattering mechanism as a summation of scattering from pure target, mixed target, and noise [169]. The eigenvalue decomposition method proposed by Cloude was unique, however, some approximations required to be undertaken for interpretation of scattering mechanisms, as indicated by van Zyl who used eigenvector analysis of hermitian covariance matrix to express scattering from azimuthally symmetric media, like natural terrain [393]. Touzi indicated the change in some of the parameters, like β with change in polarization basis for asymmetrical targets. In order to overcome this limitation, he developed a roll-invariant decomposition

method by performing eigenvector analysis of scattering vector [374, 376]. A theoretical evaluation of multilook effect indicated that entropy was underestimated, anisotropy was overestimated, and alpha was either underestimated or overestimated due to speckle effect [233]. Therefore, an algorithm for removing this bias was proposed in [211]. An approach providing an alternative to entropy and alpha was given in [301].

Second category of incoherent decomposition was *model based decomposition*. The first model based decomposition was proposed by Freeman and Durden [138] for expressing average scattering mechanism as the linear sum of three physically based independent scattering mechanisms, namely volume, double-bounce, and surface scattering. This method works well for detection of natural targets such as forests, flooded and non-flooded regions, etc., [219]. The limitation of this approach is assumption of reflection symmetry condition, which results in occurrence of negative powers. In order to avoid this limitation, Yamaguchi [426, 428] and Yajima [425], proposed four component model based decomposition by adding another model representing helix scattering, as obtained from complex man-made targets in urban area. This method is quite good, and is able to detect both natural as well as man-made targets. Still, a problem occurs due to ambiguous nature of scattering in oriented building blocks of urban area, which exhibits volume scattering instead of double-bounce scattering. In order to overcome this limitation, four component decomposition with rotation of coherency matrix (deorientation process) was proposed by Yamaguchi [427]. Several modifications in three and four component model based decomposition methods have been made in terms of using different models of volume scattering, rotation of coherency matrix, unitary transformation of rotated coherency matrix, and generalization of decomposition methods [4, 8-10, 13, 14, 69, 71, 88-90, 213, 328, 344, 394, 442].

A large number of decomposition methods have been developed [14, 69, 80, 88, 89, 195, 213, 284, 344, 394, 425, 430, 440, 442] due to their popularity and their dependence on physical modelling of scattering mechanisms. Still there is need to analyse these decomposition methods and the effect of deorientation, quantitatively and qualitatively, for enhancement of the scattering mechanisms of various land covers.

2.3. Review Related to Land Cover Classification Methods

Classifying remotely sensed data is one of the most popular ways of land cover monitoring. Researchers have used classification methods for various applications involving land cover

monitoring, such as crop classification, forest mapping, oil spill detection, sea ice monitoring, etc. The intent of the classification process is to categorize all the pixels in an image into one of the several land cover classes. This categorized data may be used to produce thematic maps of the land covers present in an image. There are two main types of classification techniques, namely *parametric* and *non-parametric*. *Parametric classifiers* are again of two types: *supervised and unsupervised*. *Supervised classification* involves using '*a priori'* knowledge of data to "train" the classifier for identifying categories in an image [227]. Supervised methods require the user to collect samples to "train" or teach the classifier for determining decision boundaries in feature space, and such decision boundaries are significantly affected by the properties and the size of the samples used to train the classifier. On the other hand, *unsupervised classifiers* "learn" the characteristics of each class (and possibly even the number of classes) directly from the input data. Decision trees [283, 338, 433], artificial neural networks [26, 64, 147, 235, 347-350], or Support Vector Machines (SVM) [2, 302, 441] fall under the second category of classification, i.e., *non-parametric classification*, which does not involve estimation of statistical parameters prior to classification [227].

The classification of polarimetric SAR data has been performed by using several approaches. The initial work in classification was done by considering probability distribution function (pdf) of polarimetric SAR data. For polarimetric SAR (PolSAR), data it has commonly been assumed that the scattering coefficients measured at different combinations of transmitted and received polarizations are jointly Gaussian [155]. Therefore, until mid-90's classification of remotely sensed data was performed through Gaussian based conventional statistical techniques. For example, Kong [219] developed a supervised classification method for single-look polarimetric SAR image by estimating distance measure based on maximum-likelihood test. This classification method was extended by using normalized polarimetric SAR image by Yueh et al. [434], and Lim et al., [233]. Further extension of this approach was carried out by Lee et al., for multi-look polarimetric SAR image assuming Wishart distribution [214]. First unsupervised classification method was introduced by van Zyl, which was based on scattering mechanisms [392]. Rignot et al., developed a supervised classification method using conditional distribution combined with Markov Random Field (MRF) and Maximum A Posteriori (MAP) estimate [317]. Rignot et al. also developed unsupervised classification method based on fuzzy clustering [318]. Cloude and Pottier proposed unsupervised classification method [81] based on parameters obtained by eigenvalue decomposition ($H/A/\alpha$).

Lee et al., extended this algorithm by proposing iterative Wishart classifier [215]. Ferro-Famil further extended this approach for multi-frequency and interferometric polarimetric SAR image [131, 132]. Recently, Daboor et al. developed an unsupervised method by measuring Chernoff distance assuming Wishart distribution [92]. The estimation of distance measure was performed in several classification approaches, like Fuzzy c-mean classification [113], neural network method [65, 384], expectation maximization method [186], and wavelet transform [112].

The aforementioned traditional classification approaches perform well; however, their general ability for resolving interclass confusion is limited. Pixel-wise analysis of SAR imagery is generally complicated due to the presence of speckle, and requires statistical modelling to be employed. It is well known that in some circumstances, radar complex scattering coefficients are non-Gaussian in distribution. For this reason, various non-Gaussian models have been proposed to represent SAR data, and many of these have been extended to the polarimetric SAR (PolSAR) case. The multivariate K-distributions [221, 262, 434], G-distributions [139], and K-Wishart distribution [109], have been successful for modelling PolSAR data, and highlighting the importance of non-Gaussianity.

The classification of SAR images have been performed by using target decomposition. An iterative classification based on combined use of three component model based decomposition and eigenvalue decomposition was proposed by Li-wen et al. [223]. A decision tree classification approach based on decomposition methods (Pauli, Barnes, Holm, Korgager, Freeman, and H/A/α decompositions), SAR interferometry, and object oriented analysis, has been proposed by Qi et al. [305]. An unsupervised method based on scattering similarity using *H/A/α* decomposition has been proposed by Chen et al. [68]. Bhattacharya et al. have proposed generic SVM classifier based on Touzi decomposition [25]. Shimoni emphasized on using different methods of decomposition for classification purpose because each decomposition method highlights different land cover [334].

Another way of classifying polarimetric SAR images is knowledge-based classification methods, which use backscattering coefficient and their ratios of different polarizations for segregation of different land covers [27, 106, 129, 130, 250, 293, 306, 351, 386]. In these methods, the threshold of backscattering coefficients and their ratios for classification are obtained by experimental evaluation and validation. The advantage of these classification approaches is that they do not require prior assumption about distribution of SAR data. Some other polarimetric parameters, such as Ratio Vegetation Index (RVI) [12, 187], correlation

coefficient, Cross Polarization Ratio (CPR) [380], Weighted Polarization Sum (WPS) [85], Normalized Difference Polarization Index (NDPI) [435] etc., have been used for segregating or identifying different land covers. These parameters can be used in knowledge-based methods for improving their performance.

A good progress in SAR image classification using textural measures has been made. In context of SAR image classification grey level co-occurrence probability based texture measures [121, 172, 319, 441], wavelet based texture measures [61, 74, 133, 338], random field models [137, 317], and fractal based textural measures [2, 157, 290, 364] have been vastly used. Other textural features, like semivariogram [54] and lacunarity [166] have also been used for contextual classification of SAR images.

In recent years, various classification methods have been developed. Some of them are, region-based unsupervised Wishart classification [421], classification based on Collective Network of Binary Classifier (CNBC) based on divide and conquer approach [189], Polarimetric Iterative Region Growing with Semantics (PolIGRS) classification based on Wishart distribution [432], statistical classification model based on Spherically Invariant Random Vector (SIRV) model [135], spectral graph partitioning based classification [120], Radial Basis Function (RBF) based supervised classifier [172], super-pixel based contextual classification method having adaptive number of classes [229], a contextual classification based on multi-scale modified Pappas adaptive clustering and adaptive Markov Random Field [265], and supervised classification method by integrating colour as a visual feature extracted from pseudo-colour coded images obtained from decomposition [385, 386]. Some machine learning methods, like adaboost [180, 331] and random forest [390, 444] methods, have also been incorporated in SAR image classification.

Most of the above mentioned classification approaches either require estimation of statistical distribution [215], or use complex mathematical and image processing methods, like neural network, SVM, etc., except knowledge-based methods [27, 106, 129, 130, 250, 293, 306, 351, 386]. There exist some other knowledge based methods depending upon data-mining techniques using optical data, which are proved to be efficient classification methods [257-259, 282]. The statistics based and target decomposition based classification methods are pixel based methods, which exhibit high computational complexity, and have limited option for incorporating more polarimetric characteristics [444]. After reviewing these methods, knowledge-based methods provide good prospect for classification due to their dependence on

polarimetric SAR observables. The only limitation of this approach is the use of fixed value of polarimetric variables used in classification procedure, which hinders the performance of these classifiers in case of their application in different study area with different environmental condition and different sensor parameters of SAR image. A classification approach based on adaptive threshold would provide solution to this problem.

2.4. Review Related to Retrieval of Soil Moisture with SAR Data

Retrieval of Earth's surface parameters with SAR data is gaining so much attention by researchers due to sensitivity of radar backscatter to surface roughness, soil moisture, surface dielectric constant, and other biophysical parameters, like vegetation biomass, plant water content, etc., [412]. This is possible because of capability of EM wave to penetrate into surfaces, and gather their electrical and physical properties in terms of received radar echoes i.e., backscattering coefficient. Among these parameters, soil moisture is very important parameter because of its influence in several environmental applications [43, 101, 110, 111, 246, 327]. Retrieval of soil moisture is still very challenging because of perplexing effect of roughness and vegetation cover. The challenges in retrieval of soil moisture by SAR data occur due to complexities involved in developing robust methods, considering spatial and temporal variability of soil moisture [176].

Traditionally, soil moisture represents water contained in unsaturated zone (known as vadose zone) of aeration caused by pores within soil [45]. Technically, soil moisture is defined as the ratio of volume of water in soil to the total volume of soil (including water). It is known as volumetric soil moisture (cm^3/cm^3) [327]. Soil moisture is usually measured at the top surface of soil (first 5 cm of soil depth) [151], because of increase in attenuation of EM wave with increase in soil depth.

Soil moisture is directly related to its dielectric constant, which varies significantly with change in moisture content of soil medium. The dielectric constant in turn is related to radar backscattering coefficient, which inspired researchers to develop soil moisture retrieval algorithms using backscattering models [388]. The soil moisture retrieval algorithms by using radar backscatter can be categorized as: theoretical, empirical, and semi-empirical. The brief review of work related to these categories is presented below:

1. Theoretical models

Theoretical models are physical models having their basis in diffraction phenomenon related to interaction between EM wave and observed media. These models provide mathematical-physical relationship of backscattering coefficient as a function of radar configuration (polarization, frequency, and incidence angle) and surface characteristics (dielectric constant and surface roughness: standard deviation of the height *s* and the correlation length *l*) [145]. Due to lack of direct solution for randomly rough surface, it was required to take approximations in theoretical models. Therefore, theoretical models are generally restricted to be applied for limited range of surface roughness.

The standard theoretical models are Kirchhoff Approximation (KA) model, Small Perturbation Model (SPM), and Integral Equation Model (IEM). The KA model uses *Stationary Phase Approximation* also known as Geometrical Optics (GO) model for characterizing very rough surface, and Kirchhoff *Scalar Approximation* also known as Physical Optics (PO) model for defining medium rough surface [387]. Based on the formulations of KA, *Tangential Plane Approximation* was performed to characterize both slightly rough and very rough surfaces [103]. The SPM model was applicable for smooth surfaces only. The gap between GO and PO was filled by *Small Slope Approximation (SSA)* [404]. Fung proposed Integral Equation Model (IEM) in which only surface scattering terms were considered, neglecting second-order statistics [145]. The modification of this approach was given by Fung et al. by introducing multiple scattering effects in KA [144]. IEM approaches to GO for very rough surface. The validity conditions of this model, covering wider range of surface roughness and simple approximations, provide rather easy yet accurate solution, which became inspiration for development of various versions of IEM, namely second version of Integral Equation Model (IEMM) [73], Integral Equation Model for Second-Order Multiple Scattering (IEM2M) [7], Improved Integral Equation Model (IIEM) [146], and Advanced Integral Equation Model (AIEM) [66, 419, 446], by exhibiting improvement in roughness description. These integral equation models approach GO for very rough surface and high frequency range (X- and C-bands). In case of slightly rough surface and low frequency (L- and S-bands), IEM approaches SPM [420]. Although a lot of development has been made in IEM, the original model is generally preferred by researchers [19].

The above mentioned theoretical models have been utilized by several researchers for retrieval of soil moisture [46, 228, 353, 354, 401, 407, 436]. The dielectric constant, and hence

soil moisture, have been retrieved by mathematical inversion of these backscatter models. However, the inversions of these models require certain restraining assumptions because of difficulty in finding closed form solution [294, 411]. Therefore, dielectric constant and surface roughness cannot be determined individually without using '*a priori'* information. The retrieval of soil moisture is difficult with theoretical models by using single polarized, single frequency, and singl-pass SAR data [403]. Due to development of these models in laboratory environment, sometimes inconsistent results are obtained for natural surfaces [19], because of spatial variability of surface roughness.

2. *Empirical models*

Empirical models require large amount of experimental soil moisture and corresponding backscatter data to develop empirical relationship by regression analysis in order to retrieve soil moisture. Various sophisticated empirical models have been developed for retrieval of soil moisture in bare soil region [17, 255, 409, 410, 445]. The advantages of these models are their simplicity and their practical applicability, which allow them to be used in vegetated area for retrieval of soil moisture [239, 367, 381].

Single frequency and single polarization SAR data does not produce satisfactory results of soil moisture in most circumstances [405]. The coefficients of empirical relationships generally vary with change in study area, time, and different data sets [115]. Thus, data and site dependency of these models are the major limiting factors, which restrict their application on large scale unless surface roughness is neglected.

3. *Semi-empirical models*

Semi-empirical models provide a compromise between complexity involved in theoretical models and simplicity related to empirical models. Unlike empirical models, semi-empirical models start with physical basis, and then, simplify theoretical backscattering models by simulation or experimental data sets. The most popular semi-empirical models were proposed by Oh et al. [273] and Dubois et al [115]. Oh model in [143], shows limitation in terms of incidence angle by producing erroneous results for low incidence angle particularly at low frequency. The Dubois model is valid for medium rough surface (ks<2.5) and incidence angle greater than 30° [115]. Other semi-empirical models are developed by Shi et al. [333], Loew and Mauser [231], Song et al. [353], and Oh et al., [274], etc. The advantages of semi-empirical models are their transferability to different study area and soil conditions. However, their applicability is limited to bare soil or sparsely vegetated soil. These methods produce

inconsistent results in presence of vegetation by underestimating soil moisture [19].

2.4.1. Soil Moisture Retrieval under Vegetation Cover

The retrieval of soil moisture is complicated in vegetated areas due to scattering and attenuation effects take place in canopy layer, and it changes with the variation in dielectric (e.g., vegetation water content) and physical characteristics (e.g., structure and type) of vegetation [191]. The vegetation canopy typically represents multiple scattering effect because of direct scattering from vegetation components, direct scattering from underlying soil attenuated by canopy, and double-bounce scattering by interaction between trunk and ground (soil) [23]. The retrieval of soil moisture under vegetation cover requires isolation of scattering contribution of underlying soil from multiple scattering of vegetation [33, 191].

In order to measure soil moisture under vegetation cover, models using Radiative Transfer (RT) theory have been proposed [23, 98, 105, 228]. One of the most popular RT model is MIchigan MIcrowave Canopy Scattering (MIMICS) model proposed by Ulaby et al. [389], which provides first-order solution of RT for three layer model consisting ground layer, trunk layer, and canopy layer. Several algorithm have been developed by using MIMICS model for retrieval of soil moisture under vegetation cover [98, 105, 228, 362]. These models are difficult to invert because of complexity caused by additional canopy parameters.

Semi-empirical models are generally developed by using Water-Cloud model (WCM), which exhibits vegetation layer as a cloud of uniformly distributed spherical particles [16]. The simplicity of WCM, motivated several researchers to model vegetation scattering [6, 33, 34, 153, 226, 337, 411].

In order to implement these models, it is required to use *'a priori'* information of vegetation parameters, like vegetation water content, canopy height, etc., [23, 191]. Therefore, it is difficult to generalize these models. Due to large number of parameters involved in these models, certain assumptions (e.g., constant canopy height and surface roughness) are required to be taken so as to reduce the number of unknown parameters [153]. These models require parameterization of vegetation canopy, and more specifically, different vegetation classes require separate parameterization [23, 33, 226]. Therefore, frequent field visits are required due to spatial variability of vegetation.

Due to difficulty related to parameterization of vegetation parameters in RT based models, change detection methods have been used for retrieval of soil moisture in vegetated

regions [254, 260, 266, 268, 275]. The change detection methods generally assume that temporal variability of surface roughness and vegetation parameters is large as compared to soil moisture [255]. Therefore, change in backscatter response between repeated acquisitions of satellite represents change in soil moisture. This assumption of time-invariance nature of scattering from vegetation, limits the application of change detection methods for retrieval of soil moisture.

After reviewing the related literatures, it is observed that retrieving soil moisture under vegetation cover is still challenging and requires contemplative study. It is noticed that physical based model may provide an alternate way to retrieve soil moisture under vegetation cover. In literatures, it has been found that transmission line theory based impedance approaches have been agreeably used for determining topsoil thickness [5] and burnt coal seam [368, 369]. This method bears great potential, and therefore, it has to be explored for soil moisture retrieval under vegetation cover with polarimetric SAR data.

2.5. Review Related to Lunar Surface Characterization

2.5.1. Theory Related to Water-Ice on Lunar Surface

The possibility of finding the evidences of water-ice deposits on lunar surface has been one of the most controversial subjects among researchers. The subject of origin and source for possible presence of water-ice on lunar surface has been hypothesised by several theories. One hypothesis is that during the formation of Moon by impact between Earth and giant astronomical Mars-sized body, early Moon got heated due to this catastrophic impact, that might have created lunar magmatic ocean [167]. Water may be transported to Moon by spallation process of comets, meteorites, micro-meteorites, asteroids, etc., [15, 230, 295]. The reaction of proton in solar wind with oxygenated minerals on lunar soils may also have formed water [75, 241, 295, 321, 365]. There are some circumstantial evidences for endogenous sources of water-ice (or hydroxyl) in lunar soil. Recent study of volcanic glasses obtained by volcanic eruptions (fire-fountains), has detected the possible evidences of water (specifically, 46 parts per million) within lunar magma [321]. Water (hydroxyl) has been identified in apatite grains of basalt samples from Apollo missions [44, 242]. Lunar outgassing may also be one of the reasons for possible presence of water [86, 87].

The postulation of cold trapped area in permanently shadowed regions was given for

explaining the stability of possible water-ice on lunar surface [414]. The permanently shadowed regions exist on Moon due to low obliquity caused by 1.6° tilt of lunar rotational axis with respect to normal to the ecliptic [15]. Therefore, during rotation of Moon, deep craters in polar region would not receive sunlight at all for billions of years. This means that floor and inner walls of these craters would remain in permanent shadow, which would result in very low temperature (<100K) inside these craters. Water molecules brought on the surface of Moon may undergo destructive phenomena, like photo-dissociation [256], meteoric bombardment [15], or solar wind sputtering [204]. However, there is a possibility that some of the molecules might eventually reach to permanently shadowed regions by ballistic trajectories, and got trapped in these cold dark regions [15]. Still, there was disagreement with this theory that water-ice deposits may remain stable in these cold-traps. Therefore, thermal analysis was performed by several researchers, who indicated that in some of the Polar Regions on Moon, temperature could be as low as 26 K [15, 204, 256], which is suitable for water-ice to remain stable. Still, questions arose about evaporation rate of water-ice in these cold-dark permanently shadowed regions. Based on equation given by Watson [414], Butler [48] suggested that it takes billions of years to evaporate 1.0 centimetre cube of water-ice at 100 K. McGovern has shown that very large area on both Polar Regions of Moon exist in permanent shadow [243], where possibility of water-ice would be high.

2.5.2. Review of Work Related to Finding the Possible Existence of Water-Ice Deposits on Lunar Surface

There have been several missions to Moon for finding possible presence of water-ice deposits on its surface. First radar-based mission to Moon was NASA's Clementine bistatic radar launched in 1994. It was a circularly polarized bistatic radar, by which it was postulated that water-ice depoists exhibit two chracteristics. One was high same sense (SC) to opposite sense (OC) circular polarization, or high circular polarization ratio (μ_c). Second property was Coherent Backscatter Opposition Effect (CBOE), which cause μ_c to become maximum at bistatic angle β=0° [270]. Based on this concept, Nozette indicated the possible presence of water-ice in paermanent shadowed region of Shakleton crater in lunar South Pole [271]. Later, contradictory results were obtained by Arecibo radar, a bistatic circularly polarized radar at fixed bistatic angle β of 0.37°. Arecibo radar exhibited high μ_c in ejecta of young craters in South Pole of Moon. Thus, it was claimed that high value of μ_c in South Polar region of Moon

is caused due to surface roughness not by water-ice [53, 361].

A ray of hope was shown by the results of Lunar Prospector Neutron Spectrometer (LPNS), which indicated the presence of excess hydrogen by measuring low level of epithermal neutron flux within 0.5 m surafce of both the lunar poles [126-128]. The results of LPNS were validated by Lunar Explorer Neutron Detector (LPND) on-board Lunar Reconnaissance Orbitor (LRO) mission [240]. Later, Lunar Crater Observation and Sensing Satellite (LCROSS) crashed the Cabeus crater of South Polar Region of Moon by spent rocket stage, and revealed the presence of water and other volatiles by observing the debris [82]. Moon Mineralogy Mapper (M^3), a spectrometer on-board Chandrayaan-1 mission, has also detected the possible evidences of excessive hydroxyl (OH) and water (H_2O) molecules on lunar surface [241, 295].

The spectrometers have successfully revealed the possible existence of water-ice deposits on lunar surface [127, 241, 295]. However, from radar point of view, it is still an unresolved problem because mixed results were obained by earlier radar based missions, Clementine and Arecibo. In 2008, Indian Space Research Organisation (ISRO) launched Chandrayaan-1 mission carrying MiniSAR (Miniature Synthetic Aperture Radar), and in 2009 [357], National Aeronautics and Space Administration (NASA) launched Lunar Reconnaissance Orbitor (LRO) carrying MiniRF SAR (Miniature Radio Frequency Synthetic Aperture Radar) [311]. Both were hybrid polarimetric SAR with transmission of circular polarization and reception of coherent linear polarizations (Horizontal:H and Vertical:V). One of the purposes of these missions was to image lunar surface, which may be helpful to find possibility of water-ice deposits in permanently shadowed regions of Moon.

SAR is a powerful tool for detection of water-ice deposits because of its three important characteristics: (i) SAR can actually “see into dark” regions of permanently shadowed areas unlike passive sensors, which require Sun for illumination purpose [359], (ii) SAR can be used for detecting volatile deposits underneath the surface of Moon due to penetration capability of electromagnetic (EM) wave [59], (ii) SAR provides full polarimetric response of backscatter from lunar surface and indicates a unique polarimetric signature (high circular polarization ratio) from water-ice deposits which is different from surrounding regolith area [372]. As mentioned earlier, high value of circular polarization ratio (μ_c) is the prime indicator for possible presence of water-ice deposits. However, ambiguity exist due to similar response obtained from rough ejecta region and rocky surface [261]. Therefore, contemplative studies are needed to resolve this ambiguity.

2.6. Conclusion

In this chapter, review of advances made in the field of SAR polarimetry and state-of-the art for target decomposition methods, classification methods, soil moisture retrieval techniques, and lunar surface characterization methods, have been discussed. Following conclusions have been drawn after comprehensive study of these methods:

- Distinct land covers describe different scattering mechanisms. Thus, characterization of various land covers is possible by defining scattering mechanisms. For this purpose, several decomposition methods have been developed. Model based decomposition methods have some advantages as compared to other existing decomposition methods due to their dependence on physical based modelling of scattering mechanisms. There is a need to study these decomposition methods and analyse the effect of deorientation in improving the scattering response from different land covers.
- SAR polarimetry is a promising science for land cover characterization because of providing fully polarimetric backscatter information of any target (or land cover). By providing full vector nature of EM wave, SAR polarimetry enables fully polarimetric linear scattering matrix to be synthesized into any other polarization, like circular and linear 45° (elliptical). Therefore, by extracting different polarimetric parameters which have strong relationship with targets, it may be possible to develop an adaptive land cover classification method with fully polarimetric SAR data.
- Several techniques have been developed for retrieval of soil moisture with SAR data. These methods either require a lot of '*a priori'* information, or behave well for the area for which they have implemented. Some of these methods assume time invariant nature of vegetation and are very complex. Thus, there is need to explore the possibility of developing a soil moisture retrieval method, which may be based on physical understanding and requires minimum or no *'a priori'* information.
- Spectroscopic and albedo based technique have positively indicated the possibility of water-ice on the surface of Moon. By utilizing properties of SAR, characterization of lunar surface can be performed, and therefore, it needs an exhaustive study.

Chapter 3

Study of Model Based Incoherent Polarimetric Decomposition Methods and Investigation of Deorientation Effect

The interpretation of SAR backscattered data for identification and classification of various land covers requires the knowledge of scattering mechanisms related to different targets. Basic scattering mechanisms are categorized as: volume, surface, and double-bounce scattering mechanisms. One possible way to characterize SAR data by means of scattering mechanisms is target decomposition methods. Over the years, several types of decomposition methods have been developed. However, model based decomposition methods have gained much popularity due to their inclination towards description of scattering mechanisms by physical based models. The model based decomposition expresses the coherency matrix in terms of various scattering components (like, volume, surface, double-bounce, and (or) helix component), which is helpful in segregation of different land covers more efficiently. In spite of this decomposition, still the major concern is characterization and labelling of various land cover classes. Therefore, in this chapter, comprehensive study of various model based decomposition methods has been performed. The investigation of deorientation process, which is expected to improve the performance of decomposition in terms of scattering behaviour, is also performed.

3.1. Introduction

Polarimetric target decomposition methods are helpful in extraction of polarimetric information from satellite data. The polarimetric target decomposition method articulates the average scattering mechanism as the summation of independent scattering mechanisms representing physical phenomenon associated with them for efficient identification of various targets. Thus, any decomposition technique decomposes the elements of scattering matrix with the objective to provide more descriptive and discriminative information of target parameters. At present, target decomposition can be performed by two distinct approaches, namely *coherent target*

decomposition and *incoherent target decomposition*.

Coherent target decomposition deals with the decomposition of the scattering matrix, and therefore, works well for characterization of coherent or point targets. These methods are prone to complications, like speckle noise because they do not require estimating second-order matrix i.e., target coherency (or, covariance) matrix. The examples of coherent target decomposition techniques are Pauli [152], Krogager [195], and Cameron [51] decompositions. *Incoherent target decomposition* decomposes second-order coherency or covariance matrices, and deals with the characterization of distributed targets. There are two types of incoherent target decomposition methods, namely eigenvalue decomposition methods [81, 284, 374] and model based decomposition methods [8-10, 12-14, 25, 70, 71, 88-90, 213, 247, 325, 328, 329, 344, 393-395, 425-428, 431, 442]. The review of these methods has been presented in section 2.2 of Chapter 2.

In this chapter, we have emphasized on model based decomposition methods because these methods effectively describe the scattering mechanisms, which may be justified by their physical interpretation. The first model based decomposition is three component model based decomposition (TCM) that provides the decomposition of covariance (or, coherency matrix) into three scattering components, namely, surface, dihedral (double-bounce), and volume scattering [138]. This model assumes reflection symmetry condition ($<S_{hh}\,S_{hv}^{*}>=<S_{vv}\,S_{hv}^{*}>=0$) due to which non-negligible powers in off-diagonal terms of covariance matrix are ignored. This assumption resulted in occurrence of negative powers in surface and double-bounce power terms due to overestimation of volume scattering. In order to avoid this limitation, Yamaguchi et.al., introduced additional component called helix scattering, which is best suited to analyse man-made structures in urban areas [425, 426, 428]. They used two volume components by changing probability distribution function (pdf) as sine function for associated orientation angles corresponding to horizontal and vertical distribution besides using volume component for uniform probability distribution function as in TCM. This decomposition method is known as four component model based decomposition method (FCM). The visual representation of all of these scattering mechanisms is given in Figure 3.1. The concept of three component model based decomposition was extended into multiple component decomposition by Zhang et al. [440] with addition of helix and wire scattering to TCM. They emphasized that dihedral structure formed by floor and walls of buildings induce double-bounce (dihedral) scattering; complex form of man-made structures (like, bridges) induce helix scattering; and linear

structures, like boundaries, window casings, and roof spaces induce wire scattering. In order to avoid the occurrence of negative powers, decomposition models with non-negative eigenvalue constraints have also been developed [394]. However, their implementation and solution depends on rotation symmetry assumption.

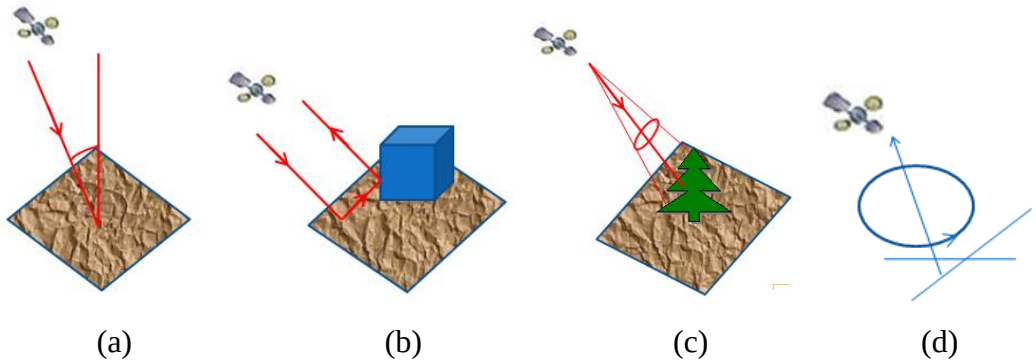

(a) (b) (c) (d)

Figure 3.1: Representation of scattering mechanisms; (a) single-bounce (surface) scattering, (b) double-bounce scattering, (c) volume scattering, and (d) helix scattering.

In model based decomposition methods, it is observed that due to similar polarimetric response, vegetation and oriented building blocks decompose into same volume scattering component by FCM. Therefore, the concept of rotation of coherency matrix around radar line-of-sight, also known as deorientation process, has been suggested to be applied prior to decomposition in order to identify oriented building blocks correctly [210, 218, 220, 326, 424]. This concept of rotation in model based decomposition has been applied by several researchers for improvement in scattering response [9, 71, 90, 328, 344, 427].

Various techniques for decomposition have been developed, but still the problem rests with volume scattering model. The possible limitation of three and four component model based scattering decomposition methods is their assumption of volume scattering model for vegetation as canopy of thin dipoles, while vegetation has to be characterized by more complex structure. Therefore, by extending the concept of non-negative eigenvalue decomposition [12, 394, 395], a new adaptive model based decomposition technique has been proposed by Arii et al. [13]. In this model, generalized volume scattering component has been proposed, by not assuming reflection symmetry condition in order to make it applicable to large range of vegetation types. Another general model based decomposition method has been developed by making use of variable volume scattering model [213] and adaptive volume scattering model

based on PolInSAR coherence [70]. Recently, a general four component model based decomposition has been proposed by double rotation of coherency matrix and utilizing additional volume scattering component for oriented dihedral structure along with traditional volume scattering models (for uniform, horizontal, and vertical distributions) [344].

The widespread popularity of model based decomposition methods accentuate the task of analysing the effect of decomposition methods on scattering mechanisms of various land covers. Therefore, in this chapter seven different three and four-component model based decomposition methods have been analysed, in which two are without deorientation and other five are with deorientation. These methods are (*i*) *three component model based decomposition (TCM)* [138] (without deorientation method); (*ii*) *four component model based decomposition method (FCM)* [425] (without deorientation method); (*iii*) *three component model based decomposition method with deorientation (TCMD)* [210], (*iv*) *three component model based decomposition method with double deorientation (orthogonal rotation and unitary transformation) and adaptive volume scattering component (TCMDDA)* [90]; (*v*) *four component model based decomposition method with deorientation (FCMD)* [427]; (*vi*) *four component model based decomposition with deorientation and additional volume scattering component (FCMDA)* [325], and (*vii*) *four component model based decomposition method with double deorientation (FCMDD)* [344]. The main purpose of this study is to visualize the effect of decomposition and deorientation on scattering response of various land covers. This analysis may explain the influence of deorientation effect on different scattering mechanisms obtained by various land covers. In this chapter, various quantitative analyses have been performed in order to check the effect of decomposition and deorientation in identification of several land covers, and for finding the possibility of using scattering components of different decomposition methods for labelling of land covers.

This chapter is organised as follows: in the section 3.2, the description of study area, SAR data and ground truth data is provided. In section 3.3, the mathematical models for all elementary scattering mechanisms are presented. Section 3.4 describes the process of orientation angle compensation (or deorientation process) and its need in decomposition methods. Section 3.5 gives the elaborated description of three and four component model based decomposition methods. Further, in section 3.6, several variants of model based decomposition methods with deorientation are discussed. The results of decomposition methods and their comprehensive analysis is reported and discussed in section 3.7. Finally, the concluding

remarks of the analysis are given in section 3.8.

3.2. Study Area and Data Description

3.2.1. Study Area

The study of model based decomposition methods and deorientation has been performed on city of Roorkee (Region-1) in the state Uttarakhand, India, having center latitude 29° 51' 45" N and longitude 77° 52' 51.03"E. The study area includes various land covers such as water (source: Ganga canal, Solani River, a rain-fed river, most part of which remains dry in summers), urban (source: Roorkee), tall vegetation (source: dense tree cover in city of Roorkee), bare soil and short vegetation (source: cropland and grassland).

The study has also been performed on Meerut city in the state Uttar Pradesh, India and New Delhi, the capital city of India. The study area in Meerut city (Region-2) mainly consist of urban, bare soil, and short vegetation regions with center latitude and longitude as 28° 58' 32" N and 77° 42' 20" E, respectively. The study area in New Delhi (Region-3) incorporates densely populated urban region as a major land cover having center latitude and longitude as 29° 39' 23" N and 77° 23' 30" E, respectively.

3.2.2. SAR Data

The study of decomposition methods on Region-1 (Roorkee) has been performed on fully polarimetric ALOS PALSAR L-band level 1.1 data in VEXCEL format (Data ID-PASL1109040617112609081100 63: Region-1-Roorkee) which has been acquired on April 6, 2009. The product has single number of looks in range and azimuth. The default off-nadir angle for polarimetric acquisition mode is 21.5° and incidence angle is 24°. The data has been provided by Earth Remote Sensing Data Analysis Center (ERSDAC).

For decomposition study on Region-2 fully polarimetric ALOS PALSAR data (Data ID-PASL1100904231713261001150001: Region-2-Meerut) acquired on April 23, 2009, has been taken. The acquisition of data for Region-3 (Data ID- PASL1100911101716261001150005: Region-3-New Delhi) has been performed on April 23, 2009. Figure 3.2 shows the RGB colour composite ALOS PALSAR image of Region-1 (Roorkee) exhibiting HH, HV, and VV as red, green, and blue colours, respectively.

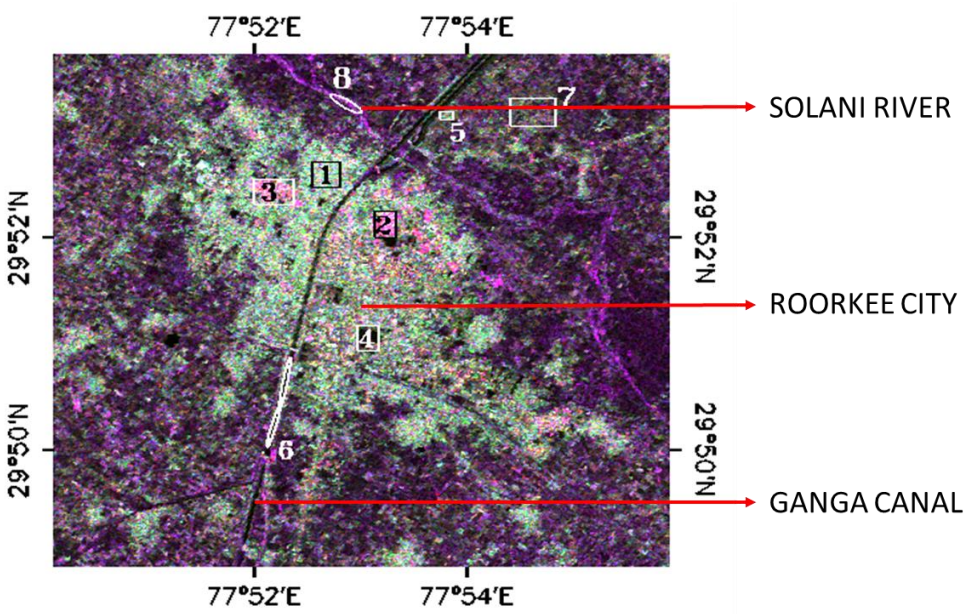

Figure 3.2: RGB colour composite image (HH-red, HV-green, VV-blue) of ALOS PALSAR data (Data ID-PASL1109040617112609081100 63) of Region-1: Roorkee.

In this chapter, the results of Region-1 i.e., Roorkee has been reported. The results of Region-2 (Meerut) and Region-3 (New Delhi) are shown in Appendix-C.

3.2.3. Ground Data

Based on ground truth survey performed by Global Positioning System (GPS) over Region-1 (Roorkee) on April 04, 2009, eight areas have been selected, as shown in Figure 3.2. These areas are designated by numbers 1 to 8. Number 1, 2, and 3 are three separate portions of urban area in the city of Roorkee titled as urban-1, urban-2, and urban-3, respectively. Number 4 represents bare ground labelled as bare soil-1. Number 5 represents tall vegetation. Number 6 denotes Ganga canal designated as water. Number 7 is a mixture of tall vegetation and short vegetation. Number 8 is actually Solani River, which was dry at the time of acquisition in April, 2009, and hence designated as bare soil-2.

3.3. Elementary Scattering Mechanisms

The model description of surface, double-bounce, volume, and helix scattering contributions is as follows:

3.3.1. Surface Scattering Model

The modelling of surface (single-bounce) scattering is performed by first-order Bragg surface scattering model for characterization of scattering from slightly rough surfaces, which have negligible cross-polarized components [138]. The scattering matrix for surface scattering is of the form,

$$[S_s]=\begin{bmatrix} R_h & 0 \\ 0 & R_v \end{bmatrix}, \tag{3.1}$$

where R_h and R_v are Bragg reflection coefficients for horizontally and vertically polarized EM waves, respectively. These coefficients are of the form,

$$R_h = \frac{\cos\theta - \sqrt{\varepsilon_r - \sin^2\theta}}{\cos\theta + \sqrt{\varepsilon_r - \sin^2\theta}}, \tag{3.2a}$$

$$R_v = \frac{(\varepsilon_r - 1)\left(\sin^2\theta - \varepsilon_r\left(1+\sin^2\theta\right)\right)}{\left(\varepsilon_r\cos\theta + \sqrt{\varepsilon_r - \sin^2\theta}\right)^2}, \tag{3.2b}$$

where ε_r is the relative dielectric constant of the surface, and θ is the local incidence angle. In general, natural surfaces have $\mathrm{Re}(\varepsilon_r) >> \mathrm{Im}(\varepsilon_r)$, which enables to assume that ε_r, R_h, and R_v are approximately real [70].

The coherency matrix obtained for surface scattering is presented as,

$$[T_s]=\begin{bmatrix} 1 & \beta^* & 0 \\ \beta & |\beta|^2 & 0 \\ 0 & 0 & 0 \end{bmatrix}, \tag{3.3}$$

where β is the real ratio defined as,

$$\beta = \frac{R_h - R_v}{R_h + R_v}, \quad |\beta| < 1, \tag{3.4}$$

3.3.2. Dihedral (Double-Bounce) Scattering Model

The double-bounce scattering is demonstrated as anisotropic dihedral scattering, in which total scattering from dihedral corner reflector is represented as the product of scattering obtained from two orthogonal Bragg-surfaces having same or different dielectric constants [138]. The double-bounce scattering is represented in the form of first-order scattering matrix as,

$$[S_d] = \begin{bmatrix} R_{sh} R_{th} e^{j2\gamma_h} & 0 \\ 0 & R_{sv} R_{tv} e^{j2\gamma_v} \end{bmatrix}, \tag{3.5}$$

where γ_h and γ_v are the propagation constants for horizontally and vertically polarized EM waves, respectively. They account for attenuation caused due to propagation of radar wave from SAR sensor to target, and then, back again to SAR sensor.

The parameters R_{sh} and R_{sv} [Equation (3.5)], corresponding to horizontally and vertically polarized Fresnel reflection coefficients, respectively, for horizontal surface, are of the form,

$$R_{sh} = \frac{\cos\theta - \sqrt{\varepsilon_s - \sin^2\theta}}{\cos\theta + \sqrt{\varepsilon_s - \sin^2\theta}}, \tag{3.6a}$$

$$R_{sv} = \frac{\varepsilon_s \cos\theta - \sqrt{\varepsilon_s - \sin^2\theta}}{\varepsilon_s \cos\theta + \sqrt{\varepsilon_s - \sin^2\theta}}, \tag{3.6b}$$

where ε_s is the dielectric constant of horizontal surface.

The parameters R_{th} and R_{tv} [Equation (3.5)] are horizontally and vertically polarized reflection coefficients, respectively, for vertical surface, which are of the form,

$$R_{th} = \frac{\cos\theta - \sqrt{\varepsilon_t - \sin^2\theta}}{\cos\theta + \sqrt{\varepsilon_t - \sin^2\theta}}, \tag{3.7a}$$

$$R_{tv} = \frac{\varepsilon_t \cos\theta - \sqrt{\varepsilon_t - \sin^2\theta}}{\varepsilon_t \cos\theta + \sqrt{\varepsilon_t - \sin^2\theta}}, \tag{3.7b}$$

where ε_t is the dielectric constant of vertical surface.

The scattering matrix given in Equation (3.5) leads to coherency matrix as,

$$[T_d] = \begin{bmatrix} |\alpha|^2 & \alpha & 0 \\ \alpha^* & 1 & 0 \\ 0 & 0 & 0 \end{bmatrix}, \tag{3.8}$$

where α is the contribution for double-bounce scattering, and is of the form,

$$\alpha = \frac{R_{sh} R_{th} e^{j2\gamma_h} + R_{sv} R_{tv} e^{j2\gamma_v}}{R_{sh} R_{th} e^{j2\gamma_h} - R_{sv} R_{tv} e^{j2\gamma_v}}, \quad |\alpha| < 1, \tag{3.9}$$

3.3.3. Volume Scattering Model

For volume scattering, several models have been proposed based on the incorporation of HV backscattering components, which is dominant for volume scattering phenomenon. Considering

a general case, where scatterers might be oriented, and the scattering matrix can be written as [138],

$$[S]=\begin{bmatrix} S_{hh} & S_{hv} \\ S_{hv} & S_{vv} \end{bmatrix}, \tag{3.10}$$

For incorporation of orientation of scatterers, the scattering matrix in Equation (3.10) is rotated by angle θ about radar line-of-sight as [138]

$$[S(\theta)]=[R_2(\theta)][S][R_2(\theta)]^{*T}, \tag{3.11}$$

where $R_2(\theta)$is rotation matrix. The '*T' indicates conjugate transpose of rotation matrix $R_2(\theta)$.

The oriented scattering matrix in Equation (3.11) leads to formation of oriented Pauli scattering vector as,

$$\kappa_p(\theta)=\left[S_{hh}(\theta)+S_{vv}(\theta),\quad S_{hh}(\theta)-S_{vv}(\theta),\quad 2S_{hv}(\theta)\right], \tag{3.12}$$

The coherency matrix for oriented volume scatterers is obtained as,

$$[T_v]=\int \kappa_p(\theta)\cdot\kappa_p^{*T}(\theta)p(\theta)d\theta, \tag{3.13}$$

where $p(\theta)$ is probability distribution function (pdf), which takes into account the orientation of scatterers instigating volume scattering. For representing volume scatterers in different orientation, distinct pdfs (uniform, sine, cosine, etc.,) can be chosen. The widely used scattering models for volume scattering based on different pdf are described as follows:

a. For uniform distribution [138]

The uniform distribution is assumed to represent radar scattering from canopy of randomly oriented dipoles. For uniformly distributed scatterers, the probability distribution function is taken as,

$$p(\theta)=1/2\pi, \qquad 0\le\theta\le 2\pi \quad \text{with} \int_0^{2\pi} \mathrm{p}(\theta)\mathrm{d}\theta=1, \tag{3.14}$$

Assuming very thin cylindrical scatterers, the scattering matrices for horizontal and vertical dipoles are obtained as,

$$[S_v]^{horizontal\_dipole}=\begin{bmatrix} 1 & 0 \\ 0 & 0 \end{bmatrix}, \tag{3.15a}$$

$$[S_v]^{vertical\_dipole}=\begin{bmatrix} 0 & 0 \\ 0 & 1 \end{bmatrix}, \tag{3.15b}$$

The coherency matrix using Equations (3.12), (3.13), and any of (3.15) is obtained as,

$$[T_v]^{uniform} = \frac{1}{4}\begin{bmatrix} 2 & 0 & 0 \\ 0 & 1 & 0 \\ 0 & 0 & 1 \end{bmatrix}, \tag{3.16}$$

b. ***For horizontal distribution [425, 426, 428]***

For horizontally distributed scatterers cosine distribution is assumed, i.e.,

$$p(\theta) = \frac{1}{2}\cos\theta, \qquad 0 < \theta < 2\pi\,, \tag{3.17}$$

By using Equation (3.13), (3.15a) and (3.17), the coherency matrix is obtained as,

$$[T_v]^{horizontal} = \frac{1}{30}\begin{bmatrix} 15 & -5 & 0 \\ -5 & 7 & 0 \\ 0 & 0 & 8 \end{bmatrix}, \tag{3.18}$$

c. For vertical distribution [425, 426, 428]

In case of vertical distribution of scatterers, sine distribution is taken as,

$$p(\theta) = \frac{1}{2}\sin\theta, \quad 0 < \theta < 2\pi\,, \tag{3.19}$$

The coherency matrix thus obtained by using Equations (3.13), (3.15b), and (3.19) as,

$$[T_v]^{vertical} = \frac{1}{30}\begin{bmatrix} 15 & 5 & 0 \\ 5 & 7 & 0 \\ 0 & 0 & 8 \end{bmatrix}, \tag{3.20}$$

d. For oriented dihedral scattering [325]

In some special cases such as right angle dihedral structures (e.g., buildings and their walls, and river and bridge, etc.,), it may happen that one of the surfaces of dihedral construction is oriented with respect to radar illumination, which makes HV backscattering component to appear in dominance. Thus, in order to incorporate HV component by oriented dihedral construction, pdf $p(\theta)$ is chosen as a function having its peak value at zero degree, and is represented as,

$$p(\theta) = \frac{1}{2}\cos\theta, \qquad -\frac{\pi}{2} < \theta < \frac{\pi}{2}\,, \tag{3.21}$$

This gives the coherency matrix, by using Equations (3.13) and (3.21) as,

$$[T_v]^{dihedral} = \frac{1}{15}\begin{bmatrix} 0 & 0 & 0 \\ 0 & 7 & 0 \\ 0 & 0 & 8 \end{bmatrix}, \tag{3.22}$$

3.3.4. Helix Scattering Model

The helix scattering component is generated in heterogeneous areas, like urban and other complex man-made targets. This component is generated by helicity of targets, which generates left or right circular polarization for all the incident linearly polarized waves [425, 426, 428]. The scattering matrices for left and right helix, and their corresponding coherency matrix is given by [425, 426, 428],

$$[S]^{right-helix} = \frac{e^{j2\theta}}{2}\begin{bmatrix} 1 & -j \\ -j & -1 \end{bmatrix} \text{ and } [S]^{left-helix} = \frac{e^{-j2\theta}}{2}\begin{bmatrix} 1 & j \\ j & -1 \end{bmatrix}, \tag{3.23a}$$

$$[T_c] = \frac{1}{2}\begin{bmatrix} 0 & 0 & 0 \\ 0 & 1 & \pm j \\ 0 & \pm j & 1 \end{bmatrix}, \tag{3.23b}$$

3.4. Orientation Angle Compensation

SAR imaging in rugged terrain leads to scattering matrix values of fully polarimetric SAR data to be changed due to shift in polarization orientation angle θ, which is the angle of rotation of surface normal to the incidence plane by radar line-of-sight. The shift in polarization orientation angle is a function of range slope, azimuth slope, and radar look angle [210], and is given as,

$$\tan\theta = \frac{\tan\omega}{-\tan\gamma\cos\phi + \sin\phi}, \tag{3.24}$$

where,

tan ω=Azimuth slope,

tan γ = Slope in ground range,

ϕ = Radar look angle.

Due to this shift in orientation angle, rotation of incidence plane about radar line-of-sight to the surface normal takes place which increases the cross-polarized radar response, and makes coherency matrix reflection symmetric. This shift in polarization orientation angle leads to befuddled classification due to ambiguous scattering response obtained from randomly distributed targets. The compensation of this effect is performed by deorientation process [210, 424], which transforms the target scattering vector by rotation about the radar line-of-sight.

This process enhances co-polarization response and reduces the effect of randomly fluctuating orientation, and therefore, it resolves the ambiguity in scattering between two randomly oriented targets. The deorientation effects resulted in getting same scattering response from differently oriented similar targets, and different scattering response from distinct targets which might be producing same response without deorientation.

For implementation of deorientation effect, first it is required to rotate the coherency matrix about radar line-of-sight by angle θ as [427],

$$T(\theta) = [R(\theta)][T][R(\theta)]^{*T} = \begin{bmatrix} T_{11}(\theta) & T_{12}(\theta) & T_{13}(\theta) \\ T_{12}^{*}(\theta) & T_{22}(\theta) & T_{23}(\theta) \\ T_{13}^{*}(\theta) & T_{23}^{*}(\theta) & T_{33}(\theta) \end{bmatrix}, \tag{3.25}$$

where, $R(\theta)$ is the orthogonal rotation matrix defined as,

$$R(\theta) = \begin{bmatrix} 1 & 0 & 0 \\ 0 & \cos 2\theta & \sin 2\theta \\ 0 & -\sin 2\theta & \cos 2\theta \end{bmatrix}, \tag{3.26}$$

The terms of oriented coherency matrix are represented as,

$$T_{11}(\theta) = T_{11}, \tag{3.27a}$$

$$T_{12}(\theta) = T_{12}\cos 2\theta + T_{13}\sin 2\theta, \tag{3.27b}$$

$$T_{13}(\theta) = T_{13}\cos 2\theta - T_{12}\sin 2\theta, \tag{3.27c}$$

$$T_{23}(\theta) = j\,\mathrm{Im}(T_{23}), \tag{3.27d}$$

$$T_{22}(\theta) = T_{22}\cos^2 2\theta + T_{33}\sin^2 2\theta + \mathrm{Re}(T_{23})\sin 4\theta, \tag{3.27e}$$

$$T_{33}(\theta) = T_{33}\cos^2 2\theta + T_{22}\sin^2 2\theta - \mathrm{Re}(T_{23})\sin 4\theta, \tag{3.27f}$$

The interpretation for the component of coherency matrix is given in section A2.4 of Appendix- A.

The aim of deorientation is to minimize cross-polarized radar response, which is obtained from T_{33} component of rotated coherency matrix [Equation (3.27f)]. Now, for obtaining the minimum of $T_{33}(\theta)$, the derivative of $T_{33}(\theta)$ is equated to zero, and the polarization orientation angle θ is obtained as [210],

$$\theta = \frac{1}{4}\tan^{-1}\left(\frac{2\,\mathrm{Re}(T_{23})}{T_{22} - T_{33}}\right), \tag{3.28}$$

In general, for azimuthal symmetric media, T_{22} is greater than T_{33}. Thus, in specific cases, where numerator is zero, arctangent becomes approximately equal to $\pm\pi$. However, Equation

(3.28) shows that θ is in the range of $-\pi/4$ to $+\pi/4$. In order to obtain useful information, it is required to remove bias by adding π for matching the orientation angle corresponding to azimuth slope angle as [210],

$$\eta = \frac{1}{4}\left[\tan^{-1}\left(\frac{2\,\mathrm{Re}(T_{23})}{T_{22}-T_{33}}\right)+\pi\right], \tag{3.29}$$

Now, the correct orientation angle becomes,

$$\theta = \begin{cases} \eta, & \text{if } \eta \le \pi/4 \\ \eta - \pi/2, & \text{if } \eta > \pi/4 \end{cases}, \tag{3.30}$$

3.5. Model Based Basic Incoherent Polarimetric Decomposition Approaches

Model based incoherent decomposition methods make use of physical models for representing various scattering components, and determining their parameters using physical interpretation. The most important task of model based decomposition methods is to represent scattering components associated with targets mathematically, and to provide their interpretation based on physical basis [79]. The description of basic polarimetric decompositions i.e., three and four component model based decomposition methods has been discussed as follows:

3.5.1. Three Component Model Based Decomposition (TCM)

The three-component model based decomposition, proposed by Freeman, represents the coherency matrix T as the sum of three independent scattering mechanisms, namely surface scattering modelled by first-order Bragg scattering from rough surface, volume scattering modelled by thin randomly oriented cylindrical particles, and double-bounce scattering modelled by dihedral reflector with orthogonal surfaces of materials having different dielectric constants [138]. Decomposed coherency matrix T can be expressed as [138],

$$[T] = f_s[T_s] + f_d[T_d] + f_v[T_v], \tag{3.31a}$$

$$[T] = \frac{f_s}{1+|\beta|^2}\begin{bmatrix} 1 & \beta^* & 0 \\ \beta & |\beta|^2 & 0 \\ 0 & 0 & 0 \end{bmatrix} + \frac{f_d}{1+|\alpha|^2}\begin{bmatrix} |\alpha|^2 & \alpha & 0 \\ \alpha^* & 1 & 0 \\ 0 & 0 & 0 \end{bmatrix} + \frac{f_v}{4}\begin{bmatrix} 2 & 0 & 0 \\ 0 & 1 & 0 \\ 0 & 0 & 1 \end{bmatrix}, \tag{3.31b}$$

where $[T_s]$, $[T_d]$, and $[T_v]$ are coherency matrices representing surface (Equation 3.3), double-

bounce (Equation 3.8) , and volume scattering (Equation 3.16), respectively, and f_s, f_d, and f_v are expansion coefficients representing power of single-bounce, double-bounce, and volume scattering, respectively.

The Freeman decomposition (or TCM) exhibits five unknowns (f_s, f_d, f_v, α, β) and four equations, thus utilizing only five polarimetric parameters i.e., T_{11}, T_{22}, T_{33}, $Re(T_{12})$, and $Im(T_{12})$, as evident from Equation 3.31. Therefore following constraint need to be applied in order to decide the dominance of surface or double-bounce scattering [9, 392]:

If,

$$\mathrm{Re}(S_{HH}S_{VV}^{*}) \text{ or } T_{11}-T_{22}-T_{33}>0 \quad :\alpha=0:\ \text{Surface scattering dominant}, \tag{3.32a}$$

$$\mathrm{Re}(S_{HH}S_{VV}^{*}) \text{ or } T_{11}-T_{22}-T_{33}<0 \quad :\beta=0:\ \text{Double-bounce scattering dominant}, \tag{3.32b}$$

Finally, powers corresponding to surface (P_s), double-bounce (P_d), and volume scattering (P_v) components can be represented as,

$$P_s = f_s(1+|\beta|^2), \tag{3.33a}$$

$$P_d = f_d(1+|\alpha|^2), \tag{3.33b}$$

$$P_v = f_v = 4T_{33}, \tag{3.33c}$$

The total power or span is now given by,

$$SPAN = P_s + P_d + P_v = \left\langle |S_{hh}|^2 + 2|S_{hv}|^2 + |S_{vv}|^2 \right\rangle, \tag{3.34}$$

The TCM has been hypothesized by considering reflection symmetry condition ($<S_{hh}S_{hv}^{*}>=<S_{vv}S_{hv}^{*}>=0$), which is not applicable for urban area [426]. However, the ease of implementation, its simplicity, and dependence on physical significance of radar returns make it popular choice of decomposition in natural terrain [219, 426]. The flowchart of TCM is shown in Figure B.1 of Appendix-B.

3.5.2. Four Component Model Based Decomposition (FCM)

Four-component model based decomposition (FCM) is an extension of TCM (as discussed in section 3.5.1) with an additional component called helix scattering term corresponding to non-reflection symmetry condition ($<S_{hh}S_{hv}^{*}>\neq 0$ and $<S_{vv}S_{hv}^{*}>\neq 0$) [426, 428]. The helix scattering term is obtained from heterogeneous areas, like sharp targets and man-made structures. Assuming no correlation between surface, double-bounce, volume, and helix scattering

components, the decomposition of coherency matrix T can be carried out in following manner [425],

$$T = f_s[T_s] + f_d[T_d] + f_v[T_v] + f_c[T_c], \tag{3.35}$$

where f_s, f_d, f_v, and f_c are expansion coefficients representing power of surface, double-bounce, volume, and helix scattering, respectively.

The interpretation of surface and double-bounce scattering matrices (T_s and T_d, respectively) is same as in TCM [138], according to Equations (3.3) and (3.8). The helix scattering is interpreted as described in Equation (3.23). Unlike TCM, in which uniform probability distribution function has been considered for canopy scattering [Equation (3.16)], sinusoidal probability distribution function is proposed [426] for considering angle distribution associated with different tree-trunk and branches. The coherency matrices corresponding to volume scattering obtained by considering this probability distribution function are given in Equations (3.18) and (3.20) corresponding to horizontally and vertically oriented targets, respectively. The choice between symmetric (uniform distribution as in Equation (3.16)) and asymmetric (sine distribution as in Equations (3.18) and (3.20)) cases for volume scattering are selected according to the value of $10log(<|S_{vv}|^2>/<|S_{hh}|^2>)$, which is less than −2dB for horizontal distribution; greater than +2 dB for vertical distribution; and lies in between −2 dB and +2 dB for uniform distribution.

The four component decomposition yields five equations and six unknowns. Thus, only six polarimetric parameters [T_{11}, T_{22}, T_{33}, $Im(T_{23})$, $Re(T_{12})$, and $Im(T_{12})$] are used out of nine parameters in coherency matrix [T_{11}, T_{22}, T_{33}, $Re(T_{23})$, $Im(T_{23})$, $Re(T_{12})$, $Im(T_{12})$, $Re(T_{13})$, and $Im(T_{13})$]. The helix scattering power P_c is directly determined as,

$$P_c = f_c = 2\,|\,\mathrm{Im}(T_{23})\,|, \tag{3.36}$$

Now, four component model based decomposition incorporates four equations and five unknowns. The volume scattering power P_v is determined after selection based on the value of $10log(<|S_{vv}|^2>/<|S_{hh}|^2>)$, as discussed above. The dominance of surface and double-bounce scattering is determined on the basis of the sign of Real part of ($S_{hh}\,S^*_{vv}$), the conditions of which are described as follows,

$$\text{If,} \quad \begin{matrix} \mathrm{Re}(S_{hh}S^*_{vv}) \text{ or } T_{11} - T_{22} - T_{33} + P_c > 0 \\ \alpha = 0: \text{ Surface scattering dominant} \end{matrix}, \tag{3.37a}$$

$$\begin{matrix} \mathrm{Re}(S_{hh}S^*_{vv}) \text{ or } T_{11} - T_{22} - T_{33} + P_c < 0 \\ \beta = 0: \text{ Double bounce scattering dominant} \end{matrix}, \tag{3.37b}$$

At last, the power corresponding to surface and double-bounce scattering terms (i.e., P_s, and P_d, respectively) are determined by Equations (3.33 a, b).

This decomposition method is improved by adding some *ad hoc* power constraints for avoiding the occurrence of negative surface, double-bounce, and volume scattering powers. These constraints are described as follows [425]:

i. If, $P_v < 0, set\ P_c = 0$, (3.38a)

ii. If, $P_v > SPAN, set\ P_v = SPAN$, (3.38b)

iii. If, $P_v + P_c > SPAN, set\ P_v = SPAN - P_c$, (3.38c)

iv. If, $P_s < 0, set\ P_s = 0$ and $P_d = SPAN - P_v - P_c$, (3.38d)

v. If, $P_d < 0, set\ P_d = 0$ and $P_s = SPAN - P_v - P_c$, (3.38e)

The detailed procedure of FCM is presented in the form of flowchart shown in Figure B.2 of Appendix-B.

3.6. Model Based Decomposition Methods after Deorientation

Three and four component model based decomposition methods, as discussed in section 3.5, suffer from two problems: one is occurrence of negative powers for surface, double-bounce, and volume scattering, and second is occurrence of same scattering response (i.e., volume scattering) obtained from oriented urban structures and vegetation [427]. In order to overcome this problem, it was suggested to rotate the target coherency matrix about radar line-of-sight to compensate orientation effect by a process called deorientation, as discussed in section 3.4. Therefore, several model based decomposition methods have been proposed by using the concept of deorientation theory for improving the scattering response. Some of these methods, which have been studied in this chapter, are described as follows:

3.6.1. Three component Model Based Decomposition with Deorientation (TCMD)

In this case, first the deorientation of coherency matrix is performed in order to obtain rotated coherency matrix $T(\theta)$, as defined by Equation (3.25). Now, three component model based decomposition is performed in the same manner, as discussed in section 3.5.1, but with the use

of $T(\theta)$ matrix. The decomposition of $T(\theta)$ can be done as ,

$$[T(\theta)] = f_s[T_s] + f_d[T_d] + f_v[T_v], \tag{3.39}$$

In Equation (3.39), $[T_s]$, $[T_d]$, and $[T_v]$ are modelled according to TCM, and by Equations (3.3), (3.8) and (3.16), respectively. Even after deorientation, this method of decomposition uses only five polarimetric parameters, which are $T_{11}(\theta)$, $T_{22}(\theta)$, $T_{33}(\theta)$, $Re(T_{12}(\theta))$, and $Im(T_{12}(\theta))$. The complete flowchart of this decomposition is exhibited in Figure B.3 of Appendix-B.

3.6.2. Three Component Model Based Decomposition with Double Deorientation and Adaptive Volume Scattering Model (TCMDDA)

This method uses double rotation of coherency matrix in order to ensure more accurate description of scattering mechanisms. The first rotation is done by method described in section 3.4. After this rotation, called as orthogonal rotation, rotated coherency matrix $T(\theta)$ is obtained as given in Equation (3.25). The elements of this matrix are given by Equation (3.27). The rotation angle, as given in Equation (3.28), is derived by minimizing $T_{33}(\theta)$ component [Equation (3.27f)], which resulted in condition $T_{22}(\theta) > T_{33}(\theta)$. In [9], it is shown that negative surface and double-bounce powers in TCM occur due to $T_{22}(\theta) < T_{33}(\theta)$. Thus, rotation helps in improving decomposition by reducing the occurrence of negative powers.

The second rotation called unitary transformation is performed on $T(\theta)$ matrix as [90, 344],

$$T(\varphi) = [R(\varphi)][T(\theta)][R(\varphi)]^{*T} = \begin{bmatrix} T_{11}(\varphi) & T_{12}(\varphi) & T_{13}(\varphi) \\ T_{12}^{*}(\varphi) & T_{22}(\varphi) & T_{23}(\varphi) \\ T_{13}^{*}(\varphi) & T_{23}^{*}(\varphi) & T_{33}(\varphi) \end{bmatrix}, \tag{3.40}$$

where, $R(\varphi)$ is unitary transformation matrix defined as,

$$R(\varphi) = \begin{bmatrix} 1 & 0 & 0 \\ 0 & \cos 2\varphi & j\sin 2\varphi \\ 0 & j\sin 2\varphi & \cos 2\varphi \end{bmatrix}, \tag{3.41}$$

The terms of oriented coherency matrix, after unitary transformation according to Equation (3.40), are represented as,

$$T_{11}(\varphi) = T_{11}(\theta) = T_{11}, \tag{3.42a}$$

$$T_{12}(\varphi) = T_{12}(\theta)\cos 2\varphi - jT_{13}(\theta)\sin 2\varphi, \tag{3.42b}$$

$$T_{13}(\varphi) = T_{13}(\theta)\cos 2\varphi - jT_{12}(\theta)\sin 2\varphi, \tag{3.42c}$$

$$T_{23}(\varphi) = \mathrm{Re}(T_{23}(\theta)) = 0, \tag{3.42d}$$

$$T_{22}(\varphi) = T_{22}(\theta)\cos^2 2\varphi + T_{33}(\theta)\sin^2 2\varphi + \mathrm{Im}(T_{23}(\theta))\sin 4\varphi, \tag{3. 42e}$$

$$T_{33}(\varphi) = T_{33}(\theta)\cos^2 2\varphi + T_{22}(\theta)\sin^2 2\varphi - \mathrm{Im}(T_{23}(\theta))\sin 4\varphi, \tag{3. 42f}$$

The angle φ is derived in a similar manner, as described in section 3.4, by minimizing $T_{33}(\varphi)$ component provided in Equation (3.42f) , and is given as [90, 344],

$$\varphi = \frac{1}{4}\tan^{-1}\left(\frac{2\,\mathrm{Im}(T_{23}(\theta))}{T_{22}(\theta) - T_{33}(\theta)}\right), \tag{3.43}$$

The unitary transformation resulted in $T_{22}(\varphi) > T_{33}(\varphi)$ due to minimization of $T_{33}(\varphi)$ component, and thus, ensuring again the reduction in negative powers after decomposition. The negative powers in TCM, as discussed in section 3.5.1, also occur due to $T_{11} < 2T_{33}$. To overcome this problem, an adaptive volume scattering model has been proposed in [90], which is of the form,

$$[T_V]^{adaptive} = \frac{1}{\gamma + 2}\begin{bmatrix} \gamma & 0 & 0 \\ 0 & 1 & 0 \\ 0 & 0 & 1 \end{bmatrix}, \tag{3. 44}$$

where γ is an adaptive parameter, which changes the type of volume scattering with change in its value. More specifically, $\gamma = 2$ corresponds to volume scattering by canopy of randomly oriented dipoles, as given in Equation (3.16). The value $\gamma = 0$ corresponds to volume scattering model due to oriented dihedral scattering, as provided in Equation (3.22). The condition $\gamma = 1$, represents volume scattering model having maximum entropy (randomness), which is of the form [90],

$$[T_V]^{\max\_entropy} = \frac{1}{3}\begin{bmatrix} 1 & 0 & 0 \\ 0 & 1 & 0 \\ 0 & 0 & 1 \end{bmatrix}, \tag{3.45}$$

The adaptive parameter γ is determined by using the concept of similarity parameter, and is modelled as [11],

$$\gamma^* = \arg\max_{0 \le \gamma \le 2}\left\{\frac{\left|\left\langle [T(\varphi)], [T_V]^{adaptive}\right\rangle\right|}{\|[T(\varphi)]\|\,\|[T_V]^{adaptive}\|}\right\}, \tag{3.46}$$

The solution of Equation (3.46) is obtained as,

$$T_{11}(\varphi) < T_{22}(\varphi) + T_{33}(\varphi) \Rightarrow \gamma^* = \frac{2T_{11}(\varphi)}{T_{22}(\varphi) + T_{33}(\varphi)}, \tag{3.47a}$$

$$T_{11}(\varphi) > T_{22}(\varphi) + T_{33}(\varphi) \Rightarrow \gamma^* = 2, \tag{3.47b}$$

The decomposition of unitary transformed matrix *T(φ)* is performed in following manner [90, 344],

$$[T(\varphi)] = f_s[T_s] + f_d[T_d] + f_v[T_v], \tag{3.48}$$

The modelling of $[T_s]$, $[T_d]$, and $[T_v]$ are done by using Equations (3.3), (3.8), and (3.44), respectively. The only non-negative solution of Equation (3.48) exists for the following condition:

$$(T_{11}(\varphi) - \gamma^* T_{33}(\varphi))(T_{22}(\varphi) - T_{33}(\varphi)) > |T_{12}(\varphi)|^2, \tag{3.49a}$$

$$(T_{11}(\varphi) - \gamma^* T_{33}(\varphi)) > (T_{22}(\varphi) - T_{33}(\varphi)), \tag{3.49b}$$

After applying these conditions, the contributory powers of surface (P_s) and double-bounce (P_d) scattering are obtained according to Equations (3.33 a, b) and volume scattering power is obtained as,

$$P_v = f_v = (2 + \gamma^*) T_{33}(\varphi), \tag{3.50}$$

The flowchart of methodology of this algorithm is shown in Figure B.4 of Appendix-B.

3.6.3. Four Component Model Based Decomposition with Deorientation (FCMD)

In four component model based decomposition, as described in section 3.5.2, a problem in scattering response from oriented urban occurs [427]. It is observed in urban area that oriented building blocks and other man-made objects having oblique orientation with respect to radar illumination, exhibit volume scattering response (like vegetation) after four component decomposition. In order to overcome this problem, the deorientation has been suggested to be applied prior to decomposition. The decomposed rotated coherency matrix *T(θ)* is presented as [427],

$$[T(\theta)] = f_s[T_s] + f_d[T_d] + f_v[T_v] + f_c[T_c], \tag{3.51}$$

The matrices $[T_s]$, $[T_d]$, $[T_v]$, and $[T_c]$ are interpreted in the same manner as in FCM, as described in section 3.5.2. The matrices $[T_s]$, $[T_d]$, and $[T_c]$ are modelled according to Equations

(3.3), (3.8), and (3.23), respectively. The volume scattering matrix is obtained from Equations (3.16), (3.18), and (3.20), respectively, corresponding to uniform, horizontal, and vertical distribution, respectively. The decomposition process is same as FCM except the use of $T(\theta)$ instead of T. The flowchart of FCMD is demonstrated in Figure B.5 of Appendix-B.

3.6.4. Four Component Model Based Decomposition with Deorientation and Additional Oriented Dihedral Volume Scattering Model (FCMDA)

This decomposition method utilizes the concept of deorientation as discussed in section 3.4, and then uses additional volume scattering component corresponding to oriented dihedral structure according to Equation (3.22) in decomposition process. The decomposition of deoriented coherency matrix $T(\theta)$ is performed by Equation (3.51). The modelling of $[T_s]$, $[T_d]$, and $[T_c]$ is done by using Equations (3.3), (3.8), and (3.23), respectively. For volume scattering component, all four models presented in section 3.3.3, are used. The helix scattering power in this case is directly determined by using Equation (3.36) utilizing $T_{23}(\theta)$ instead of T_{23}. In order to discriminate volume scattering from vegetation and oriented dihedral structure following condition has been applied [325]:

If, $$T_{11}(\theta) - T_{22}(\theta) + \frac{1}{2} f_c > 0 \quad : \text{Vegetation induced volume scattering,} \qquad (3.52a)$$

$$T_{11}(\theta) - T_{22}(\theta) + \frac{1}{2} f_c \leq 0 \quad : \text{Dihedral induced volume scattering,} \qquad (3.52b)$$

Now, discrimination between volume scattering from vegetation is done by factor $10log(<|S_{vv}|^2>/<|S_{hh}|^2>)$, as described in section 3.5.2. After, retrieving power corresponding to volume scattering i.e., P_v, surface and double-bounce powers (P_s and P_d, respectively) are determined by using Equations (3.33a,b) and conditions (3.37a,b). The detailed description of this algorithm has been presented in Figure B.6 of Appendix-B.

3.6.5. Four Component Decomposition with Double Deorientation (FCMDD)

This method uses the concept of both orthogonal and unitary transformation of coherency matrix, as discussed in sections 3.4 and 3.6.2, respectively, before applying four component model based decomposition. After double rotation of coherency matrix, T_{23} element becomes zero, thus providing seven independent polarimetric parameters [$T_{11}(\varphi)$, $T_{22}(\varphi)$, $T_{33}(\varphi)$, $Re(T_{12}(\varphi))$, $Im(T_{12}(\varphi))$, $Re(T_{13}(\varphi))$, and $Im(T_{13}(\varphi)$]. Unlike, above mentioned all decomposition methods, this decomposition method uses all available seven polarimetric parameters. The

decomposition of double rotated coherency matrix $T(\varphi)$ is performed in following manner [344],

$$[T(\varphi)] = f_s[T_s] + f_d[T_d] + f_v[T_v] + f_c[Tc], \tag{3.53}$$

where matrices $[T_s]$, $[T_d]$, and $[T_c]$ are modelled according to Equations (3.3), (3.8), and (3.23), respectively. The coherency matrix for volume scattering $[T_v]$ is modelled by all four models described in section 3.3.3. Rest of the process is same as discussed in section 3.6.4, rather by using $T(\varphi)$.The flowchart of algorithm is presented in Figure B.7 of Appendix-B.

3.7. Results and Discussion

3.7.1. Pre-processing of Polarimetric SAR (ALOS PALSAR) Data

Pre-processing of ALOS PALSAR data has been performed using SARscape (version 4.3) software, which works in integration with Environment for Visualizing Images (ENVI) (version 4.8). The pre-processing steps are provided in flowchart shown in Figure 3.3. The step-wise description of pre-processing of ALOS PALSAR data is as follows:

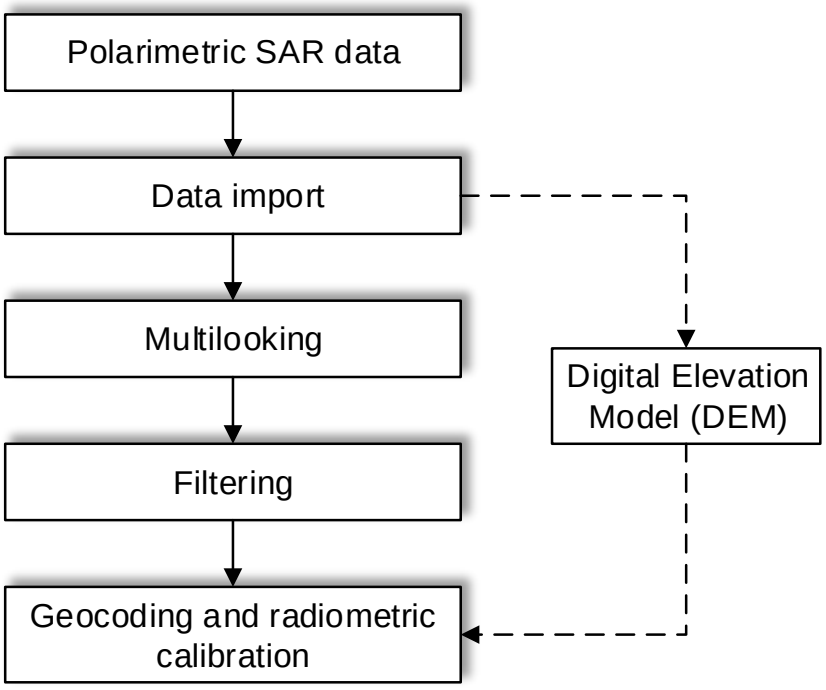

Figure 3.3: Flowchart for pre-processing of polarimetric SAR data.

Step-1: Data Import: The ALOS PALSAR data provided by ERSDAC is a single look slant range fully polarimetric complex data having four polarization channels as HH, HV, VH, and VV. This data is already focused and calibrated in order to avoid imperfect characteristics of fully polarimetric SAR acquisition system caused due to imbalance and cross-talk. Therefore, as a first step, data is imported by SARscape, which provides four single look complex files of HH, HV, VH, and VV polarizations.

Step-2: Multilooking*:* The speckle noise inherently occurring in SAR images can be reduced by averaging multiple looks, which are produced by taking average of azimuth and/or range resolution cell. This procedure is called *multilooking*. The main purpose of multilooking is to obtain approximately squared pixels. Therefore, multilooking increases radiometric resolution at the cost of degraded spatial resolution. Numbers of looks are calculated by following procedure [1]:

$$\text{Ground range resolution} = \frac{\text{pixel spacing range}}{\sin(\text{incidence angle})} \quad , \tag{3.54}$$

$$\text{Number of looks} \approx \frac{\text{Ground range resolution}}{\text{line spacing (azimuth)}} \quad , \tag{3.55}$$

For ALOS PALSAR data, pixel spacing, line spacing, and incidence angle are 9.36 m, 3.54 m, and 24°, respectively. Therefore, multilook factor is obtained as 7.

Step-3: Filtering: For speckle suppression, polarimetric filter, namely Wishart Gamma MAP filter [232], has been used in order to preserve polarimetric information of quad-polarimetric SAR data. It is a polarimetric filter which is suitable for polarimetric data, as discussed in section 2.1 of Chapter 2. The filter operates under the assumption of target reciprocity (i.e. HV=VH) [1]. Thus only three filtered complex images are produced (HH, HV, VV). It performs well in the presence of regular texture and moderate relief. The output speckle filtered covariance matrix terms [$S_{hh}.S_{hh}^*$, $S_{vv}.S_{vv}^*$, $S_{hv}.S_{hv}^*$, $Re(S_{hh}.S_{hv}^*)$, $Im(S_{hh}.S_{hv}^*)$, $Re(S_{hh}.S_{vv}^*)$, $Im(S_{hh}.S_{vv}^*)$, $Re(S_{vv}.S_{hv}^*)$, $Im(S_{vv}.S_{hv}^*)$] contain all the polarimetric information required for further computation.

Step-4: Geocoding and radiometric calibration: Geocoding is the process of geometrically correcting SAR images against terrain induced distortions by transforming slant range projection to a cartographic reference system using appropriate map-projections and digital

elevation model (DEM) [67]. DEM represents the topography of ground surface in digital format. In this study, DEM has been extracted by GTOPO 30 technique (using SARscape module) which provides global DEM map with a horizontal grid spacing of 30 arc seconds (approximately 1 km). Thus, SARscape automatically performs geocoding with the help of DEM without any user intervention. Simultaneously, radiometric calibration has been performed to rectify SAR image by providing corrections for antenna gain, system loss, antenna effective aperture, range spread loss, etc., [93]. After radiometric calibration dimensionless calibrated backscattering values have been obtained in terms of sigma naught. The backscatter value in logarithmic scale can be obtained as,

$$\sigma_{xy}^{0} = 10\log(DN_i^2 + DN_q^2), \tag{3.56}$$

where DN_i and DN_q are digital numbers (DNs) corresponding to real (i) and imaginary (q) parts of complex SAR data.

After pre-processing of SAR data according to Figure 3.3, following steps have been carried out to perform decomposition methods:

- All the filtered terms obtained in stpe-3 [i.e., ($S_{hh}.S_{hh}^*$, $S_{vv}.S_{vv}^*$, $S_{hv}.S_{hv}^*$, $Re(S_{hh}.S_{hv}^*)$, $Im(S_{hh}.S_{hv}^*)$, $Re(S_{hh}.S_{vv}^*)$, $Im(S_{hh}.S_{vv}^*)$, $Re(S_{vv}.S_{hv}^*)$, $Im(S_{vv}.S_{hv}^*)$)] have been geocoded and radio-metrically calibrated to obtain dimensionless calibrated terms.
- These geocoded terms have been used to form coherency matrixm which has been used for development of decomposition algorithm. All of these processing have been performed using MATLAB (matrix laboratory) 2010.
- Further, the decomposition methods have been applied on ALOS PALSAR data sets of Roorkee (Region-1: Data ID-PASL1109040617112609081100 63), Meerut (Region-2: Data ID-PASL1100904231713261001150001), and Delhi (Region-3: Data ID-PASL1100911101716261001150005). This chapter reports the results of ALOS PALSAR data of Roorkee i.e., Region-1. The results of Region-2 (Meerut) and Region-3 (Delhi) are given in Appendix-C.

In the following sections, the analysis of studied decomposition approaches has been presented.

3.7.2. Visual Analysis

After applying decomposition algorithm on ALOS PALSAR data of city Roorkee (Region-1), the scattering power terms related to surface (P_s), double-bounce (P_d), volume (P_v), and/or helix scattering (P_c) have been obtained.

First, the decomposition methods without deorientation i.e., three component model based decomposition (TCM) and four component model based decomposition (FCM), have been applied according to flowcharts of algorithms given in Figures B.1 and B.2 of Appendix-B, respectively. The visual representation of these decomposition methods are shown in Figure 3.4(a,b), which are RGB colour composite images with representation of double-bounce scattering power (P_d) as red, volume scattering power (P_v) as green, and surface scattering power (P_s) as blue colours. This figure shows that volume scattering (green colour) is reduced in FCM as compared to TCM within urban area (city of Roorkee). Pink colour caused due to combination of surface and double-bounce scattering is more in urban area for FCM as shown in Figure 3.4 (b). Water represented by Ganga canal (as marked in Figure 3.2), appears black in both the methods. This indicates occurrence of specular scattering phenomenon. Solani River (as marked in Figure 3.2), appears blue in both the maps of Figure 3.4, which indicates presence of surface scattering.

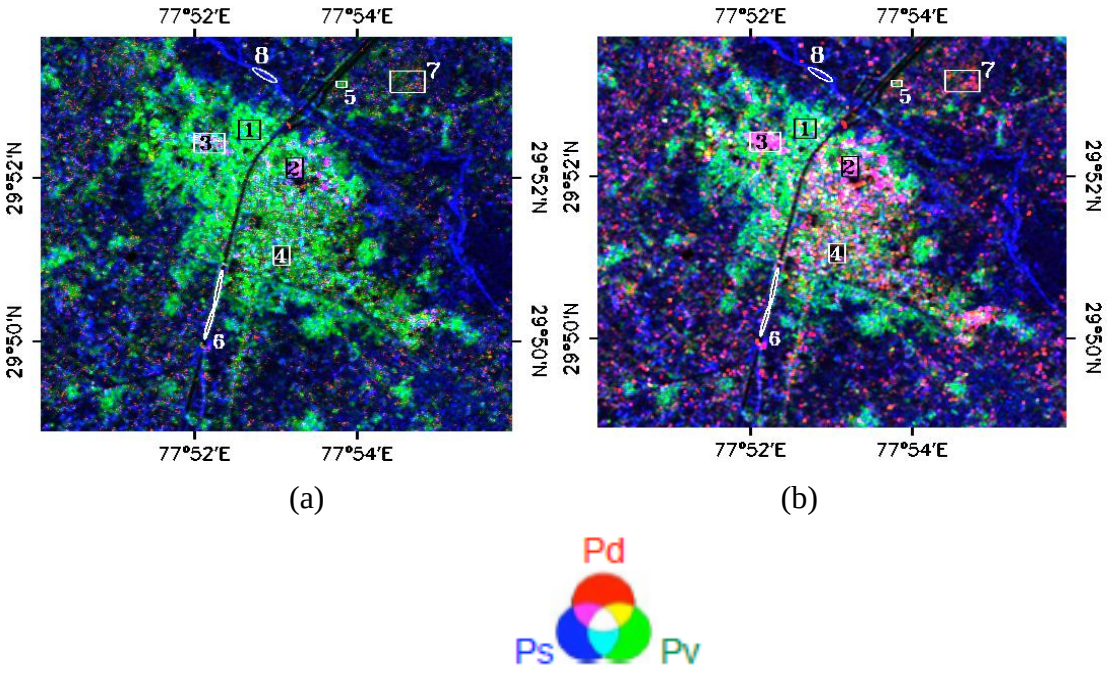

Figure 3.4: RGB colour composite images with P_d (double-bounce power) as red, P_v (volume scattering power) as green, and P_s (surface scattering power) as blue colours for: (a) three component model based decomposition (TCM), and (b) four component model based decomposition (FCM).

In a similar manner, as described above, the decomposition methods with deorientation i.e., three component model based decomposition with deorientation (TCMD), three component model based decomposition with double deorientation and adaptive volume scattering (TCMDDA), four component model based decomposition with deorientation (FCMD), four component model based decomposition with deorientation and additional oriented dihedral volume scattering (FCMDA), and four component model based decomposition with double deorientation (FCMDD), have been applied according to the flowcharts given in Figures B.3-B.7, respectively. The results of these decomposition methods are shown in Figure 3.5, which appear similar by visual inspection of RGB colour composite images. However, the results obtained by decomposition with deorientation are visually different as compared to that of methods without deorientation. The volume scattering appears to be decreased in TCMD and TCMDDA [see Figures 3.5 (a) and (b), respectively] as compared to TCM [Figure 3.4 (a)]. Similar behaviour is observed in FCMD, FCMDA, and FCMDD [Figures 3.5 (c), (d), and (e), respectively] while comparing them with FCM [Figure 3.4 (b)]. In all the decomposition methods, Ganga canal appears black in correspondence with specular scattering. Solani River appears blue exhibiting surface scattering. This behaviour of river is obtained due to its dryness and dominance of sand at the time of ALOS PALSAR data acquisition.

The analysis of decomposition maps presented in Figures 3.4 and 3.5 for all the eight areas represented in Figure 3.2 and described in section 3.2.3 is as follows:

- In urban-1 (number-1 in Figure 3.2), volume scattering is dominant in all the decomposition methods. However, it looks that volume scattering is reduced in all the decomposition methods after deorientation (i.e., TCMD, TCDDA, FCMD, FCMDA, FCMDD), as exhibited in Figure 3.5.
- In urban-2 (number-2 in Figure 3.2), combination of surface and double-bounce (pink colour) is present. Pink colour appears bright in FCM as shown in Figure 3.4 (b) exhibiting increment in double-bounce. The results of decomposition methods after deorientation in Figure 3.5 again appear same for urban-2.
- In urban-3 (number-3 in Figure 3.2), change in scattering response occur from volume scattering (green) in TCM [Figure 3.4 (a)] to mixture of surface and double-bounce (pink) in FCM [Figure 3.4 (b)]. In Figure 3.5, all the decomposition methods with deorientation exhibit combination of surface and double-bounce scattering.
- In bare soil-1 (number-4 in Figure 3.2), specular scattering (black colour) is

dominant for all the decomposition methods exhibited in Figures 3.4 and 3.5.

- In tall-vegetation class (number-5 in Figure 3.2), volume scattering appears dominant for all the decomposition results presented in Figures 3.4 and 3.5.
- In water (number-6 in Figure 3.2), specular scattering (black colour) is present for all the decomposition results exhibited in Figures 3.4 and 3.5.
- In mixed tall vegetation and short vegetation class (number-7 in Figure 3.2), all three scattering components i.e., surface, double-bounce, and volume scattering are present. In FCM [Figure 3.4 (b)], combined scattering due to surface and double-bounce appear dominant.
- In bare soil-2 (number-8 in Figure 3.2), surface scattering (blue colour) is present in all the decomposition methods without deorientation and with deorientation as exhibited in Figures 3.4 and 3.5, respectively.

The visual analysis performed in this section, indicates that decomposition methods work nicely in exhibiting scattering responses of various land covers. Deorientation process improves the scattering response of urban area by reducing volume scattering, as obtained in decomposition without deorientation. The above analysis shows that it is very cumbersome process to visually analyse the decomposition result in order to indicate the scattering behaviour of various land covers. Thus, there is a need to quantitatively analyse the decomposition results. For this purpose two types of quantitative analyses, namely pixel-wise analysis and power-wise analysis, which are described in following sections.

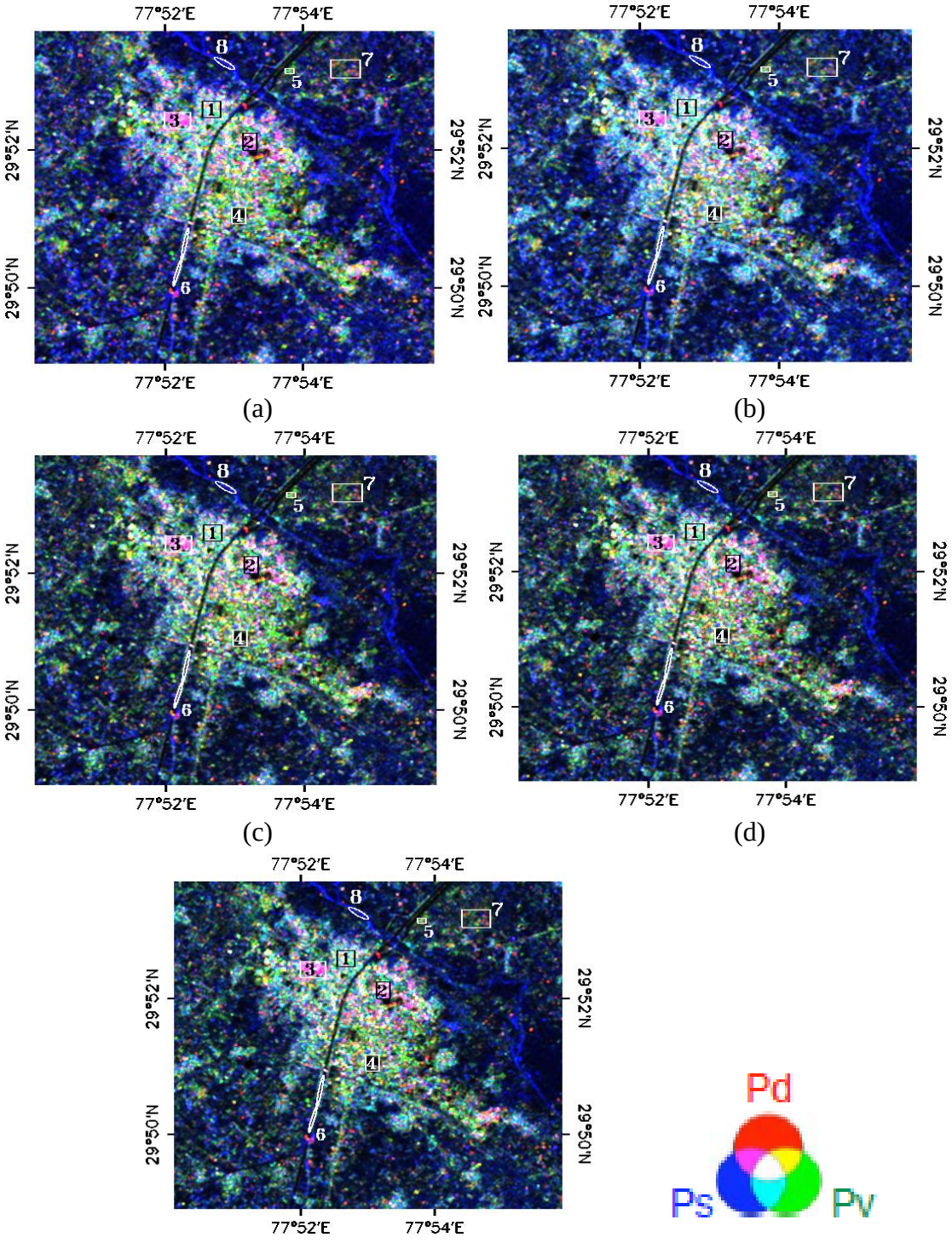

Figure 3.5: RGB colour composite images with P_d (double-bounce power) as red, P_v (volume scattering power) as green, and P_s (surface scattering power) as blue for: (a) three component model based decomposition with deorientation (TCMD), (b) three component model based decomposition with double deorientation and adaptive volume scattering (TCMDDA), (c) four component model based decomposition with deorientation (FCMD), (d) four component model based decomposition with deorientation and additional oriented dihedral volume scattering (FCMDA), and (e) four component model based decomposition with double deorientation (FCMDD).

3.7.3. Pixel Wise Quantitative Analysis for Whole Image

First, the decomposition powers representing different scattering mechanisms (P_s, P_d, P_v, *or/and* P_c) have been calculated for all the methods, i.e., TCM, TCMD, TCMDDA, FCM, FCMD, FCMDA, and FCMDD, according to algorithms presented in Figures B.1 to B.7 of Appendix-B, respectively. Further, the quantitative analysis has been performed by calculating the number of pixels (in percentage) representing each scattering mechanisms for all the decomposition methods. This analysis has been performed on whole images of all scattering contributions.

First, the comparison of quantitative analysis for three component model based decomposition methods with and without deorientation i.e., TCM, TCMD, and TCMDDA [Figures B.1, B.3, and B.4 in Appendix-B, respectively], has been performed. This analysis is as follows:

- It is observed that number of pixels (in percentage) representing P_d and P_s increase in TCMD and TCMDDA as compared with TCM.
- The increment in number of pixels for P_d is 34% in TCMD and 45% in TCMDDA as compared with TCM.
- The pixel percentage for P_s is increased by 13% and 21% in TCMD and TCMDDA, respectively, as compared with TCM.
- The pixel percentage for P_v remains almost same (>95%) in all the decomposition methods.
- Pixels having all scattering contributions (i.e., P_d, Pv, and P_s) in common increase from 44% in TCM to 76% in TCMD to 80% in TCMDD. This indicates that a lot of effort is required to segregate the land covers in terms of scattering response due to large number of common pixels representing all the scattering mechanisms with TCMD and TCMDDA.

Further, the comparison of all four component decomposition methods with and without deorientation methods i.e., FCM, FCMD, FCMDA, and FCMDD, according to Figures B.2, B.5-B.7 in Appendix-B, respectively, has been performed. The analysis of these methods is as follows:

- Number of pixels representing P_d drastically increase in FCMD, FCMDA, and FCMDD as compared with FCM. Theoretically, it is known that deorientation

process increases double-bounce power. This analysis shows that number of pixels representing double-bounce power also increase.

- In FCMD, pixels in P_d and P_s increase by 34% and 7%, respectively, as compared with FCM.
- The pixel percentage of P_d remains same (91%) in both FCMD and FCMDA, whereas it reduces to 81% in FCMDD.
- The pixel percentage of P_s is incremented by only 2% in FCMDA, and is invariant in FCMDD, as compared with FCMD.
- The pixel percentage for P_v is approximately equal (>95%) in all the decomposition methods with or without deorientation.
- Pixel percentage having helix contribution (i.e., P_c) is increases by only 2% in FCMD as compared with FCM, and is invariant in both FCMDA and FCMDD.
- Pixels representing all four scattering mechanisms are more than 50% in all the decomposition methods, i.e., FCM, FCMD, FCMDA, and FCMDD.
- Pixel percentage of all the scattering contributions are almost same in FCMD and FCMDA, which indicate that there is no effect of adding volume scattering due to oriented dihedral in FCMDA.

This pixel-wise quantitative analysis has been performed over 8 regions selected in Figure 3.2. The analysis of each region is described as follows:

- In urban-1, number of pixels (in percentage) for P_d and P_s increase considerably in decomposition methods with deorientation as compared with that of without deorientation. Pixel percentage of P_c (in four component methods) increases in FCMD, FCMDA, and FCMDD as compared with FCM, and it remains unaltered in FCMD, FCMDA, and FCMDD. In this region, number of pixels representing P_s are more than that of P_d.
- In urban-2, very slight change is observed in pixel percentages of P_s and P_d, in all the decomposition methods after deorientation. In all the decomposition methods number of pixels remain almost same (>90%). Pixels percentage of P_c reduces after deorientation.
- In urban-3, pixel percentages of P_s and P_d are same (76%) for TCM. However, pixel percentage of P_s and P_d is more in all other methods as compared with TCM. Pixel

percentage of P_c reduces after deorientation and remain same in FCMD, FCMDA, and FCMDD.

- In bare soil-1, number of pixels representing P_s is more than that of P_d and/or P_c for all the decomposition methods. Pixel percentage for P_c increases by 2% (94% to 96%) after deorientation.
- In tall vegetation, number of pixels representing P_c is quite high (>85%) for four component decompositions. The pixel percentage of P_s is more than that of P_d in all the decomposition methods.
- In water, moderate change in the pixel percentage of P_s and P_d has been observed after deorientation. The pixel percentage of P_s and P_d remain almost equal for all the decomposition methods. Pixel percentage for P_c reduces by 4% (90% to 86%) after deorientation.
- In mixed short and tall vegetation, pixel percentage for P_c remains unaltered (84%) after deorientation. The pixel percentages of P_s and P_d increase after deorientation.
- In bare soil-2, number of pixels representing P_s are quite high (>98%) as compared to P_d. In methods after deorientation (i.e., TCMD, TCMDDA FCMD, FCMDA, and FCMDD), pixel percentage of P_c, P_s and P_d is almost same (>90%).

General discussion:

In general, it can be said that after deorientation, number of pixels representing P_s and P_d increase after deorientation. The number of pixels representing P_v are almost same in all the decomposition methods. No general pattern for P_c has been observed. The main purpose of this analysis was to check the change in number of pixels representing each scattering mechanism after deorientation. It has been observed that before deorientation pixel percentages of P_s and P_d are quite low, which increase significantly after deorientation. Thus, deorientation helps in improving scattering response in terms of number of pixels for P_s and P_d.

3.7.4. Power Wise Quantitative Analysis

Further, the quantitative analysis is performed by visualising scattering contribution in terms of power percentage for each land cover in study area. The analysis has been performed on eight areas which are designated by numbers 1 to 8 in Figures 3.2, 3.4 and 3.5, representing class urban-1, urban-2, urban-3, bare soil-1, tall vegetation, water, mixture of tall and short vegetation, and bare soil-2, respectively. For these land covers, the contribution of each

scattering mechanism (i.e., P_d, P_v, P_s, and (or) and P_c) has been measured in terms of power for all studied decomposition methods (i.e., TCM, TCMD, TCMDDA, FCM, FCMD, FCMDA and FCMDD) and expressed in Figure 3.6. The analysis for each of the area is discussed as follows:

- In urban-1 (number-1 in Figures 3.2, 3.4, and 3.5), the contribution of volume scattering P_v, is more as compared to other scattering mechanisms in methods before deorientation (i.e., TCM and FCM), and in FCMDD, as observed in Figure 3.6 (a). This figure shows that in TCMD, the total scattering in urban-1 is influenced almost equally by both P_v and P_s. In TCMDDA, FCMD and FCMDA, P_s dominates P_d and P_v.
- In urban-2 (number-2 Figures 3.2, 3.4, and 3.5), the contribution of P_s is large as compared to P_d and P_v, as indicated by Figure 3.6 (b).The influence of P_v and P_c is very small in this region.
- In urban-3 (number-3 in Figures 3.2, 3.4, and 3.5), the contribution of all elementary scattering mechanisms (i.e., P_d, P_v, P_s) is significant for TCM. However, in rest of the decomposition methods, scattering is almost equally influencse by P_d and P_s with very small contribution of P_v and negligible contribution of P_c, as observed from Figure 3.6 (c).
- In bare soil-1 (number-4 in Figures 3.2, 3.4, and 3.5), as visualized from Figure 3.6 (d), surface scattering (P_s) dominates over other scattering mechanisms for all the decomposition methods. Significant role of volume scattering (P_v) is also observed in this area.
- In case of tall vegetation (Figures 3.2, 3.4, and 3.5), the influence of P_v is large as compared to other scattering types for all three component decomposition methods (i.e., TCM, TCMD, and TCMDDA) and four component decomposition (FCM), as shown in Figure 3.6(e). However, in FCMD, FCMDD, and FCMDA, the contribution of P_s is more as compared to other scattering mechanisms.
- Water (number-6 in Figures 3.2, 3.4, and 3.5), exhibits dominance of surface scattering (P_s) for all the decomposition methods except for TCM in which volume scattering (P_v) appears larger than other scattering mechanisms [Figure 3.6 (f)].
- In mixed tall vegetation and short vegetation area (number-7 in Figures 3.2, 3.4, and 3.5), the contribution of P_v is more than other scattering mechanisms in TCM, TCMD and FCM, as represented in Figure 3.6(g). However, in FCMD, FCMDA, and FCMDD, the influence of P_s is more than others (P_v, P_d, and P_c), with significant contribution of

P_v and P_d.

- In bare soil-2 (number-8 in Figures 3.2, 3.4, and 3.5), surface scattering P_s has very strong participation (more than 80%) than other scattering types for all the decomposition methods, as observed from Figure 3.6(h).

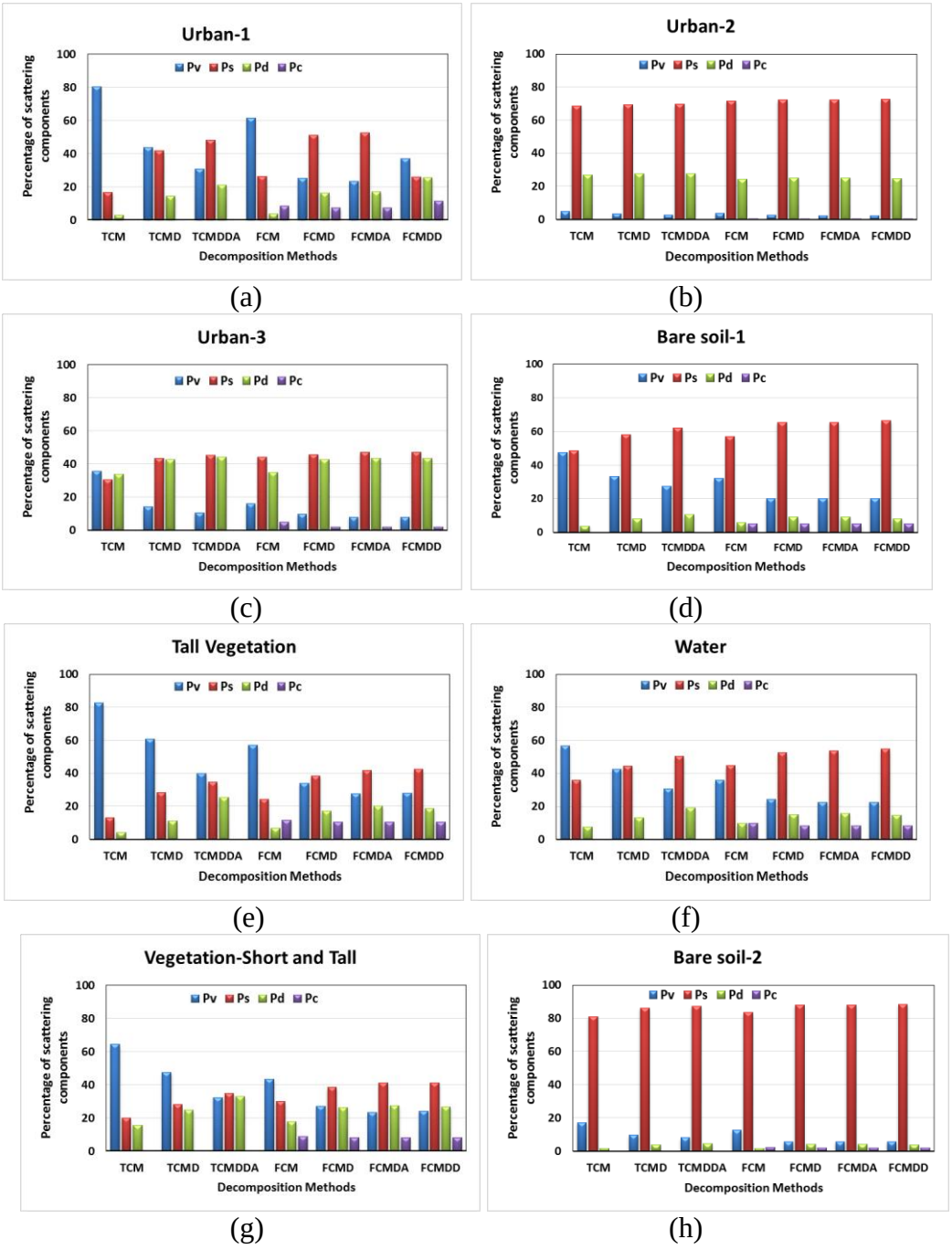

Figure 3.6: Result of power wise analysis for studied decomposition methods : (a) urban-1, (b) urban-2, (c) urban-3, (d) bare soil-1, (e) tall vegetation, (f) water, (g) mixed tall and short vegettaion, and (h) bare soil-2 regions represented by number 1 to 8, respectively, in Figure 3.2.

General discussion:

The main aim of this analysis is to observe the change in power of scattering components after deorientation. The quantitative analysis performed in this section shows that after deorientation, double-bounce power considerably increases and volume scattering considerably reduces as compared with methods without deorientation. The above analysis shows that in case of urban, short vegetation, and tall vegetation, it is difficult to generalize the scattering behaviour they produce because of complexities involved in their structures. Only bare soil exhibits strong contribution of surface scattering by all decomposition methods. After deorientation, double-bounce power is definitely increasing, however, it is not the dominant scattering mechanism in urban area. This may occur due to the presence of large amount of vegetation within urban area (Roorkee city). Therefore, the results, as obtained in [325, 344, 427], have not been observed in our study area (Region-1 Roorkee).

3.8. Conclusion

In this chapter, seven different model based decomposition methods have been studied extensively. These decomposition methods are, three component decomposition (TCM), four component decomposition (FCM); three component decomposition with deorientation (TCMD); three component decomposition with double deorientation and adaptive volume scattering (TCMDDA); four component decomposition with deorientation (FCMD); four component decomposition with deorientation and additional volume scattering (TCMDA); and four component decomposition with double deorientation (FCMDD).

Initially, the visual analysis of the results of all decomposition methods has been performed, by which it is very difficult to analyse scattering behaviour of different land covers. Generally, researches analyse the performance of decomposition methods by observing change in power of various scattering mechanisms. However, in this chapter, both pixel-wise and power-wise analysis have been carried out. In pixel-wise analysis, the relationship among scattering contributions has been visualized in terms of pixel percentage. In power-wise analysis, scattering behaviour for different land covers has been observed in terms of percentage of scattering power. Pixel wise analysis shows that number of pixels representing P_s and P_d increase significantly after deorientation. In power-wise analysis, it has been observed that power of P_v reduces, whereas powers of P_s and P_d increase after deorientation.

Conclusively, it can be said that decomposition methods work well in describing scattering behaviour of various land covers. After deorientation, scattering behaviour of these land covers improves in terms of number of pixels representing scattering mechanisms and scattering power.

Chapter 4

An Adaptive Land Cover Classification Algorithm Based on Spatial Statistics of Polarimetric SAR Indices

The polarimetric information contained in polarimetric SAR images represents great potential for characterization of natural and urban surfaces. However, it is still challenging to identify different land cover classes with polarimetric data. Most of the classification algorithms presented earlier have used fixed value of polarimetric indices for segregation of particular land cover type from other classes. However, the value of these polarimetric indices may change in accordance with the change in observation site, temporal acquisition, environmental conditions, and calibration differences among various systems, etc. Thus, the value of polarimetric indices for segregation of each land cover type has to be tuned in order to cope up with these changes. Therefore, in this chapter, a decision tree based adaptive land cover classification technique has been proposed for labelling of different clusters to their respective classes.

4.1. Introduction

SAR polarimetry is renowned for its application in land cover classification for the extraction of constructive information from satellite data in order to distinguish among various targets. Classification techniques are broadly divided into two categories- parametric and non-parametric classification methods. Parametric classifiers (e.g., supervised and unsupervised) involve estimation of statistical parameters prior to classification unlike, non-parametric classifiers. Each of these classification techniques have their inherent merits and demerits. The major disadvantage of supervised classifier is that analyst imposes the classification structure upon the data by selection of training areas which may not encompass and subsequently represent unique categories that do not fit the information classes. Unsupervised classification, or clustering also suffers from certain limitations and disadvantages. One of the major disadvantages of unsupervised classification is that natural grouping obtained as a result of

iterations in classifier, may not necessarily correspond nicely with desired informational classes, and analyst has limited control over the classes chosen by the classification process [119, 433]. There is another category of classification namely, semi-supervised classification, which falls between supervised and unsupervised classification category, by making use of both labelled and unlabelled data for training [443]. One limitation has been pointed in [234] that semi supervised classification cannot outperform supervised classification unless the analyst is absolutely certain that there is some non-trivial relationship between labels and the unlabelled distribution. Thus, it would be advantageous to opt for non-parametric classifiers, such as a decision tree classifier, which has the capability to handle not only non-normal, non-homogeneous, and noisy data, but also non-linear relations between features and classes, missing values, and numerical and categorical inputs [244]. Recently, some parametric models of sparse learning have been proposed which can also handle missing values and noisy data [100, 417]. Sparse representation classification performs the comparison of residual norms of different classes for labelling of testing samples into a particular class. Since each feature has a different contribution in classification, equal weighing of residual norms may limit the performance of classification. Classification based on sparse representation works well only when there is no similarity in training samples of submatrices of different classes. This assumption does not hold in any of the cases where various features behave in a similar manner for different classes [148]. Considering all aspects, present work uses the concept of decision tree for development of such a technique that may provide the labelling of different clusters without making any prior assumption about data. Several researchers have also shown that decision tree algorithms consistently outperform supervised and unsupervised classification techniques [106, 140, 283] .

Fully polarimetric data has been considered because of a well-known fact that fully polarimetric information plays an important role in describing scattering behaviour (Table 4.1) and physical information about the targets such as shape, orientation, symmetry, non-symmetry, or irregularity of the targets. Thus, polarimetric parameters which can physically interpret the scattering behaviour of different targets may prove useful in land cover classification of those sites, where sufficient *'a priori'* information is not available. Different polarimetric indices have been used by researchers for various applications such as backscattering coefficients of different polarizations (linear- HH,HV,VV; circular- LL, RR, RL and linear 45°-45C,45X) and their ratios have widely been used for crop

classification/vegetation identification [18, 27, 129, 130, 165, 293, 351], bare soil/vegetation discrimination [130, 162, 306, 351], and wetland/water discrimination from other classes [351]; Normalized Difference Polarization Index (*NDPI*) has been used for hazard monitoring [435]; Ratio Vegetation Index (*RVI*) for canopy characterization [12, 187]; Weighted Polarization Sum (*WPS*) for urban mapping [85], and Cross-Polarization Ratio (*CPR*) [380] for separation of bare or sparsely vegetated fields and forested areas, etc.

Table 4.1 Effect of polarized backscattering coefficients in given references

Feature	Remarks	References
$\sigma^0_{vv} \geq \sigma^0_{hh}$	Dominant surface scattering (e.g., from bare soil)	[27]
$\sigma^0_{rl} \geq \sigma^0_{rr}$	Dominant surface scattering (e.g., from bare soil)	[27]
σ^0_{hv}	Dominant multiple scattering from rough surface (e.g., from vegetation)	[27, 162, 165, 293]
$\sigma^0_{hv}/\sigma^0_{vv}$, $\sigma^0_{hv}/\sigma^0_{hh}$	• Maximize the difference between surface and volume scattering therefore have the capability to discriminate bare soil and vegetation • Very low value for smooth surfaces e.g., bare soil	[162, 165]
$\sigma^0_{hh} \geq \sigma^0_{vv}$	Dominant double bounce scattering (obtained from vertical structure)	[27, 162, 351]
$\sigma^0_{hh} \geq \sigma^0_{hv}$	Dominant double bounce scattering	[27, 162]
$\sigma^0_{rl} \approx \sigma^0_{rr}$	Dominant double bounce scattering	[27, 162]

Researchers have used various polarimetric indices, which are well described in [12, 18, 27, 85, 129, 130, 162, 165, 187, 293, 306, 351, 380, 435]. However, there is a need to explore the use of maximum polarimetric indices together in order to utilize their effect in classification of different land cover types and in the development of an adaptive land cover classification approach. Therefore, an exhaustive study was carried out for land cover classification, and a knowledge-based decision tree classification method was proposed using backscattering coefficients (σ^0_{hv}, σ^0_{hh}, σ^0_{vv}, σ^0_{rr}, σ^0_{rl}, σ^0_{ll}, σ^0_{45C}, σ^0_{45X}), cross-pol ratios ($\sigma^0_{rr}/\sigma^0_{rl}$, $\sigma^0_{hv}/\sigma^0_{vv}$, and $\sigma^0_{hv}/\sigma^0_{hh}$) and co-pol ratio ($\sigma^0_{hh}/\sigma^0_{vv}$) in [250]. The limitation of this approach is that it uses fixed values of polarimetric indices for classification of different land cover types and these values may not be same for different observation sites and satellite images. In several other

classification methods, fixed values of polarimetric indices have been used for segregation of different classes [27, 129, 130, 250, 293, 306, 351]. Although these methods have been successfully used for classification purpose, few limitations have been found in these fixed decision criterion (threshold) based classification approaches, as these classification methods are not able to adapt themselves according to different observation sites, temporal acquisition of satellite images, environmental conditions, and calibration differences among various systems, etc. Considering these limitations, an attempt was made to identify the role of several polarimetric indices (backscattering coefficients and their ratios, NDPI, WPS, entropy, RVI, and correlation coefficient) using spatial statistics for land cover classification [248]. It was observed in [248] that the developed method was potentially good for land cover classification using fully polarimetric data. However, based on experimental evaluation it was visualized that assigning the range of values to polarimetric indices in order to create a decision boundary for segregation of different land cover classes was difficult as these values were very much site dependent. Some other researchers [149, 150] have also presented the image- statistics-based approach using optical data for segregation of only two classes. However, in the present study, image-statistics-based approach has been proposed using fully polarimetric SAR data for labelling and classification of five distinct land covers, such as water, bare soil, urban, tall vegetation, and short vegetation.

This chapter deals with the task of developing an adaptive land cover classification approach, which is based on the principle of decision tree algorithm. Decision boundaries of different classes have been decided by using spatial statistics (i.e., median and standard deviation) of the best-selected polarimetric indices on the basis of separability index criterion. In order to make the algorithm adaptive in nature, unknown terms are included along with spatial statistics, for creating the decision criterion for segregation of different classes. An empirical relationship between Overall Accuracy (OA) and spatial-statistics-dependent unknown variables has been developed, which is helpful in finding the value of polarimetric indices for segregation of various classes. The obtained empirical relationship is non-linear in nature. Therefore, a Genetic Algorithm (GA)-based optimization approach has been applied to retrieve the unknown variables. The optimization has been designed in such a way that user-specific requirements (i.e., OA) have been fulfilled. The obtained unknown variables are optimum values of polarimetric indices that can be directly used in decision tree classification algorithm. The dependence of unknown variables on image statistics makes the proposed

algorithm adaptive in nature.

This chapter is organised as follows: section 4.2 provides a brief description about the test site and data used in the study. The development of proposed adaptive classification method along with the role of various polarimetric indices in labelling and classification of different land covers has been provided in section 4.3. Section 4.4 provides the discussion about the results obtained by testing and validation of proposed algorithm. The final remarks and conclusions are given in section 4.5.

4.2. Study Area and Data Used

4.2.1. Study Area

The study is carried out in city of Roorkee in the state of Uttarakhand, India. The detailed description of study area is given in section 3.2.1 of Chapter-3. As mentioned in Chapter 3, that study area has variety of land covers such as urban, bare soil, water, tall vegetation, and short vegetation.

In urban area (i.e., city Roorkee), a lot of vegetation exists. Therefore, it is worth mentioning here that the trees in urban area may behave in a different manner as compared with the trees in natural forests, and their signatures may be influenced by buildings and other man-made structures in urban area [85]. Trees in urban area may represent combination of scattering i.e., volume scattering from tree canopy and double-bounce scattering from buildings, while strong volume scattering is represented by trees in forest. Thus, if tall vegetation class (i.e., forest) is located separately from urban, both classes can be distinguished well. However, segregation of tall vegetation within urban areas is challenging because in this situation, segregation of both the classes may be hampered by each other. Therefore, caution must be taken in extending the algorithm to other areas.

4.2.2. SAR Data

The development and testing of proposed classification algorithm has been performed on same fully polarimetric ALOS PALSAR data as used in Chapter 3. In this chapter, this data is designated as “Data-1” (Data ID-PASL1109040617112609081100 63). Further, the validation of proposed algorithm has been performed on another ALOS PALSAR data (Data ID-PASL1100904061711181001150003: Data-2) acquired on same date (i.e., April 6, 2009) but at

a different time.

4.2.3. Ground Data

In order to develop the algorithm Region-of-Interest (ROI) points are required for performing two tasks; first, for training the classifier during development process, and second, for evaluating the performance of classifier by calculating the classification accuracy. Thus, extensive ground truth survey has been carried out using Global Positioning System (GPS) over the whole study region on April 4, 2009. Some ROI points have also been chosen from Google Earth imagery and topographic map of city of Roorkee. Out of total 1062 ROIs, 635 ROIs have been used for training and development of proposed adaptive classification algorithm, and remaining 427 ROIs have been used for testing and validation of the proposed algorithm. All of these points are listed in Table 4.2.

4.3. Methodology

Traditional classification methods such as K-means, minimum distance, maximum likelihood, and some other methods such as commute-time-guided transformation [99], logistic regression [72], linear discriminant analysis [114], Bayes classification [238], etc., make prior assumption about the probability density function of data set, and require large number of training samples in order to improve the classification accuracy. Thus, in this chapter, an adaptive land cover classification algorithm is proposed which does not require making assumption about the probability density function of data.

Table 4.2 Region of interest points

Class	Total	Training	Testing
Water	***197***	90	107
Urban	***295***	175	120
Tall	***300***	200	100
Short	***125***	75	50
Bare soil	***145***	95	50
Total	***1062***	***635***	***427***

Forward modelling approach is adopted for development of classification algorithm, which is carried out in three major steps-(*1*) Selection of polarimetric indices having capability to separate two classes, (*2*) Experimental evaluation of obtained polarimetric indices in order to develop the algorithm, which is based on spatial statistics such as median and standard deviation of whole image for labelling of various clusters to their own classes, (*3*) Retrieval of optimized value of polarimetric indices using Genetic Algorithm (GA)**.** The detailed description is as follows:

4.3.1. Data Pre-processing

The pre-processing of ALOS PALSAR data is performed according to description presented in section 3.7.1 of Chapter 3. The flowchart of pre-processing is presented in Figure 3.3. This processed data is then used for the development of algorithm.

4.3.2. Extraction of Polarimetric Indices

The polarimetric SAR carries out measurement in multiple polarizations (HH, VV, HV, and VH), which generally defines the scattering properties of various targets. The polarimetric indices are polarimetric SAR observables extracted from polarimetric SAR data having physical meanings that describe the scattering behaviour of different targets. It has been observed that researchers have used different polarimetric indices for several applications [12, 18, 27, 85, 129, 130, 162, 187, 248, 250, 293, 306, 351, 380, 435]. Out of these polarimetric indices, backscattering coefficients of different polarizations have widely been used by several researchers for diverse applications. Backscattering coefficient plays a major role in characterization of targets due to its dependence on electromagnetic wave parameters, such as wave frequency, polarization, and incidence angle. It also depends upon the target characteristics such as surface geometry (size, shape, orientation distribution, and spatial arrangement of objects), physical property (symmetry, non-symmetry, or irregularity of the target), and dielectric characteristics of the medium. Since fully polarimetric data can easily be synthesized into nonlinear polarizations such as circular and elliptical, the advantage of these polarizations can be exploited by backscattering coefficient because each polarization of polarimetric SAR backscattering data effectively describes scattering from certain land cover type [27, 162, 165, 245, 293, 306, 351]. The effect of polarized backscatter coefficient on different land cover types has been summarized in Table 4.1.

A knowledge-based decision tree classification method was proposed in [250]. In this

method it was demonstrated quantitatively that standard polarimetric parameters such as polarized backscattering coefficients (σ^0_{hv}, σ^0_{hh}, σ^0_{vv}, σ^0_{rr}, σ^0_{rl}, σ^0_{ll}, σ^0_{45C}, σ^0_{45X}), cross-pol ratios ($\sigma^0_{rr}/\sigma^0_{rl}$, $\sigma^0_{hv}/\sigma^0_{vv}$, and $\sigma^0_{hv}/\sigma^0_{hh}$), and co-pol ratio ($\sigma^0_{hh}/\sigma^0_{vv}$) could be used as information bearing features for making decision boundaries for classification of different land cover types such as water, bare soil, tall vegetation, short vegetation, and urban. It was found in [248] that inclusion of some more polarimetric parameters might lead to the development of effective classification algorithms. Based on above discussion, polarized backscatter coefficient of different polarizations and their ratios are extracted from polarimetric data along with some other polarimetric indices, such as *NDPI* [435]; *RVI* [12, 187]; *WPS* [85], and *CPR* [380], for development of proposed adaptive classification technique. These parameters are described as follows:

a) ***Normalized Difference Polarization Index (NDPI)*** is used to analyze the surface types including vegetation cover, soil type and roughness [435] , and is defined as,

$$NDPI = \frac{\sigma^0_{vv} - \sigma^0_{hv}}{\sigma^0_{vv} + \sigma^0_{hv}} \ , \tag{4.1}$$

High roughness areas represent high NDPI values.

b) ***Ratio Vegetation Index (RVI)*** weights the contribution of the cross-polarized returns to total power. This parameter is sensitive to biomass level, and used for estimation of vegetation cover [12, 187]. The RVI generally varies between zero and one, and is defined as,

$$RVI = \frac{8\sigma^0_{hv}}{\sigma^0_{hh} + \sigma^0_{vv} + 2\sigma^0_{hv}} \ , \tag{4.2}$$

For diffuse scattering (volume scattering) from vegetation its value is relatively high.

c) ***Weighted Polarization Sum (WPS)*** is a function of absolute value of polarimetric terms HH, HV, and VV, and is defined as [85],

$$WPS = 1000\left(|HH| + |HV| + |VV|\right)^{0.001}, \tag{4.3}$$

This feature is used to classify land covers/land use (mainly in urban area) based on their roughness. It exhibits low value for smooth surfaces while high value for rough surfaces [85].

d) ***Cross-Polarization Ratio (CPR)*** is used to discriminate between bare and sparsely vegetated fields and forested areas [380], and is defined as,

$$CPR = \frac{\sigma^0_{hv}}{\sigma^0_{hh} + \sigma^0_{hv}} \ , \tag{4.4}$$

4.3.3. Selection of Polarimetric Indices Based on Separability Index Criterion

A total of sixteen polarimetric parameters (σ^0_{rr}, σ^0_{rl}, σ^0_{ll}, σ^0_{hv}, σ^0_{hh}, σ^0_{vv}, σ^0_{45C}, σ^0_{45X}, $\sigma^0_{rr}/\sigma^0_{rl}$, $\sigma^0_{hv}/\sigma^0_{vv}$, $\sigma^0_{hv}/\sigma^0_{hh}$, $\sigma^0_{hh}/\sigma^0_{vv}$, *WPS*, *RVI*, *NDPI*, and *CPR*) are considered for development of adaptive classification algorithm on Data-1 (Data ID-PASL1109040617112609081100 63). It will be a tedious task to select the suitable features for classification. Therefore, in order to check the separability between class pairs, a measure, which is called a separability index, has been calculated for all the polarimetric indices. The main attribute required for a feature chosen for classification depends on how well the feature distinguishes between the two classes in the classification process. Based on this concept, a feature is said to offer fine separation between two classes, if the difference between the mean values of two classes is large as compared to the sum of standard deviations of those classes for that particular feature [91, 250, 418]. This index is defined as,

$$SI_{ij} = \frac{\left|\mu_i - \mu_j\right|}{S_i + S_j} \ , \tag{4.5}$$

where μ and S are the mean values and standard deviations, respectively, of classes i and j for a particular feature. In particular, value of SI_{ij} that lies between 0.8 to 1.5, indicates an authentic feature for separation of two classes i and j, whereas SI_{ij} that is greater than 2, represents feature for almost complete class pair separation. SI_{ij} that is below 0.8, represents the feature worth for rejection of those particular classes [91, 250, 418].

Initially, the concept of feature separation has been applied to five class pairs, namely, *(i) water and others (urban, tall vegetation, bare soil, and short vegetation),(ii) bare soil and others (urban, tall vegetation, water, and short vegetation),(iii) tall vegetation and others (urban, water, bare soil, and short vegetation), (iv) short vegetation and others (urban, tall vegetation, bare soil, and water) and (v) urban and others (water, tall vegetation, bare soil, and short vegetation).* Separability index values (*SI*) of these class pairs for all sixteen class

pairs are shown in Figure 4.1. It shows that bare soil has good separation capability from other classes by features $\sigma^0_{rr}/\sigma^0_{rl}$, $\sigma^0_{hv}/\sigma^0_{vv}$, $\sigma^0_{hv}/\sigma^0_{hh}$, *CPR*, *NDPI*, and *RVI*, with $SI > 2$. Water can be best separated from other classes by *WPS* only with $SI > 2$, as shown in Figure 4.1. Other authentic acceptable features that can separate water from other classes with condition $1.5 < SI < 2$ are σ^0_{rr}, σ^0_{rl}, σ^0_{ll}, σ^0_{hv}, σ^0_{hh}, σ^0_{vv}, σ^0_{45C}, and σ^0_{45X}. It is observed in this figure that there is no feature with $SI > 2$ (or 1.5) for the categories tall vegetation and others, urban and others, and short vegetation and others; hence, these classes cannot be taken as the first member to be segregated from other classes. Although the water class shows good separation capability by several features as mentioned above, bare soil has been chosen as the first member to be separated from other classes due to its better separation capability (in terms of *SI* value) as compared to class pair "water and others".

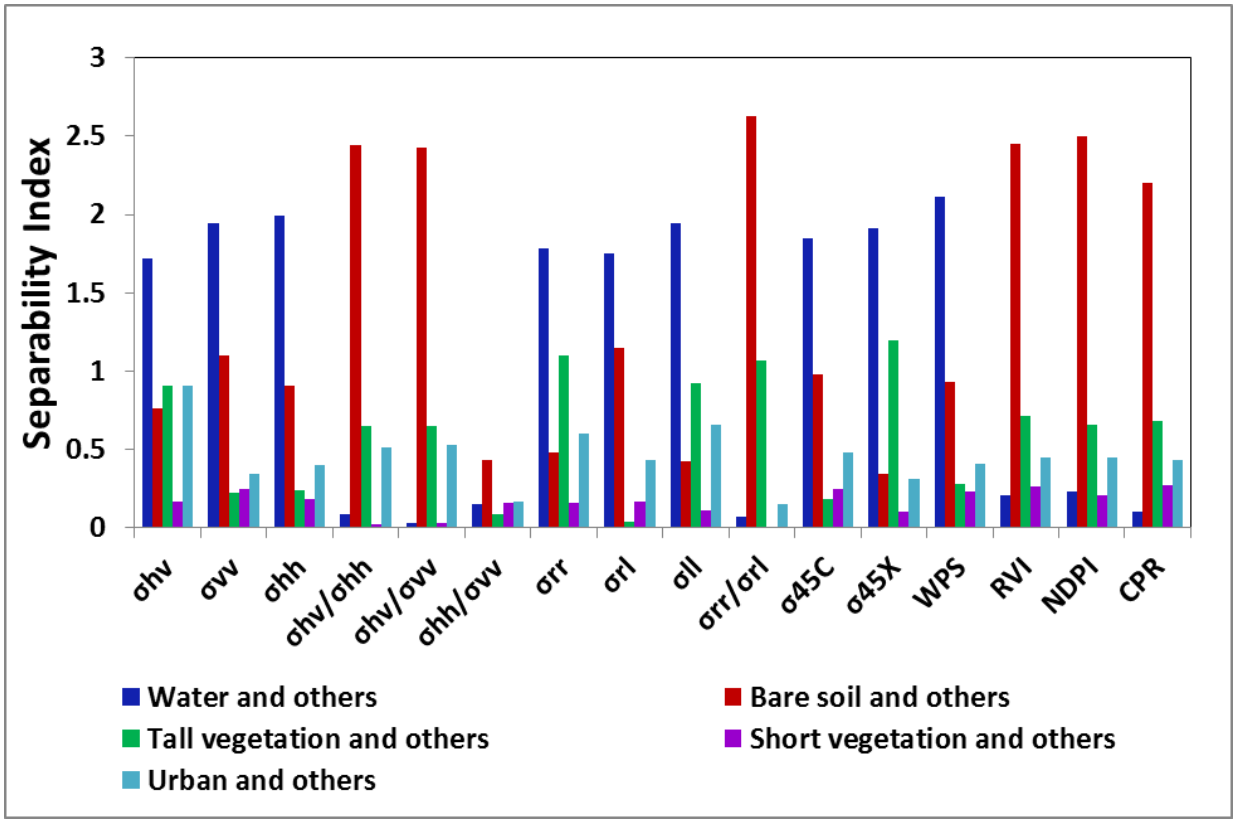

Figure 4.1: Measured separability index for class pair separation by various polarimetric features for separation of class water, bare soil, tall vegetation, short vegetation, and urban, respectively, from other remaining classes.

After selecting bare soil as the first class to be segregated from other classes, four classes (i.e., water, short vegetation, tall vegetation, and urban) are left to be separated in classification procedure. Thus, separation of remaining classes is done in following manner:

- *Separation of water with tall vegetation, short vegetation and urban:* Since water shows good separation capability from other classes after bare soil by features *WPS*, σ^0_{rr}, σ^0_{rl}, σ^0_{ll}, σ^0_{hv}, σ^0_{hh}, σ^0_{vv}, σ^0_{45C}, and σ^0_{45X}, as shown in Figure 4.1, it is selected as the next member to be segregated from other classes after excluding bare soil.
- *Separation of short vegetation with tall vegetation and urban:* After excluding classes water and bare soil, three classes i.e., short vegetation, tall vegetation, and urban, are left to be segregated in the classification procedure. Earlier, various techniques have been developed for segregation of tall vegetation from short vegetation and urban [106, 293], or vegetated areas from urban [123, 396, 438]. It has been found by some researchers [27, 293, 351] that σ^0_{hv} is the best feature for segregation of tall vegetation from other classes. However, it has been observed in [248, 250] that it is difficult to segregate tall vegetation from other classes in presence of urban. In [293], it has been shown that σ^0_{hv} has ability to segregate tall vegetation from other classes (i.e., bare soil, short vegetation, and water) only when urban has already been separated using texture feature. In [106], segregation of classes tall vegetation, short vegetation, and surfaces has been performed in the site where urban class is negligible (much less than 1% of total imaged area). Thus, in order to select next member to be segregated in adaptive classification procedure, an analysis is performed to observe the behaviour of each remaining class (i.e., short vegetation, tall vegetation, and urban) for all the polarimetric indices.

In order to demonstrate the scattering behaviour for all the polarimetric indices, 75 ROIs of each class i.e., tall vegetation, short vegetation, and urban, are considered from training ROIs listed in Table 4.2. The profiles of these classes for all 16 polarimetric features (σ^0_{rr}, σ^0_{rl}, σ^0_{ll}, σ^0_{hv}, σ^0_{hh}, σ^0_{vv}, σ^0_{45C}, σ^0_{45X}, $\sigma^0_{rr}/\sigma^0_{rl}$, $\sigma^0_{hv}/\sigma^0_{vv}$, $\sigma^0_{hv}/\sigma^0_{hh}$, $\sigma^0_{hh}/\sigma^0_{vv}$, *WPS*, *RVI*, *NDPI*, and *CPR*) are shown in Figure 4.2. Figure 4.2(a) shows that urban and tall vegetation do not have much difference in the value of σ^0_{hv}, whereas short vegetation is clearly distinguished from both tall vegetation and urban. The features σ^0_{rr} [Figure 4.2(g)], σ^0_{ll} [Figure 4.2(i)], and *WPS* [Figure 4.2(m)] show almost similar behaviour for tall vegetation and urban. The characteristic of short vegetation is overlapped with the characteristics of tall vegetation and urban at some of the

ROIs. Based on this analysis, σ^0_{hv} appears to be the best feature for separation of short vegetation from tall vegetation and urban.

The characteristics of short vegetation is overlapped with tall vegetation and urban at several ROIs for features σ^0_{vv} [Figure 4.2(b)], σ^0_{hh} [Figure 4.2(c)], $\sigma^0_{hv}/\sigma^0_{vv}$ [Figure 4.2(d)], $\sigma^0_{hv}/\sigma^0_{hh}$ [Figure 4.2(e)], σ^0_{rl} [Figure 4.2(h)], $\sigma^0_{rr}/\sigma^0_{rl}$ [Figure 4.2(j)], σ^0_{45C} [Figure 4.2(k)], σ^0_{45X} [Figure 4.2(l)], *RVI* [Figure 4.2(n)], and *CPR* [Figure 4.2(p)]. It is found that almost complete overlapping of short vegetation, tall vegetation, and urban occurs for features $\sigma^0_{hh}/\sigma^0_{vv}$ [Figure 4.2(f)] and *NDPI* [Figure 4.2(o)]. Therefore, there does not exist any clear boundary by which these classes can be separated using all of these features. The polarimetric feature $\sigma^0_{rr}/\sigma^0_{rl}$ [Figure 4.2(j)] shows a unique behaviour in which tall vegetation and urban are clearly distinguished, whereas short vegetation is overlapped with urban at some ROIs. Therefore, urban and tall vegetation are considered as the same class, whereas short vegetation as another class in the present analysis.

- *Separation of tall vegetation and urban:* After segregation of short vegetation in classification procedure, tall vegetation can be separated from urban by feature $\sigma^0_{rr}/\sigma^0_{rl}$ as shown in Figure 4.2(j).

In order to validate the analysis shown in Figure 4.2, the concept of separability index is used in order to select the features for segregation of classes tall vegetation, short vegetation, and urban in classification procedure. Thus, three class pairs, namely, *(i) water and others (*i.e. *tall vegetation, short vegetation, and urban), (ii) short vegetation and others (*i.e., *tall vegetation and urban), and (iii) tall vegetation and urban,* are formed for calculating separability index. Separability index for these class pairs is shown in Figure 4.3. This figure exhibits that all the backscattering coefficients (i.e., σ^0_{rr}, σ^0_{rl}, σ^0_{ll}, σ^0_{hv}, σ^0_{hh}, σ^0_{vv}, σ^0_{45C}, and σ^0_{45X}) and *WPS* have capability to separate water from tall vegetation, short vegetation, and urban, with $SI > 2$ for all of these features. Some acceptable features (with $SI > 1$) for separation of short vegetation from urban and tall vegetation are σ^0_{rr}, σ^0_{ll}, σ^0_{hv}, and *WPS*. Urban and tall vegetation are separated by only $\sigma^0_{rr}/\sigma^0_{rl}$ with $SI > 2$. Thus, separability index criteria (Figure 4.3) clearly confirms our previous analysis (Figure 4.2).The list of features obtained by feature separation criterion for identification of each land cover type is given in Table 4.3.

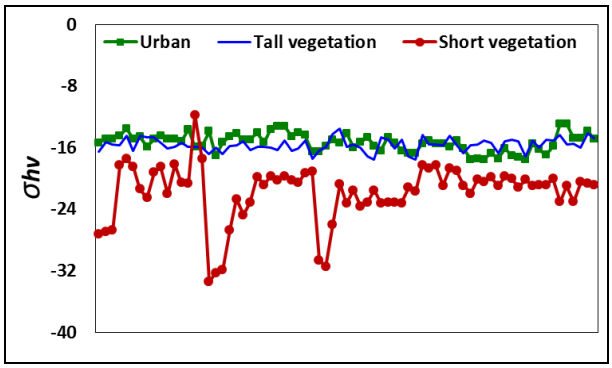

(a)

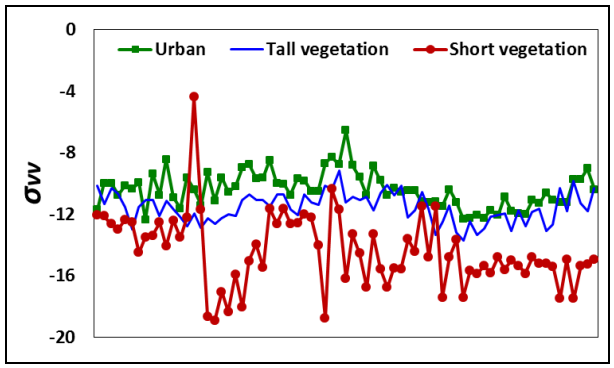

(b)

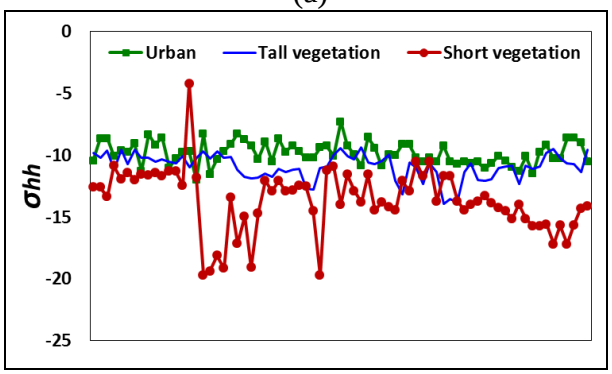

(c)

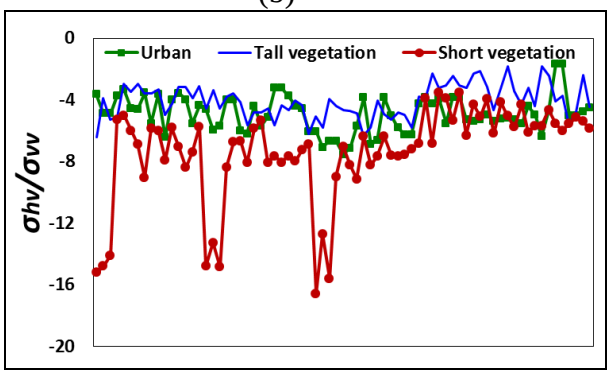

(d)

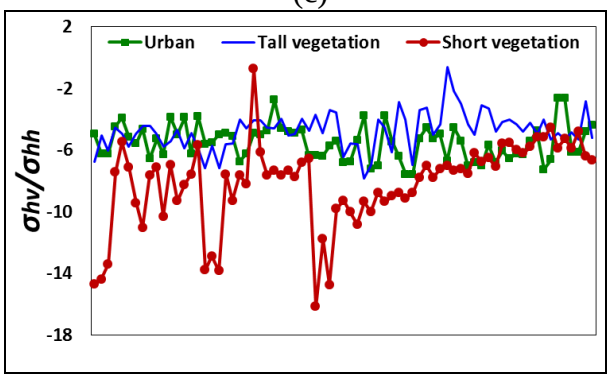

(e)

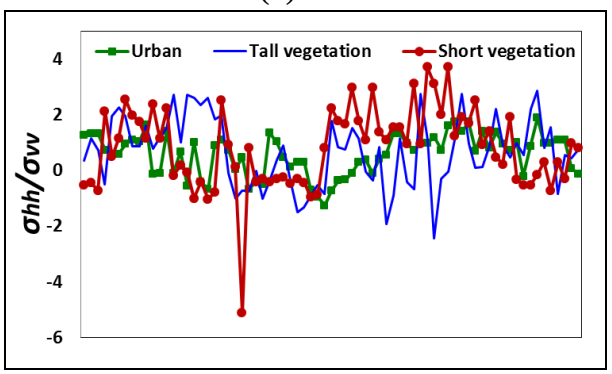

(f)

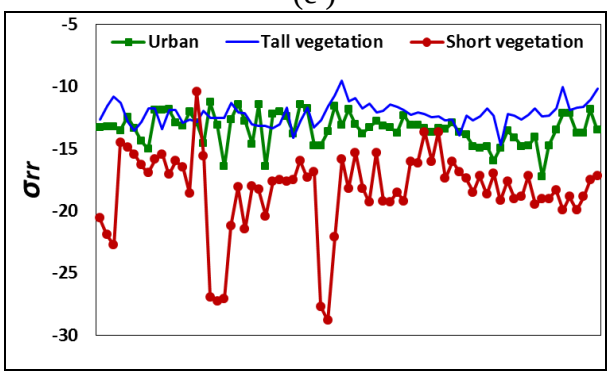

(g)

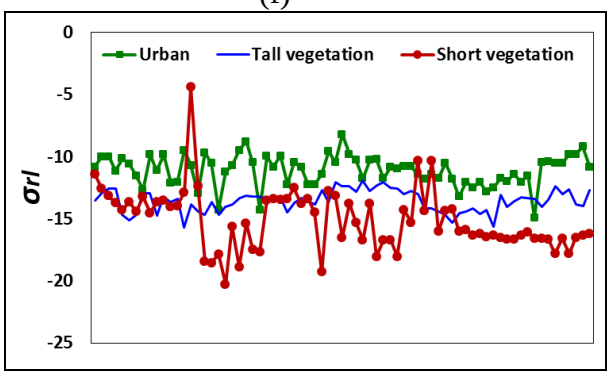

(h)

(contd…)

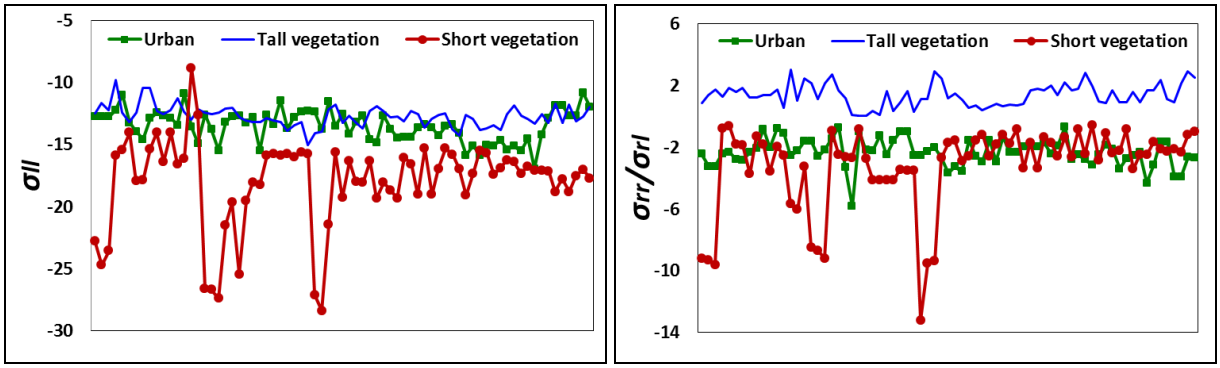

(i)

(j)

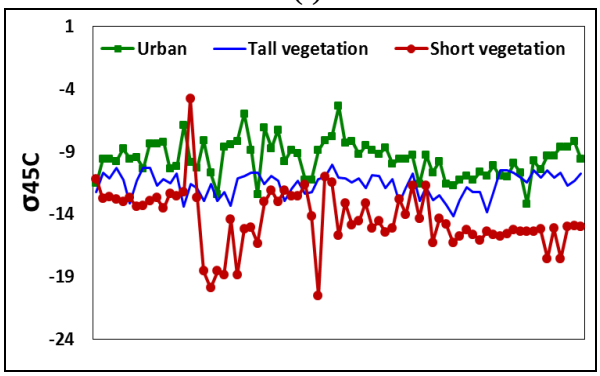

(k)

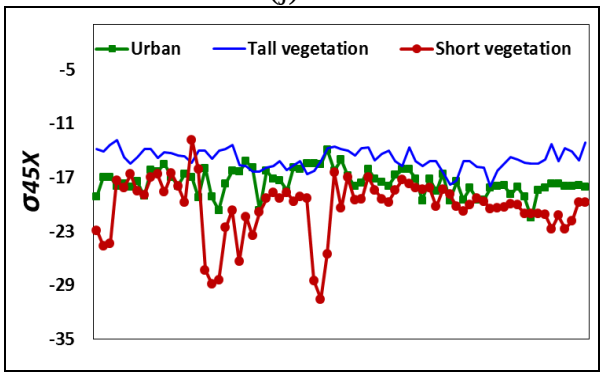

(l)

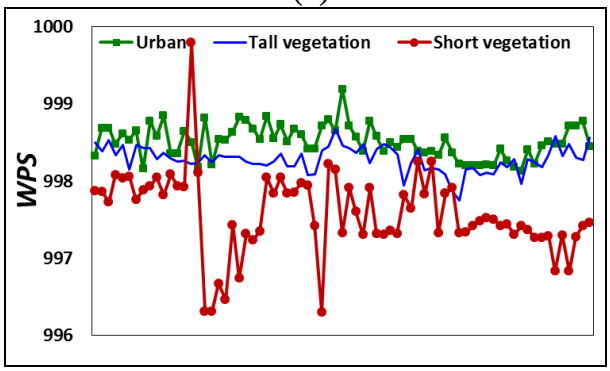

(m)

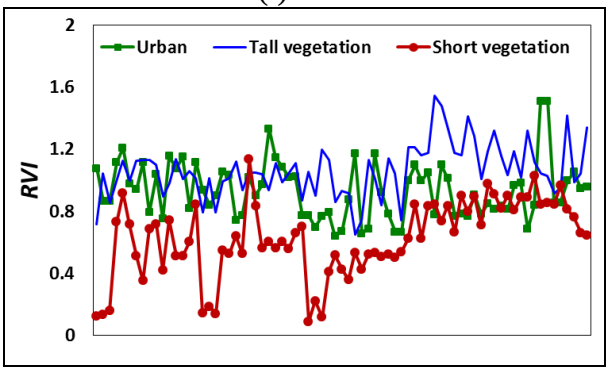

(n)

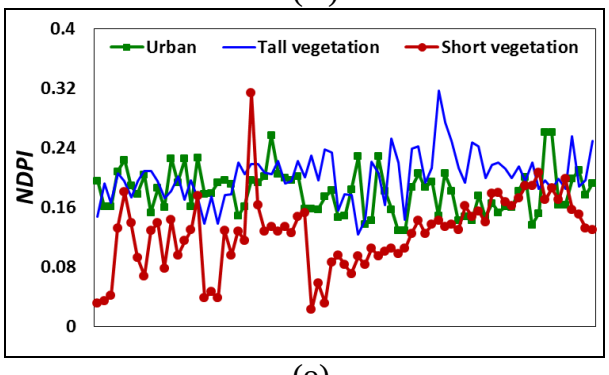

(o)

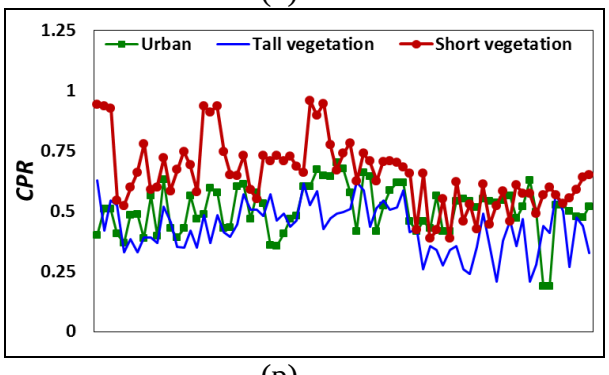

(p)

Figure 4.2: Plots showing the effect of different polarimetric indices on classes tall vegetation, urban and short vegetation. These plots [(a)-(p)] are created by taking 75 ground truth points of each class.

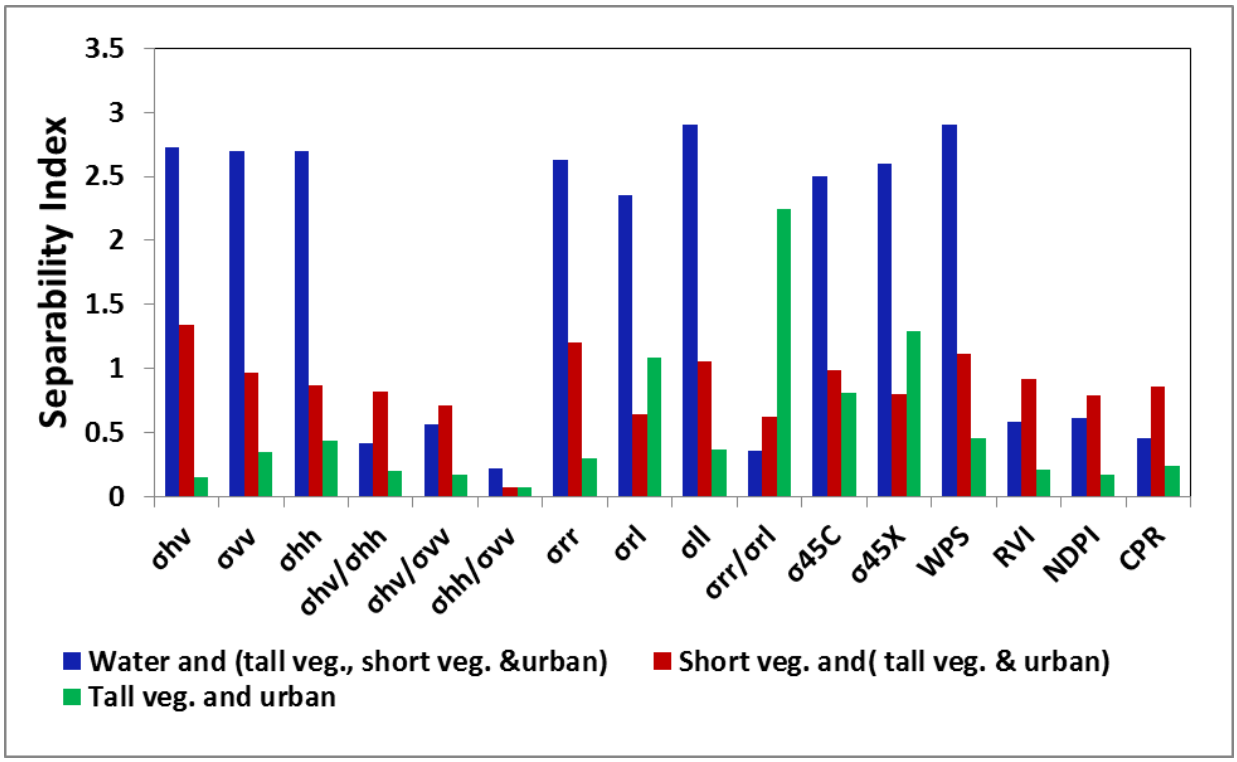

Figure 4.3: Separability index for class pair separation by various features, for separation of (class water from tall vegetation, short vegetation and urban), (class short vegetation from tall vegetation and urban), and (class tall vegetation and urban).

Table 4.3 Selected features for different land cover classes based on separability index criterion

Land cover type	**Selected feature**
Bare soil	$\sigma^0_{rr}/\sigma^0_{rl}$, $\sigma^0_{hv}/\sigma^0_{vv}$, $\sigma^0_{hv}/\sigma^0_{hh}$,*RVI, CPR, NDPI*
Water	σ^0_{rr}, σ^0_{rl}, $\sigma^0_{ll,}$ σ^0_{hv}, σ^0_{hh}, $\sigma^0_{vv,}$ σ^0_{45C} , σ^0_{45X}, *WPS*
Short vegetation	σ^0_{rr}, σ^0_{ll}, σ^0_{hv}, *WPS*
Urban	$\sigma^0_{rr}/\sigma^0_{rl}$
Tall vegetation	$\sigma^0_{rr}/\sigma^0_{rl}$

4.3.4. Model Development

The task of labelling of different land cover types with adaptive decision criterion is very challenging. Therefore, an image-statistics-based adaptive decision tree classification technique has been proposed, which utilizes local information i.e., spatial statistics: median and standard deviation, of whole images of polarimetric indices in order to create decision boundary for segregation of two classes. The process of model development is carried out in following steps:

a) Calculation of spatial statistics of image.
b) Creation of decision criterion in terms of image statistics for segregation of each class.
c) Development of decision tree classifier.
d) Performance evaluation of proposed classification method.

4.3.4.1 Calculation of spatial statistics of image

The spatial statistics of whole image i.e., median and standard deviation, are calculated for making a decision boundary in order to classify particular land cover type. Median describes the central tendency of distribution. It's less sensitivity to extreme values of distribution makes it appropriate option as compared to mean. Standard deviation is a measure of the dispersion of a set of data from its average value (median). The information about image statistics (minimum, maximum, median, and standard deviation) for whole images of all 16 polarimetric features extracted from Data-1 is listed in Table 4.4.

By using separability index criterion, polarimetric indices providing better separation between two classes (Table 4.3) have been obtained. The image statistics of these indices are calculated for the respective classes defined by training ROI (enlisted in Table 4.2). The statistics of these selected features are provided in Tables 4.5-4.9 for bare soil, water, short vegetation, tall vegetation, and urban, respectively. After analysing these Tables, it is observed that it is quite difficult to use a fixed value of any polarimetric index in the decision boundary for segregation of any class. For example, the image statistics i.e., minimum, maximum, median, and standard deviation, for feature $\sigma^0_{rr}/\ \sigma^0_{rl}$ calculated by using training ROI of bare soil are obtained as −19.24, −5.51, −12.96 and 2.35 dB, respectively as given in Table 4.5, whereas for the whole image of feature $\sigma^0_{rr}/\sigma^0_{rl}$ the image statistics are obtained as −20.23, 14.73, −3.61 and 2.98 dB, respectively as given in Table 4.4. These values infer that required deciding value of feature $\sigma^0_{rr}/\sigma^0_{rl}$ to segregate bare soil cannot be obtained by using either the median or the standard deviation of its whole image.

Table 4.4 Image statistics of polarimetric indices for whole image of Data-1

Feature	Minimum	Maximum	Median	Standard deviation
σ_{hv}	−37.53	−5.99	−23.81	4.40
σ_{vv}	−30.97	6.98	−14.99	2.83
σ_{hh}	−29.94	6.98	−14.668	3.21
σ_{hv}/σ_{vv}	−30.14	6.68	-8.52	2.94
σ_{hv}/σ_{hh}	−30.08	5.38	−9.05	2.70
σ_{hh}/σ_{vv}	−11.39	19.89	0.42	1.45
σ_{45X}	−34.51	6.34	−22.49	4.06
σ_{45C}	−32.85	6.98	−15.38	3.09
σ_{rr}	−36.00	6.57	−20.23	4.40
σ_{rl}	−31.91	6.98	−15.99	2.92
σ_{ll}	−33.29	6.27	−19.94	4.31
σ_{rr}/σ_{rl}	−20.23	14.73	−3.61	2.98
WPS	993.93	1002.31	997.29	0.69
RVI	0.0038	3.05	0.47	0.27
NDPI	−0.64	0.99	0.74	0.15
CPR	0.00098	0.78	0.11	0.067

Table 4.5 Image statistics of class bare soil (defined by training ROI) for features obtained by separability index

Feature	Minimum	Maximum	Median	Standard deviation
σ_{rr}/σ_{rl}	−19.24	−5.51	−12.96	2.3537
σ_{hv}/σ_{hh}	−26.182	−13.77	−17.28	2.7828
σ_{hv}/σ_{vv}	−26.54	−14.26	−17.85	2.8578
RVI	0.0092	0.1523	0.0702	0.035
NDPI	0.9277	0.9956	0.9677	0.0176
CPR	0.0024	0.0402	0.00937	0.0184

Table 4.6 Image statistics of class water (defined by training ROI) for features obtained by separability index

Feature	Minimum	Maximum	Median	Standard deviation
σ_{hv}	−35.85	−26.67	−31.712	2.0192
σ_{vv}	−29.63	−13.62	-21.88	3.9983
σ_{hh}	−29.95	−13.76	−22.356	3.2726
σ_{ll}	−31.05	−20.99	−27.032	1.917
σ_{rr}	−33.73	−22.68	−28.208	2.3083
σ_{rl}	−31.35	−14.55	−22.43	4.02
σ_{45X}	−32.18	−23.59	−29.206	1.7479
σ_{45C}	−30.35	−15.92	−21.978	3.97
WPS	994.27	997.56	995.74	0.7739

Table 4.7 Image statistics of class short vegetation (defined by training ROI) for features obtained by separability index

Feature	Minimum	Maximum	Median	Standard deviation
σ_{hv}	−27.52	−20.95	−23.91	1.4455
σ_{ll}	−24.98	−15.09	−19.52	2.0538
σ_{rr}	−25.47	−15.26	−19.533	2.18
WPS	996.34	998.27	997.27	0.4295

Table 4.8 Image statistics of class tall vegetation (defined by training ROI) for features obtained by separability index

Feature	Minimum	Maximum	Median	Standard deviation
σ_{hv}	−23.11	−15.04	−18.17	1.8395
σ_{rr}/σ_{rl}	0.031	6.28	0.9814	1.1955

Table 4.9 Image statistics of class urban (defined by training ROI) for features obtained by separability index

Feature	Minimum	Maximum	Median	Standard deviation
σ_{hv}	−17.53	−9.66	−14.548	1.1217
σ_{rr}/σ_{rl}	−4.81	−0.366	−1.5268	1.2088

4.3.4.2 Decision criterion for segregation of each class

An extensive and exhaustive study is performed for selecting the decision criterion required to classify a particular land cover type using image statistics (i.e., median *'M'* and standard deviation *'S'*) of polarimetric indices chosen by separability index criterion. It is observed that the required decision criterion for segregation of any class cannot be easily obtained by using median and standard deviation of whole image separately or together (i.e., $M \pm S$**).** It is known that image statistics may not be same for two images of similar sites, and hence, it is impractical to consider expression $M \pm S$ as decision criterion of selected feature for separation of any class. Therefore, in order to make the algorithm adaptive, an unknown term *'*n_i*'* is included to form different mathematical expressions (e.g., Mn_i, $M \pm n_i$, $M \pm n_iS$, $M \pm (n_i-1)S$,...) using image statistics of selected polarimetric observable. The subscript *"i"* denotes any value 1, 2, 3..., and so on, depending upon the number of mathematical expressions for selected polarimetric indices. The principle of selecting mathematical expressions for development of classification algorithm is as follows:

<u>Principle of forming mathematical expressions for development of classification algorithm</u>

By using the concept of separability index criterion, bare soil is obtained as the first entity to be separated in the classification process, and six polarimetric indices ($\sigma^0_{rr}/\sigma^0_{rl}$, $\sigma^0_{hv}/\sigma^0_{vv}$, $\sigma^0_{hv}/\sigma^0_{hh}$, *RVI*, *CPR*, and *NDPI*) are obtained for separation of bare soil from other classes. Using all of these features in making decision boundary will increase the complexity of algorithm. Therefore, only two features $\sigma^0_{rr}/\sigma^0_{rl}$ and $\sigma^0_{hv}/\sigma^0_{vv}$ have been used due to their empirical evidence and experimental validation [27, 165, 293, 380]. One can take $\sigma^0_{hv}/\sigma^0_{hh}$ instead of $\sigma^0_{hv}/\sigma^0_{vv}$ because both possess same characteristics. The procedure of selecting mathematical expressions of polarimetric feature *'*$\sigma^0_{rr}/\sigma^0_{rl}$*'* for segregation of bare soil from other classes is as follows:

- First the spatial statistics (i.e., minimum, maximum, median, and standard deviation) of whole image (Table 4.4) are compared with that of particular class, i.e., bare soil (Table 4.5) for feature $\sigma^0_{rr}/\sigma^0_{rl}$.
- After comparison, it is observed that minimum value of feature $\sigma^0_{rr}/\sigma^0_{rl}$ for whole image (−20.23 dB) and bare soil (−19.24 dB) are almost the same. Based on this fact, the

expression "$\sigma^0_{rr}/\ \sigma^0_{rl} \leq$ (mathematical formulation)" is chosen for making decision criterion so as to separate bare soil from other classes in the whole image.

- Now, in order to segregate bare soil from the whole image, mathematical expression ($M \pm S$) is tested for feature $\sigma^0_{rr}/\ \sigma^0_{rl}$. For Data-1, it is observed that up to some extent separation of bare soil is possible using expression $\sigma^0_{rr}/\ \sigma^0_{rl} \leq (M_{\sigma^0_{rr}/\ \sigma^0_{rl}} - S_{\sigma^0_{rr}/\ \sigma^0_{rl}})$, where $M_{\sigma^0_{rr}/\ \sigma^0_{rl}} = -3.61$ dB and $S_{\sigma^0_{rr}/\ \sigma^0_{rl}} = 2.98$ dB for the whole image of feature $\sigma^0_{rr}/\ \sigma^0_{rl}$.

  This is to be noted that if expression "$\sigma^0_{rr}/\ \sigma^0_{rl} \leq (M_{\sigma^0_{rr}/\ \sigma^0_{rl}} - S_{\sigma^0_{rr}/\ \sigma^0_{rl}})$" accurately classifies bare soil from other classes for any image, it does not mean that the same expression will be suitable for segregation of same class for different image of same site because of the fact that spatial statistics may be different for different images.

- In order to resolve above mentioned problem and to make algorithm adaptive in nature, an unknown term, for example, "n_1" is considered to be included in mathematical expression by which separation of bare soil from remaining classes may become possible.
- Now, the image statistics (median and standard deviation) of whole image are arranged in such a way that satisfactory results with good accuracy are obtained for separation of bare soil from other classes at certain value of "n_1".
- In order to select suitable mathematical expression, different combinations of image statistics (e.g., $M_{\sigma^0_{rr}/\ \sigma^0_{rl}}\ n_1$; $M_{\sigma^0_{rr}/\ \sigma^0_{rl}} + n_1$; $M_{\sigma^0_{rr}/\ \sigma^0_{rl}} \pm n_1\ S_{\sigma^0_{rr}/\sigma^0_{rl}}$; $M_{\sigma^0_{rr}/\ \sigma^0_{rl}} \pm (n_1-1)\ S_{\sigma^0_{rr}/\sigma^0_{rl}}$, $M_{\sigma^0_{rr}/\ \sigma^0_{rl}} \pm (n_1-2)\ S_{\sigma^0_{rr}/\sigma^0_{rl}}$,…) are evaluated for creation of decision boundary.
- It is observed that each of the expressions $[M_{\sigma^0_{rr}/\sigma^0_{rl}} - n_1\ S_{\sigma^0_{rr}/\sigma^0_{rl}}]$, $[M_{\sigma^0_{rr}/\sigma^0_{rl}} - (n_1-1)\ S_{\sigma^0_{rr}/\sigma^0_{rl}}]$, $[M_{\sigma^0_{rr}/\sigma^0_{rl}} \pm (n_1-1)\ S_{\sigma^0_{rr}/\sigma^0_{rl}}]$,..., is giving satisfactory results at different values of "n_1". However, we have selected the expression $[M_{\sigma^0_{rr}/\sigma^0_{rl}} - (n_1-1)\ S_{\sigma^0_{rr}/\sigma^0_{rl}}]$; the reason of particular selection will be discussed later in the following section.

Similarly, the mathematical expression for $\sigma^0_{hv}/\sigma^0_{vv}$ is obtained as $"\ \sigma^0_{hv}/\sigma^0_{vv} \leq [M_{\sigma^0_{hv}/\sigma^0_{vv}} - (n_2-1)\ S_{\sigma^0_{hv}/\ \sigma^0_{vv}}]"$ for segregation of bare soil from other classes. Similar procedure has been adopted for deciding the mathematical expressions of selected polarimetric indices for creation of decision boundary between different classes.

4.3.4.3 Development of decision tree classifier

The best-obtained relations for the selected polarimetric indices are used in the development of decision tree classification algorithm, which is shown in Figure 4.4. The terms used in decision

tree classifier shown in Figure 4.4 are described as follows:

$\boldsymbol{M_{\sigma^0 rr/\sigma^0 rl}}$	Median of feature $\sigma^0_{rr}/\sigma^0_{rl}$ for whole image.
$\boldsymbol{S_{\sigma^0 rr/\sigma^0 rl}}$	Standard deviation of feature $\sigma^0_{rr}/\sigma^0_{rl}$ for whole image.
$\boldsymbol{M_{\sigma^0 hv/\sigma^0 vv}}$	Median of feature $\sigma^0_{hv}/\sigma^0_{vv}$ for whole image.
$\boldsymbol{S_{\sigma^0 hv/\sigma^0 vv}}$	Standard deviation of feature $\sigma^0_{hv}/\sigma^0_{vv}$ for whole image.
$\boldsymbol{M_{\sigma^0 hv}}$	Median of feature σ^0_{hv} for whole image.
$\boldsymbol{S_{\sigma^0 hv}}$	Standard deviation of feature σ^0_{hv} for whole image.
$\boldsymbol{M_{WPS}}$	Median of feature *WPS* for whole image.
$\boldsymbol{S_{WPS}}$	Standard deviation of feature *WPS* for whole image.

The algorithm as shown in Figure 4.4, starts with discrimination between bare soil and other classes (urban, tall vegetation, short vegetation, and water), based on feature separation criterion discussed in section 4.3.3. In the decision criterion for the classification of bare soil from other classes, features $\sigma^0_{rr}/\sigma^0_{rl}$ and $\sigma^0_{hv}/\sigma^0_{vv}$ are taken because distinct relations are obtained with these features, and they also have empirical evidences [27, 165, 248, 250].

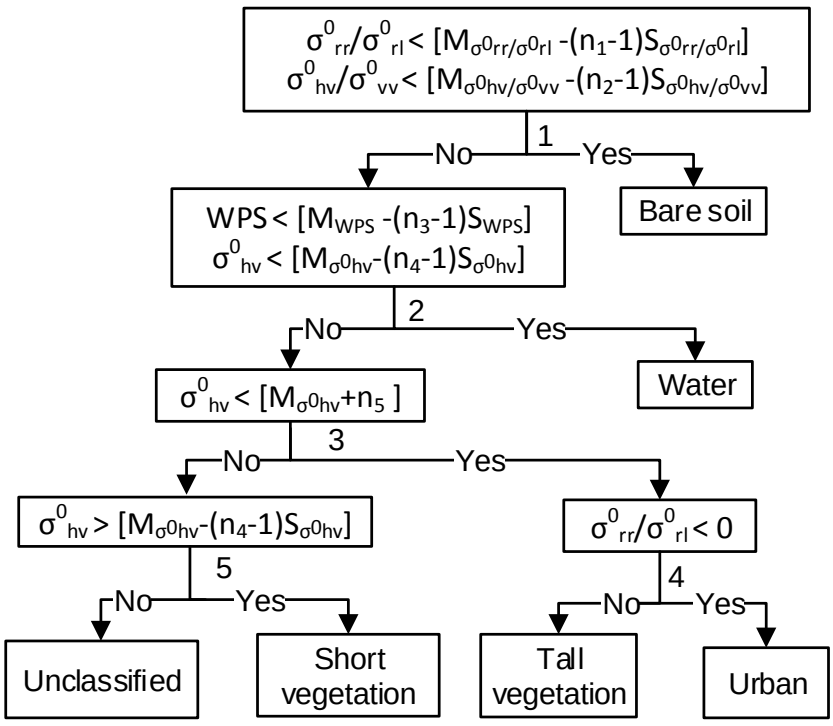

Figure 4.4: Proposed adaptive decision tree classification algorithm.

For the separation of water from other classes (after excluding bare soil), features *WPS* and all the backscattering coefficients *(σ^0's)* are obtained using separability index criterion. It is observed that all the backscattering coefficients show almost same value for water, therefore, based on empirical evidence [351] and experimental validation (i.e., $\sigma^0_{hv} \leq -30$dB for water for the L-band [250]), only σ^0_{hv} has been taken besides *WPS*. Taking into consideration the statistics (i.e., minimum, maximum, median, and standard deviation) of *WPS* and σ^0_{hv} for whole image (Table 4.4) and water (Table 4.6), the expressions "$WPS \leq [M_{WPS} - (n_3-1)\, S_{WPS}]$" and "$\sigma^0_{hv} \leq [M_{\sigma^0 hv} - (n_4-1)\, S_{\sigma^0 hv}]$" are obtained by the similar procedure, as discussed earlier.

For the separation of tall vegetation and urban from short vegetation, only σ^0_{hv} is chosen because other features, such as σ^0_{rr}, σ^0_{ll}, and *WPS*, have separability index value that is very close to 1, which may increase the false alarm and have the potential to degrade the classification performance. Another reason for taking σ^0_{hv} in decision criterion for segregation of short vegetation from tall vegetation and urban is empirical evidence and experimental validation carried out in previous research (i.e., at L-band $\sigma^0_{hv} \geq -18$dB for tall vegetation and urban [129, 250] and $\sigma^0_{hv} > -27$dB for short vegetation [293]). As shown in Figure 4.4 (node-3) the expression "$\sigma^0_{hv} > [M_{\sigma^0 hv} + n_5]$" is found suitable for segregation of tall vegetation and urban from short vegetation. Further, short vegetation is clustered by using expression " $\sigma^0_{hv} > [M_{\sigma^0 hv} - (n_4-1)\, S_{\sigma^0 hv}]$".

For the segregation of tall vegetation and urban, only $\sigma^0_{rr}/\sigma^0_{rl}$ is considered on the basis of separability index criterion shown in Figure 4.3, the scatter plot shown in Figure 4.2(j), and experimental validation [250].

The proposed decision tree classification algorithm is shown in Figure 4.4, in which different unknown terms (i.e., n_1, n_2, n_3, n_4, n_5), are used in all the mathematical expressions. The only exception is expression for σ^0_{hv}, that is used in making decision criterion for clustering of water and short vegetation at node-2 and node-5 respectively, in Figure 4.4, where same unknown term i.e., *'n_4'* is used because mathematical expression is same except the inequality in decision criterion.

Figure 4.4 exhibits that the term *(n_i-1)* multiplied by standard deviation *"S"* is subtracted from median *"M"* in expression for segregation of bare soil, water, and short vegetation, where n_i represents n_1, n_2, n_3, *and* n_4 in the corresponding expressions. The term *($n_i - 1$)* is found to be the most suitable among terms n_i, *($n_i - 1$), ($n_i - 2$), ($n_i - 3$),...*, for preserving the characteristics of respective classes observed from training ROIs for reasonable range of "n_i". Experimentally,

it is investigated that any of the terms n_i, $(n_i - 1)$, $(n_i - 2)$, $(n_i - 3)$,..., can be taken in the algorithm, because decision criterion to segregate any class will always be obtained at certain value of "n_i" using successive terms n_i, $(n_i - 1)$, $(n_i - 2)$,..., in the corresponding expressions. Considering the same value of unknown term in each expression of decision tree, it is observed that maximum overall classification accuracy is obtained at $n=1.2$ by using $n_1=n_2=n_3=n_4=n_5=n$ in the corresponding expressions of Figure 4.4, whereas maximum overall classification accuracy is obtained at n equals to 2.2 by using $(n-1)$, and 3.2 by using $(n-2)$ in the expressions. Nevertheless, we have considered term $(n_i - 1)$, so that value of unknown term "n_i" can be restricted between 1 and some other value where any class starts dominating the other classes.

4.3.4.4 Performance evaluation of proposed classification method

The performance of proposed classification algorithm (Figure 4.4) is evaluated by calculating confusion matrix (or the error matrix), which compares the classification result with ground truth information (or ROI points) and reports overall accuracy (OA), kappa coefficient, producer accuracy, and user accuracy. Out of these parameters, OA is considered. In order to make the algorithm adaptive in nature, it is required to relate OA with image statistics of polarimetric indices used in the expressions of decision tree. Therefore, in order to make unknown terms depending on image statistics, five variables are formed corresponding to mathematical expressions of polarimetric indices used in a decision tree classification algorithm, as shown in Figure 4.4. These variables are presented as follows:

$$x_1 = M_{\sigma_{rr}^0/\sigma_{rl}^0} - (n_1 - 1)S_{\sigma_{rr}^0/\sigma_{rl}^0}\ , \tag{4.6}$$

$$x_2 = M_{\sigma_{hv}^0/\sigma_{vv}^0} - (n_2 - 1)S_{\sigma_{hv}^0/\sigma_{vv}^0}, \tag{4.7}$$

$$x_3 = M_{WPS} - (n_3 - 1)S_{WPS}, \tag{4.8}$$

$$x_4 = M_{\sigma_{hv}^0} - (n_4 - 1)S_{\sigma_{hv}^0} \tag{4.9}$$

$$x_5 = M_{\sigma_{hv}^0} + n_5 \tag{4.10}$$

<u>Computation of OA in terms of x_1, x_2, x_3, x_4, and x_5</u>

It is observed that OA is quite dependent on unknown terms n_1, n_2, n_3, n_4, and n_5.Since there are five unknown terms (i.e., n_1, n_2, n_3, n_4, n_5), and it seems difficult to relate OA with these unknowns directly, therefore, first it is considered that all the unknowns are the same (n_1= n_2=n_3=n_4=n_5=n), and then OA is computed for different values of "n" using proposed

classification algorithm, as shown in Figure 4.4. The plot of OA with respect to "*n*" is shown in Figure 4.5 (a), which shows that OA significantly changes with change in value of "*n*".

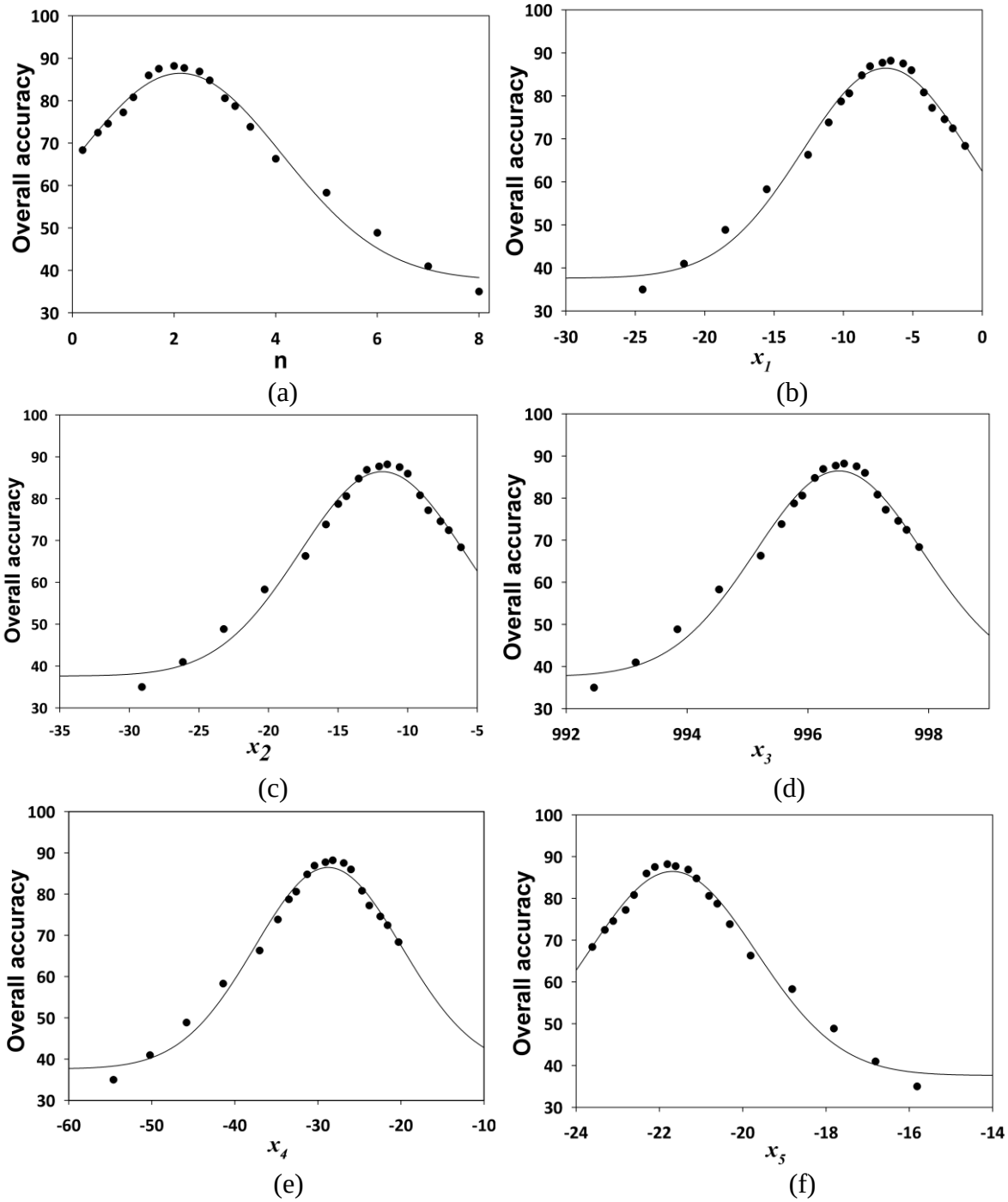

Figure 4.5: (a) Overall accuracy vs. *n*, (b) Overall accuracy vs. x_1 , (c) Overall accuracy vs. x_2 , (d) Overall accuracy vs. x_3 , (e) Overall accuracy vs. x_4, (f) Overall accuracy vs. x_5 .

Table 4.10 Mathematical formulations of Overall Accuracy (OA) with corresponding R^2 values

Performance parameter	Mathematical formulation with constant values	R^2
$OA(x_1)$	$OA(x_1) = y_1 + a_1 e^{-(1/2)\left((x_1 - c_1)/b_1\right)^2}$ y_1= 37.61;a_1=48.85; b_1=5.99; c_1 = −6.96	0.98
$OA(x_2)$	$OA(x_2) = y_2 + a_2 e^{-(1/2)\left((x_2 - c_2)/b_2\right)^2}$ y_2= 37.61;a_2=48.85; b_2=5.91; c_2 = −11.82	0.98
$OA(x_3)$	$OA(x_3) = y_3 + a_3 e^{-(1/2)\left((x_3 - c_3)/b_3\right)^2}$ y_3= 37.61;a_3=48.85; b_3=1.387; c_3 = 996.52	0.98
$OA(x_4)$	$OA(x_4) = y_4 + a_4 e^{-(1/2)\left((x_4 - c_4)/b_4\right)^2}$ y_4= 37.61;a_4=48.85; b_4=8.843; c_4 = −28.75	0.98
$OA(x_5)$	$OA(x_1) = y_5 + a_5 e^{-(1/2)\left((x_5 - c_5)/b_5\right)^2}$ y_5= 37.61;a_5=48.85; b_5=2.01; c_5 = −21.69	0.98

Now we have the values of "*n*" and its corresponding values of OA. These values of "*n*" are put in Equations (4.6)-(4.10) for obtaining the values of x_1, x_2, x_3, x_4, and x_5. After computing x_1, x_2, x_3, x_4, and x_5, OA is correlated to these variables. The plots of OA vs. these variables are shown in Figure 4.5((b)-(f)).

To obtain the relation between spatial-statistics-based expressions of particular polarimetric index (i.e., x_1, x_2, x_3, x_4, x_5) and OA, the curve fitting method is adopted. The obtained expressions with a very high R^2 value (coefficient of determination) are represented in Table 4.10. In this Table, y_1, y_2, y_3, y_4, y_5, a_1, a_2, a_3, a_4, a_5, b_1, b_2, b_3, b_4, b_5, c_1, c_2, c_3, c_4, and c_5, are constants.

In order to determine the significance of these relationships, the Kolmogorov-Smirnov

(KS) test is performed with 5% significance level. The KS value and its corresponding p-value are obtained as 0.1013 and 0.77, respectively, for all the relationships. The critical value for 5% significance level and 19 number of samples (19 observations are made) is 0.27136. The obtained KS value is less than the critical value, and the p-value is greater than 0.05 (5% significance level). This indicates that the proposed relationships for OA are statistically significant.

4.3.4.5 *Optimization algorithm to obtain the value of unknown terms*

The obtained relationships of OA, as provided in Table 4.10, are non-linear functions of unknown variables i.e., x_1, x_2, x_3, x_4, x_5. Therefore, in order to retrieve all the unknowns from nonlinear equations of OA, it is required to perform optimization. The problem statement for optimization of the proposed classification algorithm can be defined as:

> "*Find design variables (*i.e., x_1, x_2, x_3, x_4, x_5*) that optimize the objective function OA(* x_1, x_2, x_3, x_4, x_5*) (soft objective) such that OA(* x_1, x_2, x_3, x_4, x_5*) is maximized. This optimum value must satisfy user-specified constraints. These constraints are hard objectives, which need to be satisfied before the optimization of the soft objectives takes place. The constraint for hard objective is that OA as a function of individual design variable should be greater than respective user-specified lower limit and less than respective user-specified upper limit."*

The aforementioned optimization problem involves optimization of single objective subjected to several nonlinear constraints, which can be represented mathematically as,

$$\min f(x_1, x_2, x_3, x_4, x_5), \tag{4.11}$$

where

$$\begin{aligned} f(x_1, x_2, x_3, x_4, x_5) &= -OA(x_1, x_2, x_3, x_4, x_5) \\ &= -[OA(x_1) + OA(x_2) + OA(x_3) + OA(x_4) + OA(x_5)]/5 \\ &= -\left(\sum_{i=1}^{5} OA(x_i)\right)/5 \end{aligned}, \tag{4.12}$$

Subject to constraints

$$OA_{x_i}^{lb} \le OA(x_i) \le OA_{x_i}^{ub}, \tag{4.13}$$

$$lb_i \le x_i \le ub_i, \qquad i=1, 2, ...,5 \tag{4.14}$$

The mathematical expressions for OA (x_i) are provided in Table 4.10. The terms *lb* and *ub* in superscripts of Equation (4.13) and Equation (4.14) represent lower bound and upper bound, respectively. The terms OA_{xi}^{lb} and OA_{xi}^{ub} are lower and upper bounds of OA(x_i), respectively, where i=1,2,3,4,5 corresponding to unknown variables given in equations (4.6)-(4.10).In this mathematical formulation, both the constraints equations (4.13)-(4.14) must be satisfied in order to find a feasible solution. These constraints are provided to ensure that the performance of proposed adaptive classification technique always meets the requirements of end user (i.e., lower and upper bounds on OA). If it happens that there exist no feasible solution for user specified constraints, then user has to provide some other values of constraints in order to optimize the algorithm.

The optimization has been performed through Genetic Algorithm (GA), which is a globally iterative, numerical optimization method. It has been selected due to its several advantages over other traditional optimization methods, which obtain best solution using gradient and random guesses. One of the most important aspects of GA is that it is global because it has random components that test for solutions outside the current minimum, while the algorithm converges [257, 366, 447]. In this problem, lower bound and upper bound for all the constraints of OA given in Equation (4.13) are taken as 80% and 100%, respectively. The limits of design variables x_i (i.e., x_1, x_2... x_5) given in Equation (4.14) are decided on the basis of Figure 4.5. These limits, which are enlisted in Table 4.11, are selected for criterion OA > 60% in order to cover large range of values for all the variables.

Table 4.11 Lower and upper bounds for variables (x_i)

Variables	Lower bound (lb)	Upper bound (ub)
$\boldsymbol{x_1}$	−15	−1
$\boldsymbol{x_2}$	*−20*	*−5*
$\boldsymbol{x_3}$	994	999
$\boldsymbol{x_4}$	*−40*	*−20*
$\boldsymbol{x_5}$	*−24*	*−18*

The optimization of Equation (4.12) is performed through GA after applying the constraints in Equation (4.13) and Equation (4.14) by taking OA_{xi}^{lb} and OA_{xi}^{ub} as 80% and 100%, respectively, and lb_i and ub_i of x_i (i=1,2,3…5) according to Table 4.11. The optimum value of design variables x_1, x_2, x_3, x_4, and x_5 are retrieved as −6.96, −11.82, 996.52, −28.75, and −21.69, respectively. The values of image statistics (from Table 4.4) and optimum value of design variables are substituted in Equations (4.6)-(4.10) in order to get the values of respective unknown terms, which are obtained as n_1= 2.1208, n_2=2.122, n_3=2.116, n_4=2.123, and n_5 =2.12.

4.4. Results and Discussion

This section presents the result of proposed adaptive classification algorithm on two different ALOS PALSAR data sets, as described in section 4.2. The process adopted for implementation and testing of proposed classification algorithm is summarized in the form of flowchart in Figure 4.6.

4.4.1. Implementation and Testing

The optimum value of unknown terms n_1, n_2, n_3, n_4, and n_5 are obtained as 2.1208, 2.122, 2.116, 2.123, and 2.12 respectively, after optimization of Equation (4.12) by GA in which constraints of OA(x_i) are taken as 80% and 100%, whereas constraints of x_i are taken from Table 4.11. The proposed algorithm, as shown in Figure 4.4, is implemented on pixel-by-pixel basis on Data-1 (Data ID-PASL1109040617112609081100 63) after putting the optimum value of unknown terms (i.e., n_1= 2.1208, n_2=2.122, n_3=2.116, n_4=2.123, n_5 =2.12) in the corresponding expressions. Obtained result at optimum value of unknown terms is shown in Figure 4.7. The result shows that most of the pixels belonging to specific class are classified as the same category. In Figure 4.7, Solani River appears in bare soil category, which is expected because it is rain-fed river and it was almost dry during data acquisition in April 2009. The performance of this classification map is evaluated by computing confusion matrix using testing ROI given in Table 4.2. The overall accuracy is estimated as 87.59% and kappa coefficient as 0.85. The estimates of producer accuracy (in percent) and user accuracy (in percent) of classification are enlisted in Table 4.12.

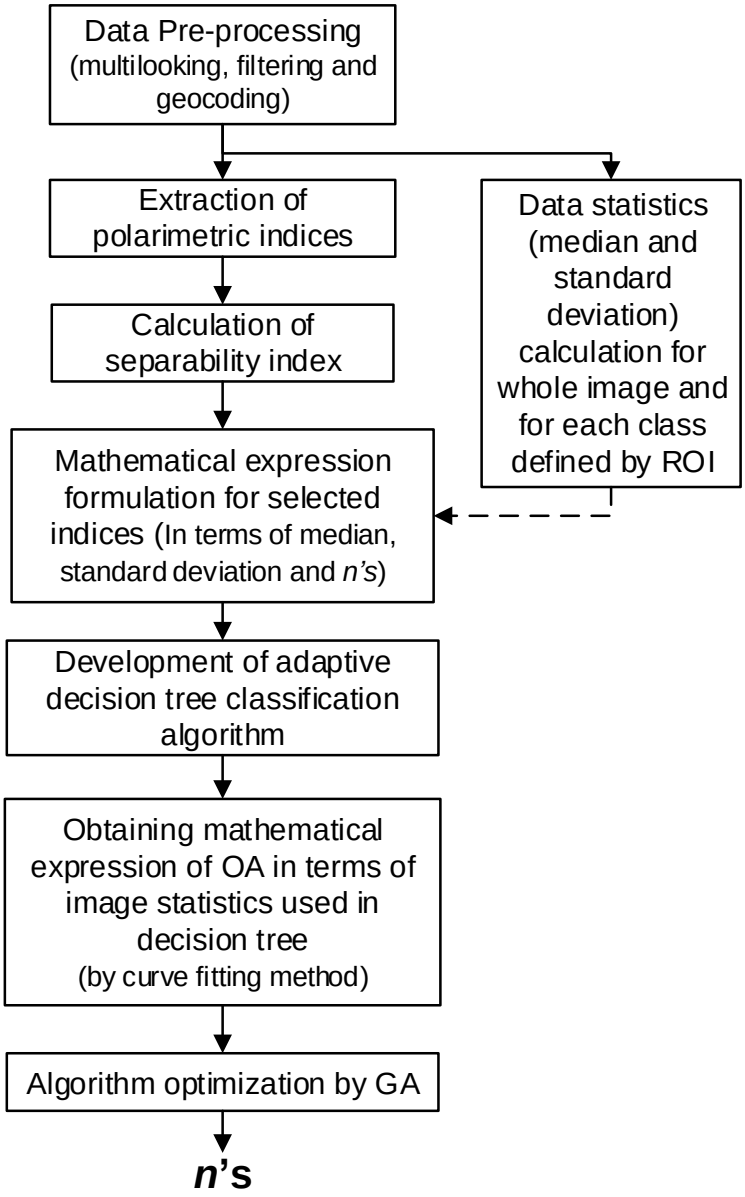

Figure 4.6: Flowchart for implementation and testing of proposed classification algorithm.

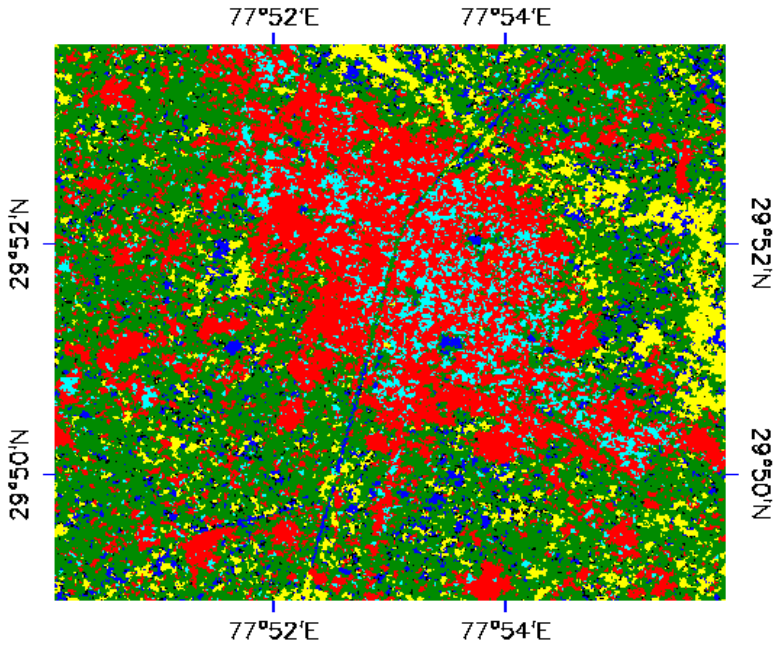

Figure 4.7: Result of proposed decision tree algorithm (water- blue; bare soil-yellow, urban-red, tall vegetation- cyan; short vegetation- green) for Data-1 at n_1=*2.1208*, n_2=*2.122*, n_3= *2.116*, n_4= *2.123*, n_5=2.12.

Table 4.12 Producer and user accuracy estimates (in percent) relative to classification of Data-1 using testing ROI.

Class	Producer accuracy (%)	User accuracy (%)
Bare soil	98	85
Water	71	98
Tall vegetation	86	92
Short vegetation	92	67
Urban	95	89

4.4.2. Validation of Algorithm

The performance of proposed adaptive classification technique is validated on another PALSAR data "Data-2" (Data ID- PASL1100904061711181001150003) acquired on date April 6, 2009. For same constraints, as applied for algorithm development, the optimum value of design variables i.e., x_1, x_2, x_3, x_4, and x_5 are obtained as −6.96, −11.82, 996.52, −28.75, and

−21.69, respectively, using optimization by GA. The image statistics of Data-2 for required polarimetric indices are enlisted in Table 4.13. After putting these image statistics and optimum value of design variables (i.e., x_1, x_2, x_3, x_4, and x_5) in Equations (4.6)-(4.10), corresponding unknown terms are obtained as n_1=2.301, n_2=2.176, n_3=2.114, n_4=2.138, and n_5=2.03. These optimum values of unknown terms are used in Figure 4.4 in order to produce classification result, which is shown in Figure 4.8. The performance of this classification map is evaluated by calculating confusion matrix using testing ROI, as listed in Table 4.2. The overall accuracy is estimated as 78.43% and kappa coefficient as 0.72. The estimates of producer accuracy (in percent) and user accuracy (in percent) of classification are enlisted in Table 4.14.

Table 4.13 Image statistics of polarimetric indices for whole image of Data-2

Feature	Minimum	Maximum	Median	Standard deviation
σ^0_{hv}	−37.29	−4.45	−23.72	4.42
$\sigma^0_{hv}/\sigma^0_{vv}$	−28.48	5.19	−8.35	2.95
$\sigma^0_{rr}/\sigma^0_{ll}$	−19.78	10.98	−3.41	2.72
WPS	993.88	1002.3	997.30	0.7

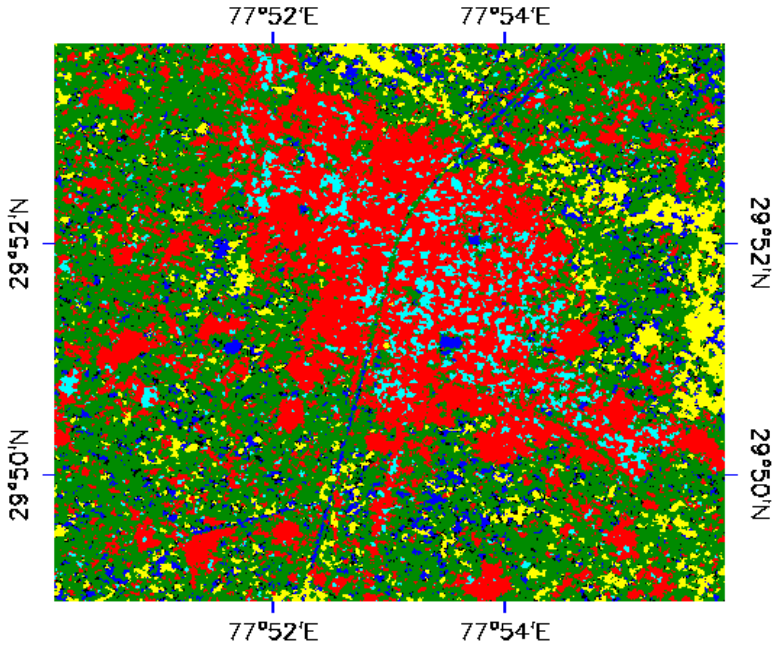

Figure 4.8: Result of proposed decision tree algorithm (water: blue; bare soil-yellow, urban-red, tall vegetation- cyan; short vegetation- green) for Data-2 at n_1=2.301, n_2= 2.176, n_3= 2.114, n_4= 2.138, and n_5=2.03.

Table 4.14 Producer and user accuracy estimates (in percent) relative to classification of Data-2 using testing ROI.

Class	Producer accuracy (%)	User accuracy (%)
Bare soil	98	85
Water	57	98
Tall vegetation	66	94
Short vegetation	84	55
Urban	97	72

4.5. Conclusion

An image statistics based adaptive land cover classification technique has been proposed. The presented method exhibits the role of various polarimetric indices (σ^0_{rr}, σ^0_{rl}, σ^0_{ll}, σ^0_{hv}, σ^0_{hh}, σ^0_{vv}, σ^0_{45C}, σ^0_{45X}, $\sigma^0_{rr}/\sigma^0_{rl}$, $\sigma^0_{hv}/\sigma^0_{vv}$, $\sigma^0_{hv}/\sigma^0_{hh}$, $\sigma^0_{hh}/\sigma^0_{vv}$, *WPS*, *RVI*, *NDPI*, and *CPR*) extracted from polarimetric data for segregation and labelling of different land cover types. The concept of separability index has been used to select polarimetric indices able to separate each class from other remaining classes. Then mathematical formulations have been formed for those indices in terms of image statistics. These expressions have been used in development of decision tree classifier. The dependence of proposed adaptive cluster labelling/classification method on statistical parameters (median and standard deviation) to select the values of polarimetric indices in order to create a decision boundary for a particular class by using the genetic algorithm approach makes the proposed algorithm adaptive in nature. The performance of proposed algorithm has been optimized in order to meet end user specific requirement (i.e., OA).

The algorithm has been developed and validated on two different ALOS PALSAR data. Two advantages of proposed method have been observed: firstly, there is no need to optimize polarimetric parameters again for running the algorithm for different images of the same site or similar sites, and secondly, no need to make any prior assumption about the distribution of data for the development of classification algorithm.

Chapter 5

Transmission Line Theory Based Impedance Approach for Retrieval of Soil Moisture

Soil moisture retrieval under vegetation cover is a contemplative task because of complexities involved in isolation of scattering responses of underlying soil from backscattering coefficient of vegetated region. In this chapter, an attempt has been made to take up this challenge of soil moisture retrieval under vegetation cover by developing multilayer model based on impedance approach of classical transmission line theory. The foundation of proposed approach lies in the principle of transmission line theory, which allows estimation of backscattering coefficient as a function of complex dielectric constant and thickness of concerned medium. A multilayer model has been developed for characterization of scattering from vegetation canopy and bare soil regions. The multilayer model for vegetation consists of one layer of vegetation and two layers of soil, whereas for bare soil, it consists two layers of soil. The soil moisture has been retrieved for upper layer of soil having depth of 5 cm. Most of the available soil moisture retrieval approaches require *'a priori'* information. However, the proposed approach requires minimum or no *'a priori'* information. This quality seems to make this algorithm a good choice for soil moisture retrieval with polarimetric SAR data.

5.1. Introduction

Soil moisture is an important land surface parameter that monitors the interaction between land surface and atmosphere by controlling the distribution of water, energy, and carbon fluxes [125, 201, 202]. It maintains water balance at local, regional, and global scale by regulating surface run-off, infiltration, evaporation, and percolation in soil [94]. These characteristics of soil moisture make it key input parameter in several disciplinary applications, such as weather forecasting [111], climate change modelling [110, 327], flood monitoring [101], draught monitoring [43], and agriculture monitoring [43, 246], etc.

Soil moisture retrieval methods can be categorized as ground based/*in situ* method and

airborne/satellite based method [291]. Conventionally, ground-based/ *in situ* measurement of soil moisture is done by gravimetric method, which comprises collection of soil samples at sampled locations, weighing of samples before and after drying (oven drying) followed by estimation of moisture content [181]. Due to high spatial and temporal fluctuations in soil moisture, it is required to take multiple samples from test sites, which is very time consuming, and cumbersome task [415]. These limitations can be compensated by the use of airborne/satellite based methods that can estimate soil moisture at much larger scale with frequent and vast spatial coverage and high spatial resolution [286, 340].The retrieval of soil moisture by using satellites or more specifically, microwave sensors, has gained much attention in past years with passive [174, 175, 291] and active [28, 101, 107, 286] methods at different frequency bands. The central idea of retrieving soil moisture by microwave sensors is established on the fact that there is a large difference in the value of dielectric constant of water (~80) and dry soil (3-5), which creates a direct relationship between soil moisture and dielectric constant of soil-water mixture due to increment in soil moisture value with increase in dielectric constant. Thus, retrieval of soil moisture can be done after measuring dielectric constant of soil, which consecutively is related to backscattering coefficient of microwave sensor [108, 266, 388]. The sensitivity of microwave sensors to variation in soil moisture and their transparency to atmosphere (>90%), make them perfect choice for soil moisture retrieval [29].

Over the past years, numerous theoretical [28, 66, 145, 315, 353], empirical [168, 205, 406], and semi-empirical methods [115, 274, 333] have been developed for retrieval of soil moisture using microwave sensors. Despite their wide use, their applicability is limited due to certain reasons. Theoretical models, such as Kirchhoff's Approximation [388], Small Perturbation Model (SPM) [315], Integral Equation Model (IEM) [145], and Advanced Integral Equation Model (AIEM) [66], have limited applicability due to small domain of validity and complexity involved in their implementation. Thus, a lot of effort is required for inversion of soil moisture from backscattering coefficient [333]. Empirical methods are easy to handle and mostly produce accurate results for the sites, datasets, and environmental conditions, under which they have been developed. However, their non-robust nature, and their need for requiring adequate amount of reference data for derivation of empirical relationships, are the main reasons for their restricted applications [20, 28, 298]. Semi-empirical models in [115, 274], tend to overestimate the radar response, and produce inconsistent results for other data sets

[19]. Application of these algorithms over vegetated surfaces causes under-estimation of soil moisture [332] because vegetated surface represents multiple scattering effect i.e., diffuse scattering from vegetation, surface scattering from underlying soil, and multiple scattering due to interaction between vegetation and underlying soil [33]. In other terms, for vegetation covered soil, the scattering from bare soil surface is very much influenced by the vegetation canopy layer, which attenuates the scattering from soil while adding its own contribution [175]. Thus, it is required to separate the scattering contribution of underlying soil from backscattering coefficient of vegetated region. Conclusively, it can be said that soil moisture retrieval under vegetation cover is still an onerous task, which needs proper attention.

There exist some methods, namely Water-Cloud model [16, 33, 304], change detection methods [254, 260, 275], and decomposition based methods [161, 177], for retrieving soil moisture in vegetated areas. The Water-Cloud model works well for retrieving soil moisture in vegetation layer, and is easy to implement. However, its implementation requires *'a priori'* knowledge of vegetation parameters, such as Plant Water Content (PWC), vegetation height, Leaf Area Index (LAI), etc., for characterization of scattering from vegetation canopy (vegetation-air mixed medium). It would be cumbersome to acquire these vegetation parameters each time for implementation of this approach, considering temporal variability of vegetation. Another limitation of this approach is the requirement of certain assumptions, such as invariability of surface roughness and plant height, for optimum and efficient inversion of soil moisture from backscattering data. The limitation of change detection methods [254, 260, 275] is that these methods assume time-invariance nature of vegetation for characterization of canopy layer. Thus, application of these methods is restricted for vegetation having narrow cycle of growth. The performance of decomposition based approaches is quite satisfactory. However, the application of these approaches requires selection of appropriate model for vegetation layer [161, 177]. In order to characterize vegetation canopy, some researchers have used optical data, and after fusing the information of optical data with microwave data (more specifically, SAR data), they have estimated soil moisture [269, 299, 408]. The application of these methods requires large amount of *'a priori'* information for their implementation. Thus, there is a need to develop such an approach that requires minimum or no *'a priori'* information. Considering this aspect, in this chapter, transmission line theory based multilayer layer model has been proposed for soil moisture retrieval in both bare soil and vegetation covered soil. Some researchers have used transmission line theory based approach for different applications,

such as estimation of thickness of burnt coal seam [368, 369] and topsoil in semiarid area [5].

It is well known that soil moisture is sensitive to various sensor parameters, such as frequency (or wavelength), incidence angle, and polarization. It has been found in literature that at low incidence angle, HH or HV polarization is better suited for soil moisture retrieval [168, 388]. As far as frequency is concerned, low range of frequencies from 1 GHz to 5 GHz (wavelength 30 cm to 5 cm) are more appropriate than higher range of frequencies (above X-band or wavelength below 3 cm), for assessment of soil moisture. It has been found that longer wavelengths at low incidence angles reduce the effect of surface roughness [168, 388]. Therefore, L-band ALOS PALSAR fully polarimetric data, which has low incidence angle (24°), has is good prospect for soil moisture retrieval. In this chapter, HH polarization has been used for retrieving soil moisture by applying multilayer model because at steep incidence angle (around 20°), HH polarization is better than VV and HV, for retrieval of soil moisture [285]. The proposed approach has also been applied on C-band Radarsat-2 data. For both the bands, retrieved soil moisture value is in good agreement with the observed soil moisture value.

The multilayer model developed in this chapter consists of two separate models that deal with retrieval of soil moisture in vegetated and bare soil regions separately. Multilayer model for vegetated region consists of three layers with one layer of vegetation (which is actually a mixture of vegetation and air) and two layers of soil, whereas multilayer model for bare soil region consists of only two layers of soil. In each of these models, impedance of each layer has been calculated in terms of their dielectric constant ($\varepsilon = \varepsilon' - j\varepsilon''$) and thickness ($t$) by using the transmission line theory. The impedance in turn is related to backscattering coefficient. Therefore, backscattering coefficient is obtained as a non-linear function of dielectric constant and thickness of each layer involved in respective models. It is known that the propagation of electromagnetic waves in soil layer leads to their attenuation, which increases with the increase in depth of soil layers. Therefore, for retrieval of soil moisture, the observation depth is only first few centimetres of soil surface, and more specifically, lies in between one tenth of wavelength to one quarter wavelength [391, 406, 407]. For this purpose, the first layer of soil has been taken as 5 cm, and second layer of soil has been assumed to be extended up to infinite length. Since most of the vegetation (short and tall agricultural vegetation) usually reach up to 400 cm. Therefore, in this chapter, thickness of vegetation-air mixed layer in multilayer model of vegetation has been considered as 5 cm to 400 cm, which probably covers short as well as long vegetation regions. It physically infers that the backscattering coefficient becomes the

function of dielectric constant of each layer in respective model. Due to non-linearity of backscattering function, Genetic Algorithm (GA) optimization technique has been used to retrieve the dielectric constant of each layer with backscattering data, which is obtained by satellite SAR data. Genetic algorithm is optimization based approach, which is used to determine maximum or minimum of any arbitrary function depending upon the nature of problem [257, 382]. It is heuristic solution search based optimization method based on the concept of Darwinian theory of natural evolution involving biological techniques, such as inheritance, mutation, selection, and crossover [163, 179]. By applying GA on three and two layer models for vegetation and bare soil, respectively, real and imaginary parts of dielectric constants of bare soil and vegetation covered soil have been retrieved. Finally, soil moisture values have been retrieved from soil dielectric constant by using widely accepted polynomial relationship proposed by Topp *et al.* [373].

The chapter is organized as follows: section 5.2 gives the description about study area and SAR data sets used for development of proposed methodology. Section 5.3 describes the theory of transmission line based impedance model for multilayer modelling approach. In section 5.4, methodology of proposed model has been discussed. The results of proposed soil moisture retrieval algorithm have been reported in section 5.5 followed by section 5.6, which includes concluding remarks.

5.2. Study Area and Data Used

5.2.1. Study Area

The proposed approach has been developed and validated on same study area i.e., Roorkee, as described in section 3.2.1 in Chapter 3.

5.2.2. SAR Data

5.2.2.1 L-band SAR data

The development and testing of proposed algorithm has been performed on L-band ALOS PALSAR data sets. The description of these data sets i.e., Data-1 (Data ID-PASL1109040617112609081100063) and Data-2 (Data ID- PASL11009040617111810011-50003), has been given in section 4.2 of Chapter-4.

5.2.2.2 C-band SAR data

In order to check the validity of proposed approach on C-band (5.45 GHz), Radarsat-2 fully polarimetric data (Data ID- PDS_01679480) has been used. The acquisition of this dataset was carried out on May 31, 2011 at incidence angle of 34˚. The study area is similar to that discussed in section 4.2.

5.2.3. Ground Data

5.2.3.1 For L-band ALOS PALSAR data

Ground truth survey was carried out on April 04, 2009 (2 days before the acquisition of ALOS PALSAR data sets) for 20 sites. From each of the sites, eight to ten samples were collected for *in situ* measurement of soil moisture. The average soil moisture data from all of these 20 sites have been used for testing and validating the algorithm on Data-1 and Data-2. The observed soil moisture range varied from 0.15 cm^3 cm^{-3} to 0.35 cm^3 cm^{-3}.

5.2.3.2 For C-band Radarsat-2 data

The survey was carried out on May 31, 2011 (day of Radarsat-2 acquisition in order to collect soil moisture samples from all 20 sites that have been used for ALOS PALSAR data sets. The observed soil moisture range varied from 0.15 cm^3 cm^{-3} to 0.40 cm^3 cm^{-3} for samples collected on May 31, 2011.

For classification of Radarsat-2 data, required training and testing samples for classes, water, urban, vegetation, and bare soil, were also collected during ground survey. These ground truth points are enlisted in Table 5.1.

Table 5.1 Ground truth points

Class	Training Samples	Testing samples
Water	201	165
Urban	203	158
Bare soil	185	104
Vegetation	105	102

5.3. Theoretical Background

5.3.1. Multilayer Model Using Transmission Line Theory Based Impedance Approach

The multilayer model utilizes the concept of transmission line theory which computes impedance of each layer in terms of complex dielectric constant and thickness of that layer [168]. In order to develop the model, it has been assumed that media is composed of infinite length of air and *n* layers of different (or same) media having diverse complex dielectric constant and thickness. The two-dimensional model of this scenario is shown in Figure 5.1. It is shown in this figure that a plane wave having transverse magnetic (TM) mode is incident on p^{th} layer at an incidence angle of θ_i. In TM mode, wave propagation from air to p^{th} layer is shown in Figure 5.2. In this case, electric field lies in *xz* plane and incident fields in air medium can be represented by referring Figure 5.2 as [297],

$$H_i = H_{yi} e^{-jk_1(x\cos\theta_i + z\sin\theta_i)}\hat{y}\,, \tag{5.1a}$$

$$E_i = Z_0 H_{yi}(\sin\theta_i \hat{x} - \cos\theta_i \hat{z}) e^{-jk_1(x\cos\theta_i + z\sin\theta_i)}\,, \tag{5.1b}$$

where $k_1 = \omega\sqrt{\mu_0\varepsilon_0}$ and Z_0 are the wave number and intrinsic wave impedance of free space (i.e., 377 ohms),respectively. The term ω is represented as $2\pi f$ with *f* symbolizing operating frequency. The terms H_i and E_i represent incident magnetic and electric field intensities, respectively, and H_{yi} represents *y*-component of incident magnetic field intensity.

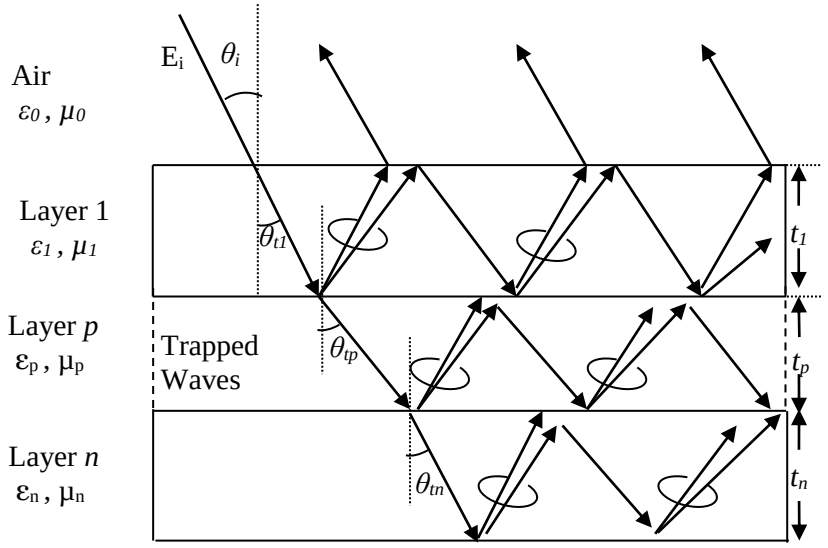

Figure 5.1: Two dimensional model [5].

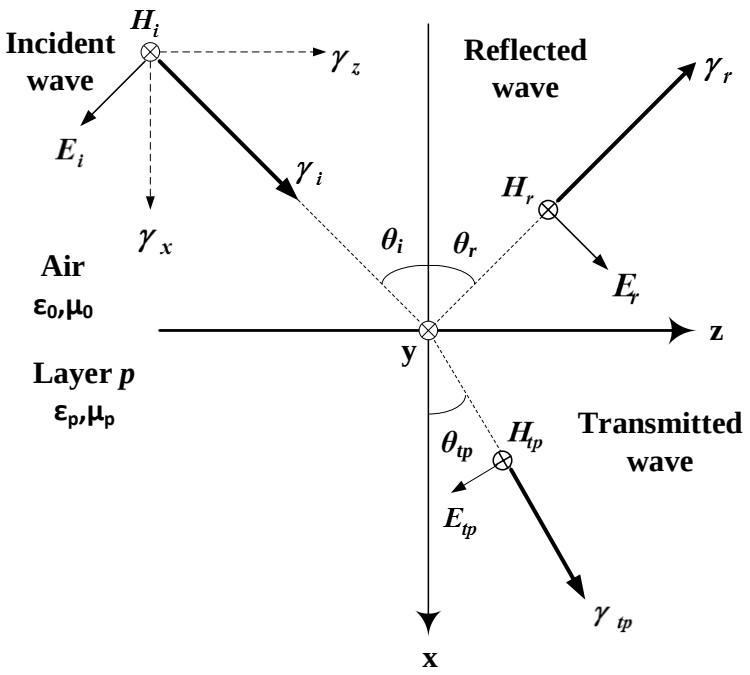

Figure 5.2: Representation of wave propagation in two different media.

In a similar manner, the reflected and transmitted fields can be represented as [297],

$$H_r = H_{yr} e^{-jk_1(-x\cos\theta_r + z\sin\theta_r)}\hat{y}\,, \tag{5.2a}$$

$$E_r = Z_0 H_{yr}(\sin\theta_r \hat{x} + \cos\theta_r \hat{z}) e^{-jk_1(-x\cos\theta_r + z\sin\theta_r)}\,, \tag{5.2b}$$

$$H_{tp} = H_{ytp} e^{-jk_p(x\cos\theta_{tp} + z\sin\theta_{tp})}\hat{y}\,, \tag{5.3a}$$

$$E_{tp} = Z_p H_{ytp}(\sin\theta_{tp} \hat{x} - \cos\theta_{tp} \hat{z}) e^{-jk_p(x\cos\theta_{tp} + z\sin\theta_{tp})}\,, \tag{5.3b}$$

where $k_p = \omega\sqrt{\mu_p \varepsilon_p}$ and Z_p are the wave number and wave impedance of p^{th} layer, respectively. The terms H_r and E_r represent reflected magnetic and electric field intensities, respectively, and H_{tp} and E_{tp} represent transmitted magnetic and electric field intensities in p^{th} layer, respectively. The term H_{yr} and H_{ytp} represents *y*-component of reflected and transmitted magnetic field intensity, respectively.

Based on transmission line concept, p^{th} layer of thickness t_p in Figure 5.1 is said to have an impedance of Z_p. Therefore, Figure 5.1 can be represented by an equivalent circuit as presented in Figure 5.3, where Z_{Cp}, Z_{Lp}, t_p, and ε_p, indicate the effective series impedance (characteristics impedance), parallel impedance, thickness, and complex dielectric constant, respectively, of p^{th} layer of media. The complex permeability (μ_p) is assumed to be constant

(or, unity) for all the layers. Z_T represents total input impedance seen looking towards the media. Considering the last layer (n^{th} layer) of model having infinite thickness, the parallel impedance Z_{Ln} can be taken as zero assuming earth as a perfect conductor. In order to reduce the complexity of analysis, the parallel impedances of other layers *i.e.*, Z_{Lp} are neglected [5].

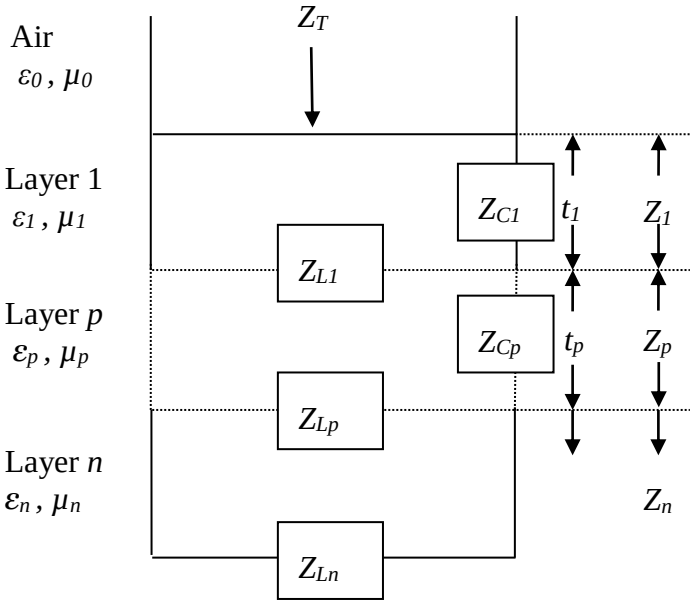

Figure 5.3: Equivalent circuit for multilayer model.

Based on transmission line theory, the total input impedance Z_T seen looking towards 1st layer is determined by,

$$Z_T = \sum_{p=1}^{n} Z_p \,, \tag{5.4}$$

$$Z_p = Z_{Cp} \frac{Z_{Lp} + Z_{Cp} \tanh \gamma_{Cp} t_p}{Z_{Cp} + Z_{Lp} \tanh \gamma_{Cp} t_p} \,, \tag{5.5}$$

where γ_{Cp} and t_p are propagation constant and thickness, respectively, of p^{th} layer of media.

At the boundary between the air and p^{th} layer of media, Snell's law is applied in order to give following relationship,

$$\sin\theta_i = \sqrt{\varepsilon_{rp}\mu_{rp}} \sin\theta_{tp} \,, \tag{5.6}$$

where ε_{rp}, μ_{rp}, and θ_{tp} are complex dielectric constant, complex permeability, and transmission angle of p^{th} layer of media, as exhibited in Figure 5.1. In whole analysis, μ_{rp} has been

considered as 1.0, and ε_{rp} is represented as $\varepsilon'_{rp}-j\varepsilon''_{rp}$, where ε'_{rp} and ε''_{rp} are real and imaginary part of complex dielectric constant, respectively.

Considering incidence of plane wave from air to media as represented in Figure 5.1, the propagation constant can be derived from Maxwell's equation as [5],

$$\gamma_{Cp} = j\omega\sqrt{\varepsilon_{rp}\mu_{rp}}\cos\theta_{tp} = j\omega\sqrt{\varepsilon_{rp}\mu_{rp} - \sin^2\theta_i}\ , \tag{5.7}$$

The effective series impedance of p^{th} layer of media is obtained by taking the component of electromagnetic fields which are perpendicular to axis of propagation (i.e., x-axis), and can be measured as,

$$Z_{Cp} = \frac{-E_{ztp}}{H_{ytp}} = Z_p\cos\theta_{tp} = Z_0\sqrt{\frac{\mu_{rp}}{\varepsilon_{rp}}}\cos\theta_{tp}\,, \tag{5.8}$$

Thus, Equation (5.5) can be represented as

$$Z_p = \frac{Z_0}{\varepsilon_{rp}}\sqrt{\varepsilon_{rp}\mu_{rp} - \sin^2\theta_i}\tanh\left(j\frac{2\pi t_p}{\lambda}\sqrt{\varepsilon_{rp}\mu_{rp} - \sin^2\theta_i}\right), \tag{5.9}$$

After substituting Equation (5.9) into Equation (5.4), total input impedance Z_T can be obtained. The reflection coefficient can then be obtained as,

$$\Gamma = \frac{Z_T - Z_0\cos\theta_i}{Z_T + Z_0\cos\theta_i}\,, \tag{5.10}$$

Finally, the backscattering coefficient is obtained as,

$$\sigma^0_{cal} = 20\log(|\Gamma|)\,, \tag{5.11}$$

Thus, backscattering coefficient obtained by Equation (5.11) is a function of complex dielectric constant and thickness of each layer.

5.4. Model Development

The flowchart of developed method is shown in Figure 5.4. It indicates that first it is required to segregate bare soil and vegetation region, by performing classification of fully polarimetric SAR data. After obtaining these regions, two separate models for vegetation and bare soil regions are developed based on approach described in section 5.3. The procedure for development of proposed model has been described below:

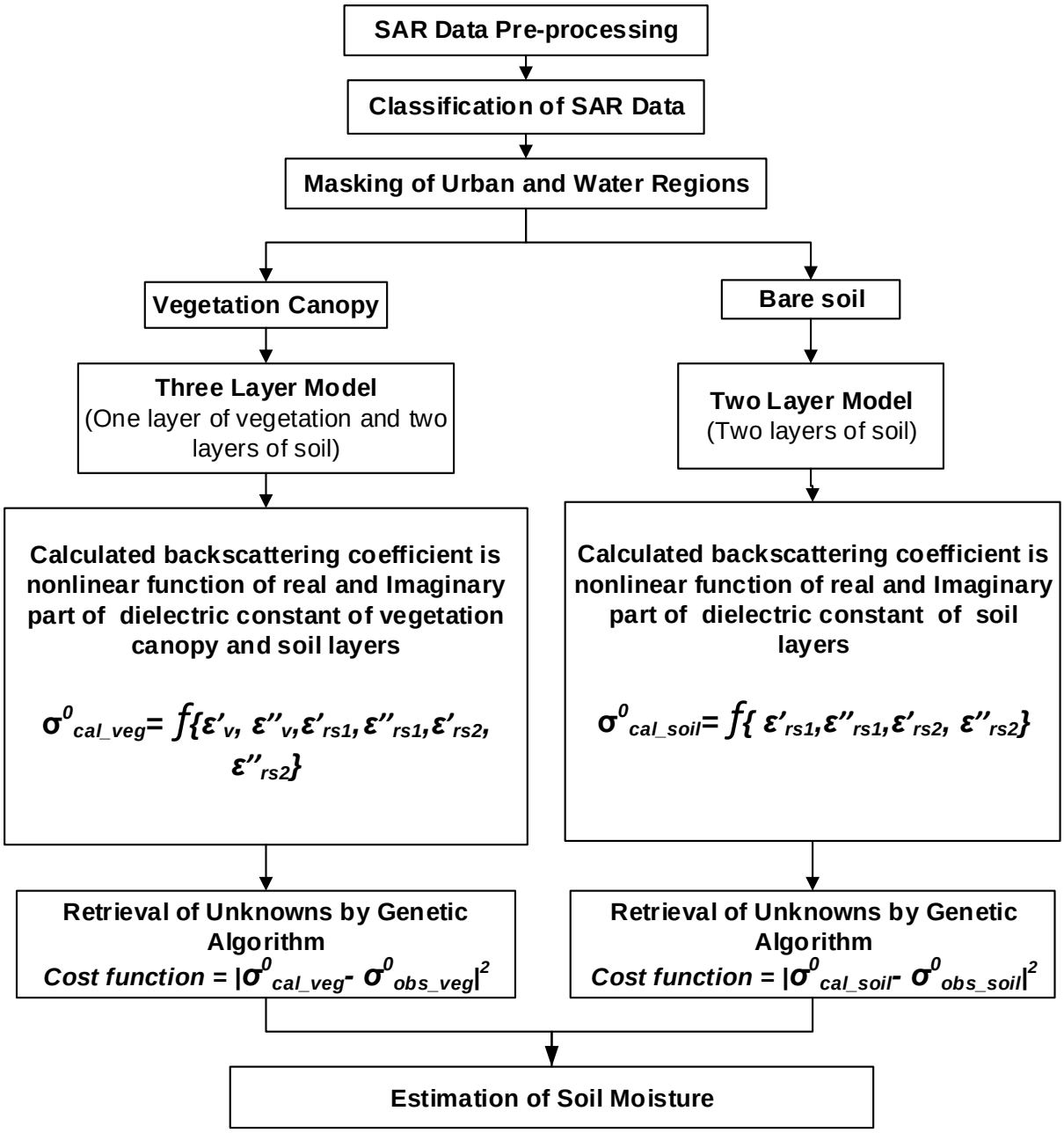

Figure 5.4: Flowchart for development of soil moisture retrieval algorithm.

5.4.1. Three Layer Model for Vegetation

For vegetated region, multilayer model, as discussed in section 5.3, having n=3 number of layers, hence, designated as three layer model, has been developed. In order to develop three layer model for vegetation, it has been assumed that media is composed of infinite length of air, one layer of vegetation-air mixture, and two layers of soil. Referring Figure 5.1 and 5.3, it can be visualized that topmost layer (or layer-1) is vegetation-air mixed layer having thickness t_1 (or t_V, where *'V'* stands for vegetation-air mixed layer), and next two layers (layer 2 and 3) are soil layers having thicknesses t_2 (or t_{S1}, where *'S1'* stands for soil layer 1), and t_3 (or t_{S2}, where *'S2'* stands for soil layer 2), respectively. The impedances of vegetation-air mixed layer and soil layers are Z_1 (or Z_V), Z_2 (or, Z_{S1}), and Z_3 (or, Z_{S2}), respectively, which are calculated by using Equation (5.9) as,

$$Z_1 = Z_V = \frac{Z_0}{\varepsilon_{rV}} \sqrt{\varepsilon_{rV}\mu_{rV} - \sin^2\theta_i} \tanh\left(j \frac{2\pi\, t_V}{\lambda} \sqrt{\varepsilon_{rV}\mu_{rV} - \sin^2\theta_i} \right), \tag{5.12a}$$

$$Z_2 = Z_{S1} = \frac{Z_0}{\varepsilon_{rS1}} \sqrt{\varepsilon_{rS1}\mu_{rS1} - \sin^2\theta_i} \tanh\left(j \frac{2\pi\, t_{S1}}{\lambda} \sqrt{\varepsilon_{rS1}\mu_{rS1} - \sin^2\theta_i} \right), \tag{5.12b}$$

$$Z_3 = Z_{S2} = \frac{Z_0}{\varepsilon_{rS2}} \sqrt{\varepsilon_{rS2}\mu_{rS2} - \sin^2\theta_i} \tanh\left(j \frac{2\pi\, t_{S2}}{\lambda} \sqrt{\varepsilon_{rS2}\mu_{rS2} - \sin^2\theta_i} \right), \tag{5.12c}$$

where, ε_{rV}, ε_{rS1}, and ε_{rS2} are complex dielectric constants, and μ_{rV}, μ_{rS1}, and μ_{rS2} are complex permeabilities of vegetation canopy and soil layers (layer 2 and 3), respectively. In this analysis, μ_{rV}, μ_{rS1}, and μ_{rS2} are taken as 1.0.

The total impedance seen looking into vegetation layer can be measured by using Equations (5.4) and (5.12) as,

$$Z_{T\_veg} = Z_1 + Z_2 + Z_3, \tag{5.13}$$

After obtaining total input impedance Z_{T_veg} in Equation (5.13), reflection coefficient ($\Gamma_{\_veg}$) in vegetated area is measured by Equation (5.10) as,

$$\Gamma_{\_veg} = \frac{Z_{T\_veg} - Z_0 \cos\theta_i}{Z_{T\_veg} + Z_0 \cos\theta_i}, \tag{5.14}$$

At last, the backscattering coefficient in vegetated area (i.e., $\sigma^0_{cal\_veg}$) can be calculated using Equations (5.11) and (5.14) as,

$$\sigma^0_{cal\_veg} = 20\log\left(\left|\Gamma_{\_veg}\right|\right), \tag{5.15}$$

The Equation (5.15) indicates that $\sigma^0_{cal\_veg}$ is non-linearly related to complex dielectric constant and thickness of all three layers of vegetation model (or three layer model). As discussed in section 5.1, thickness of first and second layers of soil (t_{S1} and t_{S2}, respectively) have been taken as 5 cm and infinite, respectively. The thickness of vegetation-air mixed layer has been varied from 5 cm to 400 cm because it is assumed that most agricultural vegetation would be covered in this range.

5.4.2. Two Layer Model for Bare Soil

In case of bare soil, multilayer model having $n=2$ numbers of layer (i.e., two layer model) has been developed. This model includes infinite layer of air and two layers of soil (soil layers 1 and 2). Thus, this model is similar to three layer model, as discussed in section 5.4.1, except exclusion of vegetation-air mixed layer. As exhibited in Figures 5.1 and 5.3, thickness of soil layers 1 and 2 are t_1 (or, t_{S1}) and t_2 (or, ts_2), respectively, and their respective impedances are Z_{S1} and Z_{S2}, respectively. The total impedance seen looking into soil layers can be determined by using Equations (5.4) and (5.9) as,

$$Z_{T\_soil} = Z_{S1} + Z_{S2} \quad , \tag{5.16a}$$

$$Z_{S1} = \frac{Z_0}{\varepsilon_{rS1}} \sqrt{\varepsilon_{rS1}\mu_{rS1} - \sin^2\theta_i}\, \tanh\left(j\frac{2\pi\, t_{S1}}{\lambda} \sqrt{\varepsilon_{rS1}\mu_{rS1} - \sin^2\theta_i} \right), \tag{5.16b}$$

$$Z_{S2} = \frac{Z_0}{\varepsilon_{rS2}} \sqrt{\varepsilon_{rS2}\mu_{rS2} - \sin^2\theta_i}\, \tanh\left(j\frac{2\pi\, t_{S2}}{\lambda} \sqrt{\varepsilon_{rS2}\mu_{rS2} - \sin^2\theta_i} \right), \tag{5.16c}$$

In a similar manner, as discussed in section 5.4.1, reflection coefficient ($\Gamma_{\_soil}$) and backscattering coefficient in bare soil region (i.e., $\sigma^0_{cal\_soil}$) are calculated by using Equations (5.10) and (5.11), respectively, as,

$$\Gamma_{\_soil} = \frac{Z_{T\_soil} - Z_0 \cos\theta_i}{Z_{T\_soil} + Z_0 \cos\theta_i}, \tag{5.17}$$

$$\sigma^0_{cal\_soil} = 20\log\left(\left|\Gamma_{\_soil}\right|\right), \tag{5.18}$$

After taking t_{S1} and t_{S2} as 5 cm and infinite respectively, Equation (5.18) that calculates backscattering coefficient for bare soil ($\sigma^0_{cal\_soil}$) becomes function of complex dielectric constant of soil layers 1 and 2.

5.4.3. Retrieval of Complex Dielectric Constant of Soil Layers Using Genetic Algorithm

The backscattering coefficients in Equations (5.15) and (5.18) represent a non-linear problem involving multiple unknowns (more than two). The well proven ability of Genetic Algorithm (GA) in handling multiple parameters together, and in production of optimal solution of any problem in any search space, makes it reliable choice to solve our problem. The most critical step of genetic algorithm is proper selection of cost function to accurately determine the solution close to optimal results. In this particular case, the cost function is formulated by backscattering coefficient calculated in multilayer model, particularly in three layer model using Equation (5.15) for vegetation (i.e., $\sigma^0_{cal\_veg}$), and in two layer model using Equation (5.18) for bare soil (i.e., $\sigma^0_{cal\_soil}$). Through GA, optimum solution for unknown parameters has been obtained by minimizing the cost function [179, 341]. The retrieval process of unknown parameter using GA for three and two layer models has been discussed as:

5.4.3.1 Retrieval of dielectric constant of soil layers in three layer model

Equation (5.15) shows that backscattering coefficient of vegetated area is related to complex dielectric constants of each layer. Considering real and imaginary part of complex dielectric constant as individual variables, $\sigma^0_{cal\_veg}$ becomes the function of six unknowns which are ε'_{rV}, ε''_{rV}, ε'_{rS1}, ε''_{rS1}, ε'_{rS2}, and ε''_{rS2}. This problem for retrieval of real and imaginary part of complex dielectric constant of vegetation-air mixed layer and soil layers, has been solved by GA. The construction of cost function for GA is done by taking calculated backscattering coefficient of Equation (5.15) and observed value of backscattering coefficient ($\sigma^0_{obs\_veg}$) using HH polarized SAR data as,

$$Cost\ Function = |\sigma^0_{cal\_veg} - \sigma^0_{obs\_veg}|^2, \tag{5.19}$$

where $\sigma^0_{obs\_veg}$ is observed value of backscattering coefficient in vegetated area which is retrieved from HH polarization channel of SAR data.

5.4.3.2 Retrieval of dielectric constant of soil layers in two layer model

The backscattering coefficient of bare soil (i.e., $\sigma^0_{cal\_soil}$) in two layer model [Equation (5.18) in section 5.4.2] is a non-linear function of real and imaginary parts of dielectric constant of two layers of soil i.e., ε'_{rS1}, ε''_{rS1}, ε'_{rS2}, and ε''_{rS2}. The retrieval of these four unknowns has been

done by using GA by minimizing the cost function, which is defined as,

$$Cost\ Function = |\ \sigma^0_{cal\_soil} - \sigma^0_{obs\_soil}\ |^2, \tag{5.20}$$

where $\sigma^0_{obs\_soil}$ is the backscattering coefficient of bare soil which is retrieved from HH polarized channel of SAR data.

5.4.4. Retrieval of Soil Moisture

Application of GA in Equations (5.19) and (5.20), helps in retrieval of real and imaginary parts of complex dielectric constant of both the layers of soil (i.e., ε'_{rS1}, ε''_{rS1}, ε'_{rS2}, and ε''_{rS2}) for vegetated area using three layer model, as discussed in section 5.4.1, and for bare soil region using two layer model, as discussed in section 5.4.2. In this analysis, soil moisture value has been retrieved by using well-known polynomial relation between volumetric soil moisture and real part of complex dielectric constant of soil, which was proposed by Topp et al. [373]. Based on this relationship, volumetric soil moisture for top layer of soil (first 5 cm) in both the regions (i.e., vegetation and bare soil) can be estimated as,

$$m_v = -5.3\times10^{-2} + 2.92\times10^{-2}\varepsilon'_{rS1} - 5.5\times10^{-4}\varepsilon'^{\,2}_{rS1} + 4.3\times10^{-6}\varepsilon'^{\,3}_{rS1}, \tag{5.21}$$

5.5. Results and Discussion

This section presents the result of proposed soil moisture retrieval algorithm of two different L-band ALOS PALSAR data sets and one Radarsat-2 data. The results are discussed as follows:

5.5.1. Implementation of Algorithm on Data-1

The steps for implementation of the algorithm have been described in Figure 5.4. The algorithm has been implemented and tested on Data-1 (Data ID-PASL1109040617112609081100 63). The step-wise description of implementation procedure has been given as follows:

1. In first step, classification of SAR data is performed, for which the adaptive classification algorithm, as developed in Chapter 4, has been used. The classified image of Data-1 has been shown in Figure 4.7, which exhibits five different classes, such as water, urban, tall vegetation, short vegetation, and bare soil in blue, red, cyan, green, and yellow colours, respectively. In this analysis, short vegetation and tall vegetation classes have been considered as single entity called vegetation.

2. In second step, urban and water classes have been masked in order to obtain only vegetation and bare soil classes. The masked classified image of Data-1 has been shown in Figure 5.5, in which vegetation and bare soil classes are represented in green and yellow colours, respectively, whereas masked urban and water classes are shown in black colour.
3. Now, in case of vegetation, three layer model, as discussed in section 5.4.1, has been applied, whereas in case of bare soil, two layer model, as discussed in section 5.4.2, has been applied. Using these models, backscattering coefficients have been calculated for both vegetated and bare soil regions i.e., $\sigma^0_{cal\_veg}$ and $\sigma^0_{cal\_soil}$, as given in Equations (5.15) and (5.18), respectively.
4. Next step is to measure backscattering coefficient for HH polarization using Data-1.This data is obtained after performing pre-processing, as described in Chapter 3 (Figure 3.3). The observed backscattering coefficient for vegetation class and bare soil class has been designated as $\sigma^0_{obs\_veg}$ and $\sigma^0_{obs\_soil}$, respectively.
5. In MATLAB, the code for GA has been implemented, which is based on the concept of evolution optimization [447]. In this algorithm, population of distinct solutions are repeatedly modified in order to improve the fitness, and to obtain optimal solution of the problem by minimizing cost function.
6. In case of vegetation, there are six unknowns consisting real and imaginary parts of dielectric constants of vegetation-air mixed layer and soil layers (i.e., ε'_{rV}, ε''_{rV}, ε'_{rS1}, ε''_{rS1}, ε'_{rS2}, and ε''_{rS2}). These unknowns are retrieved by minimizing the cost function, as given in Equation (5.19), using GA. Since retrieval of soil moisture is generally performed for first few centimeters of soil layer, the thickness of first layer of soil i.e., t_{S1}, has been considered up to 5 cm (as discussed earlier that penetration depends upon the used radar wavelength). The thickness of second layer of soil (t_{S2}) has been taken as infinite, whereas thickness of vegetation-air mixed layer (t_V) has been varied from 5 cm-400 cm.
7. In a similar manner, for bare soil class, GA has been applied over the cost function, as given in Equation (5.20), for retrieving 4 unknowns consisting real and imaginary parts of dielectric constants of soil (i.e., ε'_{rS1}, ε''_{rS1}, ε'_{rS2}, and ε''_{rS2}). In this case, t_{S1} is again set as 5 cm in order to retrieve soil moisture in first few centimetres of soil depth, and t_{S2} is considered as infinite.

8. The next step is to estimate the soil moisture for both bare soil and vegetation-covered bare soil. After applying GA in three layer model for vegetation and two layer model for bare soil, the value of real parts of dielectric constants for top layer of soil (i.e., ε'_{rS1}) have been retrieved for both models. These values of ε'_{rS1} have been used for retrieving volumetric soil moisture in top layer of soil (m_v) in both the regions i.e., bare soil and vegetation underlying soil, by using Equation (5.21). Figure 5.6 shows the moisture map for top layer of soil.
9. Figure 5.7 shows the graph of retrieved volumetric soil moisture for top layer of soil (m_v) obtained by proposed approach versus observed volumetric soil moisture for Data-1. The coefficient of determination (R^2) and Root Mean Square Error (RMSE) has been obtained as 0.74 and 0.027, respectively. Small RMSE and moderate R^2 value indicates quite good performance of proposed methodology.

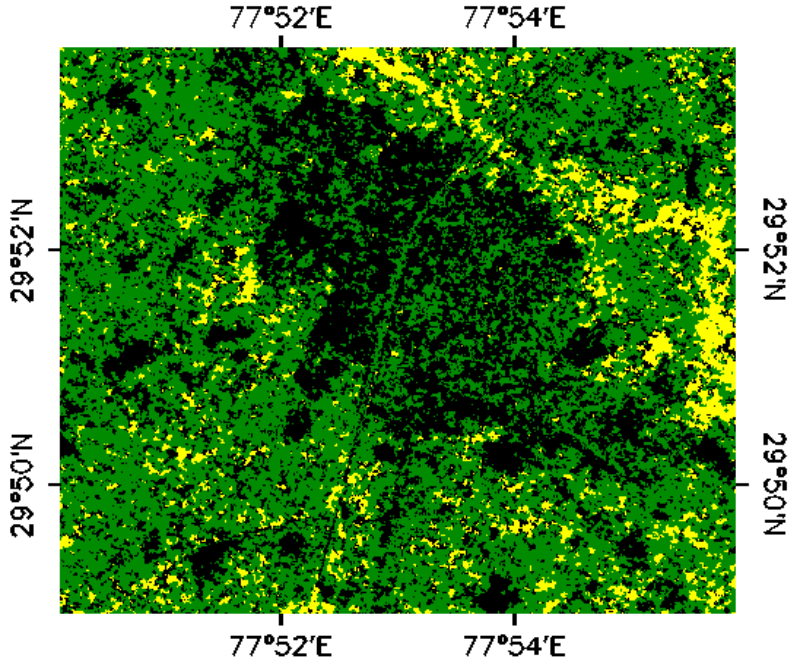

Figure 5.5: Classified masked image of Data-1 exhibiting vegetation and bare soil classes in green and yellow colours, respectively. Black region shows masked urban and water classes.

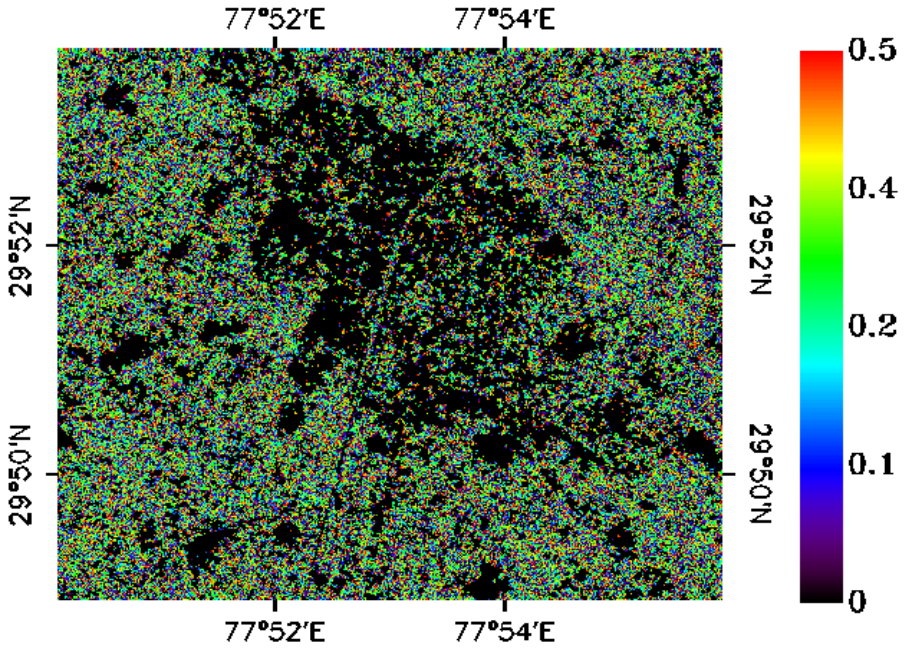

Figure 5.6: Soil moisture map for top layer of soil (m_v) using Data-1.

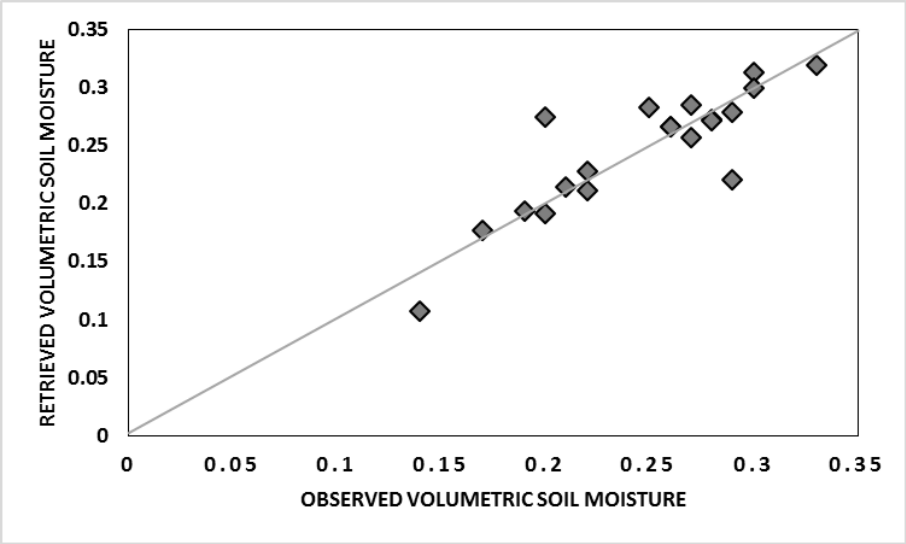

Figure 5.7: Retrieved volumetric soil moisture (m_v) versus observed volumetric soil moisture for Data-1.

5.5.2. Testing of Algorithm on Data-2

The algorithm has been tested on different ALOS PALSAR data (i.e., Data-2: Data ID-PASL1100904061711181001150003) for similar region (i.e. Roorkee). After classifying the image of Data-2 using method proposed in Chapter 4, masking of urban and water classes in classified image (Figure 4.8) has been performed. This masked classified image of data-2 has been shown in Figure 5.8, which displays vegetation in green and bare soil in yellow colour.

Now, GA has been applied for retrieving six unknowns (ε'_{rV}, ε''_{rV}, ε'_{rS1}, ε''_{rS1}, ε'_{rS2}, and ε''_{rS2}) of three layer model for vegetation and four unknowns (ε'_{rS1}, ε''_{rS1}, ε'_{rS2}, and ε''_{rS2}) of two layer model for bare soil by minimizing the cost functions, as given in Equations (5.19) and (5.20), respectively. The optimum values of ε'_{rS1} obtained from both three and two layer models for vegetation and bare soil, respectively, have been used to estimate volumetric soil moisture for top layer of soil (i.e., m_v) by Equation (5.21). The generated soil moisture map for bare soil as well as crop covered soil is shown in Figure 5.9.

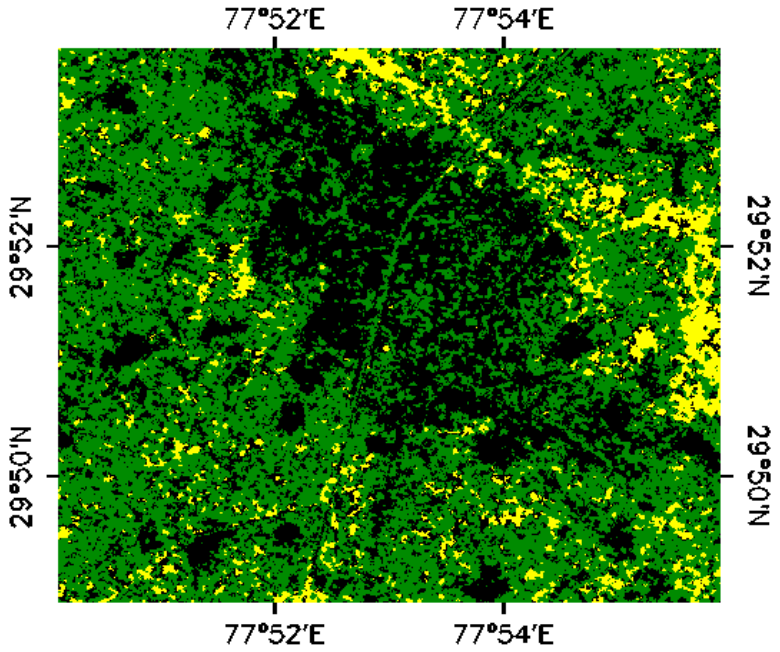

Figure 5.8: Classified masked image of Data-2 exhibiting vegetation and bare soil classes in green and yellow colours, respectively. Black region shows masked urban and water classes.

For Data-2, the quantitative result of retrieved volumetric soil moisture for top layer of soil (m_{v1}) for Data-2 versus observed volumetric soil moisture has been presented in Figure 5.10. The R^2 and RMSE error for this relationship is 0.70 and 0.039, respectively. The result of retrieved soil moisture shows good agreement with the observed value of soil moisture.

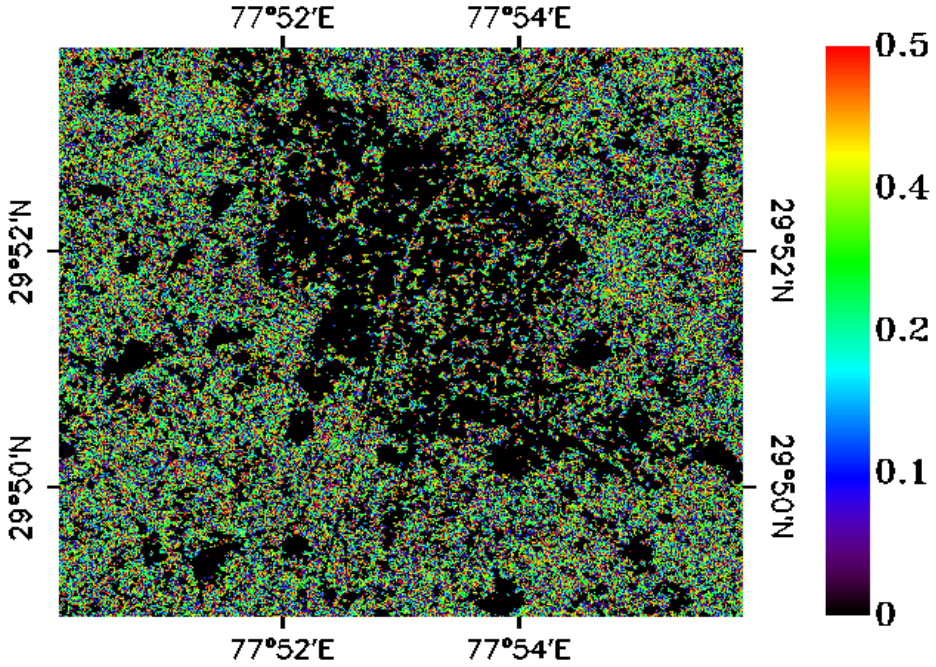

Figure 5.9: Soil moisture map for top layer of soil (m_v) using Data-2.

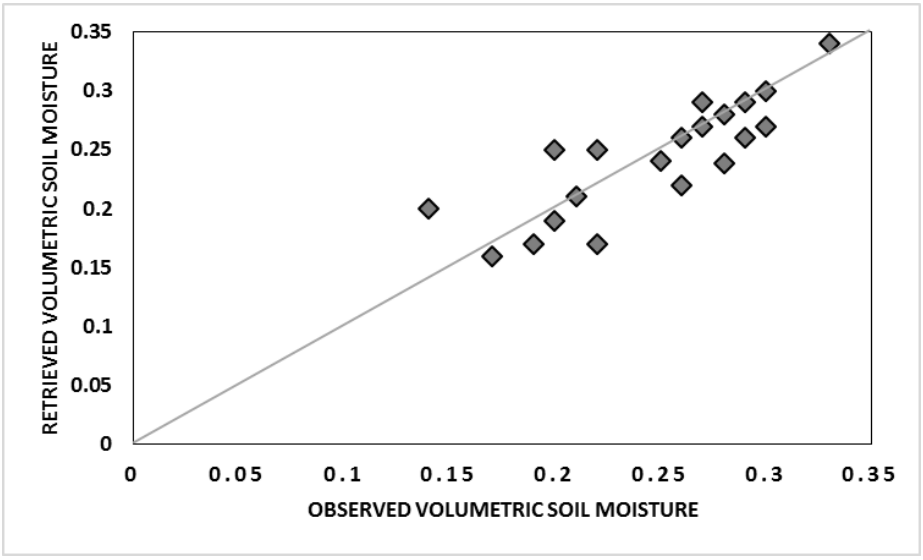

Figure 5.10: Retrieved volumetric soil moisture (m_{v1}) versus observed volumetric soil moisture for Data-2.

5.5.3. Application of Proposed Approach on C-Band Radarsat-2 Data

For the purpose of evaluating the performance of proposed soil moisture retrieval approach on C-band, Radarsat-2 data has been used. The pre-processing of Radarsat-2 data is performed in a similar manner, as described in section 3.7.1 (Figure 3.3) in Chapter 3. The application of proposed soil moisture algorithm requires masking of urban and water classes. For ALOS PALSAR data, the masking of these regions has been done after classifying data by adaptive classification algorithm proposed in Chapter 4. Since this algorithm has been developed for L-band ALOS PALSAR data. Thus, in this chapter, classification of Radarsat-2 has been carried out by supervised maximum likelihood method. This classification has been performed on layer stacked HH-HV-VV polarized bands by using training samples for water, urban, vegetation, and bare soil regions. The ground truth points for training and testing samples required for classification have been enlisted in Table-5.1. The overall classification accuracy measured by taking testing samples of all four classes has been obtained as 87%. The classified image of Radarsat-2 data exhibiting water, urban, vegetation and bare soil regions in blue, red, green and yellow colours, respectively, and its corresponding masked classified image exhibiting urban and water classes in black colour, is shown in Figure 5.11.

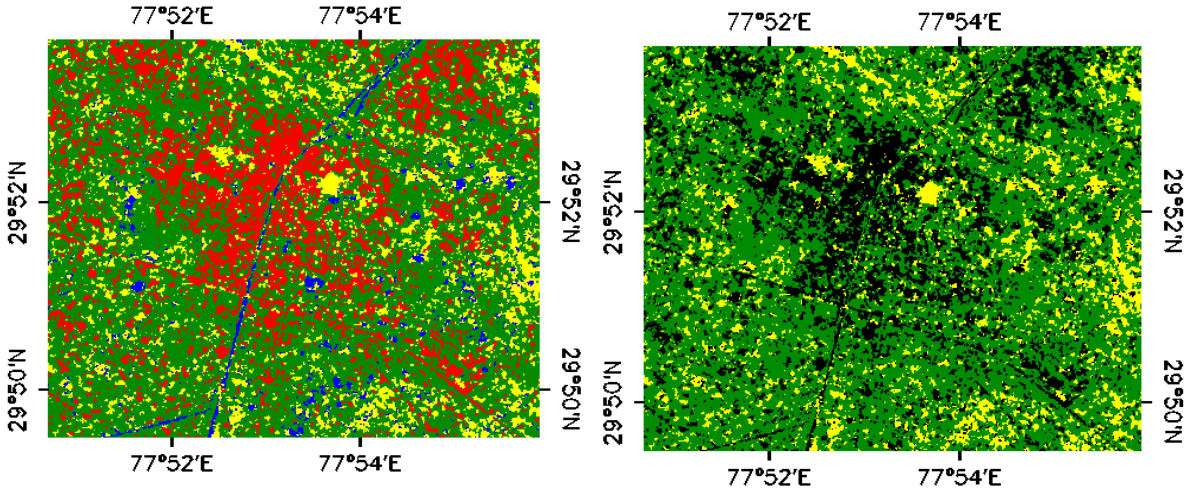

Figure 5.11: (a) Classified image of Radarsat-2 data exhibiting water, urban, bare soil and vegetation classes in blue, red, yellow, and green colours, respectively, and (b) Masked classified image exhibiting urban and water classes in black colours.

The same procedure has been adopted, as in section 5.5.1 and 5.5.2, for retrieval of unknowns associated with two and three layer models for bare soil and vegetation, respectively by minimizing the cost functions (Equation (5.20) and (5.19), respectively) using GA. Finally, soil moisture for top layer of soil and vegetation covered soil has been retrieved by Equation (5.21). This moisture map (i.e., m_v) has been shown in Figure 5.12.

The retrieval of volumetric soil moisture for top layer of soil (m_v) using Radarsat-2 data shows good agreement with the observed volumetric soil moisture as represented in Figure 5.13. The R^2 and RMSE have been obtained as 0.75 and 0.041, respectively. The retrieved volumetric soil moisture is in good agreement with the observed soil moisture.

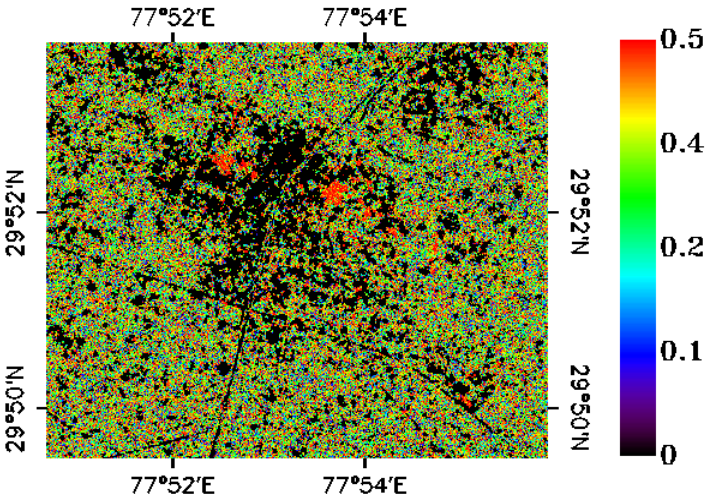

Figure 5.12: Soil moisture map for top layer of soil (m_v) using Radarsat-2 data.

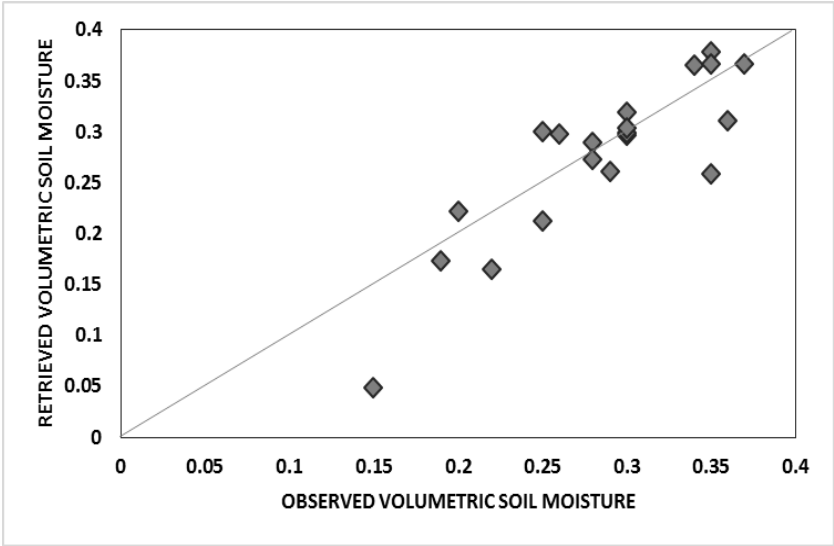

Figure 5.13: Retrieved volumetric soil moisture (m_v) versus observed volumetric soil moisture for Radarsat-2.

5.6. Conclusion

In this chapter, multilayer model based on the principle of transmission line theory has been proposed for retrieval of soil moisture in bare soil and vegetation covered soil. For vegetation and bare soil regions, three and two layer models, respectively, have been developed. Three layer model for vegetation canopy has one extra layer of vegetation as compared to that of two layer model for bare soil consisting only two layers of soil. This method estimates backscattering coefficient as a function of complex dielectric constant and thickness of each layer. In the proposed approach, the first and second layers of soil in both the models are taken as 5 cm and infinite, respectively. The vegetation layer (in three layer model) is considered to have thickness varying from 5 cm to 400 cm, assuming all the agricultural vegetation covering this range. The real and imaginary parts of dielectric constants for both bare soil and vegetated regions have been retrieved by genetic algorithm approach after minimizing cost function, which is formed by calculated backscattering coefficients in each model and HH polarized backscattering coefficient from SAR data. Further, volumetric soil moisture has been retrieved by using polynomial relation proposed by Topp et al. [373].

The proposed approach has the capability to retrieve soil moisture without having any prior knowledge about test sites. For L-band ALOS PALSAR data sets (Data-1 and Data-2), retrieved soil moisture values by proposed method exhibit good agreement with the observed (i.e., ground truth) soil moisture. The proposed approach has also been applied on C-band Radarsat-2 data, which is classified by using maximum likelihood supervised classification method. After, retrieving bare soil and vegetated regions by classification, soil moisture has been retrieved by proposed approach for top layer of soil (5 cm) and satisfactory results have been obtained for even for C-band.

Chapter 6

Study and Analysis of Hybrid Polarimetric Chandrayaan-1's MiniSAR Data for Characterization of Lunar Surface

With the advent of hybrid polarimetry, radar polarimetry has got its new dimension. It is a unique architecture in which transmitted polarization is one of the circular polarizations (left 'L'/right circular 'R'), and the received polarization is H & V linear. This configuration provides several advantages in terms of reductions in pulse repetition frequency, data volume, and system power needs, and increment in swath width [308]. These advantages provide optimum conditions for exploration of planetary surfaces. MiniSAR onboard Chandrayaan-1's mission of Indian Space Research Organisation (ISRO), India, was one such sensor. The objective of this mission was to explore lunar surface for the presence of water-ice deposits, to characterize radio-physical properties of lunar regolith, and to investigate scattering response of lunar surface [357]. On lunar surface, investigating the possibility of water-ice deposits has been a very challenging, yet fascinating task, which requires meticulous efforts. Conceptualization of MiniSAR was a breakthrough in this field for imaging permanently shadowed regions, where possibility of water- ice might be high. This chapter deals with the task of characterizing lunar surface by developing an algorithm for possible detection of water-ice, and determining its electrical and physical properties by using MiniSAR data.

6.1. Introduction

There have been several missions for lunar exploration in order to collect data of lunar surface for studying its various properties, such as dielectric constant, surface roughness, mineral composition, chemical composition (e.g., H_2, OH^-, He, etc.,), regolith density, regolith layer thickness, etc., [188, 253, 276, 336, 413]. The presence of water-ice deposits or its constituents on lunar surface has been one of the most intense matters of research by various past lunar exploration missions. Various theoretical studies and observations have been carried out in past

for discussing the presence (or absence) of water-ice or water molecules (hydroxyl) on lunar surface [15, 126-128, 414]. It was hypothesized that water or water molecules may be delivered to Moon through bombardment of water-bearing impactors such as comets, asteroids, meteorites, and micro-meteorites [15, 230, 295], or can be created by reaction between protons derived by solar wind and oxygenated minerals on lunar soil [75, 241, 295, 365]. Water can also be present on surface of Moon by various other sources, such as endogenous sources (fire fountains, apatite, outgassing) [86, 321], giant interstellar clouds, interplanetary dust particles, and solar wind[241, 278]. These volatiles (water or water molecules) can be transported through ballistic trajectories, and after reaching permanently shadowed regions, they become cold trapped [15]. It has been believed that these volatile deposits might be there for billions of years in permanently shadowed polar regions of Moon, which have average surface temperature less than 40K due to absence of solar illumination [15, 281]. Recent study by Moon Mineralogy Mapper (M^3) has detected the presence of magmatic water under lunar surface that may be generated from interiors of Moon by unknown sources [32, 190].

The possibility of finding water-ice deposits is more in permanently shadowed regions of Moon. SAR provides a possible way of imaging these regions and analyses their scattering behaviour. MiniSAR was theorized to achieve this particular goal. It was the first polarimetric SAR outside the Earth orbit, on-board India's Chandrayaan-1 mission launched by Indian Space Research Organisation (ISRO) [359]. The aim of this mission was to gather valuable facts and evidences about scattering properties of both the regions of lunar poles lying either in illumination, or in permanent shadow [357]. In radar based missions, received radar circular polarization ratio (μ_c), which is defined as the ratio of same sense circular polarization (SC) to opposite sense circular polarization (OC), has been traditionally used as a key parameter for determining the evidences of possible water-ice deposits in cold dark permanently shadowed regions. Several radar based experiments have detected the presence of water-ice after obtaining high circular polarization ratio (μ_c >1) received from polar regions of Mercury [24, 48], Jupiter [279], Mars [60], and Moon [225, 272]. High value of circular polarization ratio (μ_c >1), is caused due to density variations, particles, and voids in weakly absorbing media, like water-ice [400]. In weakly absorbing media, like ice, there exist wavelength sized forward scatterers in the form of dust, silicate rocks, voids, etc., which cause incident electromagnetic wave to undergo multiple forward scattering within the ice matrix. These multiple scattered waves interfere constructively with waves scattered in time-reversed direction (or backscatter

direction) leading to increase in SC backscatter, and hence, circular polarization ratio [261, 359]. Thus, this process known as Coherent Backscatter Opposition Effect (CBOE), which takes place in ice-matrix, gives rise to high value of μ_c. However, further studies revealed that μ_c >1 may also occur due to double-bounce effect, which takes place in rough, dry surfaces containing rocks, blocky lava flows, etc., [53, 361]. Thus, μ_c >1 assumption, is also an indicator of surface roughness. These two situations which cause high μ_c values are depicted in Figure 6.1.

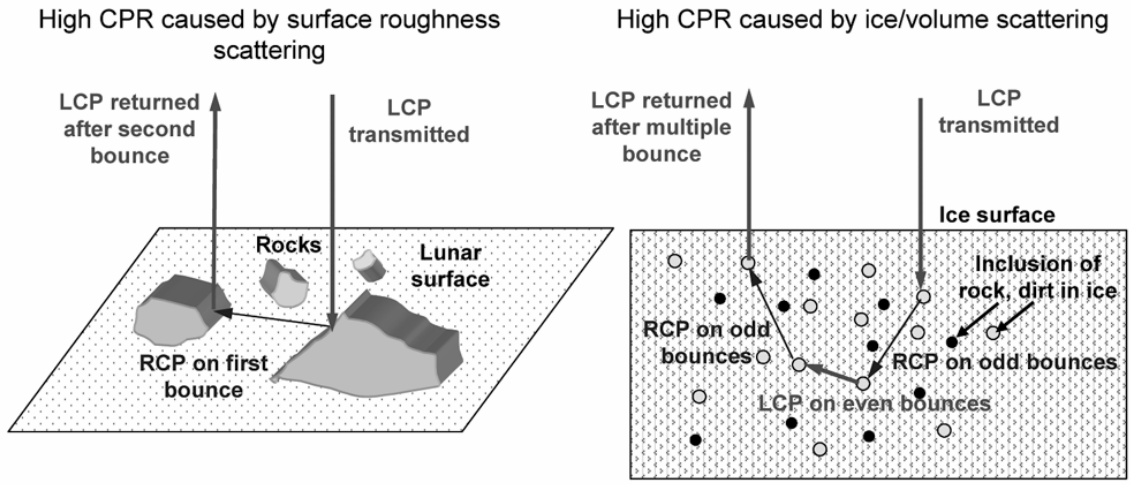

Figure 6.1: Situations depicting reasons for high circular polarization ratio [358].

Differentiation of two regions on the basis of criterion μ_c >1, is very challenging because two different phenomena are associated with lunar surface, which are volume scattering caused by dielectric mixing due to presence of planetary water-ice, and double-bounce scattering caused by surface roughness due to ejecta, rocks, or lava flows on lunar surface**.** Therefore, it is required to develop such an approach that may differentiate these two regions. One feasible way of differentiating these regions is determination of textural (or roughness) information along with scattering phenomenon associated with these regions. Therefore, in this chapter, information of two different approaches (i.e., polarimetric and fractal) have been fused for segregating craters having higher possibility of containing water-ice deposits (or dielectric mixing) from rough regions. The polarimetric approaches, '*m*-δ' decomposition [308] and '*m*-χ' decomposition [310], help in studying scattering phenomena associated with lunar surface, while fractal approach helps in identifying surfaces on the basis of their irregularity and roughness [158, 383]. Fractal based approach determines the roughness of any surface with the

renowned measure called fractal dimension (*'D'*), which has values lie in the range 2.0 to 3.0 for any surface. Characterization of lunar surface is possible by using fractal-based approach, which creates one-to-one relation between the values of fractal dimension *'D'* and texture (or roughness) measure of surfaces. It has been observed that value of *D* increases with increase in surface roughness [236, 292]. The fractal approach performs the clustering of pixels into different classes in terms of their roughness; however, it does not provide any additional information about the classes [199, 200, 249] .

Therefore, the objective of this chapter is to identify such regions on the lunar surface which have prominent volume scattering due to dielectric mixing rather than due to surface roughness, and to compute the dielectric properties of the identified region. For this purpose, in this chapter, a decision tree algorithm has been proposed for studying the possibility of volatile deposits on lunar surface by segregation of smooth regions from rough regions based on fractal dimension '*D*', and then, applying favourable conditions for likelihood of dielectric mixing due to water-ice deposits on the basis of μ_c >1 and volume scattering phenomenon. The decision criteria in the proposed algorithm have been obtained by analysing μ_c, *m*-δ decomposition, *m*-χ decomposition, and fractal dimension '*D*'. The criteria for possible existence of water-ice obtained by proposed approach have been combined with the criteria for possible icy craters proposed by Thompson et al. [371], and it has been observed that there are certain regions inside anomalous craters which satisfy the conditions proposed by both the approaches *i.e.,* proposed approach and Thompson's approach. In these common regions, the possibility of finding water-ice deposits might be high. After obtaining possible locations of water-ice deposits on lunar surface by combined approach (proposed approach and Thomson's approach), the study of electrical and physical properties such as dielectric constant of lunar surface ($\varepsilon = \varepsilon' - j\,\varepsilon''$) [52, 413], loss tangent ($tan\ \delta$) [413], and regolith bulk density (ρ_0) [124], has been performed.

The chapter is organized as follows: section 6.2 gives the description about study area and data used. The detailed description of MiniSAR data has also been discussed in this section. Section 6.3 includes the theoretical background related to child parameters, decomposition approaches, and fractal approach. The description of electrical and physical parameters has also been given in this section. In section 6.4, proposed methodology has been discussed. In section 6.5, the results of proposed algorithm using data of Peary crater have been presented. The proposed algorithm has been applied on another MiniSAR data of

Rozhdestvenskiy crater, the results of which are discussed in section 6.6. The concluding remarks have been given in section 6.7.

6.2. Study Area and Data Used

6.2.1. Study Area

For development and testing of proposed algorithm, MiniSAR data of Peary (Data-P) crater on lunar North Pole has been considered. Peary crater is large irregular shaped impact crater (diameter 77.7 km) located at 88.6° N, 33° E.

The proposed algorithm has also been tested on another MiniSAR data of Rozhdestvenskiy crater (Data-R) on North Polar Region of Moon. Rozhdestvenskiy crater is a bowl shaped large crater (diameter 177 km) located just opposite to Peary crater at 155° W, 85.2° N [359].

Illumination studies at these two craters suggest that most of the area around the higher rim lies in permanent sun illumination, while small anomalous craters (diameter <10-20 km) on the floor of these craters experience permanent shadow [47, 237, 267, 359]. Thus, possibility for presence of water-ice within these craters may be large as compared to areas around higher rim [47, 237, 267].

6.2.2. Data Description

MiniSAR was a single frequency (S-band-2.38GHz) hybrid polarity imaging radar having unique architecture among planetary radars. This sensor illuminated the lunar surface by left circular polarization (LCP) and received lunar backscatter in mutually coherent horizontal (H) and vertical (V) polarizations. In MiniSAR, the illumination of lunar surface was performed at incidence angle of 35° and ground range resolution of 150 m.

MiniSAR, being a dual polarimetric hybrid SAR system, provided four channel raw data as $|E_{LH}|^2$, $|E_{LV}|^2$, Real ($E_{LH}\ E_{LV}^*$), and Imaginary ($E_{LH}\ E_{LV}^*$) without any processing, where E represents complex voltage. The former two channels are horizontal and vertical receive amplitude images, while latter two channels are real and imaginary part of complex cross-product of horizontal and vertical receive polarizations [308]. These four channels are basic building blocks for construction of Stokes vector g, which preserves overall information of backscattered electromagnetic field, and can be represented as,

$$g = \begin{bmatrix} g_1 \\ g_2 \\ g_3 \\ g_4 \end{bmatrix} = \begin{bmatrix} \left\langle |E_{LH}|^2 + |E_{LV}|^2 \right\rangle \\ \left\langle |E_{LH}|^2 - |E_{LV}|^2 \right\rangle \\ 2\,\mathrm{Re}\left\langle E_{LH} E_{LV}^* \right\rangle \\ -2\,\mathrm{Im}\left\langle E_{LH} E_{LV}^* \right\rangle \end{bmatrix} = \begin{bmatrix} g_1 \\ m g_1 \cos 2\chi \cos 2\psi \\ m g_1 \cos 2\chi \sin 2\psi \\ -m g_1 \sin 2\chi \end{bmatrix}, \quad (6.1)$$

In second column of Equation (6.1), g_1 represents total backscattered power, g_2 represents difference of in-phase and quadrature phase received power, g_3 and g_4 are real and imaginary parts of cross-channel received power, respectively (refer Appendix-A for more details on Stokes vector). In third column of Equation (6.1), Stokes parameters (g_1, g_2, g_3, g_4) are expressed in terms of complex voltage E measured in hybrid polarimetric manner. In these expressions *Re* and *Im* represent real and imaginary parts, respectively, <...> represents multilooking (or spatial averaging), and '*' represents complex conjugate. In forth column, Stokes parameters are expressed in terms of Poincare variables χ and ψ, which are ellipticity and orientation angles, respectively, of polarization ellipse, as shown in Figure A.2 in Appendix-A [310].

6.3. Theoretical Background

Traditionally, μ_c >1 has been widely accepted criterion for identification of potential water-ice deposits on lunar surface [225, 272] and various other planetary surfaces [24, 48, 60]. However, circular polarization ratio (μ_c) alone may not be useful for finding the possible evidences for presence of water-ice deposits on lunar surface. The regions having volatile deposits exhibit μ_c >1 due to volume scattering phenomenon, as shown in Figure 6.1 [261, 359]. Thus, information about scattering mechanism may provide some additional information. Since SAR has the capability to obtain scattering information by using decomposition approaches, segregation of volume scattering dominant regions from other regions may be possible by decomposition of MiniSAR data. It is believed that μ_c >1 may also occur due to surface roughness resulted by rocks, cracks, lava flow, ejecta, etc., on lunar surface. These rough surfaces mainly contribute single and double-bounce scattering [53, 361]. However, little contribution of volume scattering may also occur due to multiple reflections on rough rocky surfaces. Thus, if roughness information is obtained by some means, it might aid in finding the possible presence of volumetric water-ice deposits on lunar surface. It is known that fractal

dimension '*D*' is capable of identifying rough and smooth surfaces based on '*D*' values [199, 200, 249, 292] . For example, 2-dimensional surfaces exhibit *D* values in between 2.0 to 3.0 with lower range corresponds to smooth surfaces and higher range corresponds to rough surfaces [292]. Therefore, fusing the information of fractal dimension '*D*' with scattering information, MiniSAR data may provide regions exhibiting volume scattering due to dielectric mixing (by water-ice) rather than due to surface roughness. Thus, in this chapter, an attempt has been made to develop an algorithm, using scattering information obtained from decomposition approaches and roughness information from fractal dimension '*D*', for identifying volume scattering regions due to dielectric mixing. Therefore, in this section review of methods related to information extraction about scattering mechanisms and roughness, has been presented.

6.3.1. Extracting Information of Scattering Mechanisms by Polarimetric Approaches

The information about scattering mechanisms can be obtained by using either child parameters or decomposition parameters. They are discussed as follows:

6.3.1.1 Child parameter extraction

The Stokes parameters are used in formation of various useful quantitative measures called child parameters, which not only describe the scattering mechanisms of different targets but also provide information related to the geophysical properties, such as dielectric permittivity, density, surface roughness, geometric shape, size, and EM penetration capability [57, 58, 311]. These child parameters are: *degree of polarization (DoP or m), circular polarization ratio (μ_c), linear polarization ratio (μ_L), degree of circular polarization (m_c), degree of linear polarization (m_L), relative LH-LV phase difference (δ), and ellipticity parameter (χ)* [308, 310]. In the proposed approach, only some of the child parameters *i.e.*, μ_c, m,δ, and χ, have been used because of their experimental validation done in earlier research, in which these parameters show capability to retrieve scattering behaviour of targets [252, 308, 310]. The detailed description of all the parameters has been presented below:

a) Degree of polarization (m)

The degree of polarization helps in determining the state of polarization of electromagnetic waves by characterizing the amount of depolarization in polarimetric SAR images [335]. It can be mathematically represented as [308],

$$m = \frac{\sqrt{(g_2^2 + g_3^2 + g_4^2)}}{g_1}\ , \qquad 0 < m < 1, \tag{6.2}$$

where m=0 denotes completely depolarized wave, m=1 denotes fully polarized wave, and 0<m<1 denotes partially polarized wave [335]. Therefore, lower m values correspond to volume scattering, whereas higher m values correspond to surface or double-bounce scattering [252].

b) Circular Polarization Ratio (μ_c)

The circular polarization ratio is defined as the ratio of the same sense circular polarization (SC) to the opposite sense circular polarization (OC), given as [308],

$$\mu_c = \frac{(g_1 - g_4)}{(g_1 + g_4)}, \qquad \mu_c \geq 0\,, \tag{6.3}$$

The criterion μ_c>1 has been a prime indicator for detection of planetary water-ice deposits [271, 272, 352].

c) Relative LH-LV phase (δ)

It is defined as the relative phase between two linearly polarized backscattered electric field vectors, which is given by [308],

$$\delta = \tan^{-1}\left(\frac{-g_4}{g_3}\right), \qquad -180° < \delta \leq 180°\,, \tag{6.4}$$

where '–' sign in numerator represents transmission of left circular polarization. It is sensitive indicator of scattering mechanisms associated with the target. The δ value clustered around +90° and around −90° reflect double-bounce and surface scattering, respectively, whereas distributed δ represents dominant volume scattering [252, 308].

d) Ellipticity angle (χ) [310]

It preserves the sense of rotation of polarization ellipse (*i.e.*, even versus odd-bounce) for transmission of electromagnetic field in circular or elliptical polarization. It is basically a shape parameter, which determines the degree up to which shape of polarization ellipse is oval [310]. It can be defined as,

$$\chi = \frac{1}{2}\sin^{-1}\left(\frac{-g_4}{m g_1}\right)\,, \tag{6.5}$$

e) Degree of circular polarization (m_c)

It is an indicator of obtaining the power contained in circularly polarized component of received radar echo. It is defined as [311],

$$m_c = \frac{-g_4}{g_1}, \tag{6.6}$$

f) *Degree of linear polarization (m_L)*

It is an indicator of multiple scattering versus subsurface scattering. In case of subsurface scattering, backscatter response will have partially polarized linear waves. In received radar response, the degree of linear polarization is defined as [311],

$$m_L = \frac{(g_2^2 + g_3^2)^{1/2}}{g_1}, \qquad m_L > 0, \tag{6.7}$$

g) Linear polarization ratio (μ_L)

It gives ratio of polarized power contained in horizontal component and in vertical component, and is defined as [357],

$$\mu_L = \frac{(g_1 - g_2)}{(g_1 + g_2)}, \tag{6.8}$$

6.3.1.2 Polarimetric decomposition approaches for segregation of scattering mechanisms

The polarimetric decomposition methods utilize polarimetric data in optimum manner by identification of two or more independent components, which assist in classifying physical scattering phenomenon associated with the observed region [3, 250, 310]. There are two polarimetric decomposition methods based on hybrid polarimetric SAR data, namely *m-δ decomposition [308]* and *m-χ decomposition [310]*. These decomposition methods provide three scattering mechanisms, *i.e.,* volume scattering, surface scattering, and double-bounce scattering. These methods are described as follows:

a) The m-δ Decomposition

The *m-δ* decomposition makes use of degree of polarization (*m*), relative LH-LV phase difference (*δ),* and first Stokes vector (g_1) as decomposition parameters, and provides fractional power related to three scattering components, which are expressed as [308],

$$f_{surface} = \sqrt{0.5[g_1 m(1-\sin\delta)]}, \tag{6.9a}$$

$$f_{double} = \sqrt{0.5[g_1 m(1+\sin\delta)]}, \tag{6.9b}$$

$$f_{volume} = \sqrt{g_1(1-m)} \quad , \tag{6.9c}$$

where $f_{surface}$, f_{double}, and f_{volume} represent power terms related to surface scattering, double-bounce scattering, and volume scattering, respectively.

b) The m-χ decomposition

In *m-χ* decomposition, degree of polarization (*m*), ellipticity parameter (*χ),* and first Stokes vector (g_1) are taken as decomposition parameters. The after-products of *m-χ* decomposition, *i.e.*, three scattering component can be expressed as [310],

$$f_{surface} = \sqrt{0.5[g_1 m(1-\sin 2\chi)]}, \tag{6.10a}$$

$$f_{double} = \sqrt{0.5[g_1 m(1+\sin 2\chi)]}, \tag{6.10b}$$

$$f_{volume} = \sqrt{g_1(1-m)}, \tag{6.10c}$$

6.3.2. Extraction of Roughness Information Using Fractal Approach

The concept of fractal geometry was introduced by Mandelbrot in 1967 for describing self-similar geometries, such as Von Koch curve, Cantor's dust, etc., for representing the characteristic of complex and irregular natural objects that cannot be analysed easily by classical Euclidean concepts [236]. Fractal based approach has been used by several researcher for determining textural features of surfaces [157-159]. In fractal geometry, fractal dimension '*D*' is the key parameter, which generalizes the concept of Euclidean geometry. Although, most natural surfaces are non-fractals, '*D'* has been represented as useful index for surface characterization [96, 313, 314]. The fractal dimension, also known as shape's similarity dimension, can be defined mathematically as [236],

$$D = \frac{\log(N_r)}{\log(1/r)}, \tag{6.11}$$

where, N_r represents the number of similar parts of an object scaled down by the ratio *r*. The above formula is applicable to strictly self-similar objects.

Fractal dimension '*D*', is a scale-independent quantity, which is used for explaining the fractional gap of geometrical structure over limited scale [203, 364]. The value of fractal dimension is always greater than the topological dimension of any object [236]. In traditional Euclidean space, a point is topologically zero-dimensional, a line is one-dimensional (1D), an area is two-dimensional (2D), and a volume is three-dimensional (3D). Thus, topological dimension of irregular natural objects cannot be represented by Euclidean geometry. Fractal

dimension '*D'*, being a non-integer quantity, helps in measuring geometric complexity and irregularity of imaged objects. A point pattern represents fractal dimension value *'D'* in between 0 and 1.0; a curve, between 1.0 and 2.0; and a surface, between 2.0 and 3.0 [236]. In general, irregularity or complexity of any object is directly proportional to the value of '*D'*. Thus, it was suggested that fractal dimension is the perfect indicator of surface roughness [292, 364]. For 2D surfaces or images, various land covers can be mapped in terms of roughness, like smooth, rough, medium rough, highly rough, and so on. Fractal dimension *'D'* can map these terms in the range between 2.0 to 3.0 [292]. Smooth 2D surfaces exhibit *'D'* value equals to 2.0, and with the increase in surface roughness, value of *'D'* increases and reaches at value 3.0 for extremely rough surfaces.

In literature, there are numerous methods for estimation of fractal dimension *'D'*, which are Box Counting Method [184, 324, 364];Triangular Prism Surface Area Method (TPSAM) [76, 97, 118, 178, 314, 363, 364]; Variogram Method [30, 97, 178, 364]; Isarithm Method [178, 364]; Fourier Spectrum Method [292, 364]; Two Dimensional Variation Method (2DVM) [30]. Among these methods, TPSAM is widely acknowledged method for producing accurate results [203].

Therefore, in this chapter, fractal dimension *'D'* has been estimated with TPSAM [363]. It can be assumed that there is non-strict direct relation between texture of land cover type and value of fractal dimension *'D'*; *i.e.*, different land covers have unique values of fractal dimension *'D'* based on their roughness/texture behaviour [292]. Thus, in this chapter, an attempt has been made to segregate smooth and rough lunar surfaces on the basis of '*D*' value in order to resolve the confusion caused by $\mu_c > 1$ assumption, so as to obtain the regions having volume scattering due to possibility of dielectric mixing resulted by volatile deposits rather than due to rough surface. The description of TPSAM method has been provided below:

6.3.2.1 Triangular Prism Surface Area Method (TPSAM)

Triangular Prism Surface Area Method is one of the most widely acclaimed approach for estimation of fractal dimension *'D'* [76, 178, 363]. In this method, three dimensional triangular prisms are formed by locating four adjacent pixels for an analysis window in the image. The intensity of these pixels are considered as height of corners of the prism, while the center pixel which is the average of four pixels forming the corners of prism, becomes the height of top of the prism. This structure in 3D space provides four triangular surfaces, the surface area of which are estimated by Heron's formula [76]. Figure 6.2 exhibits an example of triangular

prism formed by considering a square array having four pixels at its corner which are separated by distance (step size) Δ and are located at coordinates (i, j), $(i+\Delta, j)$, $(i+\Delta, j+\Delta)$, and $(i, j+\Delta)$ having pixels values a, b, c, and d, respectively. These pixel values are considered as the height of the edges of the prism, while their average e is considered as the height of the top of prism. After joining these five points, a prism is formed having four triangular facets A, B, C, and D, at its top surface. At this point total area of upper surface of prism (sum of areas of A, B, C, and D) and area of base ($\Delta \times \Delta$) are calculated. This process is repeated by increasing the step size in power of 2 and estimating total upper surface area of prism until whole image is taken for construction of prism. The base area as x-axis and upper surface area of the prism as y-axis, estimated at each step, are plotted on log-log scale. The least square estimation of this plot is used to calculate fractal dimension 'D' by subtracting slope of least square fit from 2.0, as,

$$D = 2.0 - Slope, \tag{6.12}$$

It is observed that for very rough surface having large variation in grey scale values, the prism surface area varies drastically with change in base area. Due to this large variation, slope becomes drastically negative, and thus, resulted in fractal dimension *'D'* approaching the value of 3.0. However, for very smooth surface having almost no variation in their grey scale values, there is very small change in prism area with respect to change in base area. The regression slope in this case is almost zero, and this resulted in D values near 2.0. In order to obtain comparable results of fractal dimension *'D'* for variant surfaces, the data values have been normalized between 0 and 255.

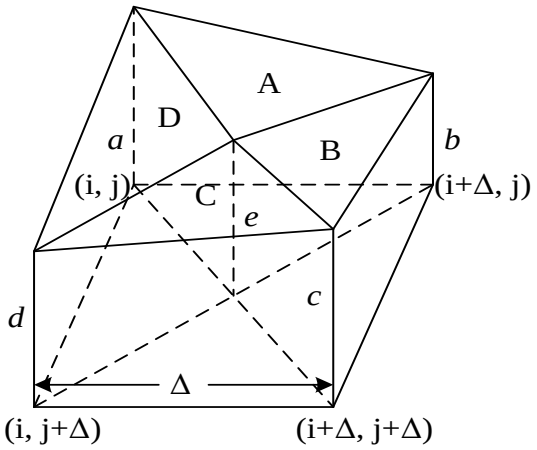

Figure 6.2: Three dimensional view of triangular prism formed with four pixels [76].

6.3.3. Thompson's Approach

For segregation of possible icy and non-icy regions on lunar surface, Thompson et al. have proposed an empirical scattering model [370, 371], which is based on collaborating effect of specular and diffuse scattering mechanisms. The model postulates that specular scattering on lunar surface is obtained from smooth (or flat) surfaces and sub-surfaces which are oriented in the direction perpendicular to the radar line-of-sight. The smoothness of these surfaces is considered at a scale of more than tenth of wavelengths of radar for enormous region. The diffuse scattering is assumed to be obtained from rough surfaces or sub-surfaces. The roughness of these areas is considered at a scale of one wavelength. This type of scattering is obtained from wavelength sized rocks, or dielectric-mixing due to ice. The backscattering response of these rough regions is proportional to cosine of incidence angle. In regions having specular scattering, opposite sense circular (OC) echo is present, whereas in regions having diffuse scattering both opposite sense circular (OC) and same sense circular (SC) echoes are present. Therefore, based on the values of these SC and OC increments, this scattering model, proposes three unique surface conditions which may cause high value of circular polarization ratio (μ_c) on lunar surface. These conditions are, (a) roughness due to fresh young craters, (b) ice or dielectric composition, and (c) double-bounce craters. The segregation of these surface conditions has been provided by the values of increment in SC and OC echoes. In this chapter, the conditions for segregating icy craters proposed by Thompson et al. [371], have been used for the analysis. These conditions are described as follows*:*

$$\alpha > 1.0, \tag{6.13}$$

$$0.5 < \gamma < 1.25, \tag{6.14}$$

$$Ratio(\alpha / \gamma) > 1.5, \tag{6.15}$$

$$0.5 < Weighted\,Sum < 1.0, \tag{6.16}$$

where α is increment in same sense circularly polarized (SC) echoes, γ is increment in opposite sense circularly polarized (OC) echoes, and weighted sum is increment in total power. These terms are defined as [370],

$$\alpha = \frac{(g_1 - g_4)}{(g_1 - g_4)_{avg}}, \tag{6.17}$$

$$\gamma = \frac{(g_1 + g_4)}{(g_1 + g_4)_{avg}}, \tag{6.18}$$

$$Weighted\,Sum = [0.12\alpha + 0.88\gamma], \tag{6.19}$$

where denominator in Equations (6.17) and (6.18), represents the averaged value of respective quantities over selected area of interest on lunar surface. The Equations (6.17) and (6.18) indicate that increment in SC and OC echoes (i.e., α and γ, respectively) represent the ratio of detected backscattered powers inside crater to the power in immediate background region in Moon [370]. The ratio (α/γ) acts as a substitute of circular polarization ratio μ_c. It can be obtained by using Equations (6.17), (6.18), and (6.3) as,

$$\frac{\alpha}{\gamma} = \frac{\mu_c}{(\mu_c)_{avg}}, \tag{6.20}$$

6.3.4. Estimation of Electrical and Physical Parameters of Lunar Surface

The real part of dielectric constant of lunar surface has been determined by using Campbell's approach [52], which is based on normalized ratio of horizontal and vertical polarizations as,

$$\varepsilon' = \left(\sin\theta_i \Big/ \sin\left\{ \cos^{-1}\left(\frac{\sigma^0_{LH}}{\sigma^0_{LV}} \right)^{0.25} \right\} - \theta_i \right)^2, \tag{6.21}$$

where θ_i, σ^0_{LH}, and σ^0_{LV} are incidence angle, backscattering coefficients for LH and LV polarizations, respectively. For MiniSAR data, the incidence angle is 35°. The Equation (6.21) was originally developed with linear polarizations (i.e., HH and VV) for determining dielectric constant over Mars equivalent environment on Earth surface [52]. However, several studies have been performed by taking LH and LV polarizations, and encouraging results have been obtained [49, 50, 164, 307].

Most of the lunar surface mainly consists of regolith layer, which is formed due to constant impacts by terrestrial objects on lunar surface. This regolith layer consists of dust, rock, minerals, and glass particles. The regolith bulk density is defined as "*the mass of the material contained within a given volume*". It is expressed in grams per cubic centimeter [56]. Experimentally, it has been found that regolith bulk density is strongly related to real part of dielectric constant as [124],

$$\rho_0 = 3.53\log\varepsilon', \tag{6.22}$$

The Equation (6.22) shows that regolith bulk density is independent of chemical compositions within regolith layer. The dependency of regolith bulk density on temperature and frequency is also negligible.

According to Wang et al., loss tangent can be expressed in terms of regolith bulk density as [413],

$$\tan\delta = 10^{(0.44\rho_0 - 2.943)}, \tag{6.23}$$

Imaginary part of dielectric constant can be determined as [124],

$$\varepsilon'' = \varepsilon' \tan\delta, \tag{6.24}$$

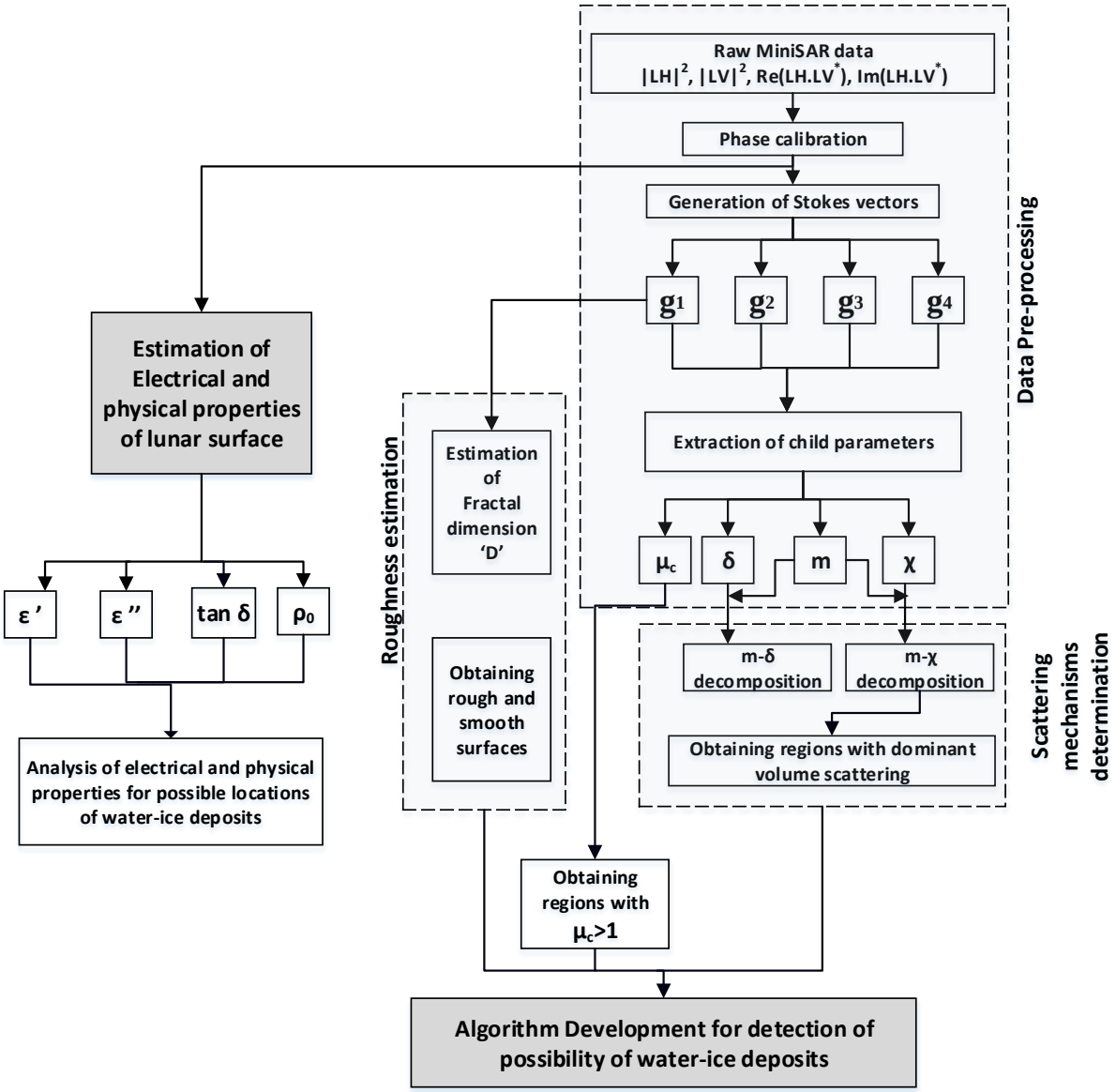

Figure 6.3: Flowchart for analysis and study of MiniSAR data.

6.4. Algorithm Development and Implementation

Based on the theoretical concept, as discussed in section 6.3, an algorithm is proposed for detection of possible water-ice deposits on lunar surface. The course of steps followed for implementation and development of algorithm, and determination of electrical and physical properties of lunar surface are presented by flowchart in Figure 6.3. This section also includes the description of pre-processing of MiniSAR data. The algorithm is developed and implemented on MiniSAR data of Peary crater (Data-P).

6.4.1. Data Pre-processing

In MiniSAR data, the transmission of left circular polarization causes the relative LH-LV phase 'δ' to be +90°. After reflection, due to change in sense of polarization, relative LH-LV phase 'δ' should be −90° [311]. However, in MiniSAR data, it has been found that relative LH-LV phase (δ) undergoes a phase shift of 45° (or −135°) in counter-clockwise direction, which makes all the lunar surface to exhibit volume scattering. Thus, phase calibration of MiniSAR data is performed prior to Stokes vector formulation. There is no need to calibrate first and second bands of MiniSAR data (i.e., $|E_{LH}|^2$ and $|E_{LV}|^2$, respectively). However, the phase calibration of third and fourth bands of MiniSAR data [Real ($E_{LH}\ E_{LV}^*$) and Imaginary ($E_{LH}\ E_{LV}^*$)] has been performed as follows [311]:

$$\mathrm{Re}(E_{LH}E_{LV}^*) = \mathrm{Re}(E_{LH}E_{LV}^*)\cos 45° - \mathrm{Im}(E_{LH}E_{LV}^*)\sin 45°, \quad (6.25a)$$

$$\mathrm{Im}(E_{LH}E_{LV}^*) = \mathrm{Re}(E_{LH}E_{LV}^*)\sin 45° + \mathrm{Im}(E_{LH}E_{LV}^*)\cos 45°, \quad (6.25b)$$

The histograms for relative LH-LV phase 'δ' of uncalibrated and calibrated MiniSAR data are shown in Figure 6.4. These histograms indicate that uncalibrated MiniSAR data (Data-P: Peary crater) shows mean relative LH-LV phase 'δ' at −135°, while calibrated data has mean relative LH-LV phase 'δ' at −90°.

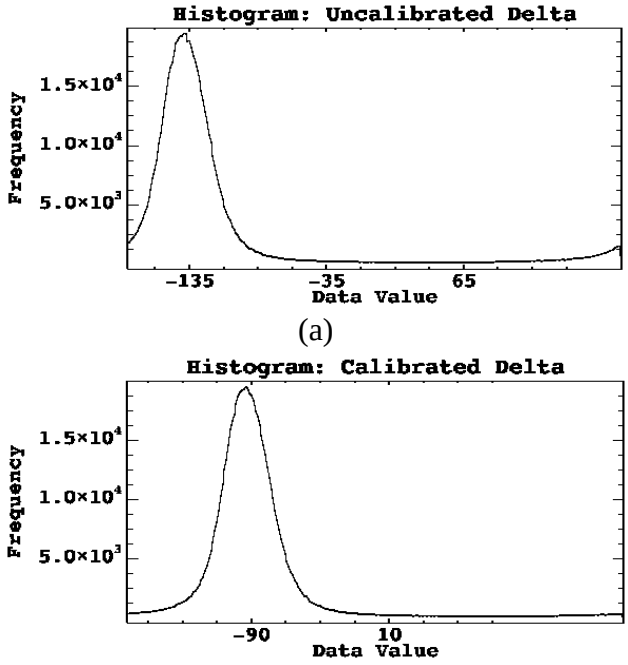

Figure 6.4: Histograms of relative LH-LH phase (δ): (a) before, and (b) after, phase calibration of MiniSAR data of Peary crater (Data-P).

After phase correction, Stokes vector have been generated by Equation (6.1). The maps of Stokes parameters i.e., g_1, g_2, g_3, and g_4 are presented in Figure 6.5. For the purpose of analysis, 12 region of interests (ROIs) have been selected over the floor of Peary crater (Data-P). These ROIs are represented as numbered rectangles on g_1 image as shown in Figure 6.5 (a). ROIs representing numbers 1 to 8, are anomalous craters on the floor of Peary crater, whereas 9-12 represent regions outside the anomalous craters.The Stokes parameters have been used for the extraction of child parameters specifically, degree of polarization (m), circular polarization ratio (μ_c), relative LH-LV phase (δ), and ellipticity angle (χ) by Equations (6.2)-(6.5), respectively. The maps of these child parameters i.e., μ_c, m, δ, and χ, are presented in Figure 6.6. These child parameters have been further used to develop proposed algorithm for possible water-ice detection, and to obtain electrical and physical parameters of lunar surface (Figure 6.3).

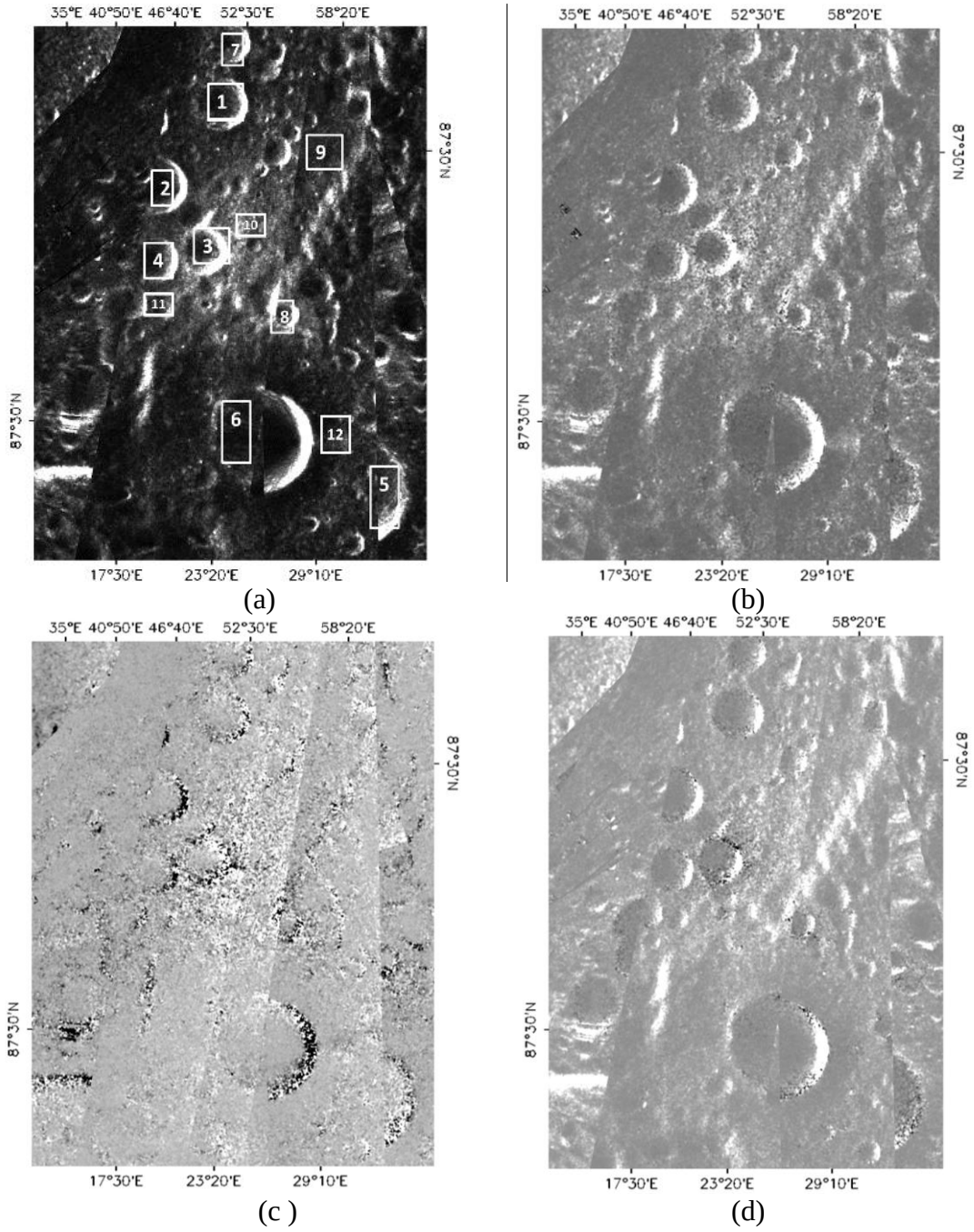

Figure 6.5: Images of Stokes vector (a) g_1, (b) g_2, (c) g_3, and (d) g_4. The region of interest areas (ROIs) on the floor of Peary crater are exhibited in (a).

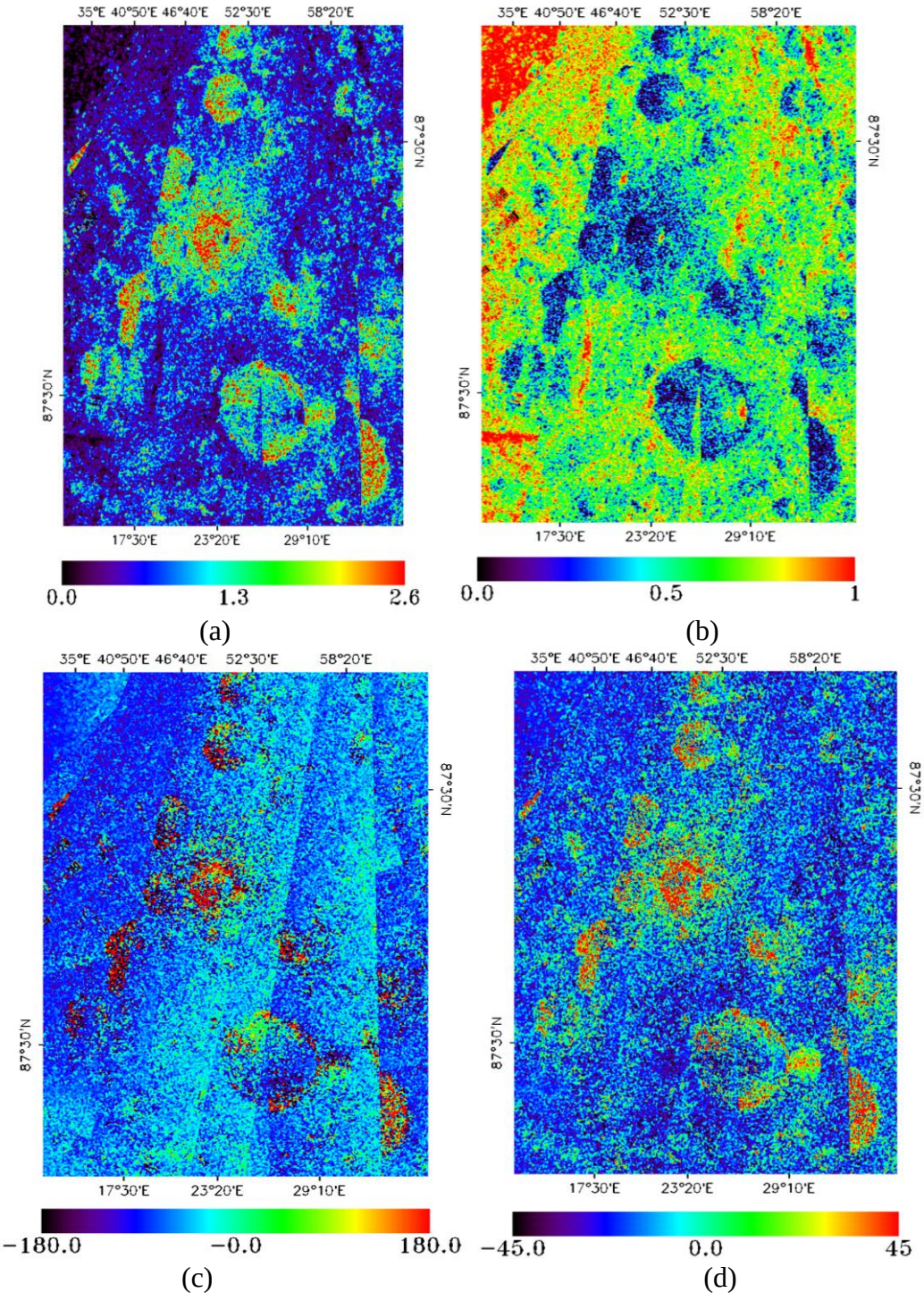

Figure 6.6: Images of child parameters: (a) circular polarization ratio (μ_c), (b) degree of polarization (m), (c) relative LH-LV phase (δ), and (d) ellipticity angle (χ) for MiniSAR data of Peary crater (Data-P).

6.4.2. Algorithm Development for Possible Existence of Water-Ice Deposits

It has been observed that identification of such regions is required that have dominant volume scattering due to dielectric mixing because they are more likely to have water-ice deposits, as elucidated in above sections. For obtaining such type of regions, several tests have to be performed i.e., segregation of regions having dominant volume scattering, segregation of smooth and rough surfaces, etc. This type of critical test can be performed by decision tree algorithm with much better way. Therefore, a decision tree algorithm has been proposed for retrieving regions exhibiting dominant volume scattering phenomenon due to dielectric mixing that may represent possibility of water-ice deposits. The decision criteria have been obtained by critically analysing child parameters [Equations (6.2)-(6.5)], decomposition parameters [Equations (6.9)-(6.10)], and fractal dimension '*D*' (section 6.3.2.1) for whole image of MiniSAR data of Peary crater, *i.e.,* Data-P. These decision criteria have been combined with the criteria for icy craters, proposed by Thompson [Equations (6.13)-(6.16)]. The steps for development of algorithm are discussed as follows:

Step 1: Obtaining regions with μ_c>1: The criterion μ_c>1 has been well-acknowledged to obtain the possible existence of volatile deposits in the form of water-ice. Therefore, regions with μ_c >1 have been obtained for inspecting the feasibility of dielectric mixing due to water-ice deposits on lunar surface. However, it may not confirm the presence of dielectric mixing due to water-ice, since μ_c >1 may also occur due to surface roughness [53, 361]. This scenario has already been depicted in Figure 6.1. Regions, which are having μ_c >1, are shown in the form of red pixels overlaid on g_1 image in Figure 6.7.

Step 2: Obtaining regions with dominant volume scattering: Dominant volume scattering is expected to be obtained either from rough surface (*i.e.*, rock, rough blocky lava flows), or due to dielectric mixing (*i.e.*, water-ice) [48, 361]. The regions with dominant volume scattering may be obtained by using following two methods:

1) Using Relative LH-LV phase δ

It is known that the values of relative LH-LV phase indicator 'δ' are near −90° for surface scattering, near +90° for dihedral scattering, and distributed between −180° and +180° for volume scattering [252]. Therefore, segregation of different scattering mechanisms on the basis of δ is possible.

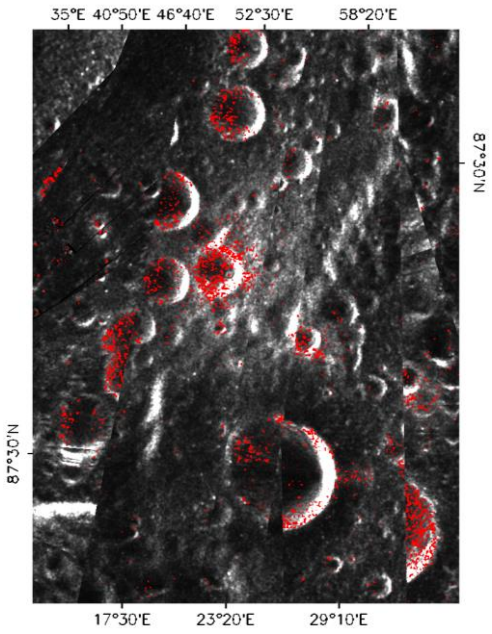

Figure 6.7: The regions with μ_c >1 in form of red pixels overlaid on g_1 image using MiniSAR data of Peary crater (Data-P).

2) Using decomposition approach

The regions with dominant volume scattering will satisfy following condition,

$$f_{volume} > (f_{double-bounce} + f_{surface}), \tag{6.26}$$

In order to satisfy inequality in Equation (6.26), decomposition parameters extracted from *m*-δ and *m*-χ decomposition approaches may be used. Putting Equations (6.9) and (6.10), respectively, in Equations (6.26), we get,

$$\sqrt{\frac{(1-\sin\delta)}{2}} + \sqrt{\frac{(1+\sin\delta)}{2}} < \sqrt{\frac{(1-m)}{m}}, \tag{6.27a}$$

$$\sqrt{\frac{(1-\sin 2\chi)}{2}} + \sqrt{\frac{(1+\sin 2\chi)}{2}} < \sqrt{\frac{(1-m)}{m}}, \tag{6.27b}$$

Equations (6.27a) and (6.27b) satisfy for the value of $m < 0.33$, however, $m < 0.35$ has been taken as threshold value to determine dominant volume scattering mechanism [199]. The regions having distributed δ and $m<0.35$, are shown in the form of red pixels overlaid on g_1 image in Figure 6.8.

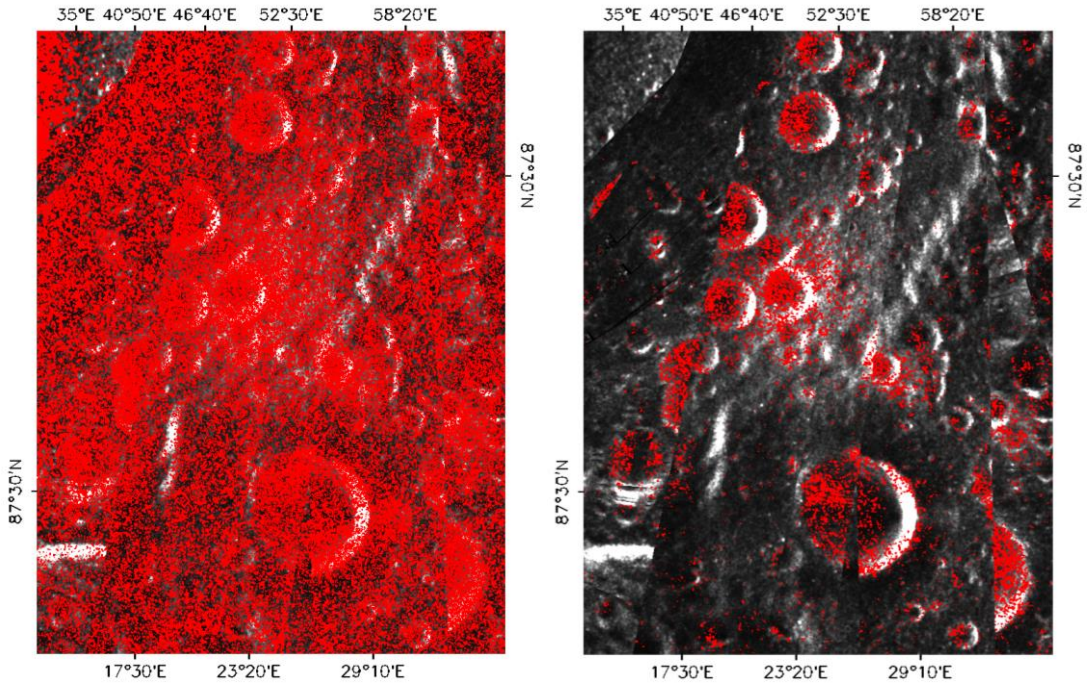

(a) (b)

Figure 6.8: Red pixels exhibiting regions with (a) distributed δ, and (b) m<0.35, on g_1 image using MiniSAR data of Peary crater (Data-P).

Thus, based on the analysis performed in steps 1 and 2, a conclusion can be made that a region on lunar surface may have prospects for presence of water-ice deposits, if pixels of those regions satisfy the conditions μ_c>1, m<0.35, and distributed δ. However, one may not provide the assurance about it because μ_c>1 can still be caused due to surface roughness. The use of fractal concept may help in solving this problem, which might be able to differentiate rough region from region having water-ice deposit by measuring fractal dimension '*D*'.

Step 3: Obtaining roughness information using fractal dimension '*D*': Surface roughness can be measured by calculating fractal dimension '*D*', which has the value between 2.0 to 3.0 for any surface. Typically, '*D*' value increases in correspondence with increment in surface roughness. More specifically, D=2.0 indicates extremely smooth surface, whereas D=3.0 indicates drastically rough surface [199, 200, 249, 290, 292]. Map of local fractal dimension *'D'* has been generated for g_1 image by moving local window over the area of interest (AOI) using Triangular Prism Surface Area Method (TPSAM), as discussed in section 6.3.2.1 [199, 200, 249]. For generation of fractal dimension '*D*' map, g_1 image has been chosen since it contains total backscattered information of imaged region.

Table 6.1 The values of *'D'* for different window size for MiniSAR data of Peary crater (Data-P)

Window	Minimum	Maximum	Mean(Me_D)	Standard deviation(σ_D)
5	1.536	3.356	2.151	0.1163
7	1.536	3.356	2.151	0.1163
9	1.596	3.126	2.173	0.092
11	1.596	3.126	2.173	0.092
13	1.596	3.126	2.173	0.093
15	1.596	3.126	2.173	0.093

Window size plays an important role for representing texture measure using fractal dimension '*D*'. Therefore, effect of window size on '*D*' values has been studied. The initial window size has been taken as 5×5, which has been incremented by step of 2 up to window size 15×15. The statistics (*i.e*., minimum, maximum, mean, and standard deviation) of '*D*' values, obtained for each window size, has been enlisted in Table 6.1, which shows that there is no change in statistics of *D* for window sizes 5×5 and 7×7. At window size 9×9, statistics of *D* change which remain almost same up to window size 15×15. The minimum values of *D* are less than 2.0 and maximum values are greater than 3.0, because natural scenes modelled as fractals are not truly self-similar, but statistically self-similar [290]. Since standard deviation values are small for window size 9×9 and window size 11×11, therefore, window size 9×9 has been selected for retrieving roughness information of lunar surface using MiniSAR data. In order to make '*D*' image compatible to all the images, warping of '*D*' image has been performed, by taking first degree polynomial warp with nearest neighbour re-sampling method using ENVI 4.8.

The '*D'* image for window size 9×9, has been classified by using unsupervised k-means classification algorithm in order to cluster lunar surface into two classes, rough and smooth [249]. The unsupervised classification approach identifies two clusters on the basis of '*D*' values [423]. As discussed above, the regions with lower *D* values correspond to smooth region, whereas those with higher *D* values correspond to rough region. Therefore, for both the classes, corresponding *D* values have been calculated. The spatial statistics (*i.e*., mean and standard deviation) of *D* values, for these two clusters obtained by k-means algorithm, have

been presented in Table 6.2. This table shows that cluster-1 belongs to regions having lower range of *D*, whereas cluster-2 belongs to higher range of *D*. Therefore, cluster-1 and cluster-2 are designated as smooth and rough surfaces, respectively. By observing minimum and maximum *D* values of both the classes in Table 6.2, it can be visualized that distinction between both the classes starts at *D=2.17*, which is also the mean value of whole *'D'* image (*i.e.*, Me_D) measured at window size 9×9, as given in Table 6.1. Thus, the criterion $D < Me_D$ has been taken to segregate smooth class from rough class.

The *D*-map and its classified image for "Data-P" is shown in Figure 6.9, where red regions exhibit smooth surface, and green regions exhibit rough surface. From the classified image in Figure 6.9(b), it has been observed that ROIs 1-8 (except ROI 5) and ROI 11,as exhibited in Figure 6.5(a), have more than 55% area occurring in smooth class, whereas ROIs 5, 9, 10 and 12 have more than 55% area occurring in rough region.

Step-4: Obtaining icy regions with Thompson's criteria: The performance of Thompson's approach for obtaining possible icy regions has been evaluated by applying Thompson's criteria given in Equations (6.13)-(6.16) on MiniSAR data of Peary crater i.e., Data-P. The result of Thompson's approach has been shown in Figure 6.10, in which red pixels overlaid on g_1 image represent regions satisfying Thompson's criteria for possible icy regions, as given in Equations (6.13)-(6.16).

Table 6.2 Spatial statistics of '*D*' values for Data-P using window 9×9 for cluster-1 and cluster-2 obtained by k-means classification

Statistics	Smooth class	Rough class
Minimum	1.596	2.1735
Maximum	2.1734	3.1267
Mean	2.1069	2.2511
Standard deviation	0.0497	0.0681

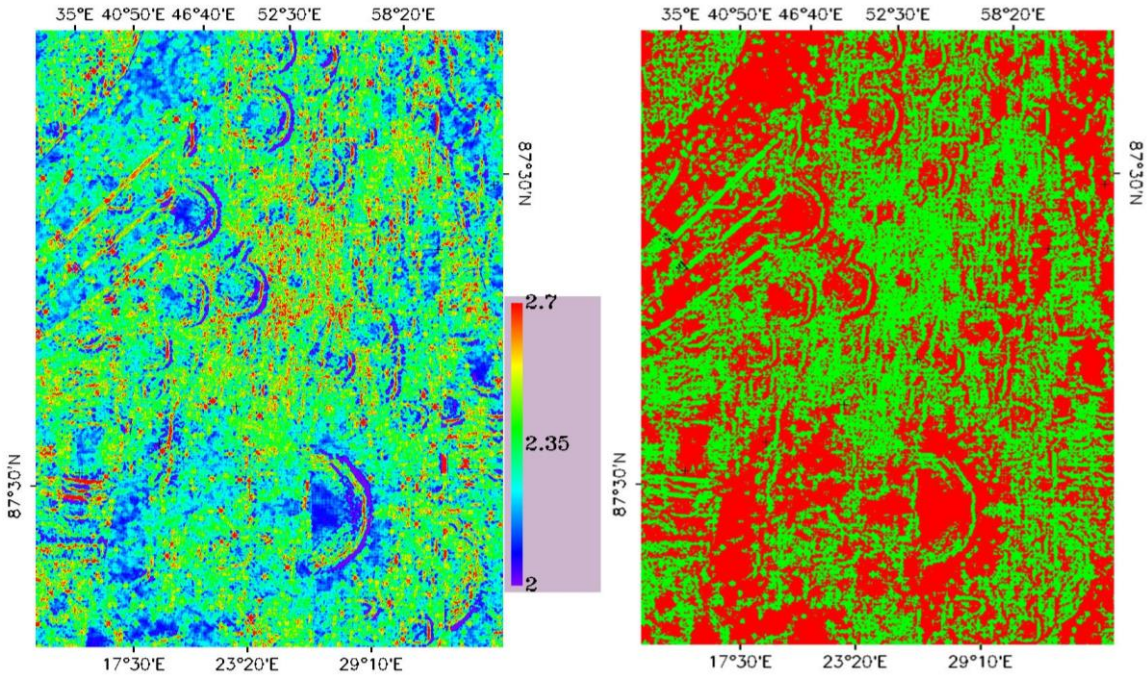

(a) (b)

Figure 6.9: The (a) fractal dimension '*D'* map, (b) its corresponding k-means classified image measured at 9×9 window size. Red and green colours in (b) represent smooth and rough classes, respectively, for MiniSAR data of Peary crater (Data-P).

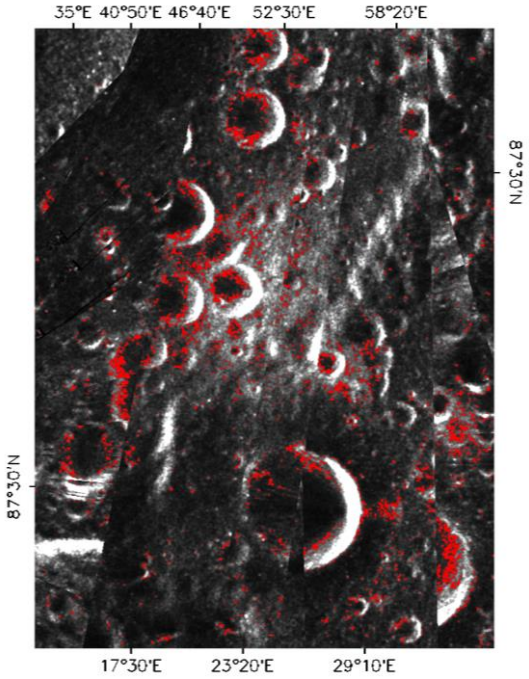

Figure 6.10: Result of Thompson's approach in which red pixels overlaid on g_1 image of Peary crater are regions satisfying Thompson's criteria for icy craters.

Step-5: Fusing all the criteria obtained in above steps for development of decision tree algorithm: The criteria obtained by critical analysis performed in steps 1-4 i.e., μ_c>1, scattering mechanism information by decomposition methods, roughness information by fractal dimension '*D*', and possible icy crater criteria of Thompson, have been taken altogether by developing a decision tree algorithm. This algorithm helps in extraction of volume scattering regions having possibility of dielectric mixing (*i.e.*, water-ice) from region exhibiting volume scattering due to surface roughness. The proposed decision tree algorithm has been shown in Figure 6.11 incorporating these boundary conditions.

In the decision tree algorithm, as shown in Figure 6.11, first, the parameter δ has been chosen for segregation of regions exhibiting surface and double-bounce scattering. The regions with δ in close proximity of −90° and +90° are said to exhibit surface scattering and double-bounce scattering, respectively [252, 308]. Thus, in the proposed decision tree approach, at node-1, the criterion $-100° < \delta < -80°$ has been taken for representing surface scattering, and at node-2, the criterion $80° < \delta < 100°$ has been taken for representing dihedral (double-bounce) scattering. Now, remaining region of lunar surface will exhibit dominant volume scattering. This volume scattering may be caused either due to presence of volatile deposits (*i.e.*, dielectric mixing), or due to surface roughness. Therefore, at node-3 of proposed decision tree, fractal dimension '*D*' has been chosen for segregating rough and smooth surfaces by using criterion $D < (Me_D)$, where Me_D is mean value of whole *D* image, as obtained in step-3 of section 6.4.2. For Data-P, this condition has been obtained as $D < 2.17$. After obtaining smooth region representing volume scattering, Thompson's criteria given in Equations (6.13)-(6.16) have been added along with the conditions $\mu_c > 1$ and $m < 0.35$ (as obtained in step-2 of section 6.4.2).These conditions at node-4 are the prime indicators for determining the presence of dielectric mixing due to water-ice deposits. Pixels satisfying the conditions at node-4 have higher possibility of containing water-ice deposits because in these regions $\mu_c > 1$ is occurring within smooth surface, and thus, volume scattering may be occurring due to dielectric mixing (*i.e.*, water-ice) only.

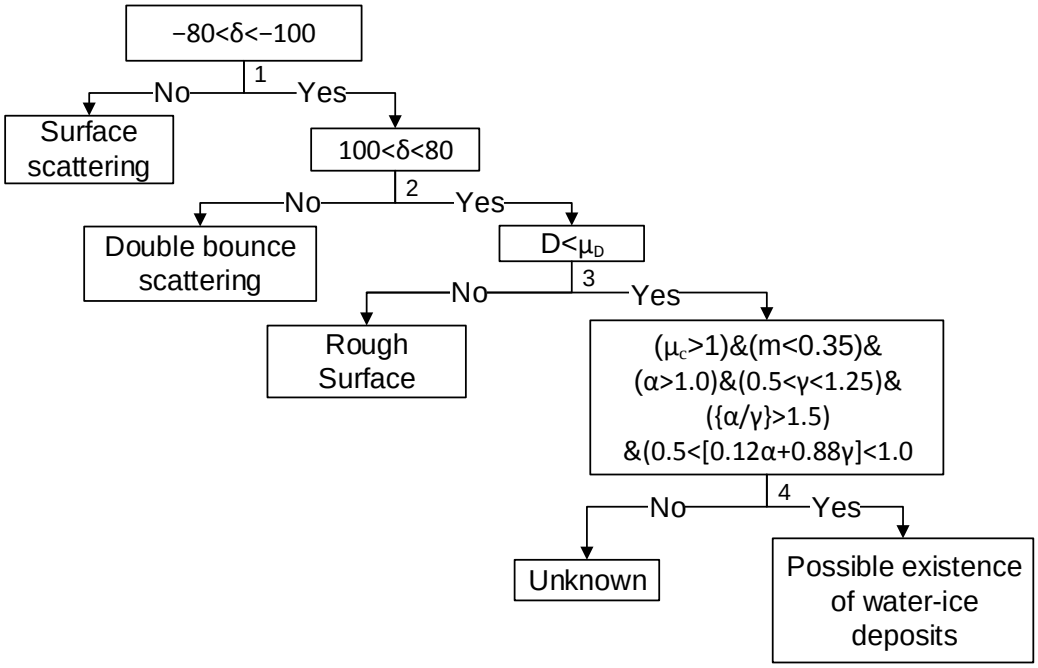

Figure 6.11: Decision tree for possible water-ice detection.

6.4.3. Determination of Electrical and Physical Properties of Lunar Surface

The electrical and physical properties of lunar surface have been evaluated by calculating real part of dielectric constant (ε'), regolith bulk density (ρ_0), loss tangent ($tan\ \delta$), and imaginary part of dielectric constant (ε'') by using Equations (6.21)-(6.24), respectively.

6.5. Results and Discussion

The proposed algorithm has been implemented on MiniSAR data of Peary crater i.e., Data-P. The results of this data are presented below:

6.5.1. Analysis of Child Parameters and Fractal Dimension *'D'*

In section 6.4.2 (step-3), window size 9×9 has been selected for obtaining the value of fractal dimension '*D*'. Therefore, all the child parameter i.e., degree of polarization '*m*', circular polarization ratio 'μ_c', relative LH-LV phase 'δ', and ellipticity angle 'χ', as obtained by Equations (6.2)-(6.5), have been estimated for window size 9×9 in order to make them compatible with fractal dimension '*D*'. The evaluation of all the child parameters, *i.e.*, μ_c, *m*, δ, χ, and *D*, measured at window size 9×9, has been performed for all 12 ROIs selected on the

floor of Peary crater (Data-P) in Figure 6.5(a). The statistical representation exhibiting maximum, minimum, mean, and standard deviation, of these parameters (μ_c, m, δ, χ, and D) have been presented in Figure 6.12 for all 12 ROIs selected in Figure 6.5(a).

The analyses for each of the parameter i.e., μ_c, m, δ, χ and D, for studying the decision tree as given in Figure 6.11, are as follows:

- Figure 6.12 (a) shows that maximum value of μ_c is greater than 2.0 for all the ROIs except ROIs 4, 9,10,11, and 12. ROI 9, which is the region outside anomalous crater, has maximum value of μ_c as 0.9. Thus, possibility of having water-ice is negligible in this region. However, in remaining ROIs (*i.e.*, ROIs 1-12 except ROI 9), there may be possibility of water-ice deposits because maximum value of μ_c is greater than 1 (criterion obtained in step-1 of section 6.4.2).
- The degree of polarization m is found to have mean values around 0.4 with standard deviation of around 0.1 for all the ROIs except ROIs 9-12, for which average m value varies between 0.5 to 0.7, as shown in Figure 6.12 (b). Thus, the criterion for dominant volume scattering i.e., $m<0.35$ as obtained in step-2 of section 6.4.2, is completely fulfilled by ROIs 1-8.
- The statistics of relative LH-LV phase δ have been presented in Figure 6.12(c), which indicates that δ is distributed between −180° (approx.) to +180° (approx.) for all the ROIs except ROI 9. For ROIs 1 to 8, average δ value ranges from −27° to −68°, and for ROI 9, it is obtained as −90°. The average δ value at ROI 9, represents the presence of surface scattering, whereas those of ROIs 1 to 8 represent the occurrence of volume scattering, as discussed in step-2 of section 6.4.2. Therefore, based on characteristics of δ value, the possibility of water-ice deposits in these ROIs (1 to 8) will be high. ROIs 10-12 have average δ value between −81° to −88°, which is close to −90°. Thus, these regions will have dominant surface scattering, and hence, have minimum possibility of water-ice.
- In Figure 6.12 (d), the statistical representation of ellipticity angle χ for all the ROIs has been shown. It shows that χ varies from −45° (approx.) to +45° (approx.) for ROIs 1 to 8, from −45° to −5° for ROI 9, from −45° to 13° for ROIs 10 and 12, and from −45° to 28° for ROI 11.
- The statistics of fractal dimension D measured at 9×9 window have been presented in Figure 6.12(e) for all the ROIs. This figure shows that mean value of D is less than 2.17

for all the ROIs except ROIs 5, 9, 10, and 12, for which mean value of *D* is found to be 2.2 (approximately). Based on the criterion $D < 2.17$ for segregating smooth regions, as obtained in step-3 of section 6.4.2, it is visualized from Figure 6.12(e) that all the ROIs have minimum value less than 2.17.

Therefore, in regions satisfying criterion $D < 2.17$, smoothness is relatively higher. If in these regions (with $D < 2.17$), all conditions obtained in section 6.4.2 i.e., $\mu_c > 1$, $m < 0.35$, and δ distributed are satisfied, the possibility for presence of water-ice deposits might be high.

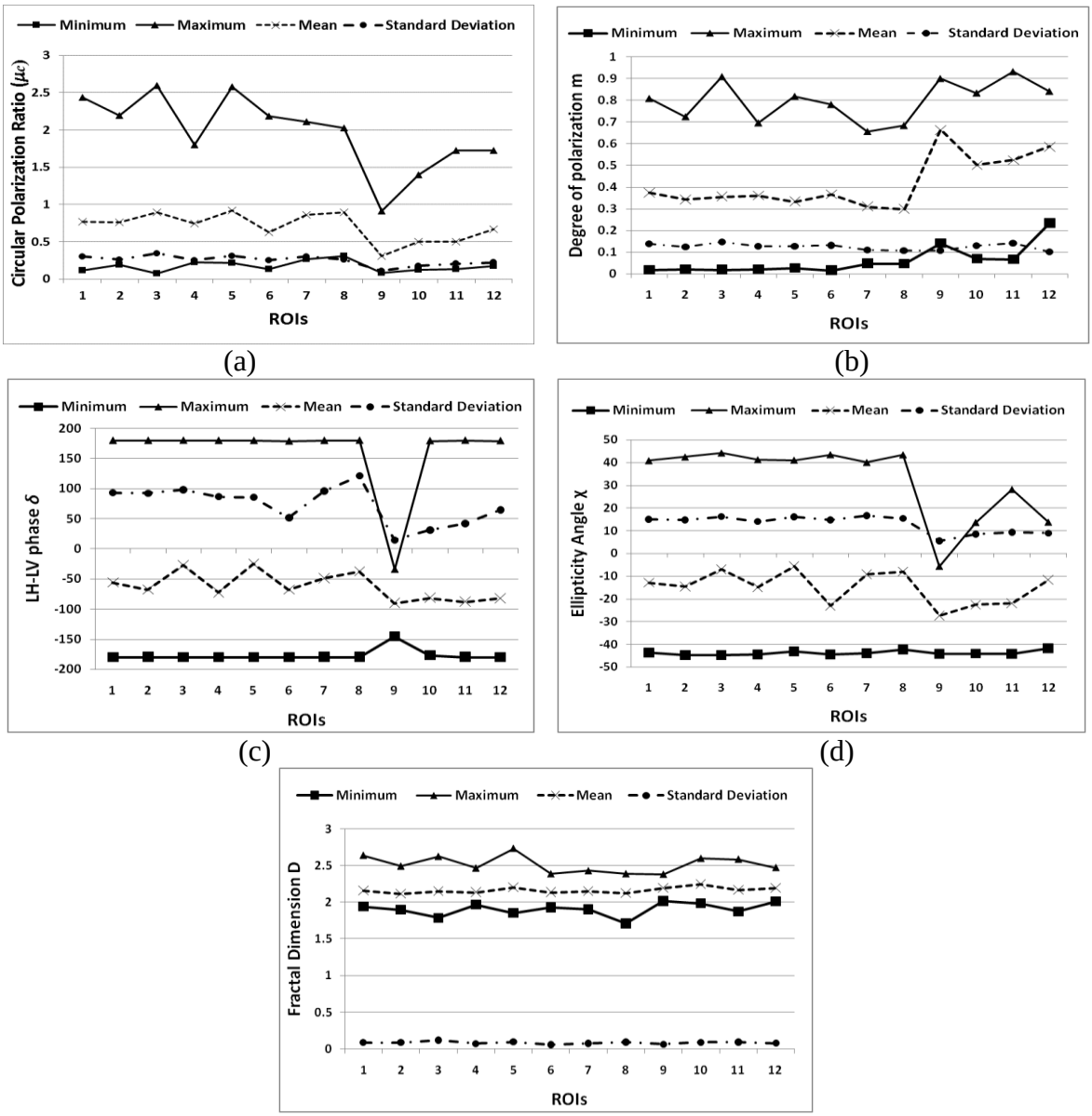

Figure 6.12: Statistics of (a) μ_c , (b) *m*, (c) δ, (d) χ, and (e) *D*, for window size 9×9, for all 12 ROIs selected in Figure 6.5 (a).

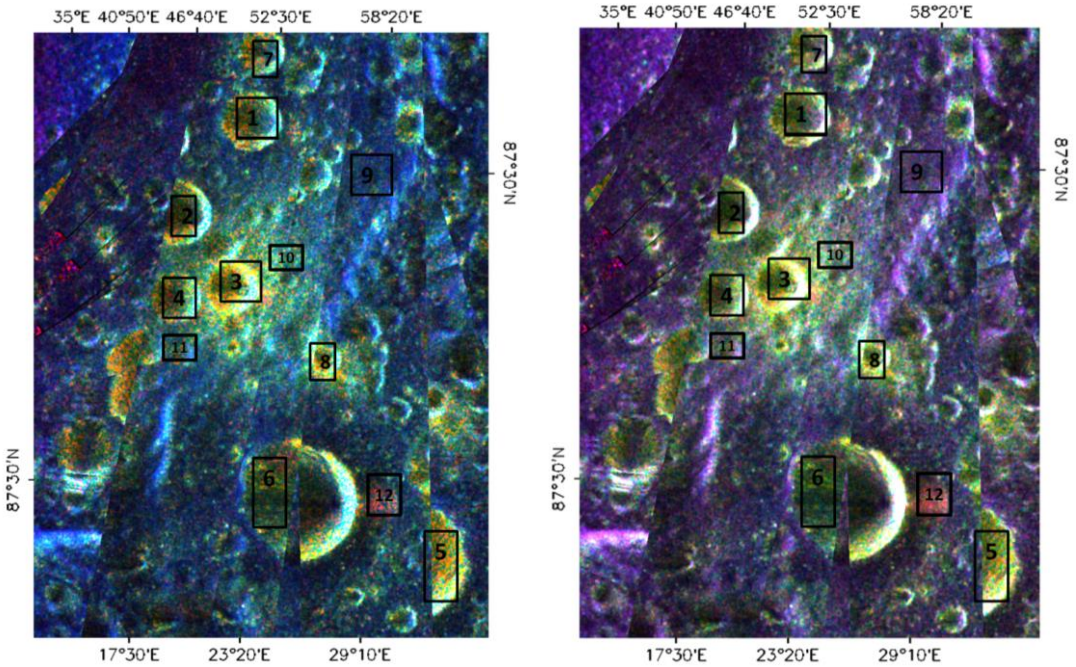

(a) (b)

Figure 6.13: RGB composite image of (a) *m*- δ, and (b) *m*-χ decompositions, with single bounce, double-bounce and volume scattering, as red, green, and blue colours respectively, for MiniSAR data of Peary crater (Data-P).

6.5.2. Analysis of Decomposition Methods

This section evaluates the performance of *m*-δ and *m*-χ decomposition methods (as discussed in section 6.3.1.2), which provides the information about the scattering behaviour of lunar surface. The visual representation of these two decomposition methods has been provided in Figure 6.13. This figure shows RGB colour composite images of *m*-δ and *m*-χ decomposition methods by taking respective f_{double}, f_{volume}, and $f_{surface}$ components, as red, green, and blue colours, respectively.

Figure 6.13 shows that ROIs 1-8 show dominance of volume scattering by both the decomposition methods. ROI 9 shows surface scattering (blue colour) and combination of surface and double-bounce scattering mechanisms, by *m*-δ [Figure 6.13 (a)] and *m*-χ [Figure 6.13(b)] decomposition methods, respectively. ROI 10 exhibits both surface and volume scattering by *m*-δ decomposition [Figure 6.13(a)]. However, by *m*-χ decomposition [Figure 6.13 (b)], some portion of ROI 10 exhibits volume scattering while other shows mixed surface and double-bounce scattering. ROI 11 shows dominance of surface scattering by *m*-δ

decomposition, and mixed surface and double-bounce scattering by *m-χ* decomposition. Major part of ROI 12 shows the dominance of double-bounce scattering. Surface scattering is also present in this ROI. Thus, based on the analysis of decomposition methods, it is possible to find water-ice deposits in ROIs 1-8 due to dominance of volume scattering in these regions.

Table 6.3 Mean value of decomposition terms over selected ROIs on Data-P (Peary crater)

ROI	***Methods***	f_{double}	f_{volume}	$f_{surface}$
1	*m-δ*	0.0671	0.2238	0.1496
	m-χ	0.0906	0.2238	0.1449
2	*m-δ*	0.0606	0.2045	0.1234
	m-χ	0.0741	0.2045	0.1219
3	*m-δ*	0.1454	0.4134	0.2799
	m-χ	0.1869	0.4134	0.2764
4	*m-δ*	0.0581	0.2176	0.1426
	m-χ	0.0794	0.2176	0.1372
5	*m-δ*	0.1192	0.3252	0.1768
	m-χ	0.1422	0.3252	0.1768
6	*m-δ*	0.0335	0.1597	0.1085
	m-χ	0.0424	0.1597	0.1067
7	*m-δ*	0.0595	0.1911	0.0988
	m-χ	0.0711	0.1911	0.0985
8	*m-δ*	0.0908	0.2571	0.1279
	m-χ	0.0992	0.2571	0.1303
9	*m-δ*	0.0201	0.1462	0.2081
	m-χ	0.0632	0.1462	0.1991
10	*m-δ*	0.0451	0.2663	0.2621
	m-χ	0.0999	0.2663	0.2473
11	*m-δ*	0.0407	0.2259	0.2422
	m-χ	0.0932	0.2259	0.2283
12	*m-δ*	0.0673	0.1792	0.1951
	m-χ	0.1180	0.1792	0.1771

Further, for more specific discussion, the quantitative analysis has been performed for both the decomposition methods by observing the contribution of each decomposition term, *i.e.*, f_{double}, f_{volume}, and $f_{surface}$ [obtained in Equations (6.9) and (6.10)], for all 12 ROIs selected in Figure 6.5 (a). The results are presented in Table 6.3. It indicates that volume scattering term is invariant for both the decomposition methods, as also evident from Equations (6.9c) and (6.10c). For ROIs 1 to 8 and 10, the contribution of volume scattering is more as compared to single and double-bounce scattering, for both the decomposition methods. In ROIs 9 and 11, surface scattering is more as compared to volume and double-bounce scattering. This result for ROI 9 and 11 is acceptable because ejecta or region outside anomalous crater is expected to give more single-bounce (or surface) scattering. In ROI 12, the contribution of volume scattering is more as compared to single and double-bounce scattering for m-χ decomposition, whereas the contribution of surface scattering is more as compared to volume and double-bounce scattering, for m-δ decomposition. This quantitative analysis also suggests the presence of water-ice deposits in ROIs 1 to 8 because of more volume scattering as compared to surface and double-bounce scattering, in these regions.

6.5.3. Analysis of Proposed Decision Tree Algorithm (Figure 6.11)

This section presents the analysis of all the conditions for obtaining possible locations of water-ice deposits, as presented in proposed decision tree algorithm (Figure 6.11). Since all the criteria, as obtained in section-6.4.2, have been incorporated in proposed algorithm, possible locations having dielectric-mixing due to presence of water-ice deposits, may possibly be identified. For this purpose, the percentage of pixels satisfying these criteria (as obtained in steps 1-4 of section 6.4.2), which are $\mu_c > 1$, $m < 0.35$, δ distributed, $D < 2.17$, and Thompson's criteria, have been calculated, and analysed for all the ROIs selected in Figure 6.5(a). The result of proposed algorithm and all the criterions obtained in step 1-4 of section-6.4.2 have been summarized in Table 6.4. Table 6.4 shows that ROIs 1-8 have significant percentage of pixels satisfying criterion $\mu_c > 1$. For these ROIs, more than 45% pixels satisfy criterion $m < 0.35$, which indicates the occurrence of volume scattering mechanism. All the ROIs from 1-8, except ROI 5, have more than 65% pixels satisfying criterion $D < 2.17$, the necessary condition for representing smooth region. The relative LH-LV phase δ has been found to be distributed in ROIs 1-8, as also evident from Figure 6.12(c). ROI 9 has no pixel satisfying criteria $\mu_c > 1$. Thus, for this ROI, there is no possibility of having dielectric-mixing due to water-ice.

Table 6.4 Analysis based on criteria obtained in section 6.4.2 and proposed decision tree (Figure 6.11)

ROI	Pixel % : $\mu_c > 1$	Pixel %: m<0.35	Pixel % :D<2.17	δ	Pixel %: Thompson's Approach	Pixel % proposed algorithm	Possibility of dielectric mixing due to water ice
1	19%	45%	67%	Distributed	17.40%	0.93%	Yes
2	16%	54%	79%	Distributed	11.96%	0.74%	Yes
3	33%	50%	65%	Distributed	12.71%	2.9%	Yes
4	14%	47%	75%	Distributed	13.93%	0.61%	Yes
5	32%	57%	39%	Distributed	26.24%	2.02%	Yes
6	8%	46%	78%	Distributed	4.08%	0.18%	Yes
7	27%	63%	69%	Distributed	14.31%	0.21%	Yes
8	30%	70%	73%	Distributed	30.74%	4.35%	Yes
9	0%	2%	30%	Non Distributed	0.71%	0%	No
10	1%	12%	22%	Distributed	8.5%	0.14%	Negligible
11	3%	12%	57%	Distributed	12.27%	0.15%	Negligible
12	7%	1%	49%	Distributed	24.38%	0%	Negligible

The percentage of pixels satisfying Thompson's criteria (>4%) is quite good for all the ROIs except ROI 9. For ROI 9, very less percentage of pixels satisfy Thompson's criteria. Appreciable pixels (>8%) satisfy Thompson criteria for ROIs 10, 11, and 12, which are regions outside anomalous craters. In these regions, very less pixels (< 7%) satisfy criteria $\mu_c > 1$, which is favourable condition for dielectric-mixing. Based on *m-δ* and *m-χ* decomposition method (Table 6.3), it has been observed that ROI 11 exhibits dominant surface scattering, which is not the favourable condition for dielectric-mixing. However, Thompson's approach shows that 12.27% pixels in ROI 11 represent possibility of water-ice. On the other hand, proposed approach (Figure 6.11) shows that only 0.15% pixels, which is almost negligible, have

possibility of dielectric mixing in ROI 11. According to illumination study carried out in [47, 237, 267, 359], the regions outside anomalous craters may be illuminated by sun. Thus, the probability for existence of water-ice deposits may be less in these regions (ROIs 9-12). Unlike Thompson's approach, proposed decision tree method (Figure 6.11) has identified that these regions (ROIs 9-12) have very less possibility of water-ice deposits. Thus, the result of proposed decision tree algorithm (Figure 6.11) in Table 6.4, indicates there is more possibility of water-ice deposits to be present in ROIs 1-8 as compared to ROIs 9-12. The visual representation for the result of proposed decision tree (Figure 6.11), is expressed in Figure 6.14, which exhibits red pixels overlaid on g_1 image. These red pixels indicate regions having possibility of water-ice deposits.

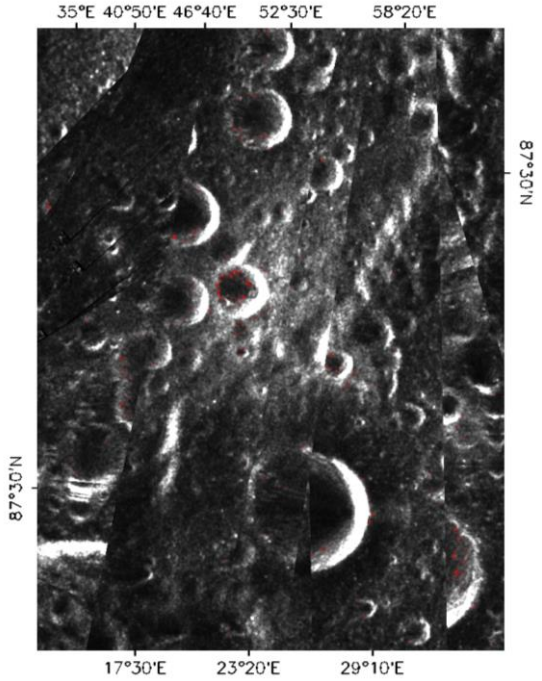

Figure 6.14: Result of decision tree (Figure 6.11) exhibiting regions having possibility of water-ice deposits in the form of red pixels overlaid on g_1 image using MiniSAR data of Peary crater.

6.5.4. Estimation of Electrical and Physical Properties

The maps of electrical and physical parameter i.e., real part of dielectric constant i.e., ε' (Equation 6.21), imaginary part of dielectric constant i.e., ε'' (Equation 6.24), loss tangent i.e., $tan\ \delta$ (Equation 6.23), and regolith bulk density i.e., ρ_0 (Equation 6.22), are presented in Figure 6.15. These values are estimated for possible icy regions (Figure 6.14) obtained by proposed approach (Figure 6.11). The mean value of ε' for possible icy regions has been obtained as 3.01. The mean values of ε'', $tan\ \delta$, and ρ_0 for possible icy regions have been obtained as 0.034, 0.008, and 1.97 g/cm^3.

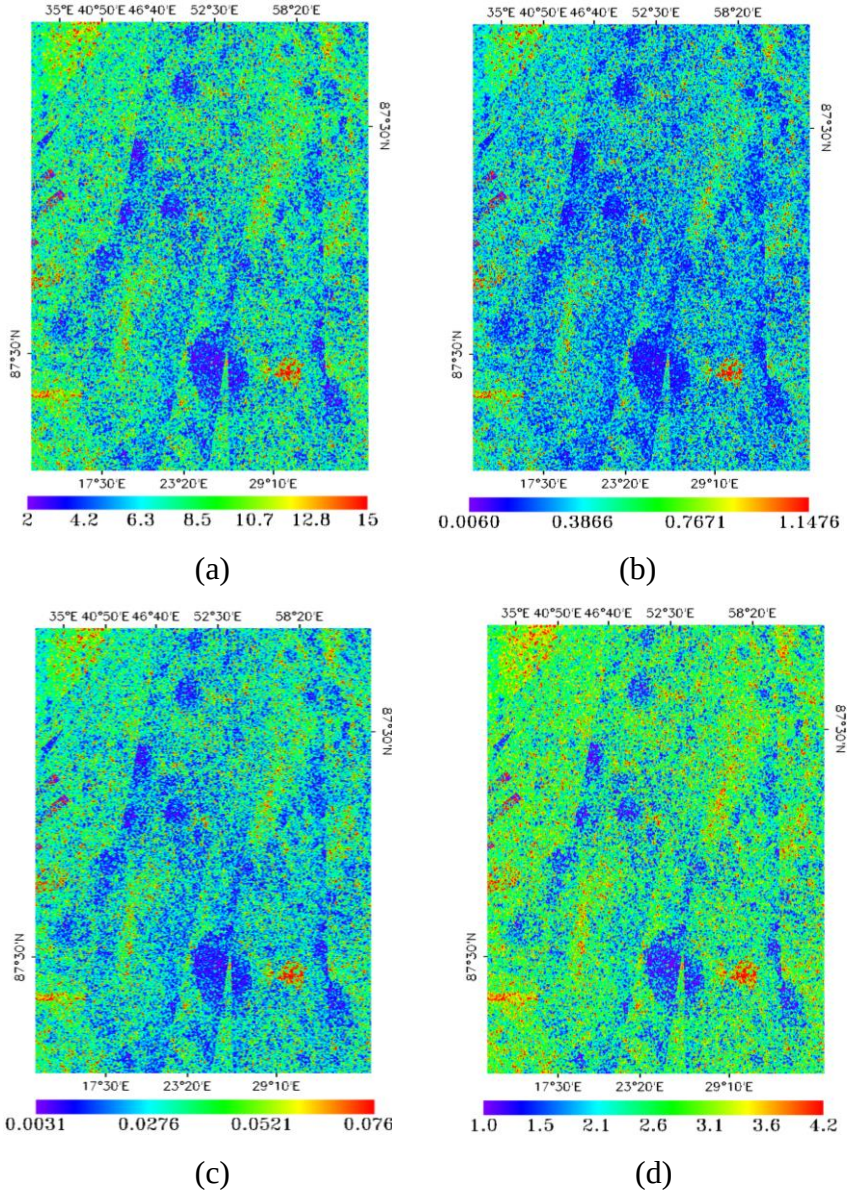

Figure 6.15: Visual representation of (a) real part of dielectric constant (ε'), (b) imaginary part of dielectric constant (ε''), (c) loss tangent ($tan\ \delta$), and (d) Regolith bulk density (ρ_0).

6.5.5. Application of Proposed Algorithm on another MiniSAR Data

The proposed algorithm has also been applied on MiniSAR data of Rozhdestvenskiy crater (Data-R), as described in section 6.2. After pre-processing, as described in section 6.4.1 and Figure 6.3, Stokes vector (g_1, g_2, g_3, and g_4) and child parameters (μ_c, m,δ, *and* χ) have been generated for window size 9×9, as discussed in section 6.4.2 (step-3). The '*D*' image has been generated by using local window size 9×9 through TPSAM method, as discussed in section 6.3.2.1, and then classified into two classes: rough and smooth by k-means algorithm. For "Data-R", the mean value of '*D*' i.e., Me_D has been obtained as 2.15.

The g_1 image of Data-R has been shown in Figure 6.16, in which 8 ROIs on the floor of Rozhdestvenskiy crater have been selected for the analysis. ROIs 1 and 2 are anomalous craters, whereas ROIs 3-8 are regions outside the anomalous craters on the floor of Rozhdestvenskiy crater.

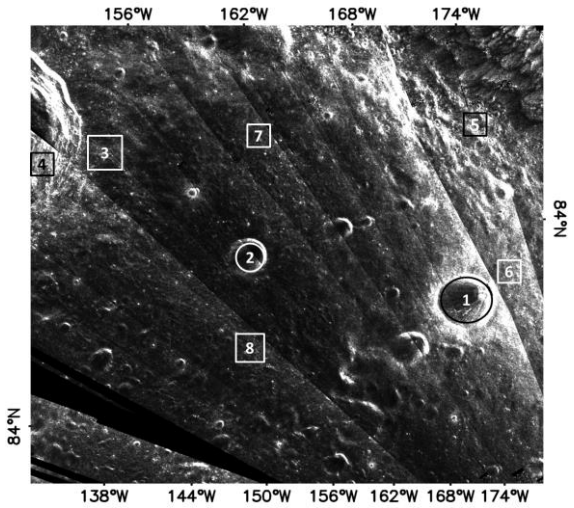

Figure 6.16: The g_1 image representing selected ROIs on the floor of Rozhdestvenskiy crater.

The result of Thompson's approach as given in Equations (6.13)-(6.16), and decision tree as shown in Figure 6.11, have been presented in Table 6.5. Comparing the results of these two methods in Table 6.5, it is observed that ROIs 1 and 2 have appreciable percentage of pixels satisfying criteria for possible presence of water-ice deposits. Table 6.5 shows that ROIs 3-6 show good percentage of pixels (>8%) exhibiting icy regions by Thompson's approach. However, the result of proposed approach (Figure 6.11) show very less percentage of pixels (<2%) satisfying the criteria for possible presence of water-ice. ROIs 7 and 8 show almost

negligible percentage of pixels (<0.3%) fulfilling the criteria of possible icy regions by both the methods. Thus, ROIs 1 and 2 show evidences of water-ice by proposed approach (Figure 6.11), whereas potential of having volatile deposits is negligible for ROIs 3-8, as depicted in Table 6.5. In this section, the visual representation for the ROIs having possibility of water-ice i.e., ROIs 1 and 2 has been provided. Figure 6.17, represent possible locations of water-ice deposits in ROI-1 and ROI-2, respectively, for method presented in Figures 6.11. In these figures, red pixels overlaid on g_1 image are the results of proposed algorithm (Figure 6.11).

Table 6.5 Results of Thompson's approach [Equations (6.13)-(6.16)], and proposed decision tree approach (Figure 6.11), for MiniSAR data of Rozhdestvenskiy crater (Data-R)

ROI	Pixel % : Thompson's approach	Pixel % : Modified decision tree in Figure 6.11	Pixel % : Possibility of dielectric mixing due to water ice
1	23.76%	1.65%	Yes
2	7.05%	1.07%	Yes
3	8.1%	0.03%	Negligible
4	8.64%	0.06%	Negligible
5	22.46%	0.64%	Negligible
6	15.61%	0.21%	Negligible
7	0.27%	0%	No
8	0.13%	0.003%	Negligible

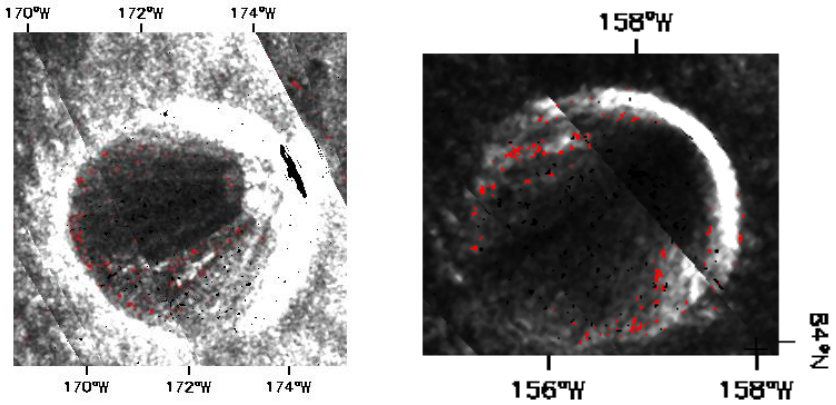

(a) (b)

Figure 6.17: Red pixels exhibiting possible locations for water-ice deposits on g_1 image for (a) ROI-1, and (b) ROI-2, using proposed algorithm (Figure 6.11).

Further, the electrical and physical parameter i.e., real part of dielectric constant i.e., ε' (Equation 6.21), imaginary part of dielectric constant i.e., ε'' (Equation 6.24), loss tangent i.e., $tan\ \delta$ (Equation 6.23), and regolith bulk density i.e., ρ_0 (Equation 6.22), have been computed for icy regions obtained by proposed approach. The mean value of ε', ε'', $tan\ \delta$ and ρ_0 for icy regions are obtained as 2.9, 0.038, 0.006, and 0.98 g/cm^3, respectively.

6.6. Conclusion

In this chapter, a decision tree method has been proposed, which has attempted to resolve the ambiguity caused by $\mu_c > 1$ assumption. The criterion $\mu_c > 1$ creates ambiguity in a sense that it not only provides indication of possible presence of water-ice deposits but also indicates the presence of surface roughness. Therefore, the principle of fractals has been utilized, for obtaining roughness information through a parameter called fractal dimension *D*. It is expected that dielectric mixing due to water-ice deposits exhibits volume scattering. Therefore, in this chapter, scattering information has been retrieved by using m-δ and m-χ decomposition approaches. The exhaustive study has been carried out by analysing μ_c, m-δ, and m-χ decomposition approaches, and fractal dimension *D*, in order to obtain criteria for possible water-ice detection. The proposed decision tree approach utilizes the criteria for possible icy regions suggested by Thompson et al. along with criteria based on μ_c, m-δ and m-χ decomposition approaches, and fractal dimension *D*. This decision tree provides segregation of regions representing volume scattering resulted from volatile deposits rather than surface roughness. By visualizing the results of proposed approach, it can be concluded that the proposed approach has the capability to minimize the ambiguity created due to characterization by using μ_c alone. After retrieving regions having possible existence of water-ice deposits on lunar surface, the electrical and physical characteristics such as real part of dielectric constant (ε'), imaginary part of dielectric constant (ε''), loss tangent ($tan\ \delta$), and regolith bulk density (ρ_0), are estimated for possible icy regions.

Chapter 7

Conclusions and Future Scope

The objective of this thesis is to project shortcomings and provide solutions for classification and retrieval of surface parameters of Earth and Moon by polarimetric SAR data. The polarimetric properties of SAR data are utilized in well-defined manner by extracting polarimetric parameters. Polarimetric parameters have great potential for describing scattering behaviour, electrical properties, and physical properties such as shape, orientation, size, symmetry, non-symmetry, or irregularity of targets. Therefore, in this thesis, emphasis is given to utilize polarimetric parameters to characterize and retrieve surface parameters of Earth and lunar surface by using minimum or no '*a priori*' information. This chapter concludes the contributions made in the thesis followed by recommendations for further scope of research.

7.1. Contributions of the Thesis

The thesis is divided into two parts-first part is related to critical analysis of fully polarimetric SAR data (ALOS PALSAR and/or Radarsat-2) for characterization and surface parameter retrieval of Earth's surface. In this part, three tasks have been performed: analysis of model based decomposition and deorientation; identification and classification of different land covers by adaptive approach; and retrieval of soil moisture under vegetation cover by transmission line theory based model. The second part of thesis deals with the characterization of lunar surface using hybrid polarimetric SAR data (MiniSAR). The tasks carried out in this part are, analysis of scattering behaviour of lunar surface by critical observation of polarimetric parameters and decomposition parameters based on hybrid polarimetry; development of algorithm for possible water-ice detection; and estimation of electrical and physical parameters of lunar surface.

Chapter three, contributes in the field of model based target decomposition theorems, and provides an elaborated analysis of scattering mechanisms (surface 'P_s', double-bounce 'P_d', volume 'P_v' and/or helix 'P_c' scattering) obtained from different land covers after applying deorientation. Analysed methods without deorientation are three component decomposition (TCM) [138] and four component decomposition method (FCM) [425]. Analysed methods with

single deorientation (orthogonal rotation) are three component decomposition method with deorientation (TCMD) [210], four component decomposition method with deorientation (FCMD) [427], and four component decomposition with deorientation and additional volume scattering model (FCMDA) [325]. Two methods with double deorientation (orthogonal rotation and unitary transformation) are analysed, which are three component decomposition method with double deorientation and adaptive volume scattering (TCMDDA) [90] and four component decomposition method with double deorientation (FCMDD) [344]. Key issues addressed in this chapter are as follows:

- Visual analysis of decomposition methods is quite helpful in observing scattering response of different land covers. Certain land covers such as urban exhibit improvement in scattering response after deorientation. It has been observed that after deorientation, volume scattering considerably reduces in urban area. Change in scattering response is observed after deorientation. However, the decomposition results of all the methods with deorientation appear almost same.
- Pixel wise quantitative analysis of scattering terms indicates that pixel percentages for P_d and P_s increase after deorientation. Number of pixels representing P_v remain almost same for all the decomposition methods with or without deorientation. Number of pixels having all scattering mechanisms in common also increase in decomposition methods with deorientation.
- Power wise quantitative analysis of scattering terms indicates that power of P_v reduces after deorientation. The increment in powers of P_d and P_s has been observed after deorientation. This analysis shows that characterization of urban and vegetation (short and tall) is difficult because of different scattering responses obtained by each decomposition methods. Bare soil exhibit strong surface scattering power by all the decomposition methods.

Chapter four, presents an adaptive decision tree based land cover classification approach, in which decision criterion are formed by utilizing spatial statistics (median and standard deviation) based adaptive threshold of polarimetric indices. The algorithm is based on obtaining optimum threshold of polarimetric indices based on overall accuracy provided by end user using genetic algorithm (GA). The contributions made in this chapter are as follows:

- The chapter provides an exhaustive analysis of sixteen polarimetric indices (σ^0_{rr}, σ^0_{rl},

σ^0_{ll}, σ^0_{hv}, σ^0_{hh}, σ^0_{vv}, σ^0_{45C}, σ^0_{45X}, σ^0_{rr}/ σ^0_{rl}, $\sigma^0_{hv}/\sigma^0_{vv}$, $\sigma^0_{hv}/\sigma^0_{hh}$, $\sigma^0_{hh}/\sigma^0_{vv}$, *WPS, RVI, NDPI,* and *CPR*). The role of these polarimetric indices has been observed and analysed in characterization and segregation of different land covers.

- The chapter presents a systematic way to obtain polarimetric indices providing best separation between two different classes by using the concept of separability index.
- The algorithm has been tested and validated on two different ALOS PALSAR data of Roorkee. After optimization of algorithm for classification accuracy between 80% and 100% by GA, classification maps for both data sets have been generated. The estimation of confusion matrix based on ROIs collected during ground survey shows overall accuracy and kappa coefficient for first data as 87.59% and 0.85, respectively, and for second data as 78.43% and 0.72, respectively.
- The algorithm does not use fixed threshold and is adaptive in nature by making use of spatial statistics (median and standard deviation) of polarimetric indices. Based on end user requirement of overall classification accuracy, the algorithm adapts itself to tune threshold of polarimetric indices used in classification algorithm.
- The proposed adaptive classification algorithm works well for similar sites and satellite sensors without any further need of tuning the threshold of polarimetric indices.

Chapter five, addresses the problem of retrieving soil moisture under vegetation cover. This problem has been solved by developing multilayer model for bare soil (two layers of soil) and vegetated regions (two layers of soil and one layer for vegetation-air mixture) on the basis of conventional transmission line theory, which allows the estimation of impedance or backscattering coefficient in terms of complex dielectric constants of considered media at constant thickness (depth in case of soil and height in case of vegetation). The thickness of first layer of soil has been taken as 5 cm, and second layer as infinite. The thickness of vegetation-air mixed layer has been considered to be varied from 5 cm to 400 cm, assuming most of the agricultural vegetation covered in this range. The value of dielectric constant of each layer have been retrieved by GA and soil moisture for first layer of soil has been estimated by relationship given by Topp et al. [373]. Following inferences have been drawn in this chapter:

- The proposed soil moisture algorithm works well for both bare soil and vegetated regions. The main highlight of this algorithm is its ability to estimate soil moisture for

vegetation having height up to 400 cm.

- The soil moisture values retrieved by proposed approach shows good agreement with the observed value of soil moisture for both frequency bands L and C, by suing ALOS PALSAR data and Radarsat-2 data, respectively.
- The advantage of this method lies in its simplicity and dependence on physical concept of transmission line theory.
- The proposed soil moisture retrieval algorithm requires minimum amount of '*a priori*' knowledge about test site.

*Chapter six***,** represents second part of the thesis in which an algorithm for possible detection of water-ice on lunar surface has been developed. The study has been performed on hybrid polarimetric MiniSAR data of Peary and Rozhdestvenskiy craters on North Polar Region of Moon. The key issue addressed in this chapter is the ambiguity resulted by $\mu_c > 1$ criterion, which represents scattering from both possible icy regions and rough regions. The water-ice deposits on lunar surface are expected to produce volume scattering. Therefore, the main objective of this chapter is to obtain volume scattering in smooth regions having $\mu_c > 1$ criterion. Further, the electrical and physical parameters i.e., real part of dielectric constant (ε'), imaginary part of dielectric constant (ε''), loss tangent ($tan\ \delta$), and regolith bulk density (ρ_0) have been computed. The contributions made in this chapter are as follows:

- In this chapter, confusion caused by $\mu_c > 1$ criterion, has been resolved by using fractal dimension '*D*', which exhibits one-to-one relationship with surface roughness.
- Based on fractal dimension '*D*', the criterion for obtaining smooth regions has been estimated as $D < Me_D$, where Me_D represents mean value of *D*.
- The chapter uses polarimetric approaches (m-δ and m-χ decomposition methods) for obtaining scattering response. The criterion for dominant volume scattering (as expected from water-ice) has been estimated as $m < 0.35$.
- Based on δ value, criteria for surface and double-bounce scattering mechanisms have been selected as $-100 < \delta < -80$ and $80 < \delta < 100$, respectively. The volume scattering is exhibited by remaining region on lunar surface.
- The decision tree formed by combining all the above mentioned criteria and Thompson's criteria [371] for possible icy craters, show possibility of having water-ice on some of the anomalous craters on the floor of Peary and Rozhdestvenskiy craters.

In a nutshell, the contributions of proposed research work are as follows:

- First contribution of the thesis is to provide both pixel wise and power wise elaborated analyses of model based decomposition methods and deorientation effect for various land covers.
- Second contribution of the present research work is to provide a new way to use polarimetric parameters for characterization land covers using adaptive and scene-independent classification algorithm.
- Third contribution is the use of classical concept of transmission line theory for retrieval of soil moisture in both vegetated and bare soil areas requiring minimum *'a priori'* information about sites. The algorithm works well for both L- and C- frequency bands.
- Fourth major contribution is the development of algorithm for determining possible presence of water-ice deposits on lunar surface. This algorithm resolves the ambiguity caused due to same scattering response presented by both rough and icy regions through high value of circular polarization ratio, by using the concept of fractal dimension, a concept used for representing roughness.

Thus, present research work covers variant applications of SAR polarimetry with emphasis on requiring negligible prior information about study area.

7.2. Future Scope

Present thesis work has the scope and possibilities to extend it further. A few major ones are listed as follows:

- The present research work provides the solution of adaptive classification of various land covers using L-band ALOS PALSAR data. The design strategies of proposed classification algorithm can be utilized for application based on different SAR sensors operating at different frequency.
- Currently available Indian satellite RISAT-1 provides huge scope in extending proposed classification algorithm for C-band because of providing amplitude, phase, and polarization state of backscattered wave in both linear and hybrid polarimetric mode. Therefore, beneficial features of some more polarimetric parameters can be exploited

for characterization of various land covers.

- Differentiation of scattering response obtained from urban and tall vegetation (trees) is still an open challenge.
- Fusion of several satellite sensors will provide more parameters for discrimination of different land covers. Therefore, proposed classification algorithm can be generalized to make it scene and sensor independent.
- Further analysis is required to check the feasibility of proposed soil moisture retrieval algorithm for application in forest region.
- Some scattering models based on IEM, SPM, PO etc., are required to be developed for estimating lunar surface parameters such as dielectric constant, roughness, and regolith thickness, for parameterization of surface and subsurface properties.

Appendix- A

Foundation of SAR Polarimetry

A1. Wave Polarimetry

A1.1. Polarization of Electromagnetic Wave

Considering an orthogonal coordinate system (*h*, *v*, *k*) as shown in Figure A.1, a monochromatic plane EM wave propagating in positive direction *k* through loss-less medium can be expressed in terms of location vector *r* and time *t* as [40],

$$\begin{aligned} E(r,t) &= E_h(r,t)\hat{h} + E_v(r,t)\hat{v} \\ &= E_{0h}\cos\{(\omega t - kr) + \delta_h\}\hat{h} + E_{0v}\cos\{(\omega t - kr) + \delta_v\}\hat{v}, \end{aligned} \tag{A.1}$$

where E_{0h} and E_{0v} are the amplitudes of horizontally and vertically polarized EM waves. The terms δ_h and δ_v are the phases of these two orthogonal components and ω is angular frequency [37]. The elimination of the term (ωt-kr) leads to the following equation of ellipse by using some trigonometric identities:

$$\left(\frac{E_h}{E_{0h}}\right)^2 + \left(\frac{E_v}{E_{0v}}\right)^2 - 2\left(\frac{E_h}{E_{0h}}\right)\left(\frac{E_v}{E_{0v}}\right)\cos\delta = \sin^2\delta, \tag{A.2}$$

where δ denotes the phase difference between E_h and E_v and is defined as,

$$\delta = \delta_h - \delta_v, \tag{A.3}$$

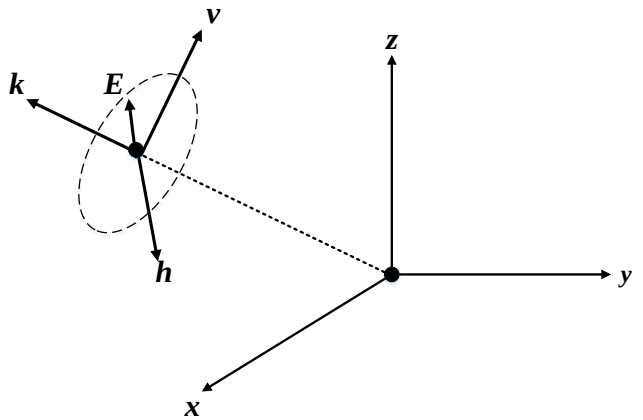

Figure A.1: Description of coordinate system [160].

The extremity of electric field vector of a harmonic plane EM wave describes an elliptical locus in equiphase plane (plane perpendicular to direction of propagation) over time at fixed point in space, as shown in Figure A.2. This property of EM wave is known as *polarization* [165].

The polarization state of EM wave is expressed by orientation, shape, and size of the polarization ellipse accompanied by the sense of rotation of electric field vector, while observing the wave in such a way that it travels away from observer [165]. These parameters are defined as follows:

- The size of polarization ellipse is defined by semi-major axis *a* and semi-minor axis *b* of polarization ellipse, which are related to amplitude of EM wave components as [42],

$$A = \sqrt{a^2 + b^2} = \sqrt{E_{0h}^2 + E_{0v}^2} \ , \tag{A.4}$$

- The orientation angle ψ is defined as the angle between the major axis of the polarization ellipse and positive *h* - axis. This parameter describes the inclination of the ellipse, and is given by relation [102],

$$\tan 2\psi = (\tan 2\alpha)\cos\delta, \qquad 0 \le \psi \le \pi, \tag{A.5}$$

where α is a constructive variable representing absolute phase angle, which is defined as,

$$\tan\alpha = \frac{E_{0v}}{E_{0h}}, \qquad 0 \le \alpha \le \frac{\pi}{2}, \tag{A.6}$$

Therefore,

$$\tan 2\psi = \frac{2E_{0h}E_{0v}}{E_{0h}^2 - E_{0v}^2}\cos\delta, \qquad 0 \le \psi \le \pi, \tag{A.7}$$

- The ellipticity angle χ is defined as the ratio of minor and major semi-axes of polarization ellipse. It describes the shape of the ellipse, and is represented as [102],

$$\tan\chi = \pm\frac{b}{a}, \tag{A.8}$$

or,

$$\sin 2\chi = (\sin 2\alpha)\sin\delta = \frac{2E_{0h}E_{0v}}{E_{0h}^2 + E_{0v}^2}\sin\delta, \qquad \frac{-\pi}{4} \le \chi \le \frac{\pi}{4} \ , \tag{A.9}$$

- The sense of rotation of electric field vector is described by the sign of ellipticity angle χ. The positive value represents left-handed polarizations, whereas negative value represents right-handed polarizations [165].

In general, the EM wave is elliptically polarized. However, two extreme cases occur when ellipse collapses to a line and a circle. These two particular cases are [377]:

- **Linear polarization** :

$$\left.\begin{aligned} &\delta = \delta_h - \delta_v = n\pi, \quad n = 0,1,2,3... \\ &\chi = 0 \end{aligned}\right\}, \quad \text{(A.10)}$$
$$\psi = 0 : \text{horizontal polarization},\ \psi = \frac{\pi}{2} : \text{vertical polarization}$$

- **Circular polarization**:

$$\left.\begin{aligned} &\delta = \delta_h - \delta_v = \pm(2n\pi + \frac{\pi}{2}), \quad n = 0,1,2,3... \\ &E_{0h} = E_{0v} \\ &\chi = \pm\frac{\pi}{4} \end{aligned}\right\}, \quad \text{(A.11)}$$

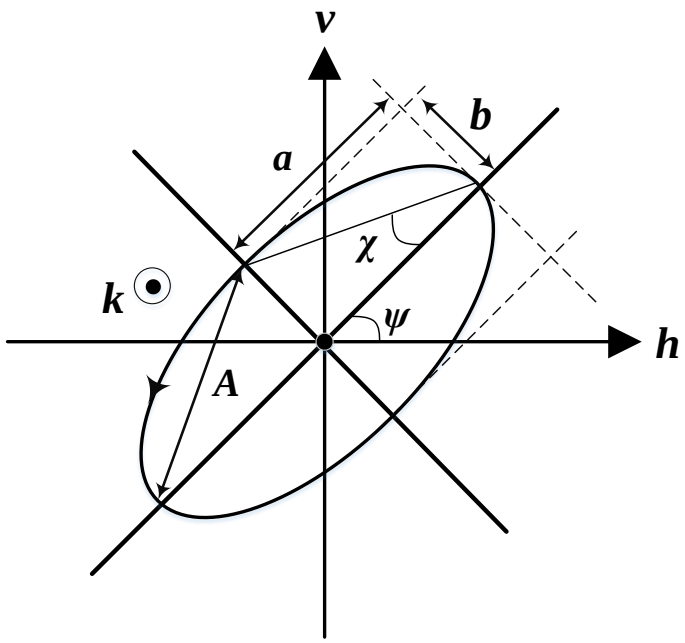

Figure A.2: Polarization ellipse [165].

A1.2. Stokes Vector

Stokes vector represents the polarization of EM wave in terms of power quantities directly observed by radar systems [42, 102]. The Stokes vector can be defined as [416],

$$g = \begin{bmatrix} g_1 \\ g_2 \\ g_3 \\ g_4 \end{bmatrix} = \begin{bmatrix} E_{0h}^2 + E_{0h}^2 \\ E_{0h}^2 - E_{0h}^2 \\ 2E_{0h}E_{0v}\cos\delta \\ 2E_{0h}E_{0v}\sin\delta \end{bmatrix}, \tag{A.12}$$

The Stokes parameters are useful in defining the polarization, amplitude, and phase of EM wave. The Stokes parameter g_1 represents the total power in polarized EM wave; g_2 represents the power contained in horizontally or vertically polarized EM wave; g_3 represents power contained in linearly polarized EM wave oriented at 45° or 135°; and g_4 represents the power contained in right or left circularly polarized EM wave. The non-zero value of any of the parameter i.e., g_2, g_3, or g_4 represents the existence of polarized part of EM wave [42].

The term degree of polarization, which describes the correlation between E_h and E_v is expressed as the ratio of power in completely polarized wave to the total power, and is defined as [416],

$$m = \frac{\sqrt{g_2^2 + g_3^2 + g_4^2}}{g_1}, \tag{A.13}$$

For completely polarized wave m=1 and for polarized wave $0<m<1$.

A1.3. Poincare Sphere

The Stokes vector can be represented as a Cartesian coordinates of a point on a sphere known as Poincare sphere, which helps in graphical representation of polarization states of wave [42, 165]. The Stokes vector is related to canonical angular variables (χ and ψ) of polarization ellipse, as defined in Equations (A.7) and (A.9), by following relation,

$$\tan 2\psi = \frac{g_3}{g_2}, \tag{A.14}$$

$$\sin 2\chi = \frac{g_4}{\sqrt{g_2^2 + g_3^2 + g_2^2}}, \tag{A.15}$$

Therefore, the Stokes vector represented in Equation (A.12) is expressed as [165],

$$g = \begin{bmatrix} g_1 \\ g_2 \\ g_3 \\ g_4 \end{bmatrix} = g_1 \begin{bmatrix} 1 \\ \cos 2\chi \cos 2\psi \\ \cos 2\chi \sin 2\psi \\ \sin 2\chi \end{bmatrix}, \tag{A.16}$$

Figure A.3 represents Poincare sphere, in which (g_2, g_3, g_4) represents a spherical coordinate of a point on sphere of radius g_1. The Poincare sphere provides an exclusive representation of each polarization state on the surface of sphere. The angles 2χ and 2ψ are the latitude and longitude of each polarization state. The Poincare sphere provides mapping of linear polarizations at the equator (χ =0°) and circular polarization at the poles. The portion of Poincare sphere above the equator i.e., χ > 0°, represents left-handed polarizations, and below the equator i.e., χ < 0°, represents right-handed polarizations. Thus, the Poincare sphere provides one-to-one mapping of all possible polarization states and points on sphere [42, 102].

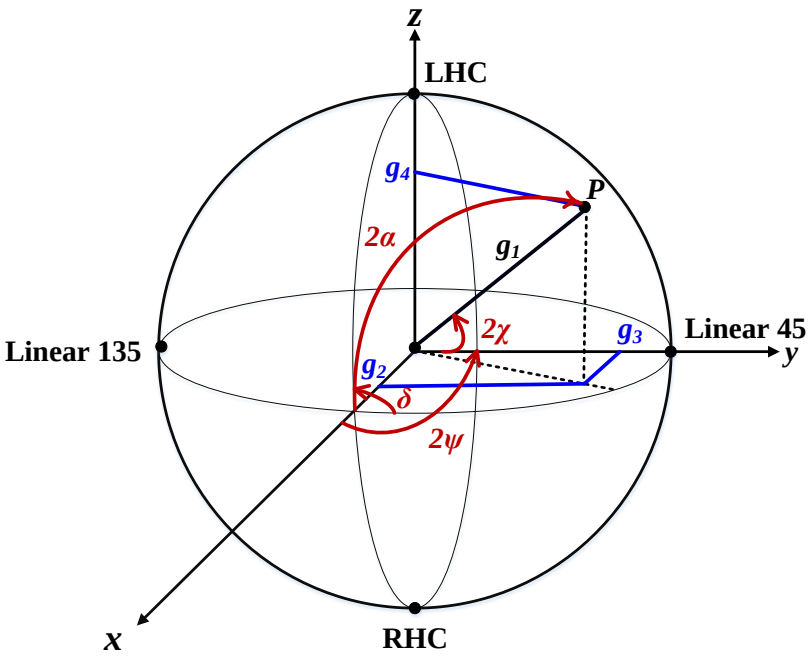

Figure A.3 : Poincare sphere [165].

A1.4. Polarization Ratio

Polarization ratio is defined as the ratio of orthogonal components of electric field vector E as [42],

$$\rho = \frac{E_v}{E_h} = \frac{E_{0v}}{E_{0h}} e^{j\delta} = \tan\alpha \, e^{j\delta}, \tag{A.17}$$

where α and δ are known as Deschamps parameters for defining the polarization states of EM wave [see Equation (A.6)]. The polarization ratio ρ can also be expressed in terms of orientation angle ψ and ellipticity angle χ by [422],

$$\rho = \frac{\tan\psi + j\tan\chi}{1 - j\tan\psi\tan\chi}, \tag{A.18}$$

Therefore, polarization ratio ρ changes with change in polarization basis.

A1.5. Jones Vector

Jones vector represents the wave polarization of plane monochromatic electric field by utilizing least possible information [219].

Equation (A.1) can be written as,

$$E(r,t) = \begin{bmatrix} E_{0h}\cos(\omega t - kr + \delta_h) \\ E_{0v}\cos(\omega t - kr + \delta_v) \end{bmatrix} = \mathrm{Re}\left\{ \begin{bmatrix} E_{0h}e^{j\delta_h} \\ E_{0v}e^{j\delta v} \end{bmatrix} e^{-jkr}e^{j\omega t} \right\} = \mathrm{Re}\left\{ E(r)e^{j\omega t} \right\}, \tag{A.19}$$

The Jones vector can then be defined as,

$$E = E(r)\big|_{r=0} = \begin{bmatrix} E_h \\ E_v \end{bmatrix} = \begin{bmatrix} E_{0h}e^{j\delta_h} \\ E_{0v}e^{j\delta v} \end{bmatrix}, \tag{A.20}$$

Thus, Jones vector determines the amplitude and phase of electric field vector.

In general, the polarization state of electric field expressed by Jones vector can be represented in any arbitrary orthogonal basis (m, n) as,

$$E = E_m\hat{m} + E_n\hat{n}, \tag{A.21}$$

Jones vector [Equation (A.21)] can be expressed in terms of polarization ratio given in Equation (A.17) as,

$$E_{mn} = \begin{bmatrix} E_m \\ E_n \end{bmatrix} = |E_m|e^{j\delta_m}\begin{bmatrix} 1 \\ \rho \end{bmatrix}, \tag{A.22}$$

After some manipulations Equation (A.22) can be written as,

$$E = |E|e^{j\delta_m}\frac{1}{\sqrt{1+\rho\rho_*}}\begin{bmatrix} 1 \\ \rho \end{bmatrix}, \tag{A.23}$$

with

$$|E| = \sqrt{E_m E_m^{\,*} + E_n E_n^{\,*}} = A, \tag{A.24}$$

Table A.1 provides the value of polarization basis for different bases [42].The information provided by Jones vector is equivalent to that of polarization ellipse parameters. Jones vector in terms of polarization ellipse parameters (χ and ψ) and initial phase (υ) can be represented as,

$$E = Ae^{j\upsilon}\begin{bmatrix}\cos\chi\cos\psi - j\sin\chi\sin\psi \\ \cos\chi\sin\psi + j\sin\chi\cos\psi\end{bmatrix} = Ae^{j\upsilon}\begin{bmatrix}\cos\psi & -\sin\psi \\ \sin\psi & \cos\psi\end{bmatrix}\begin{bmatrix}\cos\chi \\ j\sin\chi\end{bmatrix}, \tag{A.25}$$

Table A. 1 Polarization state description in terms of orientation angle ψ, ellipticity angle χ, polarization ratio ρ, and Jones vector E [42]

Polarization	Linear horizontal	Linear vertical	Linear 45	Linear 135	Left circular	Right circular
χ	0	0	0	0	$\pi/4$	$-\pi/4$
ψ	0	$\pi/2$	$\pi/4$	$-\pi/4$	0 to π	0 to π
ρ	0	∞	1	-1	j	$-j$
E	$\begin{bmatrix}1\\0\end{bmatrix}$	$\begin{bmatrix}0\\1\end{bmatrix}$	$\frac{1}{\sqrt{2}}\begin{bmatrix}1\\1\end{bmatrix}$	$\frac{1}{\sqrt{2}}\begin{bmatrix}-1\\1\end{bmatrix}$	$\frac{1}{\sqrt{2}}\begin{bmatrix}1\\j\end{bmatrix}$	$\frac{1}{\sqrt{2}}\begin{bmatrix}1\\-j\end{bmatrix}$

A1.6. Special Unitary Group

Jones vector in Equation (A.25) can be written as [40],

$$\begin{aligned} E &= Ae^{j\upsilon}\begin{bmatrix}\cos\psi & -\sin\psi \\ \sin\psi & \cos\psi\end{bmatrix}\begin{bmatrix}\cos\chi & j\sin\chi \\ j\sin\chi & \cos\chi\end{bmatrix}\begin{bmatrix}1\\0\end{bmatrix} \\ &= A\begin{bmatrix}\cos\psi & -\sin\psi \\ \sin\psi & \cos\psi\end{bmatrix}\begin{bmatrix}\cos\chi & j\sin\chi \\ j\sin\chi & \cos\chi\end{bmatrix}\begin{bmatrix}e^{j\upsilon} & 0 \\ 0 & e^{-j\upsilon}\end{bmatrix}\begin{bmatrix}1\\0\end{bmatrix}, \\ &= A\begin{bmatrix}\cos\psi & -\sin\psi \\ \sin\psi & \cos\psi\end{bmatrix}\begin{bmatrix}\cos\chi & j\sin\chi \\ j\sin\chi & \cos\chi\end{bmatrix}\begin{bmatrix}e^{j\upsilon} & 0 \\ 0 & e^{-j\upsilon}\end{bmatrix}\hat{m} \\ &= A\,U_2(\psi)\,U_2(\chi)\,U_2(\upsilon)\hat{m} \end{aligned} \tag{A.26}$$

where $\hat{m} = \hat{h}$ represents unit vector corresponding to horizontal polarization. The matrices $U_2(\psi)$, $U_2(\chi)$, and $U_2(\upsilon)$ are the rotation matrices of special unitary group corresponding to orientation angle ψ, ellipticity angle χ, and absolute phase υ, respectively [219, 416, 422]. After combining these unitary rotation matrices, Equation (A.26) can be written as,

$$E = A\,U_2(\psi,\chi,\upsilon)\hat{m}\,, \tag{A.27}$$

These unitary matrices satisfy following conditions [316]:

$$U_2{}^{-1} = U_2{}^{*T} \text{ and } |U_2| = 1, \tag{A.28}$$

In a similar way, Equation (A.23) can be written as [416],

$$E = A\frac{1}{\sqrt{1+\rho\rho_*}}\begin{bmatrix}1 & -\rho^*\\ \rho & 1\end{bmatrix}\begin{bmatrix}e^{j\delta_i} & 0\\ 0 & e^{-j\delta_i}\end{bmatrix}\hat{m}, \tag{A.29}$$

where,

$$\delta_i = \upsilon - \tan^{-1}(\tan\psi\tan\chi)\,, \tag{A.30}$$

This angle δ_i corresponds to reference phase of transformed polarization basis. After comparing Equations (A.26) and (A.29), it can be written as [416],

$$U_2(\psi,\chi,\upsilon) = \frac{1}{\sqrt{1+\rho\rho_*}}\begin{bmatrix}1 & -\rho^*\\ \rho & 1\end{bmatrix}\begin{bmatrix}e^{j\delta_i} & 0\\ 0 & e^{-j\delta_i}\end{bmatrix}, \tag{A.31}$$

A1.7. Change in Polarization Basis

Transformation of polarization basis is very important concept of SAR polarimetry. Two conditions need to be followed for polarization basis transformation: (a) amplitude should remain invariant, and (b) ortho-normality conditions must be preserved. A monochromatic plane wave can be expressed as a linear sum of orthogonal components of electric field obtained in any reference polarization basis [416]. There exist numerous numbers of polarization bases. Let's suppose, polarization states in an arbitrary orthogonal basis (*x, y*) are required to be converted in another polarization basis (*a, b*). The Jones vector in these bases can be represented as,

$$E = E_x\hat{x} + E_y\hat{y} = E_a\hat{a} + E_b\hat{b}\,, \tag{A.32}$$

The corresponding Jones vector in these two bases are obtained as,

$$E_{xy} = \begin{bmatrix}E_x\\ E_y\end{bmatrix} \text{ and } \quad E_{ab} = \begin{bmatrix}E_a\\ E_b\end{bmatrix}, \tag{A.33}$$

By using unitary transformation matrices $U_2(\psi, \chi, \upsilon)$,

$$E = E_aU_2(\psi,\chi,\upsilon)\hat{x} + E_bU_2(\psi,\chi,\upsilon)\hat{y}\,, \tag{A.34}$$

which can be expressed as,

$$\begin{bmatrix} E_a \\ E_b \end{bmatrix} = U_2(\psi, \chi, \upsilon)^{-1} \begin{bmatrix} E_x \\ E_y \end{bmatrix}, \tag{A.35}$$

or,

$$E_{ab} = U_{2(xy \to ab)} E_{xy}, \tag{A.36}$$

where

$$U_{2(xy \to ab)} = U_2(\psi, \chi, \upsilon)^{-1} = U_2(-\psi) U_2(-\chi) U_2(-\upsilon), \tag{A.37}$$

A1.8. Polarization Description for Partially Polarized Wave

The electric field vector represented in Equation (A.1) is completely polarized monochromatic plane wave tracing well defined fixed polarization ellipse. However, there exists another class of waves known as quasi-monochromatic or partially polarized waves having time-varying amplitude and phase parameters, which do not define well defined polarization ellipse. These waves occur due to interaction of monochromatic plane EM wave with time-dependent scatterers [219].

The quasi-monochromatic plane wave at fixed point in space can be represented as,

$$E(t) = \begin{bmatrix} E_h(t) \\ E_v(t) \end{bmatrix} = \begin{bmatrix} E_{0h}(t) e^{j\delta_h(t)} \\ E_{0v}(t) e^{j\delta_v(t)} \end{bmatrix} = \left[E_{0h}(t) e^{j\delta_h(t)} \hat{h} + E_{0v}(t) e^{j\delta_v(t)} \hat{v} \right] e^{j\bar{\omega}\, t}, \tag{A.38}$$

where $\bar{\omega}$ is the mean wave frequency. Since, transmission in SAR is done at narrowband, wave frequency ω satisfies following condition [42]:

$$\bar{\omega} - \frac{1}{2}\Delta\omega \le \omega \le \bar{\omega} + \frac{1}{2}\Delta\omega, \quad \text{with} \quad \frac{\Delta\omega}{\omega} << 1, \tag{A.39}$$

where $\Delta\omega$ represents the spread in wave frequency. The time varying nature of $E_{0h}(t)$, $E_{0v}(t)$, and $\delta(t)$ resulted in spectral spread of Δf such that $\Delta f << \omega/2\pi$. If the reception of narrowband scattered wave is done in time interval τ such that $\tau << 2\pi/\Delta f$, the parameters $E_{0h}(t)$, $E_{0v}(t)$, and $\delta(t)$ are assumed to be constant over time. This characteristics corresponds to behaviour of monochromatic plane wave having mean wave frequency of $\bar{\omega}$. The second case is when the reception of scattered wave is done in longer time interval such that $\tau >> 2\pi/\Delta f$. In this case, the parameters $E_{0h}(t)$, $E_{0v}(t)$, and $\delta(t)$ no longer remain constant over time [378]. Such types of waves are known as partially polarized waves. Due to time dependence nature of these waves, their characterization is possible by time-averaged statistics. Therefore, the concept of wave

coherency matrix was introduced [429]. The wave coherency matrix is time-averaged product of Jones vector with its conjugate transpose, and can be expressed as,

$$J = \left\langle E.E^{*T} \right\rangle$$

$$J = \begin{bmatrix} \langle J_{hh} \rangle & \langle J_{hv} \rangle \\ \langle J_{vh} \rangle & \langle J_{vv} \rangle \end{bmatrix} = \begin{bmatrix} \left\langle |E_h|^2 \right\rangle & \left\langle E_h E_v^{\,*} \right\rangle \\ \left\langle E_v E_h^{\,*} \right\rangle & \left\langle |E_v|^2 \right\rangle \end{bmatrix}, \tag{A.40}$$

where <…> represents ensemble averaging or time averaging. Equation (A.40) can be written in terms of Stokes vector (Equation (A.12)) as,

$$J = \frac{1}{2}\begin{bmatrix} \langle g_1 \rangle + \langle g_2 \rangle & \langle g_3 \rangle - j\langle g_4 \rangle \\ \langle g_3 \rangle + j\langle g_4 \rangle & \langle g_1 \rangle - \langle g_2 \rangle \end{bmatrix}, \tag{A.41}$$

The Stokes vector in Equation (A.12) thus can be expressed for partially polarized wave as,

$$g = \begin{bmatrix} J_{hh} + J_{vv} \\ J_{hh} - J_{vv} \\ J_{hv} + J_{vh} \\ j(J_{hv} - J_{vh}) \end{bmatrix}, \tag{A.42}$$

Equation (A.42) can be represented as the sum of completely polarized and completely unpolarized components of wave by [194],

$$g = \begin{bmatrix} (1-m)g_1 \\ 0 \\ 0 \\ 0 \end{bmatrix} + \begin{bmatrix} mg_1 \\ g_2 \\ g_3 \\ g_4 \end{bmatrix}, \tag{A.43}$$

where mg_1 is the completely polarized part, and $(1\text{-}m)\, g_1$ is the unpolarized part of EM wave.

The wave coherency matrix J is hermitian positive semi-definite matrix having non-negative eigenvalues, and it satisfies following condition [416]:

$$\left\langle |J| \right\rangle \geq 0, \text{ or, } \quad \langle g_1 \rangle^2 \geq \langle g_2 \rangle^2 + \langle g_3 \rangle^2 + \langle g_4 \rangle^2, \tag{A.44}$$

Due to hermitian matrix characteristics defined in Equation (A.44), trace (sum of diagonal elements) and determinant of matrix remains constant irrespective of unitary transformation. Therefore, Stokes vector will also be basis-invariant along with total power and degree of polarization.

A2. Scattering Polarimetry

In scattering scenario, it is required to relate polarization behaviour of transmitted and scattered wave. This section provides the polarization description of scatterer by defining different matrices which are as follows:

A2.1. Scattering Matrix

The illumination of a scatterer by EM wave changes the polarization state and degree of polarization of incident wave depending upon the geometrical properties of targets. For deterministic and time-invariant targets, this transformation behaviour is expressed by 2×2 complex matrix called scattering matrix [339]. This matrix is known as Sinclair matrix in backscattering scenario, and Jones matrix in forward scattering scenario. The scattering matrix relates Jones vector of incident and scattered wave as [379, 429],

$$E^s = \frac{e^{jkr}}{r}[S]E^i$$
$$\begin{bmatrix} E_h^s \\ E_v^s \end{bmatrix} = \frac{e^{jkr}}{r}\begin{bmatrix} S_{hh} & S_{hv} \\ S_{vh} & S_{vv} \end{bmatrix}\begin{bmatrix} E_h^i \\ E_v^i \end{bmatrix}, \quad \text{(A.45)}$$

where r is the distance between target and antenna. The term e^{jkr} accounts for phase shift caused due to propagation of wave from transmitter to scatterer, and the term r^{-1} accounts for attenuation between incident and scattered wave due to spherical nature of wave [165]. The first subscript in [S] matrix in Equation (A.45) denote the transmitted polarization and the second subscript denote the received polarization. This matrix forms the basis of SAR polarimetry. In case of reciprocal target, scattering matrix is symmetrical with $S_{hv}=S_{vh}$.

A2.2. Polarimetric Scattering Phenomenon

Figure A.4 shows the coordinate system of a scattering problem in which fully polarized EM wave E^i is incident on a scatterer in the direction k_i. The receiver accepts the scattered wave E^s from the direction k_s. At receiver location there are two conventions for representing coordinate systems. The representation of scattered field in (h_1^s, v_1^s, k_1^s) coordinate system is called Back-Scatter Alignment (BSA), and in (h_2^s, v_2^s, k_2^s) coordinate system is called Forward Scatter Alignment (FSA). BSA is generally used in radar mono-static case for characterizing backscattering, whereas FSA is used in bi-static cases [165].

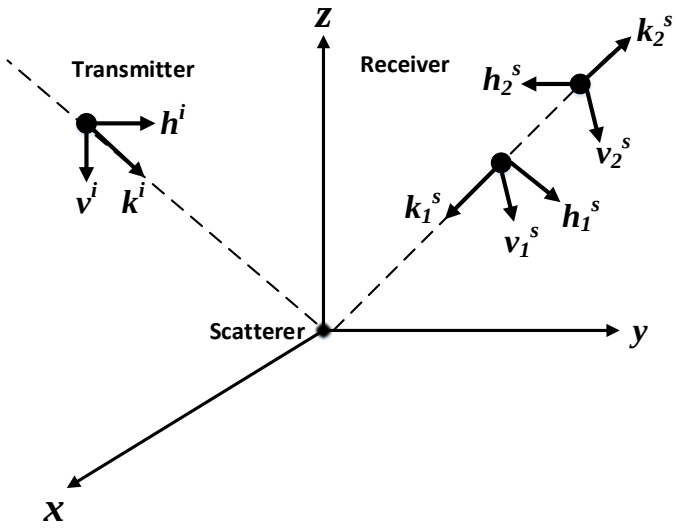

Figure A.4: Coordinate system and scattering geometry.

A2.3. Scattering Target Vector for Backscattering Cases

The scattering target vector help in describing scattering performance of distributed scatterers. In order to extract physical constructive information from 2×2 scattering matrix [Equation (A.45)], vectorization of scattering matrix is performed for obtaining scattering target vector [80]. Mathematically, target vector can be expressed as,

$$\kappa = V([S]) = \frac{1}{2} Trace([S]\Psi), \tag{A.46}$$

where *V(.)* denotes the vectorization operator. The term Ψ represents 2×2 complex basis matrix which is orthonormal under hermitian inner product, and κ represents target vector, which is expressed as,

$$\kappa = [\kappa_1, \quad \kappa_2, \quad \kappa_3, \quad \kappa_4]^T, \tag{A.47}$$

In SAR polarimetry, two basis matrices are used in general which are, lexicographic basis Ψ_L and Pauli basis Ψ_P.

The lexicographic basis Ψ_L is represented by [80],

$$\Psi_L = 2\left\{\begin{bmatrix}1 & 0\\ 0 & 0\end{bmatrix}, \begin{bmatrix}0 & 1\\ 0 & 0\end{bmatrix}, \begin{bmatrix}0 & 0\\ 1 & 0\end{bmatrix}, \begin{bmatrix}0 & 0\\ 0 & 1\end{bmatrix}\right\}, \tag{A.48}$$

Vectorization of [*S*] by Ψ_L using Equation (A.46) gives lexicographic scattering vector κ_L defined by,

$$\kappa_L = [S_{hh}, \quad S_{hv}, \quad S_{vh}, \quad S_{vv}]^T, \tag{A.49}$$

The Pauli basis Ψ_P is related to Pauli spin matrix as [80],

$$\Psi_P = \sqrt{2}\left\{\begin{bmatrix}1 & 0\\ 0 & 1\end{bmatrix},\begin{bmatrix}1 & 0\\ 0 & -1\end{bmatrix},\begin{bmatrix}0 & 1\\ 1 & 0\end{bmatrix},\begin{bmatrix}0 & -j\\ j & 0\end{bmatrix}\right\}, \tag{A.50}$$

After vectorization by Equation (A.46) leads to Pauli scattering vector κ_P of the form,

$$\kappa_P = \left[S_{hh}+S_{vv},\quad S_{hh}-S_{vv},\quad S_{hv}+S_{vh},\quad j(S_{vh}-S_{hv})\right]^T, \tag{A.51}$$

The components of Pauli scattering vector are related to physical mechanisms which are described as follows [78]:

- $S_{hh}+S_{vv}$: Isotropic surface scattering.
- $S_{hh}-S_{vv}$: Isotropic dihedral scattering.
- $S_{hv}+S_{vh}$: Isotropic dihedral scattering having relative phase shift of $\pi/4$ with respect to horizontal.
- $j(S_{vh}-S_{hv})$: Isotropic cross-polarizer, which transforms the incident wave into their orthogonal polarization states. This term appears in backscatter case only in the presence of Faraday rotation.

In backscattering scenario, for reciprocal scatterer having $S_{hv}=S_{vh}$, the scattering vectors in Equations (A.49) and (A.51) can be written as [322],

$$\kappa_L = \left[S_{hh},\quad \sqrt{2}S_{hv},\quad S_{vv}\right]^T, \tag{A.52}$$

$$\kappa_P = \left[S_{hh}+S_{vv},\quad S_{hh}-S_{vv},\quad 2S_{hv}\right]^T, \tag{A.53}$$

In Equation (A.52), $\sqrt{2}$ is multiplied to cross-polar terms in order to satisfy conservation of norm (equals span or total power of scattering matrix) under polarization unitary basis transformation [80, 378].

A2.4. Matrices for Distributed Targets

The scattering matrix expressed in Equation (A.45) is useful in characterization of scattering from point targets or stationary targets. However, in nature most of the scatterers usually vary with time and/or space. Therefore, there scatterers cannot be completely described by single scattering matrix. These targets are known as partial scatterers or distributed targets or depolarizing targets. Besides natural motion of scatterers, like growth of vegetation, motion of water surface, etc., artificial motions like movement of antenna in SAR systems resulted in illumination of scatterer with respect to time and/or space. Due to spatial and/or time variations of these scatterers, statistical averaging is required for describing polarization behaviour of

these targets. The most popular matrices in SAR polarimetry in this category are covariance and coherency matrices [219].

A polarimetric covariance matrix is formed by taking the outer product of lexicographic scattering vector [Equation (A.52)] with its transposed complex conjugate as [379],

$$[C] = \left\langle \kappa_L . \kappa_L^{*T} \right\rangle , \tag{A.54}$$

$$[C] = \begin{bmatrix} \left\langle |S_{HH}|^2 \right\rangle & \sqrt{2}\left\langle S_{HH} S_{HV}^{*} \right\rangle & \left\langle S_{HH} S_{VV}^{*} \right\rangle \\ \sqrt{2}\left\langle S_{HV} S_{HH}^{*} \right\rangle & 2\left\langle |S_{HV}|^2 \right\rangle & \sqrt{2}\left\langle S_{HV} S_{VV}^{*} \right\rangle \\ \left\langle S_{VV} S_{HH}^{*} \right\rangle & \sqrt{2}\left\langle S_{VV} S_{HV}^{*} \right\rangle & \left\langle |S_{VV}|^2 \right\rangle \end{bmatrix}, \tag{A.55}$$

where <…> indicates spatial averaging, assuming homogeneous nature of the arbitrary scattering medium.

The outer product of Pauli scattering vector [Equation (A.53)] with its transposed complex conjugate gives polarimetric coherency matrix, defined as [80],

$$[T] = \left\langle \kappa_P . \kappa_p^{*T} \right\rangle , \tag{A.56}$$

which can be represented as [219]

$$[T] = \begin{bmatrix} \frac{1}{2}\left\langle |S_{HH} + S_{VV}|^2 \right\rangle & \frac{1}{2}\left\langle (S_{HH} + S_{VV})(S_{HH} - S_{VV})^{*} \right\rangle & \left\langle S_{HV}^{*}(S_{HH} + S_{VV}) \right\rangle \\ \frac{1}{2}\left\langle (S_{HH} - S_{VV})(S_{HH} + S_{VV})^{*} \right\rangle & \frac{1}{2}\left\langle |S_{HH} - S_{VV}|^2 \right\rangle & \left\langle S_{HV}^{*}(S_{HH} - S_{VV}) \right\rangle \\ \left\langle S_{HV}(S_{HH} + S_{VV})^{*} \right\rangle & \left\langle S_{HV}(S_{HH} - S_{VV})^{*} \right\rangle & 2\left\langle |S_{HV}|^2 \right\rangle \end{bmatrix}, \tag{A.57}$$

The interpretation of diagonal terms of coherency matrix is similar to component of Pauli vector, as described in section A2.3. The off-diagonal terms represent complex cross-correlation terms. The interpretation of these terms is as follows [212]:

- $T_{11} = \frac{1}{2}\left\langle |S_{HH} + S_{VV}|^2 \right\rangle$: Single-bounce scattering.
- $T_{22} = \frac{1}{2}\left\langle |S_{HH} - S_{VV}|^2 \right\rangle$: Double-bounce scattering.
- $T_{33} = 2\left\langle |S_{HV}|^2 \right\rangle$: Volume scattering.

- $T_{13} = \left\langle S_{HV}^{*}\left(S_{HH} + S_{VV}\right)\right\rangle$: Co-and cross polarized correlation affected by azimuth surface tilt.
- $T_{12} = \left\langle \left(S_{HH} + S_{VV}\right)\left(S_{HH} - S_{VV}\right)^{*}\right\rangle$: Correlation between double and single bounce scattering
- $\mathrm{Im}(T_{23}) = \mathrm{Im}\left\langle S_{HV}^{*}\left(S_{HH} - S_{VV}\right)\right\rangle$: Helix scattering.
- $\mathrm{Re}(T_{23}) = \mathrm{Re}\left\langle S_{HV}^{*}\left(S_{HH} - S_{VV}\right)\right\rangle$: Effect of azimuth terrain slope.

The covariance and coherency matrices defined in Equations (A.55) and (A.57) are positive semi-definite hermitian matrices, and have same eigenvalues [80]. These matrices are related to each other as,

$$[C] = U_3^{T}[T]U_3, \text{ or } \quad [T] = U_3[C]U_3^{T}, \tag{A.58}$$

where U_3 is special unitary matrix defined as,

$$U_3 = \frac{1}{\sqrt{2}}\begin{bmatrix} 1 & 0 & 1 \\ 1 & 0 & -1 \\ 0 & \sqrt{2} & 0 \end{bmatrix}, \tag{A.59}$$

A2.5. Basis Transformation for Scattering Matrix

Considering basis transformation from (*x,y*) to (*a,b*) as in section A1.7, redefining scattering matrix Equation (A.45) as [192],

$$E_{xy}^{s} = \left[S_{xy}\right]E_{xy}^{i}, \tag{A.60}$$

$$E_{ab}^{s} = \left[S_{ab}\right]E_{ab}^{i}, \tag{A.61}$$

The incident Jones vector in (*x,y*) basis is transformed to (*a,b*) basis according to Equation (A.36) as,

$$E_{ab}^{i} = U_{2(xy\to ab)}E_{xy}, \tag{A.62}$$

In mono-static or in in backscattering scenario (BSA convention), the scattered wave propagates in the direction opposite to that of incident wave. Therefore, scattered Jones vector in (*a, b*) basis can be written as,

$$E_{ab}^{s} = U_{2(xy\to ab)}^{*}E_{xy}^{s}, \tag{A.63}$$

where conjugate (*) sign occurs due to inversion of coordinate system. By using Equations (A.62) and (A.63), Equation (A.60) can be written as [219],

$$\left(U_{2(xy\to ab)}{}^{*}\right)^{-1}E_{ab}^{s}=\left[S_{xy}\right]U_{2(xy\to ab)}{}^{-1}E_{ab}^{i}$$
$$E_{ab}^{s}=U_{2(xy\to ab)}{}^{*}\left[S_{xy}\right]U_{2(xy\to ab)}{}^{-1}E_{ab}^{i}\quad,\tag{A.64}$$

which implies that,

$$\left[S_{ab}\right]=U_{2(xy\to ab)}{}^{*}\left[S_{xy}\right]U_{2(xy\to ab)}{}^{-1},\tag{A.65}$$

By using the properties of unitary matrix, it can be written as,

$$\left[S_{ab}\right]=U_{2}(\psi,\chi,\alpha)^{T}\left[S_{xy}\right]U_{2}(\psi,\chi,\alpha),\tag{A.66}$$

This transformation is known as "con-similarity transformation" [219]. The scattering matrix obtained in new basis should satisfy invariant conditions (i.e., invariant span and determinant) under unitary transformation. The elements of transformed scattering matrix in (*a, b*) basis can be written as [3, 37, 422],

$$\begin{aligned}
S_{aa}&=(1+\rho\rho^{*})^{-1}(S_{xx}-2\rho^{*}S_{xy}+\rho^{*2}S_{yy})e^{2j\delta}\\
S_{ab}&=S_{ba}=(1+\rho\rho^{*})^{-1}(\rho S_{xx}+(1-\rho\rho^{*})S_{xy}-\rho^{*}S_{yy}),\\
S_{bb}&=(1+\rho\rho^{*})^{-1}(\rho^{2}S_{xx}+2\rho S_{xy}+S_{yy})e^{2j\delta}
\end{aligned}\tag{A.67}$$

Let's consider change of polarization basis from linear (*h, v*) to circular (*l, r*) basis. Referring Table-A.1, for left circular polarization $\rho=j$ is introduced in Equation (A.67) for obtaining elements of scattering matrix in circular polarization as,

$$\begin{aligned}
S_{ll}&=\frac{1}{2}(S_{hh}+2jS_{hv}+S_{vv})\\
S_{rl}&=S_{lr}=\frac{1}{2}(jS_{hh}+jS_{vv})\quad,\\
S_{rr}&=\frac{1}{2}(-S_{hh}+2jS_{hv}+S_{vv})
\end{aligned}\tag{A.68}$$

A2.6. Symmetry Properties

Symmetry usually exists in all geophysical scatterers. The scattering behaviour of scatterers are completely described by scattering components of covariance/coherency matrices. Symmetry conditions impose some restrictions on number of independent components in covariance/coherency matrices based on the assumption that transformations after application of symmetry conditions remain invariant. Thus, symmetry conditions simplify the scattering problems by describing scattering behaviour of scatterers quantitatively [264]. Three symmetry

conditions observed in scatterers are reflection, rotation, and azimuthal symmetries (Figure A.5), which are described as follows:

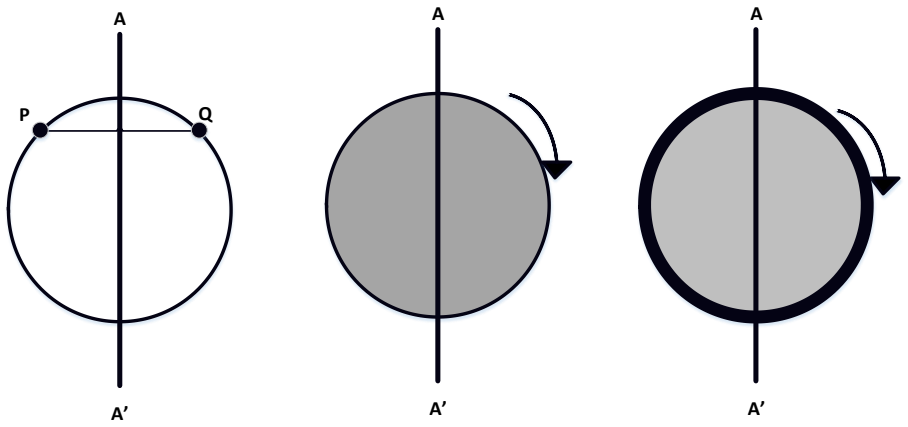

(a) (b) (c)

Figure A.5: (a) Reflection symmetry, (b) rotation symmetry, and (c) azimuthal symmetry [160].

a. Reflection symmetry

The assumption of reflection symmetry is that any scatterer located at **P** has similar scatterer located in the direction just opposite to it say, **Q**, about scattering plane **AA'**. Axis **AA'** includes the direction of radar line-of-sight, and has the possibility to be rotated by an angle θ about radar line-of-sight. This symmetry condition is depicted in Figure A.5(a).

In alignment condition ($\theta=0°$), scattering matrix and Pauli scattering vectors [Equation (A.53)] at location **P**, and its mirrored location **Q**, are of the form [264]:

$$S_P = \begin{bmatrix} S_{hh} & S_{hv} \\ S_{hv} & S_{vv} \end{bmatrix} \Rightarrow \kappa_P = \left[S_{hh} + S_{vv}, \quad S_{hh} - S_{vv}, \quad 2S_{hv}\right]^T, \tag{A.69a}$$

$$S_Q = \begin{bmatrix} S_{hh} & -S_{hv} \\ -S_{hv} & S_{vv} \end{bmatrix} \Rightarrow \kappa_P = \left[S_{hh} + S_{vv}, \quad S_{hh} - S_{vv}, \quad -2S_{hv}\right]^T, \tag{A.69b}$$

Observed coherency matrix is determined as the summation of coherency matrices obtained at **P** and **Q** as [264],

$$[T] = [T_P] + [T_Q]$$

$$[T] = \begin{bmatrix} t_{11} & t_{12} & t_{13} \\ t_{12}^* & t_{22} & t_{23} \\ t_{13}^* & t_{23}^* & t_{33} \end{bmatrix} + \begin{bmatrix} t_{11} & t_{12} & -t_{13} \\ t_{12}^* & t_{22} & -t_{23} \\ -t_{13}^* & -t_{23}^* & t_{33} \end{bmatrix}, \quad \text{(A.70)}$$

Equation (A.70) implies that after application of reflection symmetry condition, number of independent scattering components are reduced to five as compared to nine in original coherency matrix. As evident from Equation (A.70) that there is no correlation between co-polarized and cross-polarized scattering components, i.e.,

$$(S_{hh} + S_{vv})S_{hv}^* = (S_{hh} - S_{vv})S_{hv}^* = 0, \quad \text{(A.71)}$$

Reflection symmetry usually appear in smooth surface, such as water, tilled fields in the at right angle to row direction, etc., [264].

b. Rotation symmetry

Rotation symmetry assumes invariance of covariance/coherency matrix under random rotation of plane of polarization about radar line-of-sight, as presented in Figure A.5(b). Rotated coherency matrix with rotation about radar line-of sight by angle θ [80],

$$T(\theta) = R(\theta)[T]R(\theta)^{*T}, \quad \text{(A.72)}$$

where *R(θ)* is orthogonal rotation matrix defined as,

$$R(\theta) = \begin{bmatrix} 1 & 0 & 0 \\ 0 & \cos 2\theta & \sin 2\theta \\ 0 & -\sin 2\theta & \cos 2\theta \end{bmatrix}, \quad \text{(A.73)}$$

The rotation invariance condition in mathematical terms, assumes target scattering vectors (Pauli vectors for coherency matrix) to be equivalent to eigenvectors of rotation matrix *R(θ)*. These eigenvectors are represented as [80],

$$u_1 = \begin{bmatrix} 1 \\ 0 \\ 0 \end{bmatrix}, \quad u_2 = \frac{1}{\sqrt{2}} \begin{bmatrix} 0 \\ 1 \\ i \end{bmatrix}, \quad u_3 = \frac{1}{\sqrt{2}} \begin{bmatrix} 0 \\ 1 \\ -i \end{bmatrix}, \quad \text{(A.74)}$$

The rotation invariant coherency matrix is described by linear summation of outer product of eigenvectors given in Equation (A.74) as,

$$
\begin{aligned}
T &= a(u_1.u_1^{*T}) + b(u_2.u_2^{*T}) + c(u_3.u_3^{*T}) \\
&= a\begin{bmatrix} 1 & 0 & 0 \\ 0 & 0 & 0 \\ 0 & 0 & 0 \end{bmatrix} + b\begin{bmatrix} 0 & 0 & 0 \\ 0 & 1/2 & i/2 \\ 0 & -i/2 & 1/2 \end{bmatrix} + c\begin{bmatrix} 0 & 0 & 0 \\ 0 & 1/2 & -i/2 \\ 0 & i/2 & 1/2 \end{bmatrix}, \\
&= \begin{bmatrix} a & 0 & 0 \\ 0 & (b+c)/2 & i(b-c)/2 \\ 0 & i(-b+c)/2 & (b+c)/2 \end{bmatrix}
\end{aligned} \tag{A.75}
$$

where *a*, *b*, and *c*, are eigenvalues of T. The inferences drawn from equation (A.75) are as follows [160]:

- Two of the diagonal terms are equal, i.e.,

$$|S_{hh} - S_{vv}|^2 = 2|S_{hv}|^2, \tag{A.76}$$

- The term ($S_{hh}+S_{vv}$) is not correlated to any of the term ($S_{hh}-S_{vv}$) or S_{hv}, i.e.,

$$(S_{hh} + S_{vv})(S_{hh} - S_{vv})^* = (S_{hh} + S_{vv})S_{hv}^* = 0, \tag{A.77}$$

- Correlation between ($S_{hh}-S_{vv}$) and S_{hv} remains intact after rotation symmetry, i.e.,

$$(S_{hh} - S_{vv})S_{hv}^* \neq 0, \tag{A.78}$$

Rotation symmetry exists in random gyro-tropic media, like Earth's ionosphere and helical shaped targets [264].

c. Azimuthal symmetry

Azimuthal symmetry is general symmetry property, which assumes that reflection symmetry exists for all the scattering planes at all rotation angles θ [264]. Thus, it possesses the characteristics of both reflection and rotation symmetry, as visualized from Figure A.5 (c).

The Equation corresponding to azimuthal symmetry is obtained by applying the concept of reflection symmetry on rotation symmetry condition defined by Equation (A.75) as,

$$
\begin{aligned}
\mathrm{T} &= \begin{bmatrix} a & 0 & 0 \\ 0 & (b+c)/2 & i(b-c)/2 \\ 0 & i(-b+c)/2 & (b+c)/2 \end{bmatrix} + \begin{bmatrix} a & 0 & 0 \\ 0 & (b+c)/2 & -i(b-c)/2 \\ 0 & -i(-b+c)/2 & (b+c)/2 \end{bmatrix}, \\
&= \begin{bmatrix} 2a & 0 & 0 \\ 0 & (b+c) & 0 \\ 0 & 0 & (b+c) \end{bmatrix}
\end{aligned} \qquad \text{(A.79)}
$$

The Equation (A.79) indicates that by application of azimuthal symmetry, number of independent parameters reduce to two, as two of the diagonal terms are equal, as presented in Equation (A.79).

Appendix-B

Flowcharts of Model Based Decomposition Methods

B1. Three Component Model Based Decomposition (TCM)

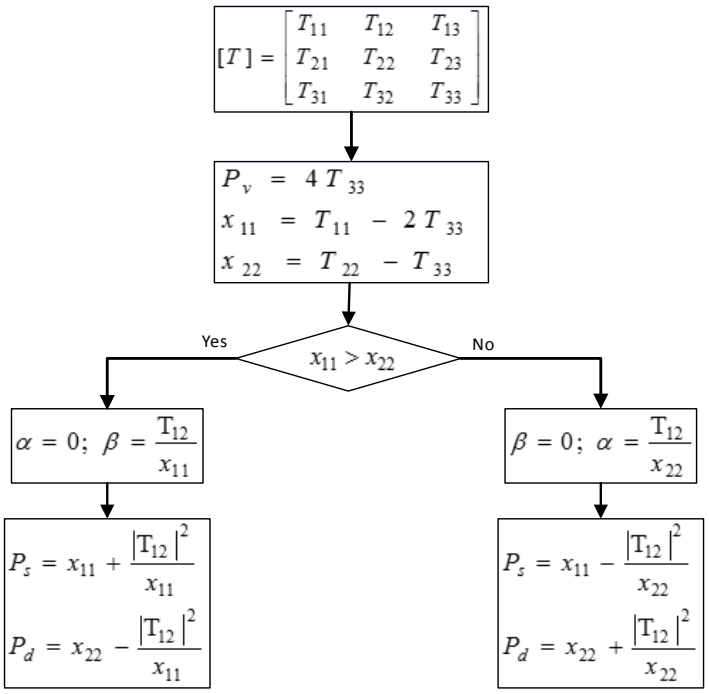

Figure B.1: Flowchart of algorithm for three component model based decomposition (TCM) [9].

B2. Four Component Model Based Decomposition (FCM)

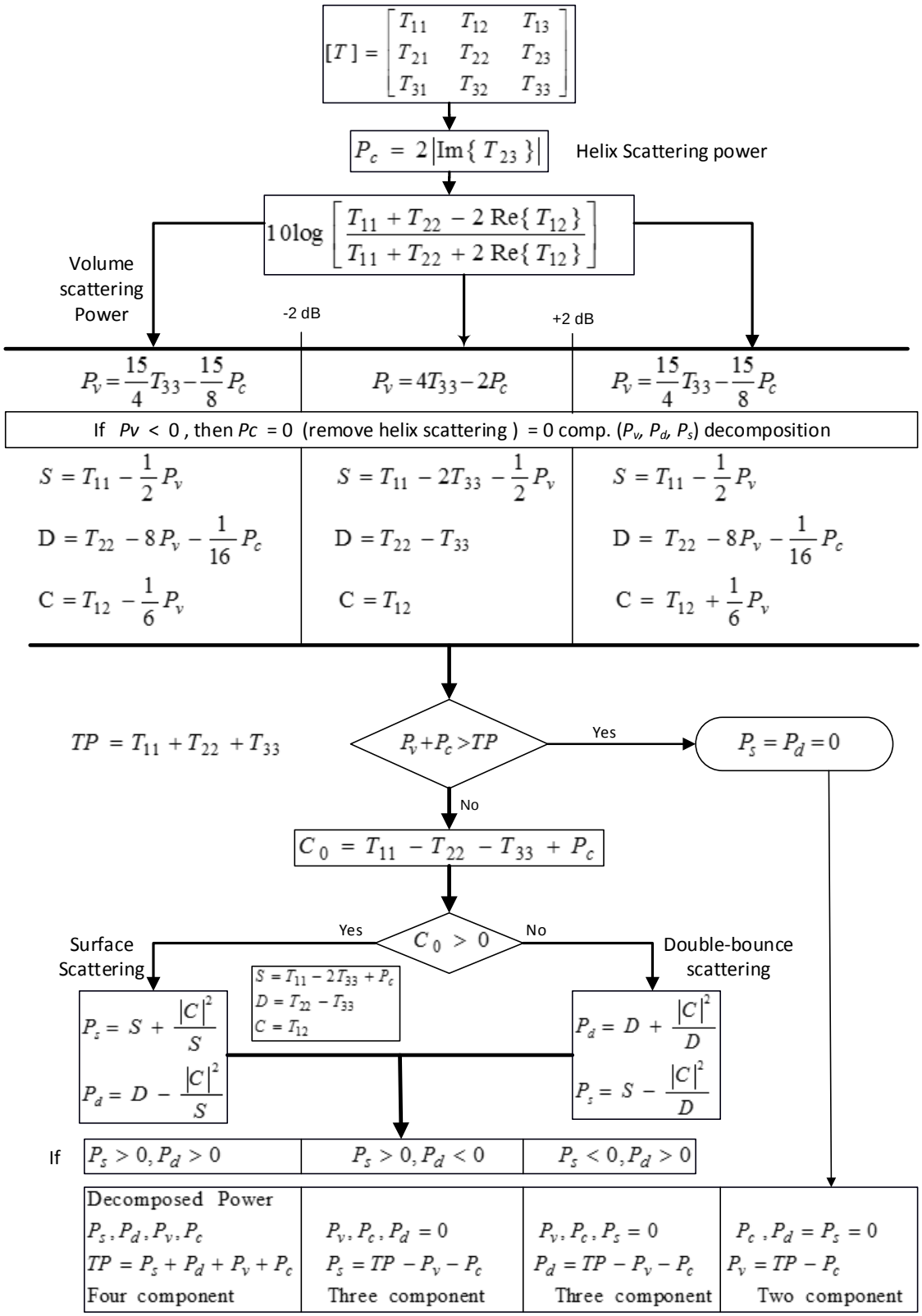

Figure B.2: Flowchart of algorithm for four component model based decomposition (FCM) [425].

B.3. Three Component Model Based Decomposition with Deorientation (TCMD)

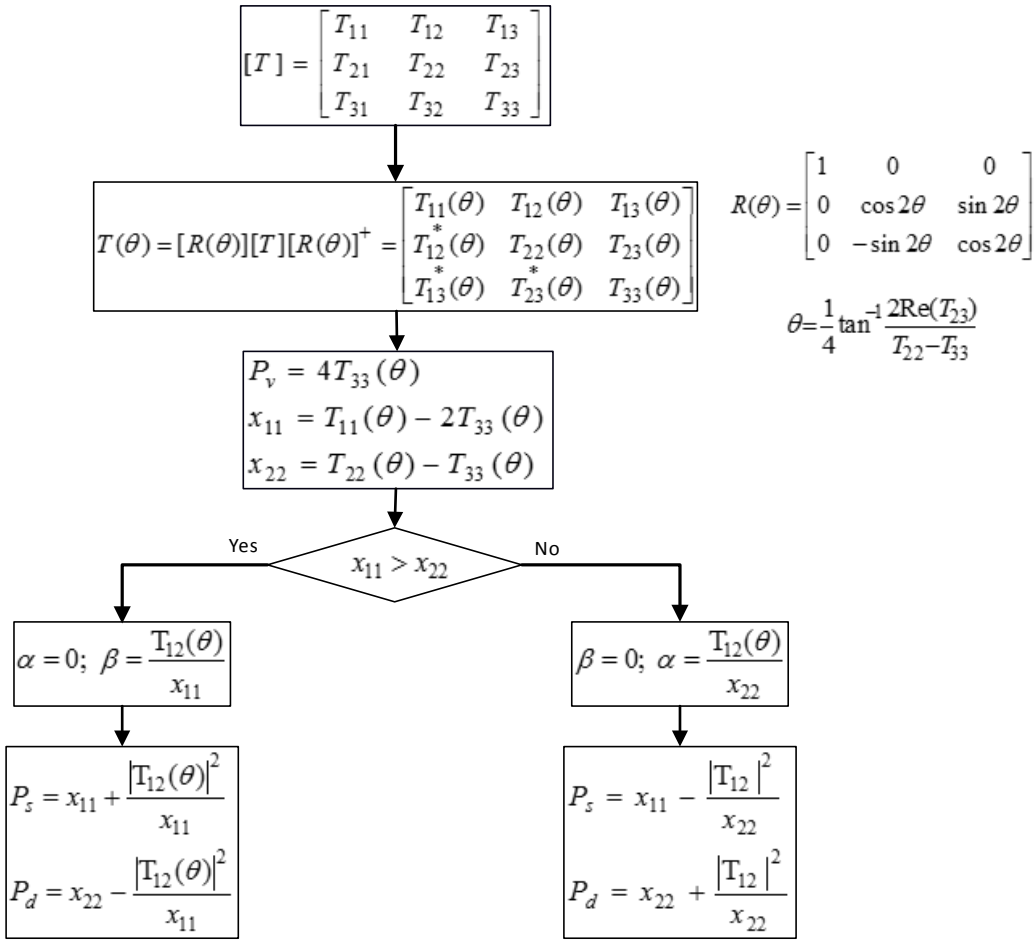

Figure B.3: Flowchart of algorithm for three component model based decomposition with deorientation (TCMD).

B4. Three Component Model Based Decomposition with Double Deorientation and Adaptive Volume Scattering Component (TCMDDA)

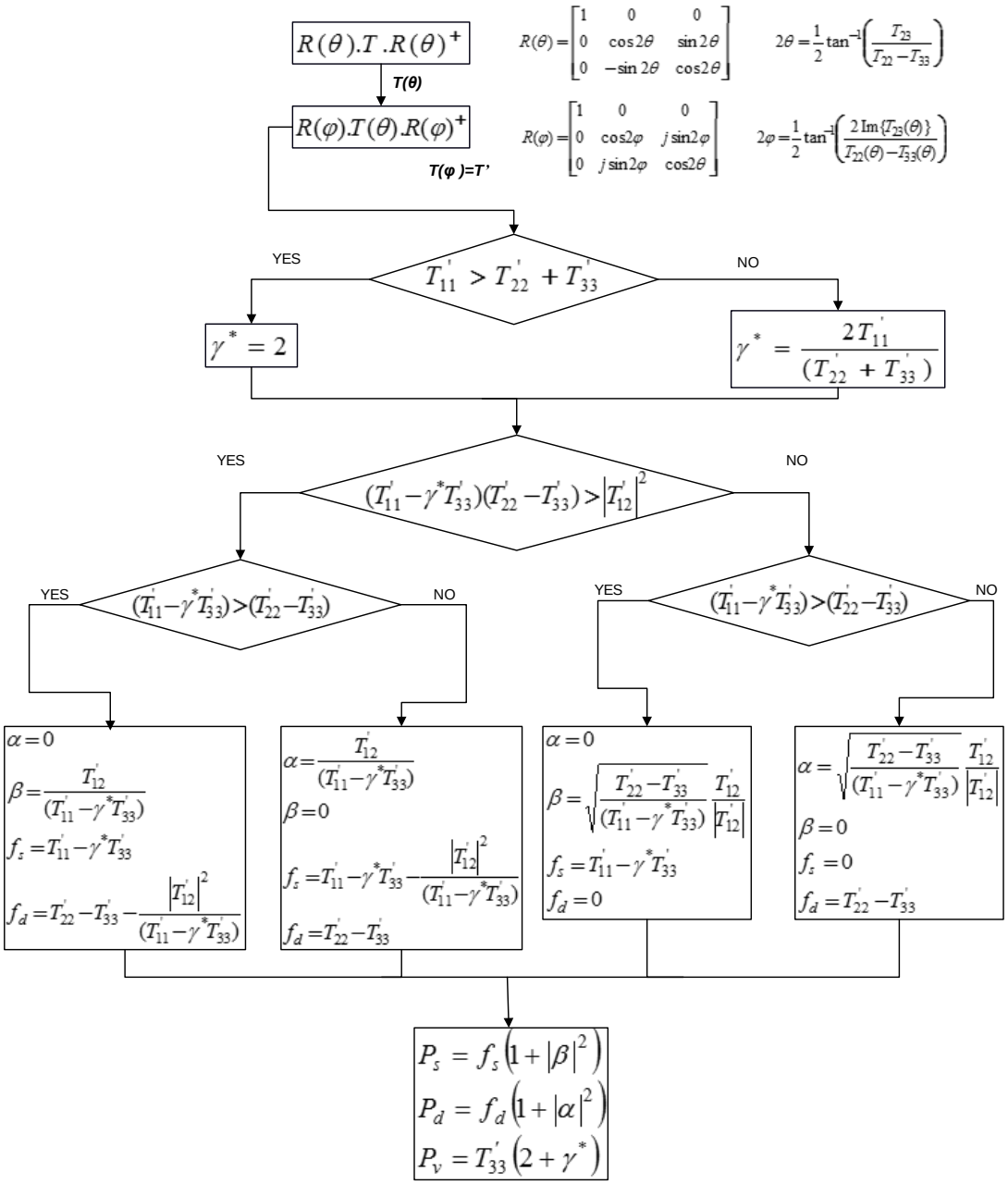

Figure B.4: Flowchart of algorithm for three component model based decomposition with double deorientation and adaptive volume scattering component (TCMDDA) [90].

B5. Four Component Model Based Decomposition with Deorientation (FCMD)

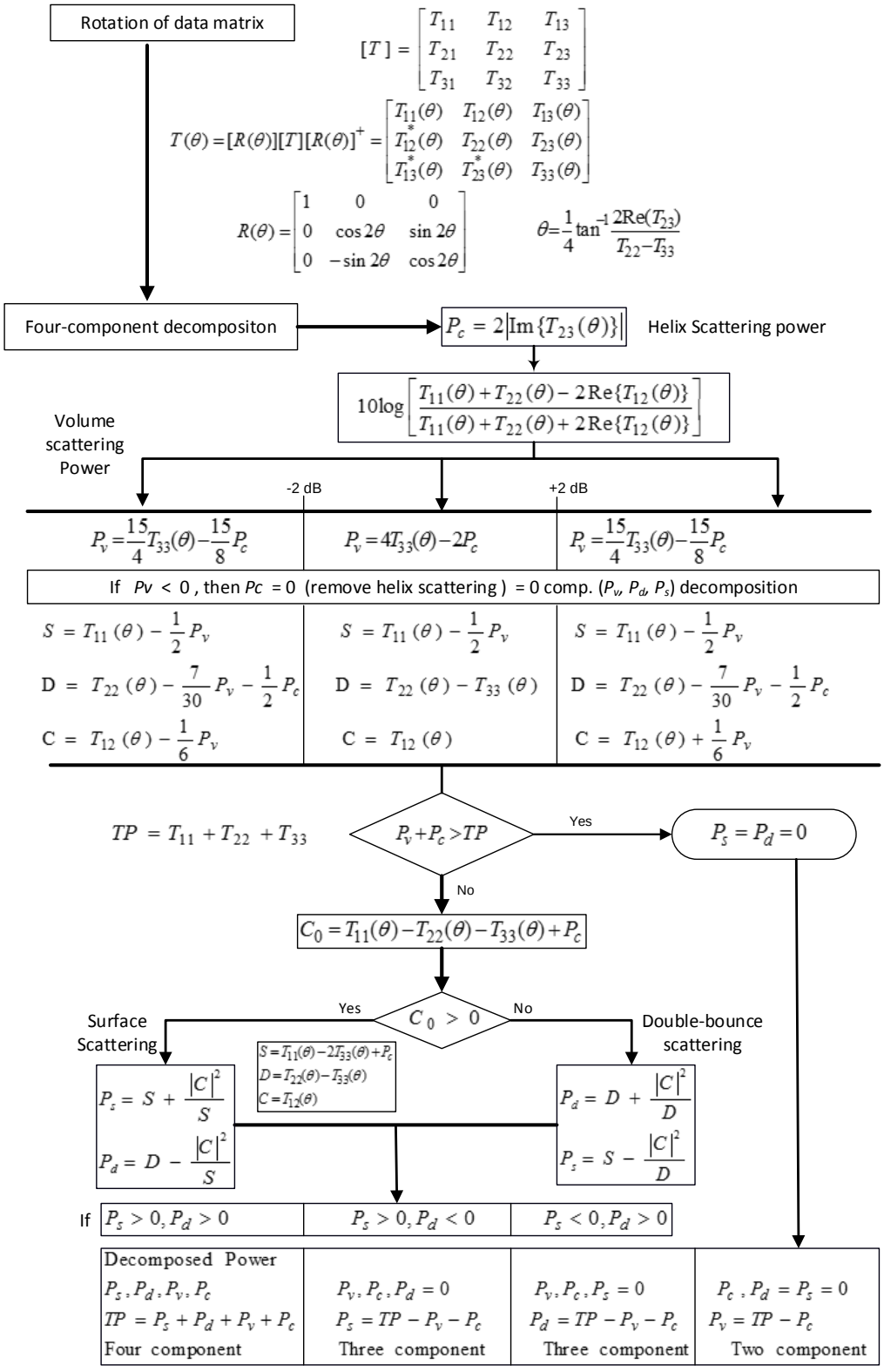

Figure B.5: Flowchart of algorithm for four component model based decomposition with deorientation (FCMD) [427].

B6. Four Component Decomposition with Deorientation and Additional Volume Scattering Model (FCMDA)

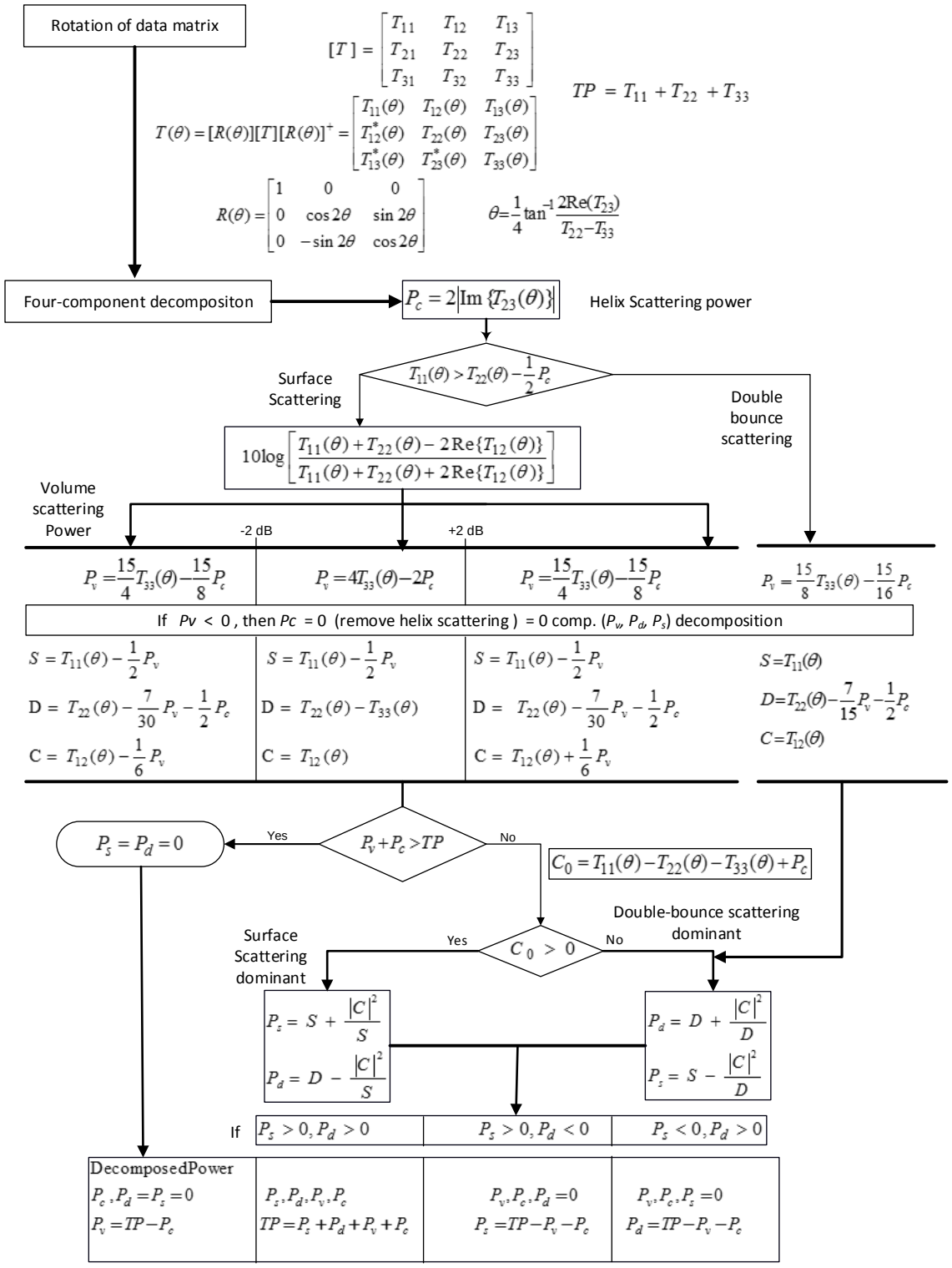

Figure B.6: Flowchart of algorithm for four component decomposition with deorientation and additional volume scattering model (FCMDA) [325].

B7. Four Component Model Based Decomposition Method with Double Deorientation (Unitary Transformation) (FCMDD)

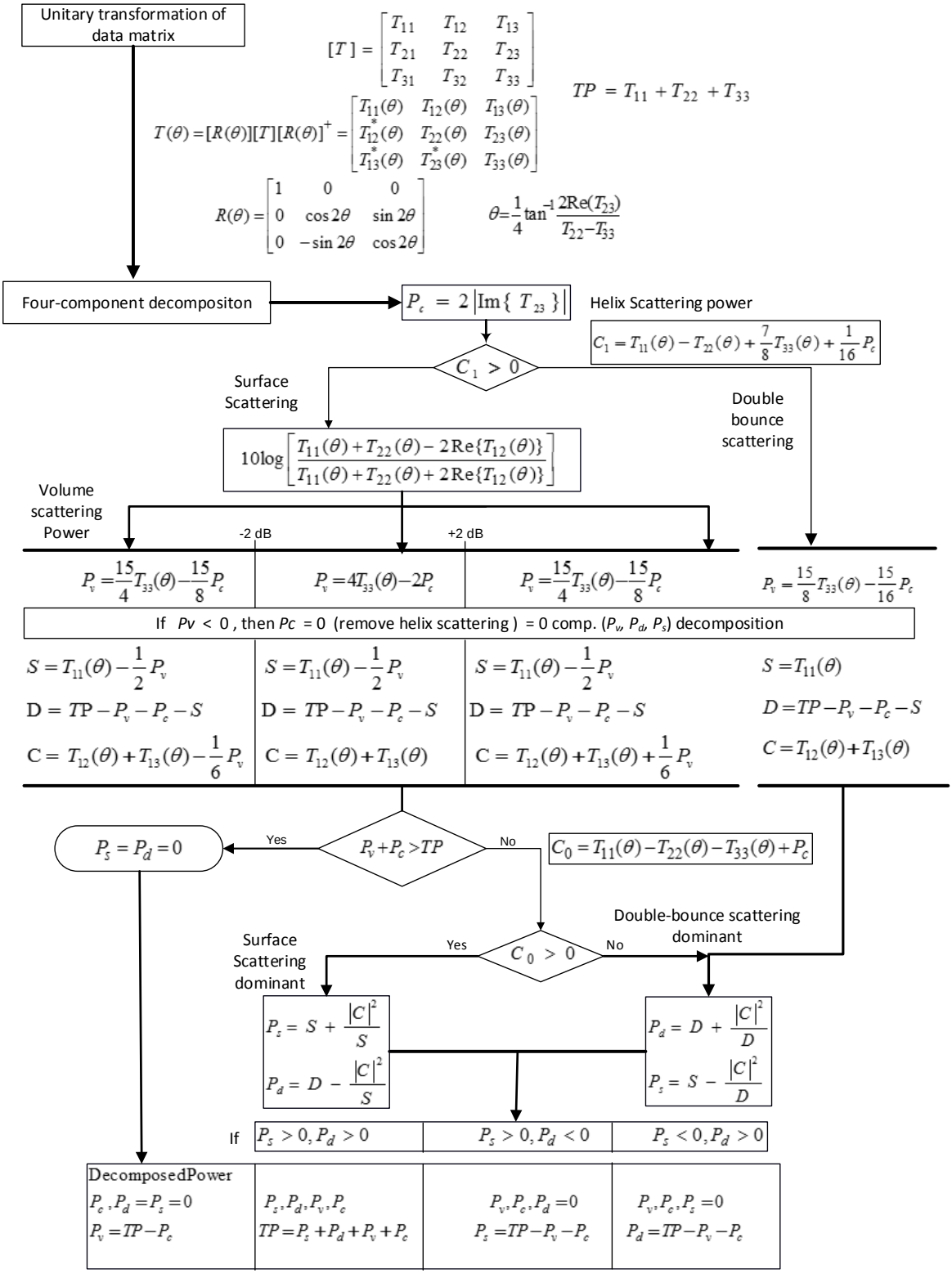

Figure B.7: Flowchart of algorithm for four component model based decomposition method with double deorientation (unitary transformation) (FCMDD) [344].

Appendix-C

Results of Model Based Decomposition Methods

C1. For Region- 2: Meerut

Data ID- PASL1100904231713261001150001

Center latitude- 28° 58' 32'' N

Center longitude -77° 42' 20'' E

In this region, five areas are selected for the analysis. In Figure C.1, numbers 1 to 4 represent urban areas designated as urban-1, urban-2, urban-3, and urban-4, respectively. White rectangle in Figure C.1, represent tall vegetation.

a) Visual analysis

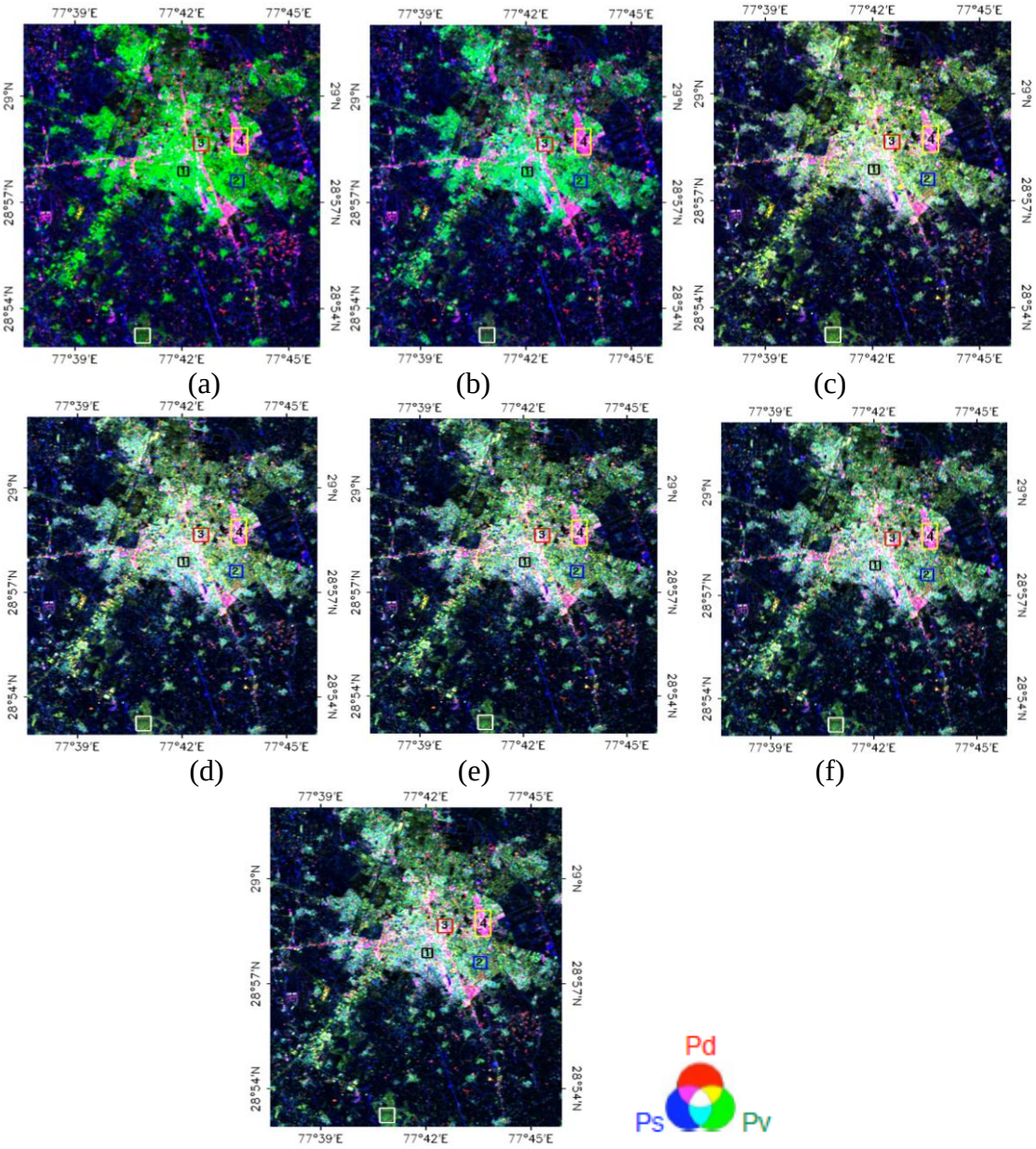

Figure C.1: RGB colour composite images with P_d as red component, P_v as green component, and P_s as blue colours for Region-2 (Meerut) : (a) TCM, (b) FCM, (c) TCMD, (d) TCMDDA, (e) FCMD, (f) FCMDA, and (g) FCMDD.

b) Power-wise quantitative analysis

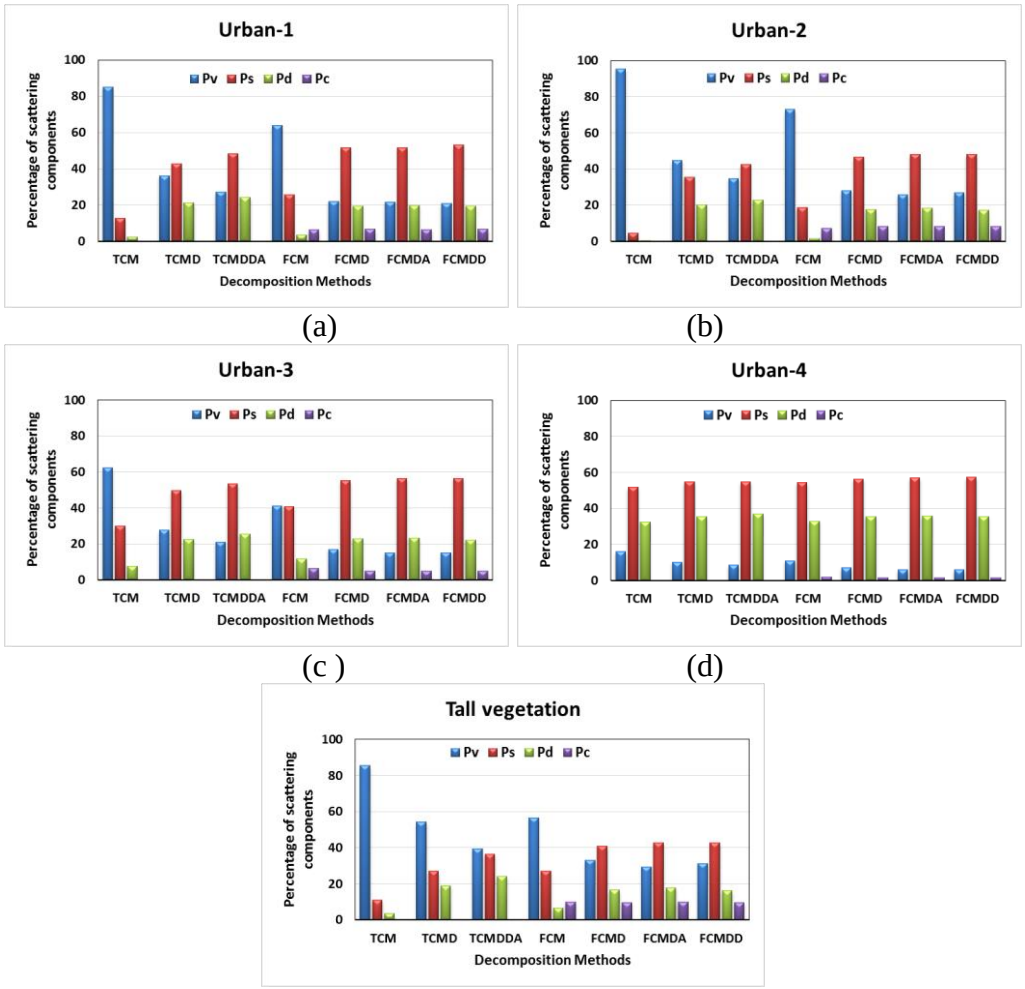

Figure C.2: Result of power wise analysis for studied decomposition methods for Region-2 (Meerut): (a) urban-1, (b) urban-2, (c) urban-3, (d) urban-4, and (e) tall vegetation, regions represented by number 1 to 4 and white rectangle, respectively, in Figure C.1.

C2. For Region-3: New Delhi

Data ID- PASL1100904231713261001150001

Center latitude- 28° 58' 32'' N

Center longitude -77° 42' 20'' E

In this region, six areas have been selected for the analysis. Numbers 1 to 5 in Figure C.3 represent urban areas designated as urban-1, urban-2, urban-3, urban-4, and urban-5, respectively. Number 6 represent bridge over the river.

a) Visual analysis

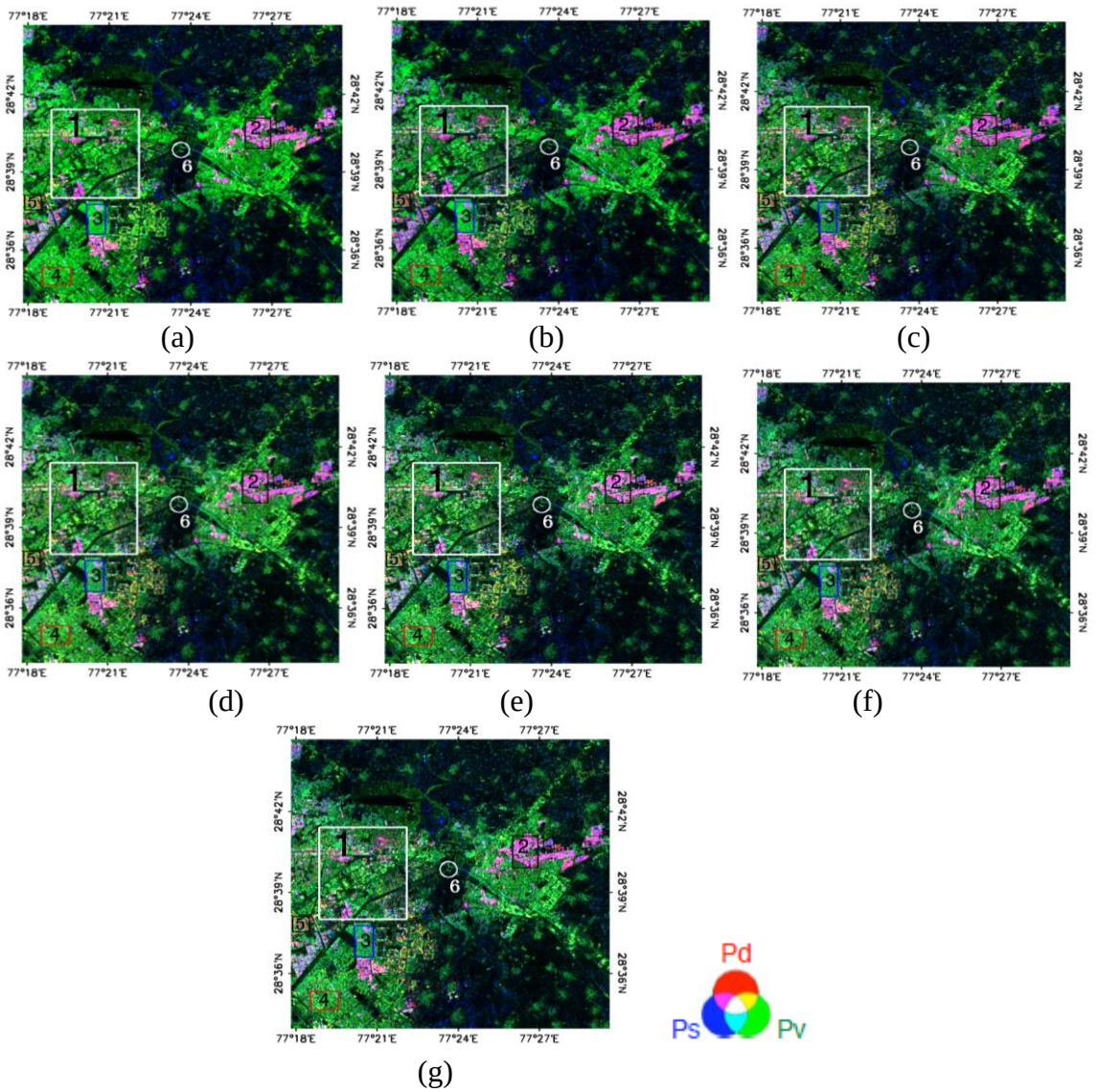

Figure C.3: RGB colour composite images with P_d as red colour, P_v as green colour, and P_s as blue colour for Region-3 (New Delhi): (a) TCM, (b) FCM, (c) TCMD, (d) TCMDDA, (e) FCMD, (f) FCMDA, and (g) FCMDD.

b) Power-wise quantitative analysis

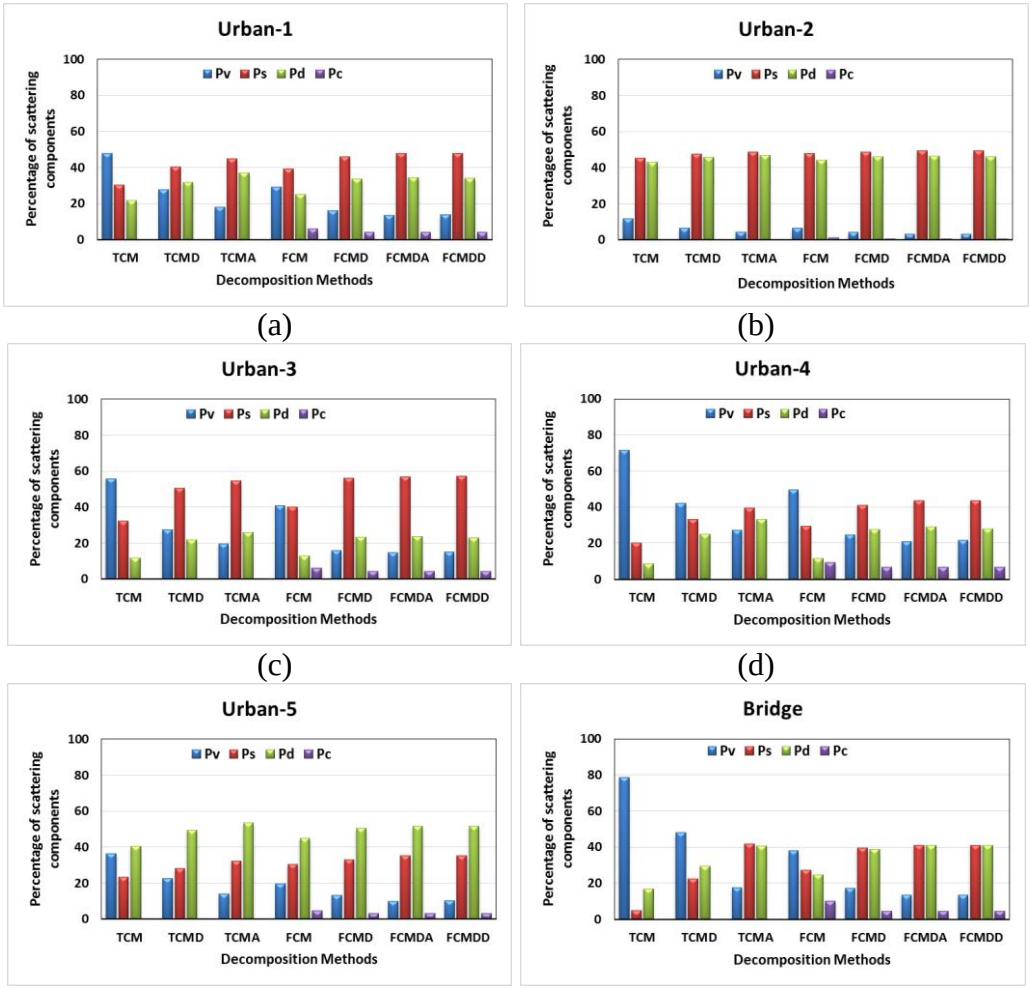

Figure C.4: Result for power wise analysis of studied decomposition methods for Region-3 (New Delhi): (a) urban-1, (b) urban-2, (c) urban-3, (d) urban-4, (e) urban-5, and (f) bridge, represented by number 1 to 6, respectively, in Figure C.3.

Author's Publications

International Journals

[1] **Mishra, P.,** and Singh, D., A Statistical Measure Based Adaptive Land Cover Classification Algorithm by Efficient Utilization of Polarimetric SAR Observables. *IEEE Transactions on Geoscience and Remote Sensing*, vol.52, no.5, pp. 2889-2900, 2014.

[2] Mittal, G., **Mishra**, **P.**, and Dharmendra Singh, Fusion of Polarimetric Channel Information of PALSAR Data for Land Cover Classification. *Geomatics, Natural Hazards and Risk*, vol. 5, no. 2, pp. 157-172, 2014.

[3] **Mishra, P.,** Singh, D., and Yamaguchi, Y., Land Cover Classification of PALSAR Images by Knowledge Based Decision Tree Classifier and Supervised Classifiers Based on SAR Observables. *Progress in Electromagnetics Research B (Published by USA)*, vol.30, pp. 47-70, 2011.

[4] **Mishra, P.,** Kumar, S., and Singh, D., An Approach for Finding Possible Presence of Water Ice Deposits on Lunar Craters Using MINISAR. *IEEE Journal of Selected Topics in Applied Earth Observations and Remote Sensing*. **Under Review**.

[5] **Mishra, P.,** and Singh, D., Multilayer model for Soil Moisture Retrieval under Vegetation Cover. *IEEE Transaction of Geoscience and Remote Sensing*. **Communicated.**

International Conferences

[1] **Mishra**, P., Singh, K.P., Singh, D., and Rajput, N. S., Critical Analysis of Deorientation Effect on Various Land Covers: An Application of PolSAR Data. *IEEE International Symposium on Geoscience and Remote Sensing (IGARSS)*, July 13-18, 2014. Quebec, Canada. **Accepted.**

[2] **Mishra, P.,** and Singh, D., Critical Analysis of Lunar Surface for its Physical Properties: An Application of MiniSAR data. *Proceedings of 45th Lunar and Planetary Institute Science Conference Abstracts*, vol. 45, pp. 1694, March 17-21, 2014, The Woodlands, Texas.

[3] **Mishra**, **P.**, Rajashekhar, U., and Singh, D., Study and Characterization of Lunar Craters Using MINI-SAR Data of Chandrayaan-1. *Proceedings of International Conference on Microwave and Photonics*, December 13-15, 2013, Dhanbad, India.

[4] Gupta, S., Singh, D., **Mishra, P.,** and Garg, S. K., Probability Density Functions Based Study for Identification of Land Cover Using SAR Data. *Proceedings of International Conference on Microwave and Photonics*, December 13-15, 2013, Dhanbad, India.

[5] **Mishra, P.,** Kumar, S., and Singh, D., An Approach to Determine Possible Existence of Water Ice Deposits on Lunar Craters Using MiniSAR Data. *Proceedings of IEEE International Symposium on Geoscience and Remote Sensing (IGARSS)*, pp. 21-24, July 21-26, 2013, Melbourne, Australia.

[6] **Mishra**, P., Goel, S., and Singh, D., An Impedance Based Approach to Determine Soil Moisture Using Radarsat-2 Data. *Proceedings of IEEE International Symposium on Geoscience and Remote Sensing (IGARSS)*, pp. 2724-2727, July 21-26, 2013, Melbourne, Australia.

[7] **Mishra, P.,** and Singh, D., Transmission Line Theory Based Two Layer Model for Determining Soil Moisture. *Proceedings of International Archives of the Photogrammetry, Remote Sensing and Spatial Information Sciences*, vol. XL-1/W1, pp. 253-256, May 21- 24, 2013, Hannover, Germany.

[8] **Mishra, P.,** and Singh, D., Role of Polarimetric Indices Based on Statistical Measures to Identify Various Land Cover Classes in ALOS PALSAR Data. *Proceedings of 3rd International Asia-Pacific Conference on Synthetic Aperture Radar (APSAR),* pp.1-4, September 26-30, 2011, Seoul, Korea.

[9] **Mishra, P.,** and Singh, D., Study of Effect of Deorientation on PALSAR Data for Land Cover Identification. *Proceedings of 39th COSPAR Scientific Assembly*, July 14-22, 2012, Mysore, India.

National Conferences

[1] **Mishra, P.,** and Singh, D., Spatial Statistics Based Adaptive Classification Approach Using L-band ALOS PALSAR Data. In *National Symposium on Space Technology for Food & Environmental Security of Indian Society of Remote Sensing and Indian Society of Geomatics,* December 5-7, 2012, New Delhi, India.

[2] **Mishra, P.,** Singh, D., and Kumar, S., Unsupervised Contextual Classification of Chandrayaan-1's Mini SAR Image Using Fractal Based Approach. In *National Symposium on Space Technology for Food & Environmental Security of Indian Society of Remote Sensing and Indian Society of Geomatics,* December 5-7, 2012, New Delhi, India.

[3] **Mishra**, **P.**, Goel, S., Singh, D., and Srivastava, V., Multilayer Modeling Approach for Measuring Soil Moisture and Thickness Using Genetic Algorithm. *Proceedings of International Conference on Microwaves, Antenna Propagation and Remote Sensing (ICMARS)*, December 11-15, 2012, Jodhpur, India.

[4] Kumar, S., Singh, D., and **Mishra**, **P.**, Fractal and Moran's I analysis for classification of Lunar surface Using Mini-SAR data of Chandrayan-1. In *National Conference on Recent Trends in Microwave Techniques and Applications, Microwave-12,* July 30- August 1, 2012, Jaipur, India.

Workshop

[1] Singh, D., and **Mishra**, **P.**, Polarimetric data application for identification of various land covers. Workshop on Second Chandrayaan-1 Mini-SAR Data Analysis, September 11, 2011, Space Application Center, Ahmedabad, India.

References

1. SARscape Help Document. .
2. Aghababaee, H., Amini, J., and Tzeng, Y.C., Contextual PolSAR Image Classification Using Fractal Dimension and Support Vector Machines. *European Journal of Remote Sensing*, vol. 46, pp. 317-332, 2013.
3. Agrawal, A. and Boerner, W.M., Redevelopment of Kennaugh's Target Characteristic Polarization State Theory Using the Polarization Transformation Ration Formalism for the Coherent Case. *IEEE Transactions on Geoscience and Remote Sensing*, vol. 27, no. 1, pp. 2-14, 1989.
4. Ainsworth, T.L., Cloude, S.R., and Lee, J.S., Eigenvector Analysis of Polarimetric SAR Data, Proceedings of *IEEE International Geoscience and Remote Sensing Symposium (IGARSS)*, Toronto, Canada, 2002, vol. 1, pp. 626-628.
5. Al-Bilbisi, H., Tateishi, R., and Tetuko, S.S.J., A Technique to Estimate Topsoil Thickness in Arid and Semi-Arid Areas of North-Eastern Jordan Using Synthetic Aperture Radar Data. *International Journal of Remote Sensing*, vol. 25, no. 19, pp. 3873-3882, 2004.
6. Alvarez-Mozos, J., Casali, J., González-Audícana, M., and Verhoest, N.E.C., Assessment of the Operational Applicability of RADARSAT-1 Data for Surface Soil Moisture Estimation. *IEEE Transactions on Geoscience and Remote Sensing*, vol. 44, no. 4, pp. 913-924, 2006.
7. Álvarez-Pérez, J.L., An Extension of the IEM/IEMM Surface Scattering Model. *Waves in Random Media*, vol. 11, no. 3, pp. 307-329, 2001.
8. An, W., Cui, Y., and Yang, J., Three-Component Decomposition for Polarimetric SAR, Proceedings of *IEEE International Geoscience and Remote Sensing Symposium (IGARSS)*, Cape Town, Africa, 2009, vol. 3, pp. III-713-III-716.
9. An, W., Cui, Y., and Yang, J., Three-Component Model-Based Decomposition for Polarimetric SAR Data. *IEEE Transactions on Geoscience and Remote Sensing*, vol. 48, no. 6, pp. 2732-2739, 2010.
10. An, W., Xie, C., Yuan, X., Cui, Y., and Yang, J., Four-Component Decomposition of Polarimetric SAR Images With Deorientation. *IEEE Geoscience and Remote Sensing Letters*, vol. 8, no. 6, pp. 1090-1094, 2011.
11. An, W., Zhang, W., Yang, J., Hong, W., and Cao, F., On the Similarity Parameter Between Two Targets for the Case of Multi-Look Polarimetric SAR. *Chinese Journal of Electronics*, vol. 18, no. 3, pp. 545-550, 2009.
12. Arii, M., van Zyl, J.J., and Yunjin, K., A General Characterization for Polarimetric Scattering From Vegetation Canopies. *IEEE Transactions on Geoscience and Remote Sensing*, vol. 48, no. 9, pp. 3349-3357, 2010.
13. Arii, M., van Zyl, J.J., and Yunjin, K., Adaptive Model-Based Decomposition of Polarimetric SAR Covariance Matrices. *IEEE Transactions on Geoscience and Remote Sensing*, vol. 49, no. 3, pp. 1104-1113, 2011.
14. Arii, M., van Zyl, J.J., and Yunjin, K., Improvement of Adaptive-Model Based Decomposition With Polarization Orientation Compensation, Proceedings of *IEEE International Geoscience and Remote Sensing Symposium (IGARSS)*, Munich, Germany, 2012, pp. 95-98.
15. Arnold, J.R., Ice in the Lunar Polar Regions. *Journal of Geophysical Research*, vol. 84, no. B10, pp. 5659-5668, 1979.

16. Attema, E. and Ulaby, F.T., Vegetation Modeled as a Water Cloud. *Radio Science*, vol. 13, no. 2, pp. 357-364, 1978.
17. Baghdadi, N., Aubert, M., Cerdan, O., Franchistéguy, L., Viel, C., Eric, M., Zribi, M., et al., Operational Mapping of Soil Moisture Using Synthetic Aperture Radar Data: Application to the Touch Basin (France). *Sensors*, vol. 7, no. 10, pp. 2458-2483, 2007.
18. Baghdadi, N., Boyer, N., Todoroff, P., El Hajj, M., and Bégué, A., Potential of SAR sensors TerraSAR-X, ASAR/ENVISAT and PALSAR/ALOS for Monitoring Sugarcane Crops on Reunion Island. *Remote Sensing of Environment*, vol. 113, no. 8, pp. 1724-1738, 2009.
19. Baghdadi, N. and Zribi, M., Evaluation of Radar Backscatter Models IEM, OH and Dubois Using Experimental Observations. *International Journal of Remote Sensing*, vol. 27, no. 18, pp. 3831-3852, 2006.
20. Baghdadi, N., Zribi, M., Loumagne, C., Ansart, P., and Anguela, T.P., Analysis of TerraSAR-X Data and Their Sensitivity to Soil Surface Parameters Over Bare Agricultural Fields. *Remote Sensing of Environment*, vol. 112, no. 12, pp. 4370-4379, 2008.
21. Balaji, C., Deiveegan, M., Venkateshan, S.P., Gairola, R.M., Sarkar, A., and Agarwal, V.K., Polarized Microwave Forward Model Simulations for Tropical Storm Fanoos. *Journal of Earth System Science*, vol. 118, no. 4, pp. 331-343, 2009.
22. Balaji, C., Deiveegan, M., Venkateshan, S.P., Gairola, R.M., Sarkar, A., and Agarwal, V.K., Retrieval of Hydrometeors From Microwave Radiances With a Polarized Radiative Transfer Model. *Journal of Earth System Science*, vol. 119, no. 1, pp. 97-115, 2010.
23. Balenzano, A., Mattia, F., Satalino, G., and Davidson, M., Dense Temporal Series of C- and L-Band SAR Data for Soil Moisture Retrieval Over Agricultural Crops. *IEEE Journal of Selected Topics in Applied Earth Observations and Remote Sensing*, vol. 4, no. 2, pp. 439-450, 2011.
24. Balogh, A., Ksanfomality, L., Steiger, R., and Harmon, J., Radar Imaging of Mercury, in *Mercury*. Springer: New York vol. 26, pp. 125-167, 2008.
25. Banerjee, B., Bhattacharya, A., and Buddhiraju, K.M., A Generic Land-Cover Classification Framework for Polarimetric SAR Images Using the Optimum Touzi Decomposition Parameter Subset—An Insight on Mutual Information-Based Feature Selection Techniques. *IEEE Journal of Selected Topics in Applied Earth Observations and Remote Sensing*, vol. 7, no. 4, pp. 1167-1176, 2014.
26. Barman, R., Prasad Kumar, B., Pandey, P.C., and Dube, S.K., Tsunami Travel Time Prediction Using Neural Networks. *Geophysical Research Letters*, vol. 33, no. 16, 2006.
27. Baronti, S., Del Frate, F., Ferrazzoli, P., Paloscia, S., Pampaloni, P., and Schiavon, G., SAR Polarimetric Features of Agricultural Areas. *International Journal of Remote Sensing*, vol. 16, no. 14, pp. 2639-2656, 1995.
28. Barrett, B.W., Dwyer, E., and Whelan, P., Soil Moisture Retrieval From Active Spaceborne Microwave Observations: An Evaluation of Current Techniques. *Remote Sensing*, vol. 1, no. 3, pp. 210-242, 2009.
29. Behari, J., *Microwave Dielectric Behaviour of Wet Soils*. Vol. 8. Springer: New York, 2006.
30. Berizzi, F., Bertini, G., Martorella, M., and Bertacca, M., Two-Dimensional Variation Algorithm for Fractal Analysis of Sea SAR Images. *IEEE Transactions on Geoscience and Remote Sensing*, vol. 44, no. 9, pp. 2361-2373, 2006.
31. Bhandari, S.M. and Varma, A.K., Potential of Simultaneous Dual-Frequency Radar

Altimeter Measurements From TOPEX/Poseidon for Rainfall Estimation Over Oceans. *Remote Sensing of Environment*, vol. 58, no. 1, pp. 13-20, 1996.
32. Bhattacharya, S., Saran, S., Dagar, A., Chauhan, P., Chauhan, M., Ajai, and Kiran Kumar, A.S., Endogenic Water on the Moon Associated With Non-Mare Silicic Volcanism: Implications for Hydrated Lunar Interior. *Current Science*, vol. 105, no. 5, pp. 685-694, 2013.
33. Bindlish, R. and Barros, A.P., Parameterization of Vegetation Backscatter in Radar-Based Soil Moisture Estimation. *Remote Sensing of Environment*, vol. 76, no. 1, pp. 130-137, 2001.
34. Bindlish, R., Jackson, T., Sun, R., Cosh, M., Yueh, S., and Dinardo, S., Combined Passive and Active Microwave Observations of Soil Moisture During CLASIC. *IEEE Geoscience and Remote Sensing Letters*, vol. 6, no. 4, pp. 644-648, 2009.
35. Boerner, W.M., Recent Advances in Extra-Wide-Band Polarimetry, Interferometry and Polarimetric Interferometry in Synthetic Aperture Remote Sensing and its Applications. *IEE Proceedings Radar, Sonar and Navigation*, vol. 150, no. 3, pp. 113-124, 2003.
36. Boerner, W.M., Cloude, S.R., Lee, J.S., Papathanassiou, K.P., and Lukowski, T.I., Advances in Extra Wide-Band Multi-Modal Air/Space-Borne Radar Polarimetry, POL-IN-SAR Imaging and its Applications, Proceedings of *IEEE International Geoscience and Remote Sensing Symposium (IGARSS)*, Toronto, Canada, 2002, vol. 1, pp. 408-410
37. Boerner, W.M., El-Arini, M., Chung-Yee, C., and Mastoris, P., Polarization Dependence in Electromagnetic Inverse Problems. *IEEE Transactions on Antennas and Propagation*, vol. 29, no. 2, pp. 262-271, 1981.
38. Boerner, W.M., Foo, B.Y., and Eom, H.J., Interpretation of the Polarimetric Co-Polarization Phase Tern in Radar Images Obtained With the JPL Airborne L-Band SAR System. *IEEE Transactions on Geoscience and Remote Sensing*, vol. GE-25, no. 1, pp. 77-82, 1987.
39. Boerner, W.M., Jordan, A.K., and Kay, I., Introduction to the Special Issue on Inverse Methods in Electromagnetics. *IEEE Transactions on Antennas and Propagation*, vol. 29, no. 2, pp. 185-189, 1981.
40. Boerner, W.M., Wei-ling, Y., Xi, A.Q., and Yamaguchi, Y., On the Basic Principles of Radar Polarimetry: The Target Characteristic Polarization State Theory of Kennaugh, Huynen's Polarization Fork Concept, and its Extension to the Partially Polarized Case. *Proceedings of the IEEE*, vol. 79, no. 10, pp. 1538-1550, 1991.
41. Boerner, W.M. and Yamaguchi, Y., A State-of-the-Art Review in Radar Polarimetry and its Applications in Remote Sensing. *IEEE Aerospace and Electronic Systems Magazine*, vol. 5, no. 6, pp. 3-6, 1990.
42. Boerner, W.M., Yan, W.L., Xi, A.Q., and Yamaguchi, Y., Basic Concepts of Radar Polarimetry, in *Direct and Inverse Methods in Radar Polarimetry*, Boerner, W.M., et al., Editors. Springer: Netherlands, vol. 350, pp. 155-245, 1992.
43. Bolten, J.D., Crow, W.T., Xiwu, Z., Jackson, T.J., and Reynolds, C.A., Evaluating the Utility of Remotely Sensed Soil Moisture Retrievals for Operational Agricultural Drought Monitoring. *IEEE Journal of Selected Topics in Applied Earth Observations and Remote Sensing*, vol. 3, no. 1, pp. 57-66, 2010.
44. Boyce, J.W., Liu, Y., Rossman, G.R., Guan, Y., Eiler, J.M., Stolper, E.M., and Taylor, L.A., Lunar Apatite wth Terrestrial Volatile Abundances. *Nature*, vol. 466, no. 7305, pp. 466-469, 2010.
45. Brian, W.B. and George, P.P., Satellite Remote Sensing of Surface Soil Moisture, in

Remote Sensing of Energy Fluxes and Soil Moisture Content. CRC Press, pp. 85-120, 2013.

46. Bryant, R., Moran, M.S., Thoma, D.P., Collins, C.D.H., Skirvin, S., Rahman, M., Slocum, K., et al., Measuring Surface Roughness Height to Parameterize Radar Backscatter Models for Retrieval of Surface Soil Moisture. *IEEE Geoscience and Remote Sensing Letters*, vol. 4, no. 1, pp. 137-141, 2007.
47. Bussey, D.B.J., Fristad, K.E., Schenk, P.M., Robinson, M.S., and Spudis, P.D., Planetary Science: Constant Illumination at the Lunar North Pole. *Nature*, vol. 434, no. 7035, pp. 842-842, 2005.
48. Butler, B.J., Muhleman, D.O., and Slade, M.A., Mercury: Full-Disk Radar Images and the Detection and Stability of Ice at the North Pole. *Journal of Geophysical Research: Planets*, vol. 98, no. E8, pp. 15003-15023, 1993.
49. Calla, O.P.N., Mathur, S., and Jangid, M., Comparision of Dielectric Constant of Apollo 17 Samples With MINI-RF and TALS, Proceedings of *LPI Contributions: Large Meteorite Impacts and Planetary Evolution V*, Sudbury, Canada, 2013, vol. 1737, pp. 3007.
50. Calla, O.P.N., Mathur, S., and Jangid, M., Study of Plato Crater With the Mini-RF, Proceedings of *Lunar and Planetary Institute Science Conference Abstracts*, The Woodlands, Texas, 2013, vol. 44, pp. 1854.
51. Cameron, W.L. and Leung, L.K., Feature Motivated Polarization Scattering Matrix Decomposition, Proceedings of *IEEE International Radar Conference*, Arlington, Texas, 1990, vol. 1, pp. 549-557.
52. Campbell, B.A., Grant, J.A., and Maxwell, T., Radar Penetration in Mars Analog Environments, Proceedings of *Lunar and Planetary Institute Science Conference Abstracts*, 2002, vol. 33, pp. 1616.
53. Campbell, D.B., Campbell, B.A., Carter, L.M., Margot, J.L., and Stacy, N.J.S., No Evidence for Thick Deposits of Ice at the Lunar South Pole. *Nature*, vol. 443, no. 7113, pp. 835-837, 2006.
54. Carr, J.R. and De Miranda, F.P., The Semivariogram in Comparison to the Co-occurrence Matrix for Classification of Image Texture. *IEEE Transactions on Geoscience and Remote Sensing*, vol. 36, no. 6, pp. 1945-1952, 1998.
55. Carrea, L. and Wanielik, G., Polarimetric SAR Processing Using the Polar Decomposition of the Scattering Matrix, Proceedings of *IEEE International Geoscience and Remote Sensing Symposium (IGARSS)*, Sydney, Australia, 2001, vol. 1, pp. 363-365.
56. Carrier, W.D., Olhoeft, G.R., and Mendell, W., Physical Properties of the Lunar Surface, in *Lunar Source Book*, Grant H. Heiken, Vaniman, D.T., and French, B.M., Editors. Cambridge University Press: New York, pp. 475-594, 1991.
57. Carter, L.M., Campbell, D.B., and Campbell, B.A., Impact Crater Related Surficial Deposits on Venus: Multipolarization Radar Observations With Arecibo. *Journal of Geophysical Research: Planets*, vol. 109, no. E6, pp. E06009, 2004.
58. Carter, L.M., Campbell, D.B., and Campbell, B.A., Volcanic Deposits in Shield Fields and Highland Regions on Venus: Surface Properties From Radar Polarimetry. *Journal of Geophysical Research*, vol. 111, no. E6, pp. E06005, 2006.
59. Carter, L.M., Campbell, D.B., and Campbell, B.A., Geologic Studies of Planetary Surfaces Using Radar Polarimetric Imaging. *Proceedings of the IEEE*, vol. 99, no. 5, pp. 770-782, 2011.
60. Carter, L.M., Rincon, R., and Berkoski, L., Mapping the Upper Subsurface of Mars

Using Radar Polarimetry, Proceedings of *LPI Contributions: Concepts and Approaches for Mars Exploration*, Houston, Texas, 2012, vol. 1679, pp. 4285.
61. Chamundeeswari, V.V., Singh, D., and Singh, K., An Analysis of Texture Measures in PCA-based Unsupervised Classification of SAR Images. *IEEE Geoscience and Remote Sensing Letters*, vol. 6, no. 2, pp. 214-218, 2009.
62. Chandrasekhar, S., *Radiative Transfer*. Courier Dover Publications: New York,, 1960.
63. Charbonneau, F., Brisco, B., Raney, R.K., McNairn, H., Liu, C., Vachon, P.W., Shang, J., et al., Compact Polarimetry Overview and Applications Assessment. *Canadian Journal of Remote Sensing*, vol. 36, no. S2, pp. S298-S315, 2010.
64. Chen, C.T., Chen, K.S., and Lee, J.S., The Use of Fully Polarimetric Information for the Fuzzy Neural Classification of SAR Images. *IEEE Transactions on Geoscience and Remote Sensing*, vol. 41, no. 9, pp. 2089-2100, 2003.
65. Chen, K.S., Huang, W.P., Tsay, D.H., and Amar, F., Classification of Multifrequency Polarimetric SAR Imagery Using a Dynamic Learning Neural Network. *IEEE Transactions on Geoscience and Remote Sensing*, vol. 34, no. 3, pp. 814-820, 1996.
66. Chen, K.S., Wu, T.D., Tsang, L., Li, Q., Shi, J., and Fung, A.K., Emission of Rough Surfaces Calculated by the Integral Equation Method With Comparison to Three-Dimensional Moment Method Simulations. *IEEE Transactions on Geoscience and Remote Sensing*, vol. 41, no. 1, pp. 90-101, 2003.
67. Chen, P.H. and Dowman, I.J., SAR Image Geocoding Using a Stereo-SAR DEM and Automatically Generated GCPs, Proceedings of *International Archives of Photogrammetry and Remote Sensing*, Amsterdam, 2000, vol. XXXIII, pp. 38-45.
68. Chen, Q., Kuang, G., Li, J., Sui, L., and Li, D., Unsupervised Land Cover/Land Use Classification Using PolSAR Imagery Based on Scattering Similarity. *IEEE Transactions on Geoscience and Remote Sensing*, vol. 51, no. 3, pp. 1817-1825, 2013.
69. Chen, S.W. and Sato, M., General Polarimetric Model-Based Decomposition for Coherency Matrix, Proceedings of *IEEE International Geoscience and Remote Sensing Symposium (IGARSS)*, Munich, Germany, 2012, pp. 99-102.
70. Chen, S.W., Wang, X.S., Li, Y.Z., and Sato, M., Adaptive Model-Based Polarimetric Decomposition Using PolInSAR Coherence. *IEEE Transactions on Geoscience and Remote Sensing*, vol. 52, no. 2, pp. 1705 - 1718, 2014.
71. Chen, S.W., Wang, X.S., Xiao, S.P., and Sato, M., General Polarimetric Model-Based Decomposition for Coherency Matrix. *IEEE Transactions on Geoscience and Remote Sensing*, vol. 52, no. 3, pp. 1843-1855, 2014.
72. Cheng, Q., Varshney, P.K., and Arora, M.K., Logistic Regression for Feature Selection and Soft Classification of Remote Sensing Data. *IEEE Geoscience and Remote Sensing Letters*, vol. 3, no. 4, pp. 491-494, 2006.
73. Chin-Yuan, H., Fung, A.K., Nesti, G., Sieber, A.J., and Coppo, P., A Further Study of the IEM Surface Scattering Model. *IEEE Transactions on Geoscience and Remote Sensing*, vol. 35, no. 4, pp. 901-909, 1997.
74. Chumsamrong, W., Thitimajshima, P., and Rangsanseri, Y., Wavelet-Based Texture Analysis for SAR Image Classification, Proceedings of *IEEE International Geoscience and Remote Sensing Symposium (IGARSS)*, Hamburg, Germany, 1999, vol. 3, pp. 1564-1566.
75. Clark, R.N., Detection of Adsorbed Water and Hydroxyl on the Moon. *Science*, vol. 326, no. 5952, pp. 562-564, 2009.
76. Clarke, K.C., Computation of the Fractal Dimension of Topographic Surfaces Using the Triangular Prism Surface Area Method. *Computers & Geosciences*, vol. 12, no. 5, pp.

713-722, 1986.
77. Cloude, S.R., Target Decomposition Theorems in Radar Scattering. *Electronics Letters*, vol. 21, no. 1, pp. 22-24, 1985.
78. Cloude, S.R., Uniqueness of Target Decomposition Theorems in Radar Polarimetry, in *Direct and Inverse Methods in Radar Polarimetry*, Boerner, W.M., et al., Editors. Springer Netherlands, vol. 350, pp. 267-296, 1992.
79. Cloude, S.R., *Polarisation: Applications in Remote Sensing*. Oxford University Press Inc.: New York, 2010.
80. Cloude, S.R. and Pottier, E., A Review of Target Decomposition Theorems in Radar Polarimetry. *IEEE Transactions on Geoscience and Remote Sensing*, vol. 34, no. 2, pp. 498-518, 1996.
81. Cloude, S.R. and Pottier, E., An Entropy Based Classification Scheme for Land Applications of Polarimetric SAR. *IEEE Transactions on Geoscience and Remote Sensing*, vol. 35, no. 1, pp. 68-78, 1997.
82. Colaprete, A., Schultz, P., Heldmann, J., Wooden, D., Shirley, M., Ennico, K., Hermalyn, B., et al., Detection of Water in the LCROSS Ejecta Plume. *Science*, vol. 330, no. 6003, pp. 463-468, 2010.
83. Copeland, J.R., Radar Target Classification by Polarization Properties. *Proceedings of the IRE*, vol. 48, no. 7, pp. 1290-1296, 1960.
84. Corr, D.G., Cloude, S.R., Ferro-Famil, L., Hoekman, D.H., Partington, K., Pottier, E., and Rodrigues, A., A Review of the Applications of SAR Polarimetry and Polarimetric Interferometry-An ESA-Funded Study, Proceedings of *Applications of SAR Polarimetry and Polarimetric Interferometry*, Frascati, Italy, 2003, vol. 529, pp. 1.
85. Corr, D.G., Walker, A., Benz, U., Lingenfelder, I., and Rodrigues, A., Classification of Urban SAR Imagery Using Object Oriented Techniques, Proceedings of *IEEE International Geoscience and Remote Sensing Symposium (IGARSS)*, Toulouse, France, 2003, vol. 1, pp. 188-190.
86. Crotts, A.P.S., Lunar Outgassing, Transient Phenomena, and the Return to the Moon. I. Existing Data. *The Astrophysical Journal*, vol. 687, no. 1, pp. 692, 2008.
87. Crotts, A.P.S. and Hummels, C., Lunar Outgassing, Transient Phenomena, and the Return to the Moon. II. Predictions and Tests for Outgassing/Regolith Interactions. *The Astrophysical Journal*, vol. 707, no. 2, pp. 1506, 2009.
88. Cui, Y., Yamaguchi, Y., Yang, J., and Kobayashi, H., On Exact Model-Based Scattering Decomposition of Polarimetric SAR Data, Proceedings of *IEEE International Symposium on Antennas and Propagation*, Chicago, USA, 2012, pp. 106-109.
89. Cui, Y., Yamaguchi, Y., Yang, J., Kobayashi, H., Park, S.E., and Singh, G., On Complete Model-Based Decomposition of Polarimetric SAR Coherency Matrix Data. *IEEE Transactions on Geoscience and Remote Sensing*, vol. 52, no. 4, pp. 1991-2001, 2014.
90. Cui, Y., Yamaguchi, Y., Yang, J., Park, S.E., Kobayashi, H., and Singh, G., Three-Component Power Decomposition for Polarimetric SAR Data Based on Adaptive Volume Scatter Modeling. *Remote Sensing*, vol. 4, no. 6, pp. 1559-1572, 2012.
91. Cumming, I.G. and van Zyl, J.J., Feature Utility in Polarimetric Radar Image Classificatiion, Proceedings of *IEEE International Geoscience and Remote Sensing Symposium (IGARSS)*, Vancouver, Canada, 1989, vol. 3, pp. 1841-1846.
92. Dabboor, M., Collins, M.J., Karathanassi, V., and Braun, A., An Unsupervised Classification Approach for Polarimetric SAR Data Based on the Chernoff Distance for

Complex Wishart Distribution. *IEEE Transactions on Geoscience and Remote Sensing*, vol. 51, no. 5, pp. 4200-4213, 2013.
93. Darymli, K.E., Understanding the Significance of Radiometric Calibration for SAR Imagery: A Radar Equation Perspective, Proceedings of *IEEE Newfoundland Electrical and Computer Engineering Conference*, Toronto, Canada, 2012, pp. 1-6.
94. Davenport, I.J., Fernández-Gálvez, J., and Gurney, R.J., A Sensitivity Analysis of Soil Moisture Retrieval From the Tau-Omega Microwave Emission Model. *IEEE Transactions on Geoscience and Remote Sensing*, vol. 43, no. 6, pp. 1304-1316, 2005.
95. Davidovitz, M. and Boerner, W.M., Extension of Kennaugh's Optimal Polarization Concept to the Asymmetric Scattering Matrix Case. *IEEE Transactions on Antennas and Propagation*, vol. 34, no. 4, pp. 569-574, 1986.
96. De Cola, L., Fractal Analysis of a Classified Landsat Scene. *Photogrammetric Engineering and Remote Sensing*, vol. 55, no. 5, pp. 601-610, 1989.
97. De Jong, S.M. and Burrough, P.A., A Fractal Approach to the Classification of Mediterranean Vegetation Types in Remotely Sensed Images. *Photogrammetric Engineering and Remote Sensing*, vol. 61, no. 8, pp. 1041-1053, 1995.
98. De Roo, R.D., Du, Y., Ulaby, F.T., and Dobson, M.C., A Semi-Empirical Backscattering Model at L-Band and C-Band for a Soybean Canopy with Soil Moisture Inversion. *IEEE Transactions on Geoscience and Remote Sensing*, vol. 39, no. 4, pp. 864-872, 2001.
99. Deng, Y., Dai, Q., Wang, R., and Zhang, Z., Commute Time Guided Transformation for Feature Extraction. *Computer Vision and Image Understanding*, vol. 116, no. 4, pp. 473-483, 2012.
100. Deng, Y., Dai, Q., and Zhang, Z., Graph Laplace for Occluded Face Completion and Recognition. *IEEE Transactions on Image Processing*, vol. 20, no. 8, pp. 2329-2338, 2011.
101. Deschamps, A., Pultz, T.J., Pietroniro, A., and Best, K., Temporal Soil Moisture Estimates From RADARSAT-1 and ENVISAT ASAR for Flood Forecasting, Proceedings of *IEEE International Geoscience and Remote Sensing Symposium (IGARSS)*, Anchorage, USA, 2004, vol. 3, pp. 2119-2122.
102. Deschamps, G.A., Techniques for Handling Elliptically Polarized Waves With Special Reference to Antennas: Part II-Geometrical Representation of the Polarization of a Plane Electromagnetic Wave. *Proceedings of the IRE*, vol. 39, no. 5, pp. 540-544, 1951.
103. Didascalou, D., Dottling, M., Geng, N., and Wiesbeck, W., An Approach to Include Stochastic Rough Surface Scattering into Deterministic Ray-Optical Wave Propagation Modeling. *IEEE Transactions on Antennas and Propagation*, vol. 51, no. 7, pp. 1508-1515, 2003.
104. Digby-Argus, S., Hawkins, R.K., and Singh, K.P., Microwave Remote Sensing of Ice in Lake Melville and the Labrador Sea. *IEEE Journal of Oceanic Engineering*, vol. 12, no. 3, pp. 503-517, 1987.
105. Dobson, M.C., Pierce, L., Sarabandi, K., Ulaby, F.T., and Sharik, T., Preliminary Analysis of ERS-1 SAR for Forest Ecosystem Studies. *IEEE Transactions on Geoscience and Remote Sensing*, vol. 30, no. 2, pp. 203-211, 1992.
106. Dobson, M.C., Pierce, L.E., and Ulaby, F.T., Knowledge-Based Land-Cover Classification Using ERS-1/JERS-1 SAR Composites. *IEEE Transactions on Geoscience and Remote Sensing*, vol. 34, no. 1, pp. 83-99, 1996.
107. Dobson, M.C. and Ulaby, F.T., Active Microwave Soil Moisture Research. *IEEE Transactions on Geoscience and Remote Sensing*, vol. GE-24, no. 1, pp. 23-36, 1986.

108. Dobson, M.C., Ulaby, F.T., Hallikainen, M.T., and El-Rayes, M.A., Microwave Dielectric Behavior of Wet Soil-Part II: Dielectric Mixing Models. *IEEE Transactions on Geoscience and Remote Sensing*, vol. 23, no. 1, pp. 35-46, 1985.
109. Doulgeris, A.P., Anfinsen, S.N., and Eltoft, T., Classification With a Non-Gaussian Model for PolSAR data. *IEEE Transactions on Geoscience and Remote Sensing*, vol. 46, no. 10, pp. 2999-3009, 2008.
110. Douville, H. and Chauvin, F., Relevance of Soil Moisture for Seasonal Climate Predictions: A Preliminary Study. *Climate Dynamics*, vol. 16, no. 10-11, pp. 719-736, 2000.
111. Drusch, M., Initializing Numerical Weather Prediction Models With Satellite-Derived Surface Soil Moisture: Data Assimilation Experiments With ECMWF's Integrated Forecast System and the TMI Soil Moisture Data Set. *Journal of Geophysical Research*, vol. 112, no. D3, 2007.
112. Du, L.J., Lee, J.S., Hoppel, K., and Mango, S.A., Segmentation of SAR Images Using the Wavelet Transform. *International Journal of Imaging Systems and Technology*, vol. 4, no. 4, pp. 319-326, 1992.
113. Du, L.J., Lee, J.S., and Mango, S.A., Fuzzy Classification of Earth Terrain Covers Using Multi-Look Polarimetric SAR Image Data, Proceedings of *IEEE International Geoscience and Remote Sensing Symposium (IGARSS)*, Tokyo, Japan, 1993, pp. 1602-1604.
114. Du, Q., Unsupervised Real-Time Constrained Linear Discriminant Analysis to Hyperspectral Image Classification. *Pattern Recognition*, vol. 40, no. 5, pp. 1510-1519, 2007.
115. Dubois, P.C., van Zyl, J.J., and Engman, T., Measuring Soil Moisture With Imaging Radars. *IEEE Transactions on Geoscience and Remote Sensing*, vol. 33, no. 4, pp. 915-926, 1995.
116. Durden, S.L., van Zyl, J.J., and Zebker, H.A., Modeling and Observation of the Radar Polarization Signature of Forested Areas. *IEEE Transactions on Geoscience and Remote Sensing*, vol. 27, no. 3, pp. 290-301, 1989.
117. Edmond, N., Adaptive Speckle Filtering in Radar Imagery, in *Land Applications of Radar Remote Sensing*, Holecz, F., et al., Editors. InTech, 2014.
118. Emerson, C.W., Lam, N.S.N., and Quattrochi, D.A., A Comparison of Local Variance, Fractal Dimension, and Moran's I as Aids to Multispectral Image Classification. *International Journal of Remote Sensing*, vol. 26, no. 8, pp. 1575-1588, 2005.
119. Enderle, D.I.M. and Weih, R.C., Integrating Supervised and Unsupervised Classification Methods to Develop a More Accurate Land Cover Classification. *Journal of the Arkansas Academy of Science* vol. 59, pp. 65-73, 2005.
120. Ersahin, K., Cumming, I.G., and Ward, R.K., Segmentation and Classification of Polarimetric SAR Data Using Spectral Graph Partitioning. *IEEE Transactions on Geoscience and Remote Sensing*, vol. 48, no. 1, pp. 164-174, 2010.
121. Ersahin, K., Scheuchl, B., and Cumming, I., Incorporating Texture Information into Polarimetric Radar Classification Using Neural Networks, Proceedings of *IEEE International Geoscience and Remote Sensing Symposium (IGARSS)*, Anchorage, USA, 2004, vol. 1.
122. Evans, D.L., Applications of Imaging Radar Data in Earth Science Investigations. *Electronics & Communication Engineering Journal*, vol. 11, no. 5, pp. 227-234, 1999.
123. Evans, D.L., Farr, T.G., van Zyl, J.J., and Zebker, H.A., Radar Polarimetry: Analysis Tools and Applications. *IEEE Transactions on Geoscience and Remote Sensing*, vol.

26, no. 6, pp. 774-789, 1988.
124. Fa, W., Wieczorek, M.A., and Heggy, E., Modeling Polarimetric Radar Scattering From the Lunar Surface: Study on the Effect of Physical Properties of the Regolith Layer. *Journal of Geophysical Research*, vol. 116, no. E3, 2011.
125. Fang, B. and Lakshmi, V., Soil Moisture at Watershed Scale: Remote Sensing Techniques. *Journal of Hydrology*, vol. 516, pp. 258-272, 2014.
126. Feldman, W.C., Lawrence, D.J., Elphic, R.C., Barraclough, B.L., Maurice, S., Genetay, I., and Binder, A.B., Polar Hydrogen Deposits on the Moon. *Journal of Geophysical Research: Planets*, vol. 105, no. E2, pp. 4175-4195, 2000.
127. Feldman, W.C., Maurice, S., Binder, A.B., Barraclough, B.L., Elphic, R.C., and Lawrence, D.J., Fluxes of Fast and Epithermal Neutrons From Lunar Prospector: Evidence for Water Ice at the Lunar Poles. *Science*, vol. 281, no. 5382, pp. 1496-1500, 1998.
128. Feldman, W.C., Maurice, S., Lawrence, D.J., Little, R.C., Lawson, S.L., Gasnault, O., Wiens, R.C., et al., Evidence for Water Ice Near the Lunar Poles. *Journal of Geophysical Research: Planets*, vol. 106, no. E10, pp. 23231-23251, 2001.
129. Ferrazzoli, P., Guerriero, L., and Schiavon, G., Experimental and Model Investigation on Radar Classification Capability. *IEEE Transactions on Geoscience and Remote Sensing*, vol. 37, no. 2, pp. 960-968, 1999.
130. Ferrazzoli, P., Paloscia, S., Pampaloni, P., Schiavon, G., Sigismondi, S., and Solimini, D., The Potential of Multifrequency Polarimetric SAR in Assessing Agricultural and Arboreous Biomass. *IEEE Transactions on Geoscience and Remote Sensing*, vol. 35, no. 1, pp. 5-17, 1997.
131. Ferro-Famil, L., Pottier, E., and Lee, J.S., Unsupervised Classification and Analysis of Natural Scenes from Polarimetric Interferometric SAR Data, Proceedings of *IEEE International Geoscience and Remote Sensing Symposium (IGARSS)*, Sydney, Australia, 2001, vol. 6, pp. 2715-2717
132. Ferro-Famil, L., Pottier, E., and Lee, J.S., Unsupervised Classification of Multifrequency and Fully Polarimetric SAR Images Based on the H/A/Alpha Wishart Classifier. *IEEE Transactions on Geoscience and Remote Sensing*, vol. 39, no. 11, pp. 2332-2342, 2001.
133. Fletcher, N.D. and Evans, A.N., Minimum Distance Texture Classification of SAR Images Using Wavelet Packets, Proceedings of *IEEE International Geoscience and Remote Sensing Symposium (IGARSS)*, Toronto, Canada, 2002, vol. 3, pp. 1438-1440.
134. Foo, B.y., Chaudhuri, S.K., and Boerner, W.M., Polarization Correction and Extension of the Kennaugh-Cosgriff Target-Ramp Response Equation to the Bistatic Case and Applications to Electromagnetic Inverse Scattering. *IEEE Transactions on Antennas and Propagation*, vol. 38, no. 7, pp. 964-972, 1990.
135. Formont, P., Pascal, F., Vasile, G., Ovarlez, J., and Ferro-Famil, L., Statistical Classification for Heterogeneous Polarimetric SAR Images. *IEEE Journal of Selected Topics in Signal Processing*, vol. 5, no. 3, pp. 567-576, 2011.
136. Foucher, S., Farage, G., and Bénié, G.B., Polarimetric SAR Image Filtering With Trace-Based Partial Differential Equations. *Canadian Journal of Remote Sensing*, vol. 33, no. 3, pp. 226-236, 2007.
137. Frankot, R.T. and Chellappa, R., Lognormal Random-Field Models and Their Applications to Radar Image Synthesis. *IEEE Transactions on Geoscience and Remote Sensing*, vol. GE-25, no. 2, pp. 195-207, 1987.
138. Freeman, A. and Durden, S.L., A Three-Component Scattering Model for Polarimetric

SAR Data. *IEEE Transactions on Geoscience and Remote Sensing*, vol. 36, no. 3, pp. 963-973, 1998.
139. Freitas, C.C., Frery, A.C., and Correia, A.H., The Polarimetric G Distribution for SAR Data Analysis. *Environmetrics*, vol. 16, no. 1, pp. 13-31, 2005.
140. Friedl, M.A. and Brodley, C.E., Decision Tree Classification of Land Cover From Remotely Sensed Data. *Remote Sensing of Environment*, vol. 61, no. 3, pp. 399-409, 1997.
141. Frost, V.S., Stiles, J.A., Shanmugam, K.S., Holtzman, J.C., and Smith, S.A., An Adaptive Filter for Smoothing Noisy Radar Images. *Proceedings of the IEEE*, vol. 69, no. 1, pp. 133-135, 1981.
142. Frost, V.S., Stiles, J.A., Shanmugan, K.S., and Holtzman, J., A Model for Radar Images and its Application to Adaptive Digital Filtering of Multiplicative Noise. *IEEE Transactions on Pattern Analysis and Machine Intelligence*, vol. 4, no. 2, pp. 157-166, 1982.
143. Fung, A.K. and Chen, K.S., An Update on the IEM Surface Backscattering Model. *IEEE Geoscience and Remote Sensing Letters*, vol. 1, no. 2, pp. 75-77, 2004.
144. Fung, A.K., Dawson, M.S., Chen, K.S., Hsu, A.Y., Engman, E.T., O'Neill, P.O., and Wang, J., A Modified IEM Model for Scattering from Soil Surfaces with Application to Soil Moisture Sensing, Proceedings of *IEEE International Geoscience and Remote Sensing Symposium (IGARSS)*, Lincoln, Nebraska, 1996, vol. 2, pp. 1297-1299.
145. Fung, A.K., Li, Z., and Chen, K.S., Backscattering From a Randomly Rough Dielectric Surface. *IEEE Transactions on Geoscience and Remote Sensing*, vol. 30, no. 2, pp. 356-369, 1992.
146. Fung, A.K., Liu, W.Y., Chen, K.S., and Tsay, M.K., An Improved IEM Model for Bistatic Scattering From Rough Surfaces. *Journal of Electromagnetic Waves and Applications*, vol. 16, no. 5, pp. 689-702, 2002.
147. Gairola, R.M., Pokhrel, S., Varma, A.K., and Agarwal, V.K., Multiparameter Microwave Retrieval Algorithms: Performance of Neural Networks. *Current Science*, vol. 91, no. 10, 2006.
148. Gao, Y., Liao, S., and Shen, D., Prostate Segmentation by Sparse Representation Based Classification, Proceedings of *International Conference on Medical Image Computing and Computer-Assisted Intervention*, Toronto, Canada, 2011, vol. 15, pp. 451-458.
149. Gautam, R., Singh, D., and Mittal, A., A Rough Set Classifilcation Based Approach to Detect Hotspots in NOAA/AVHRR Images, Proceedings of *Fourth International Conference on Intelligent Sensing and Information Processing*, Bangalore, India, 2006, pp. 122-127.
150. Gautam, R.S., Singh, D., and Mittal, A., An Efficient Contextual Algorithm to Detect Subsurface Fires With NOAA/AVHRR Data. *IEEE Transactions on Geoscience and Remote Sensing*, vol. 46, no. 7, pp. 2005-2015, 2008.
151. George, P.P., Hywel, M.G., Wouter, D., Angelika, X., and Alexander, G., Surface Soil Moisture Estimation, in *Remote Sensing of Energy Fluxes and Soil Moisture Content*. CRC Press, pp. 29-48, 2013.
152. Germond, A.L., Pottier, E., and Saillaid, J., Bistatic Radar Polarimetry Theory, in *Ultra-Wideband Radar Technology*. CRC Press: London, 2001.
153. Gherboudj, I., Magagi, R., Berg, A.A., and Toth, B., Soil Moisture Retrieval Over Agricultural Fields From Multi-Polarized and Multi-Angular RADARSAT-2 SAR Data. *Remote Sensing of Environment*, vol. 115, no. 1, pp. 33-43, 2011.
154. Ghosh, A., Varma, A.K., Shah, S., Gohil, B.S., and Pal, P.K., Rain Identification and

Measurement Using Oceansat-II Scatterometer Observations. *Remote Sensing of Environment*, vol. 142, no. 0, pp. 20-32, 2014.
155. Goodman, N.R., Statistical Analysis Based on a Certain Multivariate Complex Gaussian Distribution (An Introduction). *Annals of Mathematical Statistics*, pp. 152-177, 1963.
156. Graves, C.D., Radar Polarization Power Scattering Matrix. *Proceedings of the IRE*, vol. 44, no. 2, pp. 248-252, 1956.
157. Grazzini, J., Turiel, A., and Yahia, H., Presegmentation of High-Resolution Satellite Images With a Multifractal Reconstruction Scheme Based on an Entropy Criterium, Proceedings of *IEEE International Conference on Image Processing*, Genoa, Italy, 2005, vol. 1, pp. 649-652.
158. Grazzini, J., Turiel, A., Yahia, H., and Herlin, I., A Multifractal Approach for Extracting Relevant Textural Areas in Satellite Meteorological Images. *Environmental Modelling & Software*, vol. 22, no. 3, pp. 323-334, 2007.
159. Grazzini, J., Yahia, H., Herlin, I., and Turiel, A., Analysis and Comparison of Functional Dependencies of Multiscale Textural Features on Monospectral Infrared Images, Proceedings of *IEEE International Geoscience and Remote Sensing Symposium (IGARSS)*, Toulouse, France, 2003, vol. 3, pp. 2045 - 2047.
160. Hajnsek, I., Inversion of Surface Parameters Using Polarimetric SAR, Ph. D. Thesis, Institute of Geography, Department of Geomatics, Friedrich-Schiller University Jena, Jena, Thuringia, Germany, 2001.
161. Hajnsek, I., Jagdhuber, T., Schon, H., and Papathanassiou, K.P., Potential of Estimating Soil Moisture Under Vegetation Cover by Means of PolSAR. *IEEE Transactions on Geoscience and Remote Sensing*, vol. 47, no. 2, pp. 442-454, 2009.
162. Hallberg, B., Smith-Jonforsen, G., Ulander, L.M.H., and Sandberg, G., A Physical-Optics Model for Double-Bounce Scattering From Tree Stems Standing on an Undulating Ground Surface. *IEEE Transactions on Geoscience and Remote Sensing*, vol. 46, no. 9, pp. 2607-2621, 2008.
163. Haupt, R.L., An Introduction to Genetic Algorithms for Electromagnetics. *IEEE Antennas and Propagation Magazine*, vol. 37, no. 2, pp. 7-15, 1995.
164. Heggy, E., Fa, W., Thompson, T.W., Ustinov, E., Bussey, B., and Spudis, P., Exploring Dielectric Properties of the Lunar Cratonic Fills From the Mini-RF Observations Onboard Chandrayaan and LRO, Proceedings of *Lunar and Planetary Institute Science Conference Abstracts*, The Woodlands, Texas, 2010, vol. 41, pp. 2031.
165. Henderson, F.M. and Lewis, A.J., *Principles and Applications of Imaging Radar: Manual of Remote Sensing*. Third ed. Vol. 2. John Wiley and Sons: New York, 1998.
166. Henebry, G.M. and Kux, H.J.H., Lacunarity as a Texture Measure for SAR Imagery. *Remote Sensing*, vol. 16, no. 3, pp. 565-571, 1995.
167. Hess, P.C. and Parmentier, E.M., A Model for the Thermal and Chemical Evolution of the Moon's Interior: Implications for the Onset of Mare Volcanism. *Earth and Planetary Science Letters*, vol. 134, no. 3, pp. 501-514, 1995.
168. Holah, N., Baghdadi, N., Zribi, M., Bruand, A., and King, C., Potential of ASAR/ENVISAT for the Characterization of Soil Surface Parameters Over Bare Agricultural Fields. *Remote Sensing of Environment*, vol. 96, no. 1, pp. 78-86, 2005.
169. Holm, W.A. and Barnes, R.M., On Radar Polarization Mixed Target State Decomposition Techniques, Proceedings of *IEEE National Radar Conference*, USA, 1988, pp. 249-254.
170. Huynen, J.R., Measurement of the Target Scattering Matrix. *Proceedings of the IEEE*, vol. 53, no. 8, pp. 936-946, 1965.

171. Huynen, J.R., Phenomenological Theory of Radar Targets, Ph.D. Thesis, University of Technology, Delft, The Netherlands, 1970.
172. Ince, T., Kiranyaz, S., and Gabbouj, M., Evolutionary RBF Classifier for Polarimetric SAR Images. *Expert Systems with Applications*, vol. 39, no. 5, pp. 4710-4717, 2012.
173. Ioannidis, G.A. and Hammers, D.E., Optimum Antenna Polarizations for Target Discrimination in Clutter. *IEEE Transactions on Antennas and Propagation*, vol. 27, pp. 357-363, 1979.
174. Jackson, T.J., O'Neill, P.E., and Swift, C.T., Passive Microwave Observation of Diurnal Surface Soil Moisture. *IEEE Transactions on Geoscience and Remote Sensing*, vol. 35, no. 5, pp. 1210-1222, 1997.
175. Jackson, T.J., Schmugge, T.J., and Wang, J.R., Passive Microwave Sensing of Soil Moisture Under Vegetation Canopies. *Water Resources Research*, vol. 18, no. 4, pp. 1137-1142, 1982.
176. Jagdhuber, T., Hajnsek, I., Bronstert, A., and Papathanassiou, K.P., Soil Moisture Estimation Under Low Vegetation Cover Using a Multi-Angular Polarimetric Decomposition. *IEEE Transactions on Geoscience and Remote Sensing*, vol. 51, no. 4, pp. 2201-2215, 2013.
177. Jagdhuber, T., Hajnsek, I., Papathanassiou, K.P., and Bronstert, A., Soil Moisture Estimation Using a Multi-Angular Modified Three Component Polarimetric Decomposition, Proceedings of *IEEE International Geoscience and Remote Sensing Symposium (IGARSS)*, Cape Town, Africa, 2009, vol. 5, pp. V-5-V-8.
178. Jaggi, S., Quattrochi, D.A., and Lam, N.S.N., Implementation and Operation of Three Fractal Measurement Algorithms for Analysis of Remote-Sensing Data. *Computers & Geosciences*, vol. 19, no. 6, pp. 745-767, 1993.
179. Jin, Y.Q. and Wang, Y., A Genetic Algorithm to Simultaneously Retrieve Land Surface Roughness and Soil Wetness. *International Journal of Remote Sensing*, vol. 22, no. 16, pp. 3093-3099, 2001.
180. Jiong, C., Yilun, C., and Yang, J., A Novel Supervised Classification Scheme Based on Adaboost for Polarimetric SAR, Proceedings of *International Conference on Signal Processing*, Beijing, China, 2008, pp. 2400-2403.
181. Johnson, A.I., *Methods of Measuring Soil Moisture in the Field*. US Government Printing Office: Washington, 1962.
182. Jones, R.C., A New Calculus for the Treatment of Optical Systems. *Journal of the Optical Society of America*, vol. 31, no. 7, pp. 488-493, 1941.
183. Kales, M.L., Techniques for Handling Elliptically Polarized Waves With Special Reference to Antennas: Part III - Elliptically Polarized Waves and Antennas. *Proceedings of the IRE*, vol. 39, no. 5, pp. 544-549, 1951.
184. Keller, J.M., Chen, S., and Crownover, R.M., Texture Description and Segmentation Through Fractal Geometry. *Computer Vision, Graphics, and Image Processing*, vol. 45, no. 2, pp. 150-166, 1989.
185. Kennaugh, E.M. and Sloan, R.W., Effects of Type of Polarization on Echo Characteristics,In DTIC Document,1952.
186. Kersten, P.R., Lee, J.S., and Ainsworth, T.L., Unsupervised Classification of Polarimetric Synthetic Aperture Radar Images Using Fuzzy Clustering and EM clustering. *IEEE Transactions on Geoscience and Remote Sensing*, vol. 43, no. 3, pp. 519-527, 2005.
187. Kim, Y. and van Zyl, J.J., A Time-Series Approach to Estimate Soil Moisture Using Polarimetric Radar Data. *IEEE Transactions on Geoscience and Remote Sensing*, vol.

47, no. 8, pp. 2519-2527, 2009.
188. King, J.H. and Ness, N.F., Lunar Magnetic Permeability Studies and Magnetometer Sensitivity. *Geophysical Research Letters*, vol. 4, no. 4, pp. 129-132, 1977.
189. Kiranyaz, S., Ince, T., Uhlmann, S., and Gabbouj, M., Collective Network of Binary Classifier Framework for Polarimetric SAR Image Classification: An Evolutionary Approach. *IEEE Transactions on Systems, Man, and Cybernetics, Part B: Cybernetics*, vol. 42, no. 4, pp. 1169-1186, 2012.
190. Klima, R., Cahill, J., Hagerty, J., and Lawrence, D., Remote Detection of Magmatic Water in Bullialdus Crater on the Moon. *Nature Geoscience*, vol. 6, no. 9, pp. 737-741, 2013.
191. Kornelsen, K.C. and Coulibaly, P., Advances in Soil Moisture Retrieval from Synthetic Aperture Radar and Hydrological Applications. *Journal of Hydrology*, vol. 476, pp. 460-489, 2013.
192. Kostinski, A.B. and Boerner, W.M., On Foundations of Radar Polarimetry. *IEEE Transactions on Antennas and Propagation*, vol. 34, no. 12, pp. 1395-1404, 1986.
193. Kostinski, A.B. and Boerner, W.M., On the Polarimetric Contrast Optimization. *IEEE Transactions on Antennas and Propagation*, vol. 35, no. 8, pp. 988-991, 1987.
194. Kostinski, A.B., James, B.D., and Boerner, W.M., Optimal Reception of Partially Polarized Waves. *Journal of the Optical Society of America*, vol. 5, no. 1, pp. 58-64, 1988.
195. Krogager, E., New Decomposition of the Radar Target Scattering Matrix. *Electronics Letters*, vol. 26, no. 18, pp. 1525-1527, 1990.
196. Kuan, D.T., Sawchuk, A., Strand, T.C., and Chavel, P., Adaptive Restoration of Images With Speckle. *IEEE Transactions on Acoustics, Speech and Signal Processing*, vol. 35, no. 3, pp. 373-383, 1987.
197. Kuan, D.T., Sawchuk, A.A., Strand, T.C., and Chavel, P., Adaptive Noise Smoothing Filter for Images With Signal-Dependent Noise. *IEEE Transactions on Pattern Analysis and Machine Intelligence*, vol. 7, no. 2, pp. 165-177, 1985.
198. Kubota, T., Shige, S., Hashizume, H., Aonashi, K., Takahashi, N., Seto, S., Takayabu, Y.N., et al., Global Precipitation Map Using Satellite-Borne Microwave Radiometers by the GSMaP Project: Production and Validation. *IEEE Transactions on Geoscience and Remote Sensing*, vol. 45, no. 7, pp. 2259-2275, 2007.
199. Kumar, S., Study and Classification of Lunar Surface Using Mini-SAR Data, M. Tech. Thesis, Department of Electronics and Communication Engineering, Indian Institute of Technology Roorkee, Roorkee, India, 2012.
200. Kumar, S., Singh, D., and Mishra, P., Fractal and Moran's I Analysis for Classification of Lunar Surface Using Mini-SAR Data of Chandrayaan-I, in *National Conference on Recent Trends in Microwave Techniques and Applications, Microwave-12*, Jaipur, 2012.
201. Lakshmi, V., Remote Sensing of Soil Moisture. *ISRN Soil Science*, vol. 2013, no. 424178, 2013.
202. Lakshmi, V., Wood, E.F., and Choudhury, B.J., A Soil-Canopy-Atmosphere Model for Use in Satellite Microwave Remote Sensing. *Journal of Geophysical Research*, vol. 102, no. D6, pp. 6911-6927, 1997.
203. Lam, N.S.N., Qiu, H.l., Quattrochi, D.A., and Emerson, C.W., An Evaluation of Fractal Methods for Characterizing Image Complexity. *Cartography and Geographic Information Science*, vol. 29, no. 1, pp. 25-35, 2002.
204. Lanzerotti, L.J. and Brown, W.L., Ice in the Polar Regions of the Moon. *Journal of*

Geophysical Research, vol. 86, no. B5, pp. 3949-3950, 1981.
205. Leconte, R., Brissette, F., Galarneau, M., and Rousselle, J., Mapping Near-Surface Soil Moisture With RADARSAT-1 Synthetic Aperture Radar Data. *Water Resources Research*, vol. 40, no. 1, 2004.
206. Lee, J.S., Digital Image Enhancement and Noise Filtering by Use af Local Statistics. *IEEE Transactions on Pattern Analysis and Machine Intelligence*, vol. 2, no. 2, pp. 165-168, 1980.
207. Lee, J.S., Refined Filtering of Image Noise Using Local Statistics. *Computer Graphics and Image Processing*, vol. 15, no. 4, pp. 380-389, 1981.
208. Lee, J.S., Speckle Analysis and Smoothing of Synthetic Aperture Radar Images. *Computer Graphics and Image Processing*, vol. 17, no. 1, pp. 24-32, 1981.
209. Lee, J.S., A Simple Speckle Smoothing Algorithm for Synthetic Aperture Radar Images. *IEEE Transactions on Systems, Man and Cybernetics*, vol. 13, no. 1, pp. 85-89, 1983.
210. Lee, J.S. and Ainsworth, T.L., The Effect of Orientation Angle Compensation on Coherency Matrix and Polarimetric Target Decompositions. *IEEE Transactions on Geoscience and Remote Sensing*, vol. 49, no. 1, pp. 53-64, 2011.
211. Lee, J.S., Ainsworth, T.L., Kelly, J.P., and Lopez Martinez, C., Evaluation and Bias Removal of Multilook Effect on Entropy/Alpha/Anisotropy in Polarimetric SAR Decomposition. *IEEE Transactions on Geoscience and Remote Sensing*, vol. 46, no. 10, pp. 3039-3052, 2008.
212. Lee, J.S., Ainsworth, T.L., Schuler, D.L., Kasilingam, D., and Boerner, W.M., Interpreting Off-Diagonal Terms in Polarimetric Coherency Matrix, Proceedings of *IEEE International Geoscience and Remote Sensing Symposium (IGARSS)*, Sydney, Australia, 2001, vol. 2, pp. 913-915.
213. Lee, J.S., Ainsworth, T.L., and Wang, Y., Generalized Polarimetric Model-Based Decompositions Using Extended Incoherent Scattering Models, Proceedings of *IEEE International Geoscience and Remote Sensing Symposium (IGARSS)*, Munich, Germany, 2012, pp. 1421-1424.
214. Lee, J.S. and Grunes, M.R., Classification of Multi-look Polarimetric SAR Data Based on Complex Wishart Distribution, Proceedings of *National Telesystems Conference*, Washington, DC, USA, 1992, pp. 7/21-7/24.
215. Lee, J.S., Grunes, M.R., Ainsworth, T.L., Du, L.J., Schuler, D.L., and Cloude, S.R., Unsupervised Classification Using Polarimetric Decomposition and the Complex Wishart Classifier. *IEEE Transactions on Geoscience and Remote Sensing*, vol. 37, no. 5, pp. 2249-2258, 1999.
216. Lee, J.S., Grunes, M.R., and De Grandi, G., Polarimetric SAR Speckle Filtering and its Implication for Classification. *IEEE Transactions on Geoscience and Remote Sensing*, vol. 37, no. 5, pp. 2363-2373, 1999.
217. Lee, J.S., Grunes, M.R., Schuler, D.L., Pottier, E., and Ferro-Famil, L., Scattering-Model-Based Speckle Filtering of Polarimetric SAR Data. *IEEE Transactions on Geoscience and Remote Sensing*, vol. 44, no. 1, pp. 176-187, 2006.
218. Lee, J.S., Krogager, E., Schuler, D.L., Ainsworth, T.L., and Boerner, W.M., On the Estimation of Polarization Orientation Angles Induced From Azimuth Slopes using Polarimetric SAR Data, Proceedings of *IEEE International Geoscience and Remote Sensing Symposium (IGARSS)*, Honolulu, USA, 2000, pp. 1310-1312 vol.3.
219. Lee, J.S. and Pottier, E., *Polarimetric Radar Imaging: From Basics to Applications*. CRC Press, 2009.

220. Lee, J.S., Schuler, D.L., and Ainsworth, T.L., Polarimetric SAR Data Compensation for Terrain Azimuth Slope Variation. *IEEE Transactions on Geoscience and Remote Sensing*, vol. 38, no. 5, pp. 2153-2163, 2000.
221. Lee, J.S., Schuler, D.L., Lang, R.H., and Ranson, K.J., K-Distribution for Multi-look Processed Polarimetric SAR Imagery, Proceedings of *IEEE Geoscience and Remote Sensing Symposium (IGARSS)*, Pasedena, USA, 1994, vol. 4, pp. 2179-2181.
222. Lee, J.S., Yueh, S.H., and Schuler, D.L., Polarimetric Analysis of Scatterometer Data for Ocean Surface Wind Measurement, Proceedings of *IEEE International Geoscience and Remote Sensing Symposium (IGARSS)*, Anchorage, USA, 2004, vol. 1, pp. 208-211.
223. Li-wen, Z., Xiao-guang, Z., and Yong-mei, J., Iterative Classification of Polarimetric SAR Image Based on the Freeman Decomposition and Scattering Entropy, Proceedings of *Asian and Pacific Conference on Synthetic Aperture Radar*, Huangshan, China, 2007, pp. 473-476.
224. Li, D. and Zhang, Y., Huynen Dichotomy-Based Radar Target Adaptive Extraction, in *Progress In Electromagnetics Research Symposium*, Stockholm, Sweden, 2013.
225. Lichtenberg, C.L., Bistatic Radar Observations of the Moon Using the Clementine Spacecraft and Deep Space Network, Ph. D. Thesis, The Johns Hopkins University, Ann Arbor, 2000.
226. Lievens, H. and Verhoest, N.E.C., On the Retrieval of Soil Moisture in Wheat Fields From L-Band SAR Based on Water Cloud Modeling, the IEM, and Effective Roughness Parameters. *IEEE Geoscience and Remote Sensing Letters*, vol. 8, no. 4, pp. 740-744, 2011.
227. Lillesand, T.M., Kiefer, R.W., and Chipman, J.W., *Remote Sensing and Image Interpretation*. Fifth ed. John Wiley & Sons, Inc.: New York, 2004.
228. Lin, H., Chen, J., Pei, Z., Zhang, S., and Hu, X., Monitoring Sugarcane Growth Using ENVISAT ASAR Data. *IEEE Transactions on Geoscience and Remote Sensing*, vol. 47, no. 8, pp. 2572-2580, 2009.
229. Liu, B., Hu, H., Wang, H., Wang, K., Liu, X., and Yu, W., Superpixel-Based Classification With an Adaptive Number of Classes for Polarimetric SAR Images. *IEEE Transactions on Geoscience and Remote Sensing*, vol. 51, no. 2, pp. 907-924, 2013.
230. Liu, Y., Guan, Y., Zhang, Y., Rossman, G.R., Eiler, J.M., and Taylor, L.A., Direct Measurement of Hydroxyl in the Lunar Regolith and the Origin of Lunar Surface Water. *Nature Geoscience*, vol. 5, no. 11, pp. 779-782, 2012.
231. Loew, A. and Mauser, W., A Semiempirical Surface Backscattering Model for Bare Soil Surfaces Based on a Generalized Power Law Spectrum Approach. *IEEE Transactions on Geoscience and Remote Sensing*, vol. 44, no. 4, pp. 1022-1035, 2006.
232. Lopes, A., Goze, S., and Nezry, E., Polarimetric Speckle Filters for SAR Data, Proceedings of *IEEE International Geoscience and Remote Sensing Symposium (IGARSS)*, Houston, USA, 1992, vol. 1, pp. 80-82.
233. Lopez-Martinez, C., Pottier, E., and Cloude, S.R., Statistical Assessment of Eigenvector-Based Target Decomposition Theorems in Radar Polarimetry. *IEEE Transactions on Geoscience and Remote Sensing*, vol. 43, no. 9, pp. 2058-2074, 2005.
234. Lu, T.T., Fundamental Limitations of Semi-Supervised Learning, Master of Mathematics Thesis, Department of Computer Science, University of Waterloo, Waterloo, Canada,, 2009.
235. Mahesh, C., Prakash, S., Sathiyamoorthy, V., and Gairola, R.M., Artificial Neural Network Based Microwave Precipitation Estimation Using Scattering Index and

Polarization Corrected Temperature. *Atmospheric Research*, vol. 102, no. 3, pp. 358-364, 2011.
236. Mandelbrot, B.B., *The Fractal Geometry of Nature*. W. H. Freeman and Company: New York, 1982.
237. Margot, J.L., Campbell, D.B., Jurgens, R.F., and Slade, M.A., Topography of the Lunar Poles From Radar Interferometry: A Survey of Cold Trap Locations. *Science*, vol. 284, no. 5420, pp. 1658-1660, 1999.
238. Marzano, F.S., Scaranari, D., Montopoli, M., and Vulpiani, G., Supervised Classification and Estimation of Hydrometeors From C-Band Dual-Polarized Radars: A Bayesian Approach. *IEEE Transactions on Geoscience and Remote Sensing*, vol. 46, no. 1, pp. 85-98, 2008.
239. Mattia, F., Le Toan, T., Picard, G., Posa, F.I., D'Alessio, A., Notarnicola, C., Gatti, A.M., et al., Multitemporal C-Band Radar Measurements on Wheat Fields. *IEEE Transactions on Geoscience and Remote Sensing*, vol. 41, no. 7, pp. 1551-1560, 2003.
240. McClanahan, T.P., Mitrofanov, I.G., Boynton, W.V., Sagdeev, R., Trombka, J.I., Starr, R.D., Evans, L.G., et al., Correlation of Lunar South Polar Epithermal Neutron Maps: Lunar Exploration Neutron Detector and Lunar Prospector Neutron Spectrometer, Proceedings of *Lunar and Planetary Institute Science Conference Abstracts*, The Woodlands, Texas, 2010, vol. 41, pp. 1395.
241. McCord, T.B., Taylor, L.A., Combe, J.P., Kramer, G., Pieters, C.M., Sunshine, J.M., and Clark, R.N., Sources and Physical Processes Responsible for OH/H_2O in the Lunar Soil as Revealed by the Moon Mineralogy Mapper (M^3). *Journal of Geophysical Research: Planets*, vol. 116, no. E6, pp. E00G05, 2011.
242. McCubbin, F.M., Steele, A., Hauri, E.H., Nekvasil, H., Yamashita, S., and Hemley, R.J., Nominally Hydrous Magmatism on the Moon. *Proceedings of the National Academy of Sciences*, vol. 107, no. 25, pp. 11223-11228, 2010.
243. McGovern, J.A., Bussey, D.B.J., Greenhagen, B.T., Paige, D.A., Cahill, J.T.S., and Spudis, P.D., Mapping and Characterization of Non-Polar Permanent Shadows on the Lunar Surface. *Icarus*, vol. 223, no. 1, pp. 566-581, 2013.
244. McNairn, H., Champagne, C., Shang, J., Holmstrom, D., and Reichert, G., Integration of Optical and Synthetic Aperture Radar (SAR) Imagery for Delivering Operational Annual Crop Inventories. *ISPRS Journal of Photogrammetry and Remote Sensing*, vol. 64, no. 5, pp. 434-449, 2009.
245. McNairn, H., Duguay, C., Brisco, B., and Pultz, T.J., The Effect of Soil and Crop Residue Characteristics on Polarimetric Radar Response. *Remote Sensing of Environment*, vol. 80, no. 2, pp. 308-320, 2002.
246. McNairn, H., Merzouki, A., Pacheco, A., and Fitzmaurice, J., Monitoring Soil Moisture to Support Risk Reduction for the Agriculture Sector Using RADARSAT-2. *IEEE Journal of Selected Topics in Applied Earth Observations and Remote Sensing*, vol. 5, no. 3, pp. 824-834, 2012.
247. Mishra, P., Kumar, S., and Singh, D., An Approach to Determine Possible Existence of Water Ice Deposits on Lunar Craters Using MiniSAR Data, Proceedings of *IEEE International Geoscience and Remote Sensing Symposium (IGARSS)*, Melbourn, Australia, 2013, pp. 21-24.
248. Mishra, P. and Singh, D., Role of Polarimetric Indices Based on Statistical Measures to Identify Various Land Cover Classes in ALOS PALSAR Data, Proceedings of *3rd International Asia-Pacific Conference on Synthetic Aperture Radar*, Seoul, Korea, 2011, pp. 1-4.

249. Mishra, P., Singh, D., and Kumar, S., Unsupervised Contextual Classification of Chandrayaan-1's Mini SAR Image Using Fractal Based Approach, in *National Symposium on Space Technology for Food & Environmental Security of Indian Society of Remote Sensing and Indian Society of Geomatics*, New Delhi, India, 2012.
250. Mishra, P., Singh, D., and Yamaguchi, Y., Land Cover Classification of PALSAR Images by Knowledge Based Decision Tree Classifier and Supervised Classifiers Based on SAR Observables. *Progress In Electromagnetics Research B*, vol. 30, pp. 47-70, 2011.
251. Misra, T., Rana, S.S., Desai, N.M., Dave, D.B., Arora, R.K., Rao, C.V.N., Bakori, B.V., et al., Synthetic Aperture Radar Payload on-board RISAT-1: Configuration, Technology and Performance. *Current Science* vol. 104, no. 4, 2013.
252. Mohan, S., Das, A., and Chakraborty, M., Studies of Polarimetric Properties of Lunar Surface Using Mini-SAR Data. *Current Science*, vol. 101, no. 2, pp. 159-164, 2011.
253. Moore, H.J., Boyce, J.M., Schaber, G.G., and Scott, D.H., Lunar Remote Sensing and Measurements. *US Geological Survey Professional Paper*, vol. 1046-B, pp. B1-B78, 1980.
254. Moran, M.S., Hymer, D.C., Qi, J., and Kerr, Y., Comparison of ERS-2 SAR and Landsat TM Imagery for Monitoring Agricultural Crop and Soil Conditions. *Remote Sensing of Environment*, vol. 79, no. 2, pp. 243-252, 2002.
255. Moran, M.S., Peters-Lidard, C.D., Watts, J.M., and McElroy, S., Estimating Soil Moisture at the Watershed Scale With Satellite-Based Radar and Land Surface Models. *Canadian Journal of Remote Sensing*, vol. 30, no. 5, pp. 805-826, 2004.
256. Morgan, T.H. and Shemansky, D.E., Limits to the Lunar Atmosphere. *Journal of Geophysical Research*, vol. 96, no. A2, pp. 1351-1367, 1991.
257. Mota, G.L.A., Feitosa, R.Q., Coutinho, H.L.C., Liedtke, C.E., Müller, S., Pakzad, K., and Meirelles, M.S.P., Multitemporal Fuzzy Classification Model Based on Class Transition Possibilities. *ISPRS Journal of Photogrammetry and Remote Sensing*, vol. 62, no. 3, pp. 186-200, 2007.
258. Mota, G.L.A., Muller, S., Feitosa, R.Q., Coutinho, H.L.C., Meireiles, M.S.P., and Vieira, H., An Evaluation of Knowledge-Based Interpretation Applied to Low-Resolution Satellite Images, Proceedings of *IEEE International Geoscience and Remote Sensing Symposium (IGARSS)*, Toulouse, France, 2003, vol. 6, pp. 3896-3898.
259. Mota, G.L.A., Pakzad, K., Muller, S., Meirelles, M.S.P., Feitosa, R.Q., and Coutinho, H.L.C., A Framework for Automatic Low-Resolution Satellite Image Interpretation Based on Spectral, Contextual and Multitemporal Knowledge, Proceedings of *XXTH Congress of International Society for Photogrammetry and Remote Sensing*, Istanbul, 2004, vol. XXXV, pp. 216-221.
260. Narayan, U., Lakshmi, V., and Jackson, T.J., High-Resolution Change Estimation of Soil Moisture Using L-Band Radiometera nd Radar Observations Made During the SMEX02 Experiments. *IEEE Transactions on Geoscience and Remote Sensing*, vol. 44, no. 6, pp. 1545-1554, 2006.
261. Neish, C.D., Bussey, D.B.J., Spudis, P.D., Marshall, W., Thomson, B.J., Patterson, G.W., and Carter, L.M., The Nature of Lunar Volatiles as Revealed by Mini-RF Observations of the LCROSS Impact Site. *Journal of Geophysical Research*, vol. 116, no. E1, pp. E01005, 2011.
262. Nezry, E., Lopes, A., Ducrot-Gambart, D., Nezry, C., and Lee, J.S., Supervised Classification of K-Distributed SAR Images of Natural Targets and Probability of Error Estimation. *IEEE Transactions on Geoscience and Remote Sensing*, vol. 34, no. 5, pp.

1233-1242, 1996.
263. Nezry, E. and Yakam-Simen, F., New Distribution-Entropy Maximum A Posteriori Speckle Filters for Detected, Complex and Polarimetric SAR Data, Proceedings of *International Geoscience and Remote Sensing Symposium (IGARSS)*, Hamburg, Germany, 1999, vol. 3, pp. 1804-1806.
264. Nghiem, S.V., Yueh, S.H., Kwok, R., and Li, F.K., Symmetry Properties in Polarimetric Remote Sensing. *Radio Science*, vol. 27, no. 5, pp. 693-711, 1992.
265. Niu, X. and Ban, Y., A Novel Contextual Classification Algorithm for Multitemporal Polarimetric SAR Data. *IEEE Geoscience Remote Sensing Letters*, vol. 11, no. 3, pp. 681-685, 2014.
266. Njoku, E.G., Wilson, W.J., Yueh, S.H., Dinardo, S.J., Li, F.K., Jackson, T.J., Lakshmi, V., et al., Observations of Soil Moisture Using a Passive and Active Low-Frequency Microwave Airborne Sensor During SGP99. *IEEE Transactions on Geoscience and Remote Sensing*, vol. 40, no. 12, pp. 2659-2673, 2002.
267. Noda, H., Araki, H., Goossens, S., Ishihara, Y., Matsumoto, K., Tazawa, S., Kawano, N., et al., Illumination Conditions at the Lunar Polar Regions by KAGUYA(SELENE) Laser Altimeter. *Geophysical Research Letters*, vol. 35, no. 24, pp. L24203, 2008.
268. Notarnicola, C., A Bayesian Change Detection Approach for Retrieval of Soil Moisture Variations Under Different Roughness Conditions. *IEEE Geoscience and Remote Sensing Letters*, vol. 11, no. 2, pp. 414-418, 2014.
269. Notarnicola, C., Angiulli, M., and Posa, F., Use of Radar and Optical Remotely Sensed Data for Soil Moisture Retrieval Over Vegetated Areas. *IEEE Transactions on Geoscience and Remote Sensing*, vol. 44, no. 4, pp. 925-935, 2006.
270. Nozette, S., Lichtenberg, C.L., Spudis, P., Bonner, R., Ort, W., Malaret, E., Robinson, M., et al., The Clementine Bistatic Radar Experiment. *Science*, vol. 274, no. 5292, pp. 1495-1498, 1996.
271. Nozette, S., Shoemaker, E.M., Spudis, P., and Lichtenberg, C.L., The Possibility of Ice on the Moon. *Science*, vol. 278, pp. 144-145, 1997.
272. Nozette, S., Spudis, P.D., Robinson, M.S., Bussey, D.B.J., Lichtenberg, C., and Bonner, R., Integration of Lunar Polar Remote-Sensing Data Sets: Evidence for Ice a the Lunar South Pole. *Journal of Geophysical Research: Planets*, vol. 106, no. E10, pp. 23253-23266, 2001.
273. Oh, Y., Quantitative Retrieval of Soil Moisture Content and Surface Roughness From Multipolarized Radar Observations of Bare Soil Surfaces. *IEEE Transactions on Geoscience and Remote Sensing*, vol. 42, no. 3, pp. 596-601, 2004.
274. Oh, Y., Sarabandi, K., and Ulaby, F.T., An Empirical Model and an Inversion Technique for Radar Scattering From Bare Soil Surfaces. *IEEE Transactions on Geoscience and Remote Sensing*, vol. 30, no. 2, pp. 370-381, 1992.
275. Oldak, A., Jackson, T.J., Starks, P., and Elliott, R., Mapping Near-Surface Soil Moisture on Regional Scale Using ERS-2 SAR Data. *International Journal of Remote Sensing*, vol. 24, no. 22, pp. 4579-4598, 2003.
276. Olhoeft, G.R. and Strangway, D.W., Dielectric Properties of the First 100 Meters of the Moon. *Earth and Planetary Science Letters*, vol. 24, no. 3, pp. 394-404, 1975.
277. Oliver, C. and Quegan, S., *Understanding Synthetic Aperture Radar Images*. Artech House: Boston, 1998.
278. Ong, L., Asphaug, E.I., Korycansky, D., and Coker, R.F., Volatile Retention From Cometary Impacts on the Moon. *Icarus*, vol. 207, no. 2, pp. 578-589, 2010.
279. Ostro, S.J., Campbell, D.B., Simpson, R.A., Hudson, R.S., Chandler, J.F., Rosema,

K.D., Shapiro, I.I., et al., Europa, Ganymede, and Callisto: New Radar Results From Arecibo and Goldstone. *Journal of Geophysical Research*, vol. 97, no. E11, pp. 18227-18244, 1992.
280. Ouchi, K., Recent Trend and Advance of Synthetic Aperture Radar With Selected Topics. *Remote Sensing*, vol. 5, no. 2, pp. 716-807, 2013.
281. Paige, D.A., Greenhagen, B.T., Vasavada, A.R., Allen, C., Bandfield, J.L., Bowles, N.E., Calcutt, S.B., et al., Diviner Lunar Radiometer Experiment; Early Mapping Mission Results, Proceedings of *Abstracts of Papers Submitted to the Lunar and Planetary Science Conference*, 2010, vol. 41, pp. 2267.
282. Pakzad, K., Mota, G.L.A., Meirelles, M.S.P., Luiz, H.L.C., and Feitosa, R.Q., Automatic Interpretation of Vegetation Areas in Brazil, in *Joint Workshop of ISPRS Working Groups I/2, I/5, IC WG II/IV and the EARSeL Special Interest Group*, Hannover, Germany, 2003.
283. Pal, M. and Mather, P.M., An Assessment of the Effectiveness of Decision Tree Methods for Land Cover Classification. *Remote Sensing of Environment*, vol. 86, no. 4, pp. 554-565, 2003.
284. Paladini, R., Famil, L.F., Pottier, E., Martorella, M., Berizzi, F., and Dalle Mese, E., Lossless and Sufficient u-Invariant Decomposition of Random Reciprocal Target. *IEEE Transactions on Geoscience and Remote Sensing*, vol. 50, no. 9, pp. 3487-3501, 2012.
285. Paloscia, S., Macelloni, G., Pampaloni, P., and Santi, E., The Contribution of Multitemporal SAR Data in Assessing Hydrological Parameters. *IEEE Geoscience and Remote Sensing Letters*, vol. 1, no. 3, pp. 201-205, 2004.
286. Paloscia, S., Pampaloni, P., Pettinato, S., and Santi, E., A Comparison of Algorithms for Retrieving Soil Moisture From ENVISAT/ASAR Images. *IEEE Transactions on Geoscience and Remote Sensing*, vol. 46, no. 10, pp. 3274-3284, 2008.
287. Pandey, P.C., Gairola, R.M., and Gohil, B.S., Wind-Wave Relationship From SEASAT Radar Altimeter Data. *Boundary-Layer Meteorology*, vol. 37, no. 3, pp. 263-269, 1986.
288. Pandey, P.C. and Kakar, R.K., An Empirical Microwave Emissivity Model for a Foam-Covered Sea. *IEEE Journal of Oceanic Engineering*, vol. 7, no. 3, pp. 135-140, 1982.
289. Panigrahi, R.K. and Mishra, A.K., Comparison of Hybrid-polarization With Quad-polarization Schemes Based on Airborne SAR Images, Proceedings of *A Workshop on Advanced Antenna Technology, Indian Antenna Week*, Chandigarh, India, 2010, pp. 1-4.
290. Pant, T., Singh, D., and Srivastava, T., Advanced Fractal Approach for Unsupervised Classification of SAR Images. *Advances in Space Research*, vol. 45, no. 11, pp. 1338-1349, 2010.
291. Paulik, C., Dorigo, W., Wagner, W., and Kidd, R., Validation of the ASCAT Soil Water Index Using In Situ Data From the International Soil Moisture Network. *International Journal of Applied Earth Observation and Geoinformation*, vol. 30, pp. 1-8, 2014.
292. Pentland, A.P., Fractal-Based Description of Natural Scenes. *IEEE Transactions on Pattern Analysis and Machine Intelligence*, vol. PAMI-6, no. 6, pp. 661-674, 1984.
293. Pierce, L.E., Ulaby, F.T., Sarabandi, K., and Dobson, M.C., Knowledge-Based Classification of Polarimetric SAR Images. *IEEE Transactions on Geoscience and Remote Sensing*, vol. 32, no. 5, pp. 1081-1086, 1994.
294. Pierdicca, N., Pulvirenti, L., and Bignami, C., Soil Moisture Estimation Over Vegetated Terrains Using Multitemporal Remote Sensing Data. *Remote Sensing of Environment*, vol. 114, no. 2, pp. 440-448, 2010.
295. Pieters, C.M., Goswami, J.N., Clark, R.N., Annadurai, M., Boardman, J., Buratti, B.,

Combe, J.P., et al., Character and Spatial Distribution of OH/H_2O on the Surface of the Moon Seen by M^3 on Chandrayaan-1. *Science*, vol. 326, no. 5952, pp. 568-572, 2009.
296. Porcello, L.J., Massey, N.G., Innes, R.B., and Marks, J.M., Speckle Reduction in Synthetic Aperture Radars. *Journal of the Optical Society of America*, vol. 66, no. 11, pp. 1305-1311, 1976.
297. Pozar, D.M., *Microwave Engineering*. 4th ed. John Wiley & Sons, Inc.: New York, 2009.
298. Prakash, R., Radar Remote Sensing for Retrieval of Soil Parameters, Ph.D. Thesis, Department of Electronics and Computer Engineering, Indian Institute of Technology Roorkee, Roorkee, India, 2011.
299. Prakash, R., Singh, D., and Pathak, N.P., A Fusion Approach to Retrieve Soil Moisture With SAR and Optical Data. *IEEE Journal of Selected Topics in Applied Earth Observations and Remote Sensing*, vol. 5, no. 1, pp. 196-206, 2012.
300. Prakash, S., Mahesh, C., and Gairola, R.M., Observational Study of the Oceanic Surface Parameters in the Eastern Indian Ocean During Two Contrasting Dipole Years 2005 and 2006. *IEEE Geoscience and Remote Sensing Letters*, vol. 9, no. 5, pp. 906-909, 2012.
301. Praks, J., Koeniguer, E.C., and Hallikainen, M.T., Alternatives to Target Entropy and Alpha Angle in SAR Polarimetry. *IEEE Transactions on Geoscience and Remote Sensing*, vol. 47, no. 7, pp. 2262-2274, 2009.
302. Prasad, R., Pandey, A., Jha, S.K., Singh, K.P., and Yadav, G.S., Classification of Fields Having Different Soil Moisture Content by SVM Technique Using Bistatic Scatterometer. *Recent Research in Science and Technology*, vol. 3, no. 1, 2011.
303. Prasad, R., Sharma, S.K., and Singh, K.P., Bistatic Microwave Remote Sensing of Kidney Bean at 9.89 GHz, Proceedings of *International Conference on Electromagnetic Interference and Compatibility*, Hyderabad, India, 1997, pp. 51-56.
304. Prevot, L., Dechambre, M., Taconet, O., Vidal-Madjar, D., Normand, M., and Gallej, S., Estimating the Characteristics of Vegetation Canopies With Airborne Radar Measurements. *International Journal of Remote Sensing*, vol. 14, no. 15, pp. 2803-2818, 1993.
305. Qi, Z., Yeh, A.G.O., Li, X., and Lin, Z., A Novel Algorithm for Land Use and Land Cover Classification Using RADARSAT-2 Polarimetric SAR Data. *Remote Sensing of Environment*, vol. 118, pp. 21-39, 2012.
306. Quegan, S., Le Toan, T., Skriver, H., Gomez-Dans, J., Gonzalez-Sampedro, M.C., and Hoekman, D.H., Crop Classification With Multitemporal Polarimetric SAR Data, Proceedings of *PolInSAR*, Frascati, Italy, 2003, vol. 529, pp. 9.1.
307. Rajasekhar, U., Study and Characterisation of Lunar Craters Using Mini-SAR Data, Integrated Dual Degree Thesis, Department of Electronics and Communication Engineering, Indian Institure of Technology Roorkee, Roorkee, India, 2013.
308. Raney, R.K., Hybrid-Polarity SAR Architecture. *IEEE Transactions on Geoscience and Remote Sensing*, vol. 45, no. 11, pp. 3397-3404, 2007.
309. Raney, R.K., Hybrid-Quad-Pol SAR, Proceedings of *IEEE International Geoscience and Remote Sensing Symposium (IGARSS)*, Boston, Massachusetts, USA, 2008, vol. 4, pp. IV-491-IV-493.
310. Raney, R.K., Cahill, J.T.S., Patterson, G.W., and Bussey, D.B.J., The m-chi Decomposition of Hybrid Dual Polarimetric Radar Data With Application to Lunar Craters. *Journal of Geophysical Research* vol. 117, no. E12, pp. 1991-2012, 2012.
311. Raney, R.K., Spudis, P.D., Bussey, B., Crusan, J., Jensen, J.R., Marinelli, W., McKerracher, P., et al., The Lunar Mini-RF Radars: Hybrid Polarimetric Architecture

and Initial Results. *Proceedings of the IEEE*, vol. 99, no. 5, pp. 808-823, 2011.
312. Rao, U.R., Desai, P.S., Joshi, P.C., Pandey, P.C., Gohil, B.S., and Simon, B., Early Prediction of Onset of South West Monsoon From ERS-1 Scatterometer Winds. *Proceedings of the Indian Academy of Sciences - Earth and Planetary Sciences*, vol. 107, no. 1, pp. 33-43, 1998.
313. Read, J.M., Spatial Analyses of Logging Impacts in Amazonia Using Remotely Sensed Data. *Photogrammetric Engineering and Remote Sensing*, vol. 69, no. 3, pp. 275-282, 2003.
314. Read, J.M. and Lam, N.S.N., Spatial Methods for Characterising Land Cover and Detecting Land-Cover Changes for the Tropics. *International Journal of Remote Sensing*, vol. 23, no. 12, pp. 2457-2474, 2002.
315. Rice, S.O., Reflection of Electromagnetic Waves From Slightly Rough Surfaces. *Communications on Pure and Applied Mathematics*, vol. 4, no. 2-3, pp. 351-378, 1951.
316. Riegger, S. and Wiesbeck, W., Wide-Band Polarimetry and Complex Radar Cross Section Signatures. *Proceedings of the IEEE*, vol. 77, no. 5, pp. 649-658, 1989.
317. Rignot, E. and Chellappa, R., Segmentation of Polarimetric Synthetic Aperture Radar Data. *IEEE Transactions on Image Processing*, vol. 1, no. 3, pp. 281-300, 1992.
318. Rignot, E., Chellappa, R., and Dubois, P., Unsupervised Segmentation of Polarimetric SAR Data Using the Covariance Matrix. *IEEE Transactions on Geoscience and Remote Sensing*, vol. 30, no. 4, pp. 697-705, 1992.
319. Rodionova, N.V., A Combined Use of Decomposition and Texture for Terrain Classification of Fully Polarimetric SAR Images, Proceedings of *Workshop of PolInSAR*, Frascati, Italy, 2007.
320. Rumsey, V.H., Techniques for Handling Elliptically Polarized Waves With Special Reference to Antennas: Part I-Transmission Between Elliptically Polarized Antennas. *Proceedings of the IRE*, vol. 39, no. 5, pp. 535-540, 1951.
321. Saal, A.E., Hauri, E.H., Cascio, M.L., Van Orman, J.A., Rutherford, M.C., and Cooper, R.F., Volatile Content of Lunar Volcanic Glasses and the Presence of Water in the Moon's Interior. *Nature*, vol. 454, no. 7201, pp. 192-195, 2008.
322. Salman, R., Willms, I., Reichardt, L., Zwick, T., and Wiesbeck, W., Geometry Classification by Means of Scattering Matrix Decomposition for Ultra-Wideband Radar, Proceedings of *European Radar Conference (EuRAD)*, Nuremberg, Germany, 2013, pp. 93-96.
323. Salman, R., Willms, I., Reichardt, L., Zwick, T., Wiesbeck, W., and Thoma, R.S., On Buried Weapon Detection by Means of Scattering Matrix Decomposition for Quad-Polarized Ultra-Wideband Radar, Proceedings of *IEEE International Conference on Ultra-Wideband (ICUWB)*, Sydney, Australia, 2013, pp. 113-119.
324. Sarkar, N. and Chaudhuri, B.B., An Efficient Differential Box-Counting Approach to Compute Fractal Dimension of Image. *IEEE Transactions on Systems, Man and Cybernetics*, vol. 24, no. 1, pp. 115-120, 1994.
325. Sato, A., Yamaguchi, Y., Singh, G., and Park, S.E., Four-Component Scattering Power Decomposition With Extended Volume Scattering Model. *IEEE Geoscience and Remote Sensing Letters*, vol. 9, no. 2, pp. 166-170, 2012.
326. Schuler, D.L., Lee, J.S., and Ainsworth, T.L., Compensation of Terrain Azimuthal Slope Effects in Geophysical Parameter Studies Using Polarimetric SAR Data. *Remote Sensing of Environment*, vol. 69, no. 2, pp. 139-155, 1999.
327. Seneviratne, S.I., Corti, T., Davin, E.L., Hirschi, M., Jaeger, E.B., Lehner, I., Orlowsky, B., et al., Investigating Soil Moisture–Climate Interactions in a Changing Climate: A

Review. *Earth-Science Reviews*, vol. 99, no. 3, pp. 125-161, 2010.
328. Shan, Z., Wang, C., Zhang, H., and An, W., Improved Four-Component Model-Based Target Decomposition for Polarimetric SAR Data. *IEEE Geoscience and Remote Sensing Letters*, vol. 9, no. 1, pp. 75-79, 2012.
329. Shan, Z., Zhang, H., Wang, C., An, W., Wu, T., and Chen, X., Four-Component Model-Based Decomposition of Polarimetric SAR Data for Special Ground Objects. *IEEE Geoscience and Remote Sensing Letters*, vol. 9, no. 5, pp. 989-993, 2012.
330. Sharma, J.J., Hajnsek, I., Papathanassiou, K.P., and Moreira, A., Polarimetric Decomposition Over Glacier Ice Using Long-Wavelength Airborne PolSAR. *IEEE Transactions on Geoscience and Remote Sensing*, vol. 49, no. 1, pp. 519-535, 2011.
331. She, X., Yang, J., and Zhang, W., The Boosting Algorithm With Application to Polarimetric SAR Image Classification, Proceedings of *Asian and Pacific Conference on Synthetic Aperture Radar*, Huangshan, China, 2007, pp. 779-783.
332. Shi, J., Sun, G., Hsu, A., Wang, J., O'Neill, P., Ranson, J., and Engman, E.T., Estimation of Soil Moisture for Vegetated Surfaces Using Multi-Temporal L-Band SAR Measurements, Proceedings of *IEEE International Geoscience and Remote Sensing*, Singapore, 1997, vol. 3, pp. 1269-1271.
333. Shi, J., Wang, J., Hsu, A.Y., O'Neill, P.E., and Engman, E.T., Estimation of Bare Surface Soil Moisture and Surface Roughness Parameter Using L-band SAR Image Data. *IEEE Transactions on Geoscience and Remote Sensing*, vol. 35, no. 5, pp. 1254-1266, 1997.
334. Shimoni, M., Borghys, D., Heremans, R., Perneel, C., and Acheroy, M., Fusion of PolSAR and PolInSAR Data for Land Cover Classification. *International Journal of Applied Earth Observation and Geoinformation*, vol. 11, no. 3, pp. 169-180, 2009.
335. Shirvany, R., Chabert, M., and Tourneret, J.Y., Estimation of the Degree of Polarization for Hybrid/Compact and Linear Dual-Pol SAR Intensity Images: Principles and Applications. *IEEE Transactions on Geoscience and Remote Sensing*, vol. 51, no. 1, pp. 530-551, 2013.
336. Shkuratov, Y.G. and Bondarenko, N.V., Regolith Layer Thickness Mapping of the Moon by Radar and Optical Data. *Icarus*, vol. 149, no. 2, pp. 329-338, 2001.
337. Sikdar, M. and Cumming, I., A Modified Empirical Model for Soil Moisture Estimation in Vegetated Areas Using SAR Data, Proceedings of *IEEE International Geoscience and Remote Sensing Symposium (IGARSS)*, Anchorage, USA, 2004, vol. 2, pp. 803-806.
338. Simard, M., Saatchi, S.S., and De Grandi, G., The Use of Decision Tree and Multiscale Texture for Classification of JERS-1 SAR Data Over Tropical Forest. *IEEE Transactions on Geoscience and Remote Sensing*, vol. 38, no. 5, pp. 2310-2321, 2000.
339. Sinclair, G., The Transmission and Reception of Elliptically Polarized Waves. *Proceedings of the IRE*, vol. 38, no. 2, pp. 148-151, 1950.
340. Singh, D., Polarization Discrimination Ratio Approach to Retrieve Bare Soil Moisture at X-band, Proceedings of *IEEE International Geoscience and Remote Sensing Symposium (IGARSS)*, Seoul, Korea, 2005, vol. 1, pp. 4 pp.
341. Singh, D. and Kathpalia, A., An Efficient Modeling With GA Approach to Retrieve Soil Texture, Moisture and Roughness From ERS-2 SAR Data. *Progress In Electromagnetics Research*, vol. 77, pp. 121-136, 2007.
342. Singh, D., Singh, K.P., Herlin, I., and Sharma, S.K., Ground-Based Scatterometer Measurements of Periodic Surface Roughness and Correlation Length for Remote Sensing. *Advances in Space Research*, vol. 32, no. 11, pp. 2281-2286, 2003.

343. Singh, D., Yamaguchi, Y., Yamada, H., and Singh, K.P., Response of Microwave on Bare Soil Moisture and Surface Roughness by X-Band Scatterometer. *IEICE Transactions on Communications*, vol. 83, no. 9, pp. 2038-2043, 2000.
344. Singh, G., Yamaguchi, Y., and Park, S.E., General Four-Component Scattering Power Decomposition With Unitary Transformation of Coherency Matrix. *IEEE Transactions on Geoscience and Remote Sensing*, vol. 51, no. 5, pp. 3014-3022, 2013.
345. Singh, K.P., Monitoring of Oil Spills Using Airborne and Spaceborne Sensors. *Advances in Space Research*, vol. 15, no. 11, pp. 101-110, 1995.
346. Singh, K.P., Gray, A.L., Hawkins, R.K., and O'Neil, R.A., The Influence of Surface Oil on C-and Ku-Band Ocean Backscatter. *IEEE Transactions on Geoscience and Remote Sensing*, vol. GE-24, no. 5, pp. 738-744, 1986.
347. Singh, N., Singh, T.N., Tiwary, A., and Sarkar, K.M., Textural Identification of Basaltic Rock Mass using Image Processing and Neural Network. *Computational Geosciences*, vol. 14, no. 2, pp. 301-310, 2010.
348. Singh, R., Vishal, V., Singh, T.N., and Ranjith, P.G., A Comparative Study of Generalized Regression Neural Network Approach and Adaptive Neuro-Fuzzy Inference Systems for Prediction of Unconfined Compressive Strength of Rocks. *Neural Computing and Applications*, vol. 23, no. 2, pp. 499-506, 2013.
349. Singh, T.N., Artificial Neural Network Approach for Prediction and Control of Ground Vibrations in Mines. *Mining Technology*, vol. 113, no. 4, pp. 251-256, 2004.
350. Sinha, S., Singh, T.N., Singh, V.K., and Verma, A.K., Epoch Determination For Neural Network by Self-Organized Map (SOM). *Computational Geosciences*, vol. 14, no. 1, pp. 199-206, 2010.
351. Skriver, H., Dall, J., Le Toan, T., Quegan, S., Ferro-Famil, L., Pottier, E., Lumsdon, P., et al., Agriculture Classification Using POLSAR Data, Proceedings of *PolINSAR, ESA Special Publication*, Frascati, Italy, 2005, vol. 586, pp. 32.
352. Slade, M.A., Butler, B.J., and Muhleman, D.O., Mercury Radar Imaging: Evidence for Polar Ice. *Science*, vol. 258, no. 5082, pp. 635-640, 1992.
353. Song, K., Zhou, X., and Fan, Y., Empirically Adopted IEM for Retrieval of Soil Moisture From Radar Backscattering Coefficients. *IEEE Transactions on Geoscience and Remote Sensing*, vol. 47, no. 6, pp. 1662-1672, 2009.
354. Song, K., Zhou, X., and Fan, Y., Retrieval of Soil Moisture Content From Microwave Backscattering Using a Modified IEM Model. *Progress In Electromagnetics Research B*, vol. 26, pp. 383-399, 2010.
355. Souyris, J.C., Imbo, P., Fjortoft, R., Mingot, S., and Lee, J.S., Compact Polarimetry Based on Symmetry Properties of Geophysical Media: The $\pi/4$ Mode. *IEEE Transactions on Geoscience and Remote Sensing*, vol. 43, no. 3, pp. 634-646, 2005.
356. Souyris, J.C. and Mingot, S., Polarimetry Based on One Transmitting and Two Receiving Polarizations: The $\pi/4$ Mode, Proceedings of *IEEE International Geoscience and Remote Sensing Symposium (IGARSS)*, Toronto, Canada, 2002, vol. 1, pp. 629-631.
357. Spudis, P., Nozette, S., Bussey, B., Raney, K., Winters, H., Lichtenberg, C.L., Marinelli, W.M., et al., Mini-SAR: An Imaging Radar Experiment for the Chandrayaan-1 Mission to the Moon. *Current Science*, vol. 96, pp. 533-539, 2009.
358. Spudis, P.D. Ice on the Moon. The Space Review, 2006, Updated on: [Accessed on July 25, 2011]; Available from: http://www.thespacereview.com/article/740/1.
359. Spudis, P.D., Bussey, D.B.J., Baloga, S.M., Butler, B.J., Carl, D., Carter, L.M., Chakraborty, M., et al., Initial Results for the North Pole of the Moon From Mini-SAR,

Chandrayaan-1 Mission. *Geophysical Research Letters*, vol. 37, no. 6, pp. L06204, 2010.
360. Stacy, N.J.S. and Campbell, D.B., Stokes Vector Analysis of Lunar Radar Backscatter, Proceedings of *IEEE International Geoscience and Remote Sensing Symposium (IGARSS)*, Tokyo, Japan, 1993, pp. 30-32.
361. Stacy, N.J.S., Campbell, D.B., and Ford, P.G., Arecibo Radar Mapping of the Lunar Poles: A Search for Ice Deposits. *Science*, vol. 276, no. 5318, pp. 1527-1530, 1997.
362. Steele-Dunne, S.C., Friesen, J., and van de Giesen, N., Using Diurnal Variation in Backscatter to Detect Vegetation Water Stress. *IEEE Transactions on Geoscience and Remote Sensing*, vol. 50, no. 7, pp. 2618-2629, 2012.
363. Sun, W., Three New Implementations of the Triangular Prism Method for Computing the Fractal Dimension of Remote Sensing Images. *Photogrammetric Engineering and Remote Sensing*, vol. 72, no. 4, pp. 373, 2006.
364. Sun, W., Xu, G., Gong, P., and Liang, S., Fractal Analysis of Remotely Sensed Images: A Review of Methods and Applications. *International Journal of Remote Sensing*, vol. 27, no. 22, pp. 4963-4990, 2006.
365. Sunshine, J.M., Farnham, T.L., Feaga, L.M., Groussin, O., Merlin, F., Milliken, R.E., and A'Hearn, M.F., Temporal and Spatial Variability of Lunar Hydration As Observed by the Deep Impact Spacecraft. *Science*, vol. 326, no. 5952, pp. 565-568, 2009.
366. Swaminathan, V., Gairola, R.M., Balaji, C., Agarwal, V.K., and Venkateshan, S.P., Inverse Radiation Problem to Retrieve Hydrometeors From Satellite Microwave Radiances. *International Journal of Heat and Mass Transfer*, vol. 51, no. 7, pp. 1933-1945, 2008.
367. Taconet, O., Vidal-Madjar, D., Emblanch, C., and Normand, M., Taking into Account Vegetation Effects to Estimate Soil Moisture From C-Band Radar Measurements. *Remote Sensing of Environment*, vol. 56, no. 1, pp. 52-56, 1996.
368. Tetuko, S.S.J., Tateishi, R., and Takeuchi, N., Estimation of Burnt Coal Seam Thickness in Central Borneo Using JERS-1 SAR Data. *International Journal of Remote Sensing*, vol. 24, no. 4, pp. 879-884, 2003.
369. Tetuko, S.S.J., Tateishi, R., and Takeuchi, N., A Physical Method to Analyse Scattered Waves From Burnt Coal Seam and its Application to Estimate Thickness of Fire Scars in Central Borneo Using L-Band SAR Data. *International Journal of Remote Sensing*, vol. 24, no. 15, pp. 3119-3136, 2003.
370. Thompson, T.W., Ustinov, E.A., and Heggy, E., Modeling Radar Scattering From Icy Lunar Regoliths at 13 cm and 4 cm Wavelengths. *Journal of Geophysical Research*, vol. 116, no. E01006, pp. 1-27, 2011.
371. Thompson, T.W., Ustinov, E.A., Spudis, P.D., and Fessler, B.W., Modeling of Radar Backscatter From Icy and Rough Lunar Craters, Proceedings of *Lunar and Planetary Institute Science Conference Abstracts*, The Woodlands,Texas, 2012, vol. 43, pp. 1069.
372. Thomson, B.J., Bussey, D.B.J., Neish, C.D., Cahill, J.T.S., Heggy, E., Kirk, R.L., Patterson, G.W., et al., An Upper Limit for Ice in Shackleton Crater as Revealed by LRO Mini-RF Orbital Radar. *Geophysical Research Letters*, vol. 39, no. 14, 2012.
373. Topp, G.C., Davis, J.L., and Annan, A.P., Electromagnetic Determination of Soil Water Content: Measurements in Coaxial Transmission Lines. *Water Resources Research*, vol. 16, no. 3, pp. 574-582, 1980.
374. Touzi, R., Target Scattering Decomposition in Terms of Roll-Invariant Target Parameters. *IEEE Transactions on Geoscience and Remote Sensing*, vol. 45, no. 1, pp.

73-84, 2007.
375. Touzi, R., Compact-Hybrid Versus Linear-Dual and Fully Polarimetric SAR, Proceedings of *Proceedings of POLinSAR*, Frascati, Italy 2009, vol. 9.
376. Touzi, R., Bhattacharya, A., and Mattar, K., Multi-Resolution Target Scattering Decomposition for Urban Feature Characterization Using Polarimetric SARs, Proceedings of *IEEE International Geoscience and Remote Sensing Symposium (IGARSS)*, Cape Town, South Africa, 2009, vol. 4, pp. IV-857-IV-860.
377. Touzi, R., Boerner, W.M., Lee, J.S., and Lueneburg, E., A Review of Polarimetry in the Context of Synthetic Aperture Radar: Concepts and Information Extraction. *Canadian Journal of Remote Sensing*, vol. 30, no. 3, pp. 380-407, 2004.
378. Tragl, K., Polarimetric Radar Backscattering From Reciprocal Random Targets. *IEEE Transactions on Geoscience and Remote Sensing*, vol. 28, no. 5, pp. 856-864, 1990.
379. Tragl, K., Optimal Polarizations for Reciprocal Random Targets, in *Direct and Inverse Methods in Radar Polarimetry*, Boerner, W.M., et al., Editors. Springer: Netherlands, vol. 350, pp. 693-706, 1992.
380. Trudel, M., Charbonneau, F., and Leconte, R., Surface Roughness Classification With Multipolarized C-Band SAR Data, Proceedings of *IEEE International Geoscience and Remote Sensing Symposium (IGARSS)*, Boston, USA, 2008, vol. 2, pp. II-727-II-730.
381. Trudel, M., Charbonneau, F., and Leconte, R., Using RADARSAT-2 Polarimetric and ENVISAT-ASAR Dual-Polarization Data for Estimating Soil Moisture Over Agricultural Fields. *Canadian Journal of Remote Sensing*, vol. 38, no. 04, pp. 514-527, 2012.
382. Tseng, M.H., Chen, S.J., Hwang, G.H., and Shen, M.Y., A Genetic Algorithm Rule-Based Approach for Land-Cover Classification. *ISPRS Journal of Photogrammetry and Remote Sensing*, vol. 63, no. 2, pp. 202-212, 2008.
383. Turiel, A., Yahia, H., and Pérez-Vicente, C.J., Microcanonical Multifractal Formalism—A Geometrical Approach to Multifractal Systems: Part I. Singularity Analysis. *Journal of Physics A: Mathematical and Theoretical*, vol. 41, no. 1, pp. 015501, 2008.
384. Tzeng, Y.C. and Chen, K.S., A Fuzzy Neural Network to SAR Image Classification. *IEEE Transactions on Geoscience and Remote Sensing*, vol. 36, no. 1, pp. 301-307, 1998.
385. Uhlmann, S. and Kiranyaz, S., Integrating Color Features in Polarimetric SAR Image Classification. *IEEE Transactions on Geoscience and Remote Sensing*, vol. 52, no. 4, pp. 2197-2216, 2013.
386. Uhlmann, S. and Kiranyaz, S., Classification of Dual- and Single-Polarized SAR Images by Incorporating Visual Features. *ISPRS Journal of Photogrammetry and Remote Sensing*, vol. 90, pp. 10-22, 2014.
387. Ulaby, F.T., Moore, R.K., and Fung, A.K., Radar Remote Sensing and Surface Scattering and Emission Theory, in *Microwave Remote Sensing: Active and Passive*. Artech House: Boston, USA, vol. 2, 1982.
388. Ulaby, F.T., Moore, R.K., and Fung, A.K., Volume Scattering and Emission Theory, Advanced Systems and Applications, in *Microwave Remote Sensing: Active and Passive*. Artech House: Boston, USA, vol. 3, 1986.
389. Ulaby, F.T., Sarabandi, K., McDonald, K., Whitt, M., and Dobson, M.C., Michigan Microwave Canopy Scattering Model. *International Journal of Remote Sensing*, vol. 11, no. 7, pp. 1223-1253, 1990.
390. van Beijma, S., Comber, A., and Lamb, A., Random Forest Classification of Salt Marsh

Vegetation Habitats Using Quad-Polarimetric Airborne SAR, Elevation and Optical RS Data. *Remote Sensing of Environment*, vol. 149, no. 0, pp. 118-129, 2014.
391. Van Oevelen, P.J., Soil Moisture Variability: A Comparison Between Detailed Field Measurements and Remote Sensing Measurement Techniques. *Hydrological Sciences Journal*, vol. 43, no. 4, pp. 511-520, 1998.
392. van Zyl, J.J., Unsupervised Classification of Scattering Behavior Using Radar Polarimetry Data. *IEEE Transactions on Geoscience and Remote Sensing*, vol. 27, no. 1, pp. 36-45, 1989.
393. van Zyl, J.J., Application of Cloude's Target Decomposition Theorem to Polarimetric Imaging Radar Data, Proceedings of *SPIE*, San Diego, 1992, vol. 1748, pp. 184-191.
394. van Zyl, J.J., Arii, M., and Yunjin, K., Model-Based Decomposition of Polarimetric SAR Covariance Matrices Constrained for Nonnegative Eigenvalues. *IEEE Transactions on Geoscience and Remote Sensing*, vol. 49, no. 9, pp. 3452-3459, 2011.
395. van Zyl, J.J., Kim, Y., and Arii, M., Requirements for Model-Based Polarimetric Decompositions, Proceedings of *IEEE International Geoscience and Remote Sensing Symposium (IGARSS)* Boston, Massachusetts, USA, 2008, vol. 5, pp. 417-420.
396. van Zyl, J.J., Zebker, H.A., and Elachi, C., Imaging Radar Polarization Signatures: Theory and Observation. *Radio Science*, vol. 22, no. 4, pp. 529-543, 1987.
397. Varma, A.K. and Liu, G., A Near-Global Survey of the Horizontal Varibility of Rainfall. *Monthly Weather Review*, 2004.
398. Varma, A.K. and Liu, G., Small-Scale Horizontal Rain-Rate Variability Observed by Satellite. *Monthly Weather Review*, vol. 134, no. 10, pp. 2722-2733, 2006.
399. Varma, A.K. and Liu, G., On Classifying Rain Types Using Satellite Microwave Observations. *Journal of Geophysical Research*, vol. 115, no. D7, 2010.
400. Vasavada, A.R., Paige, D.A., and Wood, S.E., Near-Surface Temperatures on Mercury and the Moon and the Stability of Polar Ice Deposits. *Icarus*, vol. 141, no. 2, pp. 179-193, 1999.
401. Verhoest, N.E.C., De Baets, B., and Vernieuwe, H., A Takagi–Sugeno Fuzzy Rule-Based Model for Soil Moisture Retrieval From SAR Under Soil Roughness Uncertainty. *IEEE Transactions on Geoscience and Remote Sensing*, vol. 45, no. 5, pp. 1351-1360, 2007.
402. Verhoest, N.E.C. and Lievens, H., Soil Moisture Retrieval From Synthetic Aperture Radar: Facing the Soil Roughness Parameterization Problem, in *Remote Sensing of Energy Fluxes and Soil Moisture Content*. CRC Press, pp. 323, 2013.
403. Verhoest, N.E.C., Lievens, H., Wagner, W., Álvarez-Mozos, J., Moran, M.S., and Mattia, F., On the Soil Roughness Parameterization Problem in Soil Moisture Retrieval of Bare Surfaces From Synthetic Aperture Radar. *Sensors*, vol. 8, no. 7, pp. 4213-4248, 2008.
404. Voronovich, A., Small-Slope Approximation for Electromagnetic Wave Scattering at a Rough Interface of Two Dielectric Half-Spaces. *Waves in Random Media*, vol. 4, no. 3, pp. 337-367, 1994.
405. Wagner, W. and Pathe, C., Has SAR Failed in Soil Moisture Retrieval?, Proceedings of *ENVISAT & ERS Symposium*, Salzburg, Austria, 2004, pp. 6-10.
406. Walker, J.P., Houser, P.R., and Willgoose, G.R., Active Microwave Remote Sensing for Soil Moisture Measurement: A Field Evaluation Using ERS-2. *Hydrological Processes*, vol. 18, no. 11, pp. 1975-1997, 2004.
407. Walker, J.P., Troch, P.A., Mancini, M., Willgoose, G.R., and Kalma, J.D., Profile Soil Moisture Estimation Using the Modified IEM, Proceedings of *IEEE International*

Geoscience and Remote Sensing Symposium (IGARSS), Singapore, 1997, vol. 3, pp. 1263-1265.

408. Wang, C., Qi, J., Moran, S., and Marsett, R., Soil moisture Estimation in a Semiarid Rangeland Using ERS-2 and TM Imagery. *Remote Sensing of Environment*, vol. 90, no. 2, pp. 178-189, 2004.
409. Wang, J.R., Hsu, A., Shi, J.C., O'Neill, P.E., and Engman, E.T., A Comparison of Soil Moisture Retrieval Models Using SIR-C Measurements Over the Little Washita River Watershed. *Remote Sensing of Environment*, vol. 59, no. 2, pp. 308-320, 1997.
410. Wang, J.R. and Schmugge, T.J., An Empirical Model for the Complex Dielectric Permittivity of Soils as a Function of Water Content. *IEEE Transactions on Geoscience and Remote Sensing*, vol. 8, no. 4, pp. 288-295, 1980.
411. Wang, S.G., Li, X., Han, X.J., and Jin, R., Estimation of Surface Soil Moisture and Roughness From Multi-Angular ASAR imagery in the Watershed Allied Telemetry Experimental Research (WATER). *Hydrology & Earth System Sciences*, vol. 15, no. 5, 2011.
412. Wang, Y., Day, J.L., and Davis, F.W., Sensitivity of Modeled C- and L-Band Radar Backscatter to Ground Surface Parameters in Loblolly Pine Forest. *Remote Sensing of Environment*, vol. 66, no. 3, pp. 331-342, 1998.
413. Wang, Z., Li, Y., Jiang, J., and Li, D., Lunar Surface Dielectric Constant, Regolith Thickness, and 3He Abundance Distributions Retrieved From the Microwave Brightness Temperatures of CE-1 Lunar Microwave Sounder. *Science China: Earth Sciences*, vol. 53, no. 9, pp. 1365-1378, 2010.
414. Watson, K., Murray, B.C., and Brown, H., The Behavior of Volatiles on the Lunar Surface. *Journal of Geophysical Research*, vol. 66, no. 9, pp. 3033-3045, 1961.
415. Wilson, D.J., Western, A.W., and Grayson, R.B., Identifying and Quantifying Sources of Variability in Temporal and Spatial Soil Moisture Observations. *Water Resources Research*, vol. 40, no. 2, 2004.
416. Wolf, E., Coherence Properties of Partially Polarized Electromagnetic Radiation. *Il Nuovo Cimento*, vol. 13, no. 6, pp. 1165-1181, 1959.
417. Wright, J., Yang, A.Y., Ganesh, A., Sastry, S.S., and Ma, Y., Robust Face Recognition Via Sparse Representation. *IEEE Transactions on Pattern Analysis and Machine Intelligence*, vol. 31, no. 2, pp. 210-227, 2009.
418. Wu, F., Wang, C., Zhang, H., Zhang, B., and Tang, Y., Rice Crop Monitoring in South China With RADARSAT-2 Quad-Polarization SAR Data. *IEEE Geoscience and Remote Sensing Letters*, vol. 8, no. 2, pp. 196-200, 2011.
419. Wu, T.D. and Chen, K.S., A Reappraisal of the Validity of the IEM Model for Backscattering From Rough Surfaces. *IEEE Transactions on Geoscience and Remote Sensing*, vol. 42, no. 4, pp. 743-753, 2004.
420. Wu, T.D., Chen, K.S., Shi, J., Lee, H.W., and Fung, A.K., A Study of an AIEM Model for Bistatic Scattering From Randomly Rough Surfaces. *IEEE Transactions on Geoscience and Remote Sensing*, vol. 46, no. 9, pp. 2584-2598, 2008.
421. Wu, Y., Ji, K., Yu, W., and Su, Y., Region-Based Classification of Polarimetric SAR Images Using Wishart MRF. *IEEE Geoscience and Remote Sensing Letters*, vol. 5, no. 4, pp. 668-672, 2008.
422. Xi, A.Q. and Boerner, W.M., Determination of the Characteristic Polarization States of the Radar Target Scattering Matrix [S(AB)] for the Coherent, Monostatic and Reciprocal Propagation Space Using the Polarization Ratio ρ Transformation Formulation, in *Direct and Inverse Methods in Radar Polarimetry*, Boerner, W.M., et

al., Editors. Springer Netherlands, vol. 350, pp. 297-349, 1992.
423. Xiong, H., Wu, J., and Chen, J., K-Means Clustering Versus Validation Measures: A Data-Distribution Perspective. *IEEE Transactions on Systems, Man, and Cybernetics* vol. 39, no. 2, pp. 318-331, 2009.
424. Xu, F. and Jin, Y.Q., Deorientation Theory of Polarimetric Scattering Targets and Application to Terrain Surface Classification. *IEEE Transactions on Geoscience and Remote Sensing*, vol. 43, no. 10, pp. 2351-2364, 2005.
425. Yajima, Y., Yamaguchi, Y., Sato, R., Yamada, H., and Boerner, W.M., POLSAR Image Analysis of Wetlands Using a Modified Four-Component Scattering Power Decomposition. *IEEE Transactions on Geoscience and Remote Sensing*, vol. 46, no. 6, pp. 1667-1673, 2008.
426. Yamaguchi, Y., Moriyama, T., Ishido, M., and Yamada, H., Four-Component Scattering Model for Polarimetric SAR Image Decomposition. *IEEE Transactions on Geoscience and Remote Sensing*, vol. 43, no. 8, pp. 1699-1706, 2005.
427. Yamaguchi, Y., Sato, A., Boerner, W.M., Sato, R., and Yamada, H., Four-Component Scattering Power Decomposition With Rotation of Coherency Matrix. *IEEE Transactions on Geoscience and Remote Sensing*, vol. 49, no. 6, pp. 2251-2258, 2011.
428. Yamaguchi, Y., Yajima, Y., and Yamada, H., A Four-Component Decomposition of PolSAR Images Based on the Coherency Matrix. *IEEE Geoscience and Remote Sensing Letters*, vol. 3, no. 3, pp. 292-296, 2006.
429. Yan, W.L. and Boerner, W.M., Optimal Polarization States Determination of the Stokes Reflection Matrices [Mp] for the Coherent Case, and of the Mueller Matrix [M] for the Partially Polarized Case, in *Direct and Inverse Methods in Radar Polarimetry*, Boerner, W.M., et al., Editors. Springer Netherlands, vol. 350, pp. 351-385, 1992.
430. Yang, J., Peng, Y.N., Yamaguchi, Y., and Yamada, H., On Huynen's Decomposition of a Kennaugh Matrix. *IEEE Geoscience and Remote Sensing Letters*, vol. 3, no. 3, pp. 369-372, 2006.
431. You, B., Yang, J., Yin, J., and Xu, B., Decomposition of the Kennaugh Matrix Based on a New Norm. *IEEE Geoscience and Remote Sensing Letters*, vol. 11, no. 5, pp. 1000-1004, 2014.
432. Yu, P., Qin, A.K., and Clausi, D.A., Unsupervised Polarimetric SAR Image Segmentation and Classification Using Region Growing With Edge Penalty. *IEEE Transactions on Geoscience and Remote Sensing*, vol. 50, no. 4, pp. 1302-1317, 2012.
433. Yuan, H., Zhang, R., and Li, X., Extracting Wetland Using Decision Tree Classification, Proceedings of *8th WSEAS International Conference on Applied Computer and Applied Computational Science*, Hangzhou, Zhejiang, China, 2009, pp. 240-245.
434. Yueh, S.H., Kong, J.A., Jao, J.K., Shin, R.T., and Novak, L.M., K-Distribution and Polarimetric Terrain Radar Clutter. *Journal of Electromagnetic Waves and Applications*, vol. 3, no. 8, pp. 747-768, 1989.
435. Yun-gang, C., Li-juan, Y., and Ze-zhong, Z., Extraction of Information on Geology Hazard From Multi-Polarization SAR Images, Proceedings of *ISPRS Congress*, Beijing, China, 2008, vol. 37, pp. 1529–1532.
436. Yunjin, K. and van Zyl, J.J., A Time-Series Approach to Estimate Soil Moisture Using Polarimetric Radar Data. *IEEE Transactions on Geoscience and Remote Sensing*, vol. 47, no. 8, pp. 2519-2527, 2009.
437. Zebker, H.A. and van Zyl, J.J., Imaging Radar Polarimetry: A Review. *Proceedings of the IEEE*, vol. 79, no. 11, pp. 1583-1606, 1991.

438. Zebker, H.A., van Zyl, J.J., and Held, D.N., Imaging Radar Polarimetry From Wave Synthesis. *Journal of Geophysical Research*, vol. 92, no. B1, pp. 683-701, 1987.
439. Zhang, L., Zhang, J., Zou, B., and Zhang, Y., Comparison of Methods for Target Detection and Applications Using Polarimetric SAR Image. *PIERS Online*, vol. 4, no. 1, pp. 140-145, 2008.
440. Zhang, L., Zou, B., Cai, H., and Zhang, Y., Multiple-Component Scattering Model for Polarimetric SAR Image Decomposition. *IEEE Geoscience and Remote Sensing Letters*, vol. 5, no. 4, pp. 603-607, 2008.
441. Zhang, L., Zou, B., Zhang, J., and Zhang, Y., Classification of Polarimetric SAR Image Based on Support Vector Machine Using Multiple-Component Scattering Model and Texture Features. *EURASIP Journal on Advances in Signal Processing*, vol. 2010, pp. 1, 2010.
442. Zhihao, J., Jian, Y., Chunmao, Y., and Jianshe, S., Modified Three-Component Decomposition Method for Polarimetric SAR Data. *IEEE Geoscience and Remote Sensing Letters*, vol. 11, no. 1, pp. 200-204, 2013.
443. Zhu, X., Semi-Supervised Learning Literature Survey. *Computer Science, University of Wisconsin-Madison*, vol. 2, pp. 1-59, 2006.
444. Zou, T., Yang, W., Dai, D., and Sun, H., Polarimetric SAR Image Classification Using Multifeatures Combination and Extremely Randomized Clustering Forests. *EURASIP Journal on Advances in Signal Processing*, vol. 2010, pp. 4, 2010.
445. Zribi, M. and Dechambre, M., A New Empirical Model to Retrieve Soil Moisture and Roughness From C-Band Radar Data. *Remote Sensing of Environment*, vol. 84, no. 1, pp. 42-52, 2003.
446. Zribi, M., Gorrab, A., Baghdadi, N., Lili-Chabaane, Z., and Mougenot, B., Influence of Radar Frequency on the Relationship Between Bare Surface Soil Moisture Vertical Profile and Radar Backscatter. *IEEE Transactions on Geoscience and Remote Sensing*, vol. 11, no. 4, pp. 848-852, 2014.
447. Zwick, T., Haala, J., and Wiesbeck, W., A Genetic Algorithm for the Evaluation of Material Parameters of Compound Multilayered Structures. *IEEE Transactions on Microwave Theory and Techniques*, vol. 50, no. 4, pp. 1180-1187, 2002.